

Multivalent interaction-mediated biocolloidal assembly, catalysis, and phoresis

EKTA SHANDILYA

A thesis submitted for the partial fulfillment of the degree

of

Doctor of Philosophy



Department of Chemical Sciences

Indian Institute of Science Education and Research Mohali

Knowledge city, Sector 81, SAS Nagar, Manauli PO, Mohali

140306, Punjab, India

August 2023

Dedicated to
my family

Declaration

The work presented in this thesis has been carried out by me under the guidance of Dr. Subhabrata Maiti at the Indian Institute of Science Education and Research Mohali. This work has not been submitted in part or in full for a degree, a diploma, or a fellowship to any other university or institute. Whenever contributions of others are involved, every effort is made to indicate this clearly, with due acknowledgment of collaborative research and discussions. This thesis is a bonafide record of original work done by me and all sources listed within have been detailed in the bibliography.

EKTA SHANDILYA

Date:

Place:

In my capacity as the supervisor of the candidate's thesis work, I certify that the above statements by the candidate are true to the best of my knowledge.

DR. SUBHABRATA MAITI

Date:

Place:

Acknowledgments

The successful completion of this thesis is a direct result of the incredible support and collaboration from a lot of people. I would like to take this moment to express my deepest appreciation to all those who have stood by my side throughout this momentous journey. I am truly grateful to every person I have had the privilege of working with, as your contributions have played a pivotal role in shaping the outcome. Without your dedicated efforts, the trajectory would have taken a different course, but I am genuinely pleased with the way things have turned out.

First and foremost, I would like to thank my Ph.D. supervisor, Dr. Subhabrata Maiti. I am immensely grateful for his unwavering support and invaluable guidance throughout this journey. Under his mentorship, I discovered the realm of theoretical modeling, a pursuit that I never thought possible. It was his consistent encouragement that propelled me to step outside my comfort zone and pushed me to explore and simulate using advanced softwares, exceedingly even my wildest dreams. I cannot express enough gratitude for his belief in my abilities and for continuously reminding me that I had the potential to excel. His relentless pursuit of understanding and intellectual curiosity has always inspired me to strive for excellence. The stimulating discussions we have shared will forever hold a cherished place in my heart, as they have shaped my growth and deepened my understanding of the subject. Thank you for fostering an environment of intellectual stimulation and for continually motivating me to reach new heights. Thank you for your exceptional patience during this entire process. Although there are countless reasons to be thankful, it is impossible to name them all. I simply want to convey my heartfelt appreciation for being the best PI I could have ever asked for.

I thank the members of my doctoral committee, Dr. Santanu Kumar Pal and Dr. Sabyasachi Rakshit for their support, evaluation, and valuable suggestion on my thesis work.

I would like to express my sincere appreciation to Dr. Bhargav Rallabandi from the University of California, Riverside, U.S.A. for his invaluable insights and theoretical contributions to Chapter 4. His thoughtful suggestions have significantly enhanced the quality and depth of the work presented in this section. I am grateful for his expertise and the collaborative spirit which enriched the overall content of the chapter. Thank you for your valuable contributions to this work.

I owe special thanks to Priyanka and Basundhara Dasgupta for their contribution to my thesis work.

I wholeheartedly thank all the present and past members of BioSystemsChem Lab. I consider myself fortunate to be part of a group that is more like a family to me. I thank Kalpana, Sheetal, Priyanka, Rishi, Nandha, Arshdeep, Shikha, Akshi, Neetu, Surinder, Reena, Anuj, Basundhara, Yashoda, Amit Suraj, and Himanshu for being the best colleagues and a dear friend. You all hold a special place in my heart. Your presence and contributions have made my journey truly extraordinary, filled with countless cherished moments. I am immensely grateful for the opportunity to have learned so much from each one of you. Thank you for being an integral part of my journey and for enriching it in ways I could have never imagined.

I also take this opportunity to have friends for providing me the comfort of home during my stay at IISER Mohali. I want to thank Sandeep K. Rai and Roopali Khanna for being there for me through both the ups and downs. They have been steadfast companions, offering their unwavering support during my moments of vulnerability. Whether sharing laughter or shedding tears together, they are the epitome of true friends. I owe a special acknowledgment to Sandeep, who has consistently been a friend in need. From pointing out where I went wrong to guiding me on how to make things right, his counsel has been invaluable. I am truly grateful for his presence in my life. I would also like to extend my gratitude to Dipankar, Ashish, Lisha, and Anamika for playing the role of stress busters during moments of crisis. Their presence and support have been a source of immense relief and comfort during challenging times. Life would not have been so easy and joyful without them.

Finally, I want to express my heartfelt gratitude to my family, whose unwavering presence has been the cornerstone of my journey. Their blessings, support, and unconditional love have made every step of this path very easy. My mother has been my guiding light, teaching me the virtues of resilience and self-reliance. My father has always taken immense pride in my achievements and has provided me with nothing but the best. My brother has stood by my side, offering guidance, and serving as a beacon of light. My sister has been my closest confidante, offering support and understanding. I also want to extend my thanks to my grandparents for showering me with love and affection. With a heavy heart and teary eyes, I want to express my gratitude to both my maternal and paternal grandfathers, Late Mr. T.C. Sharma, and Late Mr. Hargyan Sharma, respectively. They eagerly anticipated witnessing my graduation when I first began this journey, but could not. I want to sincerely thank them for their love, blessings, and

the immense pride they always had in me. In every possible way, I want to acknowledge and thank my family for everything they have done for me. It is because of their unwavering support and sacrifices that I am who I am today. To my family, I dedicate this thesis as a testament to their love, support, and belief in me.

Ekta Shandilya

Synopsis

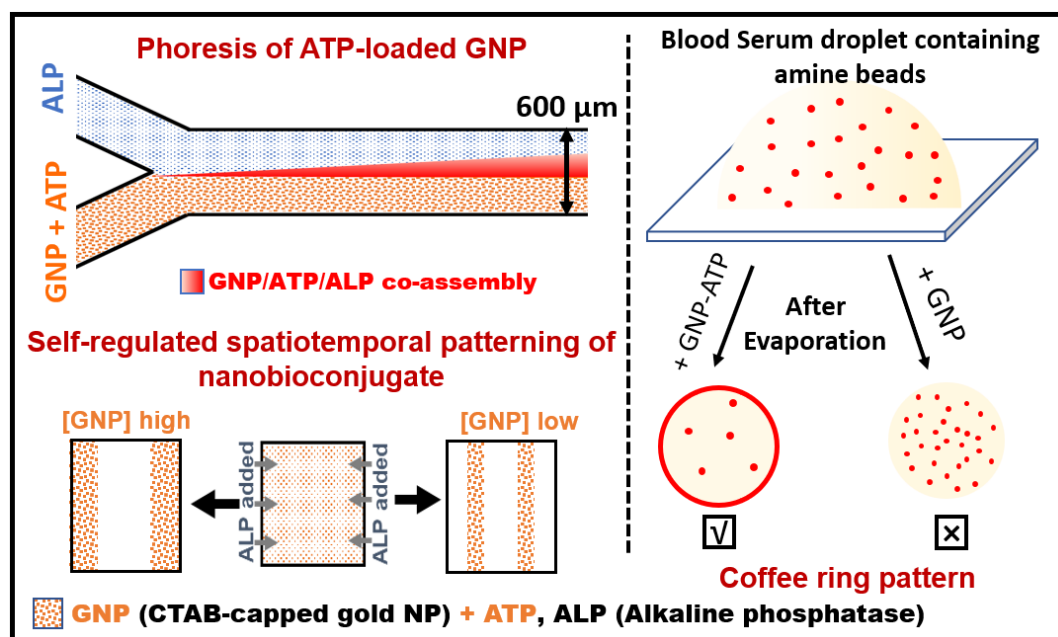
Chapter 1. Multivalent Interactions and their Cross-Domain Utility

Multivalent interactions, characterized by the simultaneous binding of multiple ligands to a receptor, have garnered significant attention in the fields of chemistry and biology due to their diverse functional implications. These interactions enable molecules or ions to engage in simultaneous and cooperative binding events, leading to enhanced affinity and selectivity. In biological systems, multivalency is a fundamental property of biomolecules like proteins, enzymes, and antibodies, allowing them to participate in complex signaling cascades and perform multiple tasks concurrently. Furthermore, multivalent interactions have found applications in chemistry and materials science, where they have been harnessed to design self-assembling materials and optimize drug efficacy by targeting multiple receptors or signaling pathways. Despite the extensive exploration of multivalent interactions in various fields, their impact on colloidal assembly, catalysis, and phoresis remains relatively understudied. By unraveling the intricacies of multivalent interactions in the realms of colloidal assembly, catalysis, and phoresis, we can unlock a wealth of possibilities. These include the development of tailored materials with controlled properties, the design of efficient catalysts for sustainable chemical transformations, and the creation of smart systems for precise drug delivery. Additionally, a deeper understanding of multivalent interactions in these areas can pave the way for advancements in nanotechnology, biomedicine, and materials science, ultimately leading to innovative solutions and transformative breakthroughs in these fields. In this thesis, we explore the role of multivalent interactions in patterning of colloids at both micro/macro-scale modulated by enzymatic action both experimentally and theoretically. We also deconvolute the dynamic nature intermediate species formed during multistep assembly formation.

Chapter 2. Self-regulatory Enzyme-actuated Micro/Macroscale Patterning of ATP-loaded Nanoparticle

Directional interactions and the precise assembly of colloids at specific locations are critical for applications such as patterning and microarrays. Here, we focus on developing strategies to achieve self-assembly and spatial control in surface patterning leveraging enzyme-substrate interaction. These efforts aim to enable precise patterning at both micro- and macroscale

environments, offering opportunities for controlled biomedical applications. In this study, we introduce two key factors that govern the self-assembly and spatial control of surfactant-functionalized nanoparticles in both micro- and macroscale environments: the synergistic affinity between enzymes, substrates, and nanoparticles, and the phoretic effect. The specific focus of this study revolves around the affinity between alkaline phosphatase (ALP) enzyme and its adenosine nucleotide-based substrates, namely adenosine mono/di/triphosphate (AM/D/TP). These substrates are noncovalently bound to the surface of nanoparticles, thereby facilitating the assembly of the overall ensemble in a spatiotemporally controllable manner. By utilizing this synergistic interactivity, we investigate the coexistence of assembly and patterning of both nanoparticles and enzymes within microfluidic channels and on glass slides. Furthermore, we explore the modulation of the coffee ring pattern, a characteristic phenomenon observed during the evaporation of colloidal droplets on a glass surface. The presence of ATP-loaded nanoparticles with enzymes influences the pattern formation, and we extend this effect to the drying of blood serum droplets, highlighting the potential for low-cost, on-the-spot disease diagnostics. Overall, these studies shed light on the aggregation and spatial patterning of nanoparticles and enzymes in microfluidic systems. The findings suggest the presence of synergistic interactions, diffusiophoretic effects, and catalytic conditions that contribute to the observed aggregation patterns. These insights have potential implications for the development of microfluidic-based

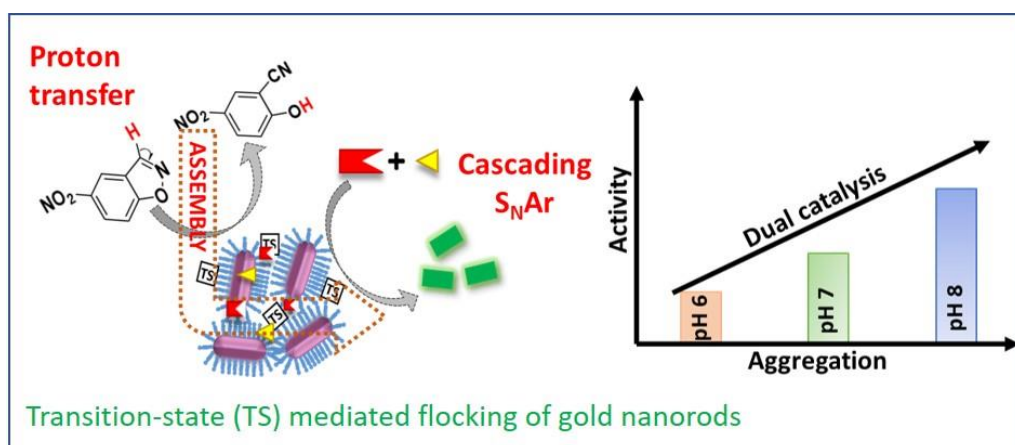


E. Shandilya, S. Maiti, *ACS Nano* 2023, 17, 5108–5120.

nanobiodevices and offer new avenues for exploring diffusiophoresis as a versatile tool for manipulating colloidal particles in chemical engineering applications.

Chapter 3. Self-Assembly of Catalytically Active Gold Nanorods: Regulating Reactivity and Demonstrating Cascading Catalytic Phenomena

Living organisms, from bacteria to birds, use communication strategies like colonization, clustering, and flocking for survival. Catalytic reactions play a crucial role in these processes, aiding the emergence of life and enabling the development of synthetic systems with desired functionalities. In this chapter, we present an exciting example of synthetic nanocatalysts capable of forming functional self-assemblies, where the catalytic process plays a central role. Specifically, cetyltrimethylammonium bromide (CTAB)-functionalized gold nanorods catalyze the Kemp Elimination (KE) reaction, a widely used model for studying biotransformation mechanisms. This catalytic conversion process leads to the enhanced flocking behavior of nanorods due to the transition state, resulting in the formation of larger assemblies. By regulating the reactivity of the nanorods towards a proton transfer reaction at different pH levels, we can control their self-assembly. The enhanced aggregation rate is attributed to the alteration of the nanorods' catalytic surface charge during reactivity. We observed an enhancement in diffusion co-efficient during reactivity which might also contribute to this assembling behavior. Additionally, our findings reveal that the nanosized hydrophobic cavities formed within the clustered nanorods can efficiently accelerate the rate of aromatic nucleophilic substitution reactions. This highlights a catalytic phenomenon that can trigger cascading reactions where the substrates and products of the initial



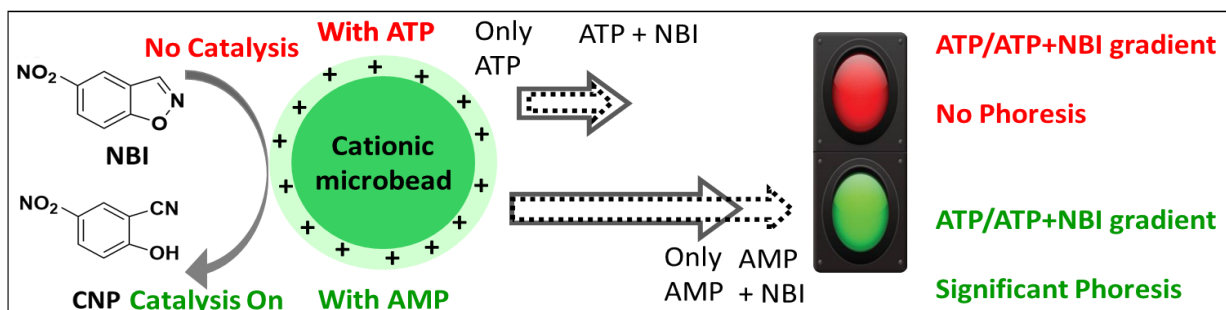
E. Shandilya, B. Dasgupta, S. Maiti, *Chem. Eur. J.* **2021**, *27*, 7831–7836.

reactions are not directly involved. Overall, this study sheds light on the dynamic nature of catalytic processes and introduces a new aspect of self-assembly in catalytically active gold nanorods. These findings enhance our understanding of dynamic catalytic processes and provides new insights into the self-assembly of catalytically active nanorods, and can have broad implications across disciplines and can inspire innovative applications in catalysis and beyond.

Chapter 4. Spatiotemporal Mapping of Colloidal Phoresis and Population Dynamics during Downregulation of Multivalent Interactivity

In cellular systems, diffusiophoretic transport of large molecules due to gradients of small molecules, such as metabolites or ATP, is ubiquitous and has recently garnered attention. Building upon this knowledge, in this chapter, we delve into the fascinating realm of multivalent interactions and their impact on colloidal transport and phoretic behavior. To understand this intriguing phenomenon, we employ a combination of theoretical models and experimental investigations. Our focus is on a fluorescent, cationic micron-sized bead (abbreviated as CMB) that exhibits diffusiophoretic motion. The CMB consists of a carboxylic acid-modified polystyrene fluorescent bead electrostatically bound with a cationic cetyltrimethylammonium bromide (CTAB)-coated gold nanorods. We explore the multivalent interaction-mediated phoretic drift of the CMB in the presence of gradients of adenosine mono-, di-, and trinucleotides (AMP/ADP/ATP) and their mixtures. Our investigations span both micro- and macroscale regimes, allowing us to gain insights into the phoretic behavior of the CMB across different length scales. Additionally, we uncover a nucleotide-specific catalytic activation behavior exhibited by the CMB. By binding to specific nucleotides, the CMB's ability to catalyze a proton-transfer reaction is either activated or deactivated, thereby directly impacting its phoretic behavior. This finding establishes a connection between catalytic activity and phoretic motion, highlighting the intricate interplay between multivalent interactions and particle transport. Moreover, we develop an autonomous system that allows for spatiotemporal control over colloidal phoretic leap—a sudden increase in the phoretic velocity. This control is achieved by precisely manipulating enzymatic in situ downregulation of multivalent interaction. By fine-tuning the hydrolysis of ATP through enzymatic regulation, we can program the occurrence and timing of the colloidal phoretic leap. This observation showcases the potential for generating spatiotemporally controlled micron-sized colloidal patterns through

the precise manipulation of multivalent interactions with small molecules, and opens up avenues for further research on multivalent interaction-mediated non-equilibrium chemistry driven by nucleotides and their impact on the motion of colloidal particles and soft matter. These findings have potential applications in designing synthetic spatiotemporally controlled catalytic systems for transportation purposes.

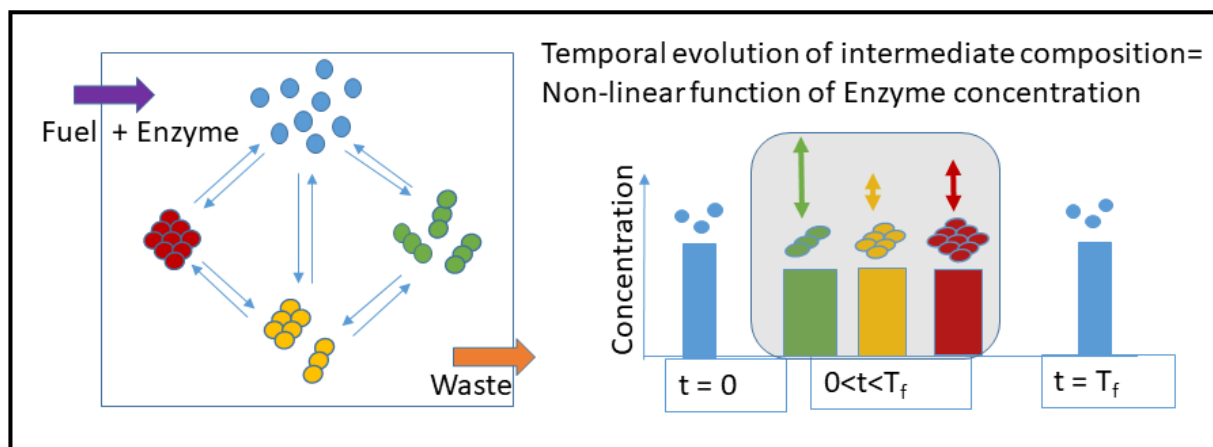


E. Shandilya, B. Rallabandi, S. Maiti, *ChemRxiv* **2023**, DOI 10.26434/chemrxiv-2023-r1djt.

Chapter 5. Kinetic Insights into Enzymatically Controlled Transiency in Multivalent Fuel-Driven Multistep Assembly

Drawing inspiration from biological systems, we explore the potential for designing synthetic systems with programmable and dynamic properties. In this chapter, we investigate multivalent fuel-driven transient self-assembly systems, aiming to unlock their potential in creating complex structures with dynamic properties. While these systems show promise, they currently fall short of the complexity found in natural systems. To bridge this gap, we focus on understanding how the composition of assembled species evolves over time and in relation to the overall dissipation strength. This knowledge is essential to fully harness the potential of fuel-responsive transient self-assembly and realize intricate systems with dynamic functionalities. To this goal, using kinetic simulation and Python-based kinetic modeling, we provide a detailed understanding of the temporal evolution of intermediate species under dissipative conditions. By modulating the strength of dissipation, we demonstrate how the compositional behavior of each intermediate species during their survival period can be finely tuned. Notably, we observe highly non-linear characteristics in the appearance and disappearance of intermediates, whether formed in the initial or penultimate assembly steps. This intriguing behavior allows us to selectively trap desired intermediates or create specific mixtures with desired compositions at predetermined time

intervals. Overall, this study advances our understanding of the intricate dynamics underlying transient self-assembly processes, while also inspiring the design of synthetic systems capable of harnessing transient and programmable properties, taking cues from the fascinating mechanisms observed in biological systems.

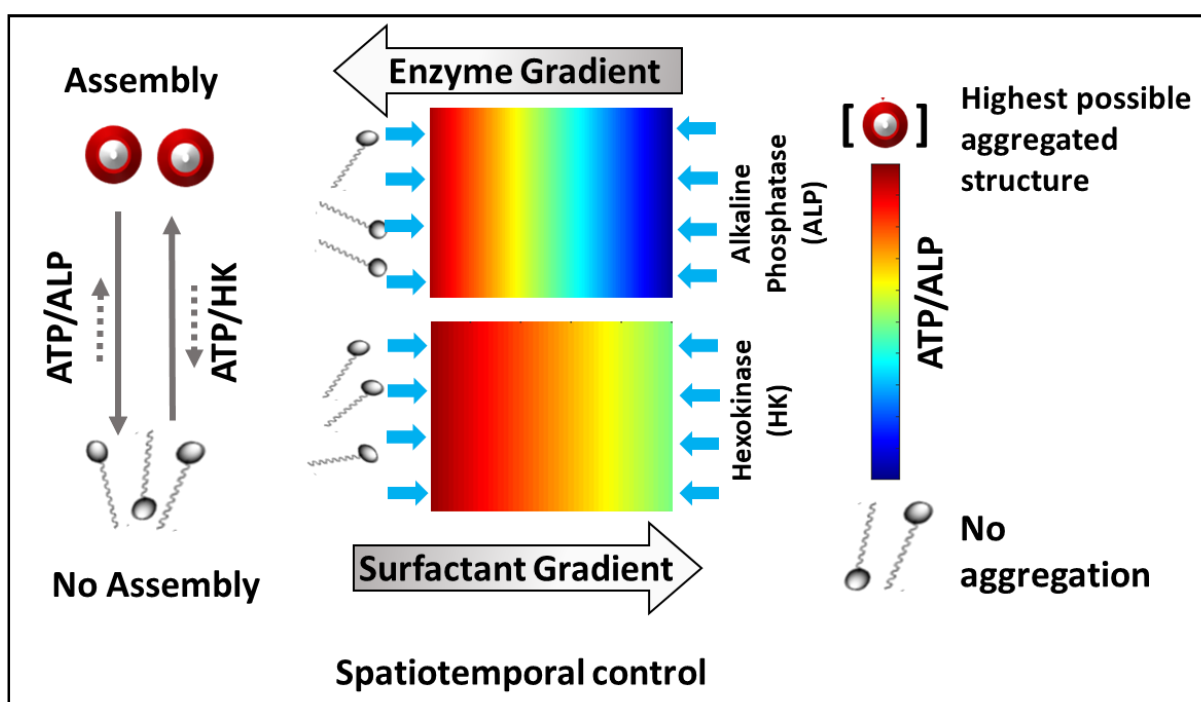


E. Shandilya, S. Maiti, *ChemSystemsChem* **2020**, 2, e1900040.

Chapter 6. Programming Spatiotemporal Organization of Nonlinear Dynamical Systems through Enzyme-Mediated Assembly Formation

The field of predicting and designing systems with dynamic self-assembling properties in a spatiotemporal fashion holds immense importance across multiple disciplines. It encompasses endeavors ranging from understanding the fundamental non-equilibrium characteristics of life to fabricating next-generation materials with life-like properties. In this context, we present a study that sheds light on the spatiotemporal dynamics of self-assembly exhibited by a surfactant, induced by the presence of adenosine triphosphate (ATP) and enzymes responsible for the degradation or conversion of ATP. Our study explores the distinct behaviors of two enzymes, alkaline phosphatase (ALP) and hexokinase (HK), in relation to the surfactant assembly driven by ATP. Surprisingly, these enzymes exhibit spatiotemporally contrasting dynamic assembly behaviors. ALP acts antagonistically, disrupting the transient self-assembling property, while HK demonstrates agonistic action, actively contributing to the sustained assembly. This revelation highlights the intriguing and complex interplay between enzymes and the self-assembled systems they influence. Exploiting this dynamic assembly behavior, we have successfully programmed the

time-dependent emergence of self-assembled structures in a two-dimensional space. This was achieved by maintaining a concentration gradient of enzymes and surfactant at different locations. The ability to spatially organize and adapt the self-organized system of interacting components opens new avenues for incorporating programmed functionality into materials. By unraveling the spatiotemporal dynamics of self-assembly and harnessing the specific behaviors of enzymes, our findings not only contribute to fundamental understanding but also paves the way for practical applications. This knowledge can guide the development of novel materials with dynamic and adaptable properties, replicating the intricacies of living systems. It also offers a promising route for engineering spatial organizational adaptability, providing a foundation for the creation of functional structures that respond to their environment in a programmable manner.



E. Shandilya¹, Priyanka¹, S. K. Brar, R. R. Mahato, S. Maiti, *Chem. Sci.* **2021**, *13*, 274–282.
(¹equally contributed)

Chapter 7. Conclusion and Future Perspectives

Multivalency plays a crucial role in dynamicity and self-assembly in biological systems. However, its influence on assembly formation, colloidal transport, and phoresis remains unexplored. We

investigated the self-assembly of cationic nanoparticles modified with surfactants, influenced by the binding of multivalent adenosine mono-, di-, and trinucleotides (AM/D/TP). This interaction was governed by the synergistic affinity between enzymes, substrates, and nanoparticles, as well as the phoretic effect. Our study revealed two types of autonomous aggregation patterns: modulation by enzyme gradients in microfluidic and macroscale conditions and surface deposition patterns using the coffee ring effect. We also utilized the coffee ring effect to introduce ATP-loaded nanoparticles into blood serum, demonstrating its potential in low-cost disease diagnostics. Furthermore, we utilized this assembly to enhance catalytic reactivity for the Kemp elimination reaction, utilizing the hydrophobic sites provided by the assembly as reactors for hydrophobic substrates. Additionally, we examined the diffusiophoretic motion of micron-sized replicas of these particles within AM/D/TP gradients in micro- and macroscale regimes. By controlling ATP hydrolysis, we achieved spatiotemporal control over colloidal phoretic leap and population dynamics, which relied on enzymatic downregulation of multivalent interactivity. We also studied the temporal evolution of intermediate species in a multi-step assembly under dissipative conditions, modulating their compositional behavior using Python-based kinetic modeling. Furthermore, we investigated the spatiotemporal dynamics of self-assembly induced by ATP and enzymes, where ALP acted antagonistically and HK showed agonistic action, leading to transient or sustained self-assemblies, respectively. This dynamic assembly behavior allowed us to program the time-dependent emergence of a self-assembled structure in a two-dimensional space, enabling spatial organizational adaptability in interacting components and the incorporation of programmed functionality. Overall, our studies illuminated the essential role of multivalency-mediated interactions in dynamicity and self-assembly and has demonstrated their potential applications in biomedical research, disease diagnostics, catalysis, materials science, and nanotechnology. These findings open new avenues for developing advanced functional materials, targeted therapies, and programmable systems with improved adaptability and performance.

List of Publications

- **Shandilya, E.**; Rallabandi, B.; Maiti, S. Spatiotemporally tuned colloidal phoretic leap in an altering multivalent interaction field. *ChemRxiv* **2023**. DOI- 10.26434/chemrxiv-2023-r1djt.
- **Shandilya, E.**; Maiti, S. Self-Regulatory Micro- and Macroscale Patterning of ATP-Mediated Nanobioconjugate. *ACS Nano* **2023**, *17* (5), 5108–5120.
- **Shandilya, E.**;¹ Priyanka; ¹ Brar, S. K.; Mahato, R. R.; Maiti, S. Spatiotemporal Dynamics of Self-Assembled Structures in Enzymatically Induced Agonistic and Antagonistic Conditions. *Chem. Sci.* **2021**, *13* (1), 274–282. (¹equal contribution)
- **Shandilya, E.**; Dasgupta, B.; Maiti, S. Interconnectivity between Surface Reactivity and Self-Assembly of Kemp Elimination Catalyzing Nanorods. *Chem. Eur. J.* **2021**, *27* (29), 7831–7836.
- **Shandilya, E.**; Maiti, S. Deconvolution of Transient Species in a Multivalent Fuel-driven Multistep Assembly under Dissipative Conditions. *ChemSystemsChem* **2020**, *2* (2), e1900040.
- **Shandilya, E.**; Bains, A. S.; Maiti, S. Enzyme-mediated Temporal Control over Conformational Disposition of a Condensed Protein in Macromolecular Crowded Media. **2023**. (Manuscript submitted)
- Mahato, R. R.; **Shandilya, E.**; Shikha; Maiti, S. Regulating Spatial Localization and Reactivity Biasness of DNazymes by Metal Ions and Oligonucleotides. *ChemBioChem* **2022**, *23* (18), e202200154.
- Shikha; **Shandilya, E.**; Priyanka; Maiti, S. Directional Migration Propensity of Calf Thymus DNA in a Gradient of Metal Ions. *Chem. Commun.* **2022**, *58* (67), 9353–9356.
- Mahato, R. R.; **Shandilya, E.**; Dasgupta, B.; Maiti, S. Dictating Catalytic Preference and Activity of a Nanoparticle by Modulating Its Multivalent Engagement. *ACS Catal.* **2021**, *11* (14), 8504–8509.
- Mahato, R. R.; Priyanka; **Shandilya, E.**; Maiti, S. Perpetuating Enzymatically-Induced Spatiotemporal PH and Catalytic Heterogeneity of a Hydrogel by Nanoparticles. *Chemical Science* **2022**, *13*, 8557-8566.
- Not part of thesis work

Table of contents

Chapter 1	1-36
1.1 General aspects of multivalency	3
1.2 Multivalency or Cooperativity?	6
1.3 Self-assembled multivalency	6
1.3.1 Role of multivalency in assembly formation	6
1.3.2. Role of increasing valency in assemblies	8
1.4 Multivalency in catalyst development	9
1.5 Kinetics of multivalent systems	12
1.6 Rate law as modeling principle of multivalent systems.....	14
1.7 Spatial patterning of dissipative self-assemblies	15
1.8 Multivalency driven diffusiophoresis	19
1.9 Diffusion and Gradient	21
1.10 Flow-induced patterning	22
1.11 Catalysis under flow conditions.....	23
1.12 References.....	25
Chapter 2	37-88
2.1. Introduction.....	38
2.2 Materials	40
2.3. Methods.....	41
2.3.1. Synthesis of Gold Nanoparticles (GNP)	41
2.3.2. Aggregation Kinetics	41
2.3.3. Transmission Electron Microscopy (TEM) Imaging.....	41
2.3.4. Diffusion Coefficient Calculation.....	42
2.3.5. HPLC measurements	43
2.3.6. Phosphatase assay	43

2.3.7. Microfluidics Measurements	44
2.3.8. Spatiotemporal Patterning of Nanoparticles over Glass Surface.....	44
2.3.9. Theoretical evaluation of migration of nanoparticles under flow conditions	45
2.3.10. Phoretic velocity calculation.....	46
2.3.10. Coffee Ring Pattern Formation.....	47
2.3.11. Calculation of capillary phoresis number	47
2.4. Results and Discussion	49
2.5. Summary.....	80
2.6. References.....	81
Chapter 3.....	89-122
3.1 Introduction.....	91
3.2 Materials	92
3.3 Methods.....	92
3.3.1 Synthesis of Gold Nanoparticles.....	92
3.3.2 Synthesis of Gold Nanorods	93
3.3.2. Synthesis and Characterization of NBI, CNP, and NBD-C8 adduct	95
3.3.2. Fabrication of carboxylate modified polystyrene beads-gold nanorods (PS-GNR) conjugate	101
3.3.4. Optical tracking and MSD analysis	101
3.4. Results and Discussion	103
3.5. Summary	117
Chapter 4.....	123-154
4.1. Introduction.....	124
4.2. Materials	125
4.3. Methods.....	126
4.3.1. Synthesis and Characterization of gold nanorods (GNR).....	126
4.3.2. Fabrication of Bead-GNR (CMB) conjugate	127

4.3.3. Activity of CMB over NBI	127
4.3.4. Stability of GNR in the presence of ATP	127
4.3.5. Microfluidic experiment and calculation of drift.....	127
4.3.6. Population dynamics study inside macroscale setup	128
4.3.7. Enzymatic activity	128
4.4. Results and Discussion	129
4.5. Summary	150
4.6. References.....	150
Chapter 5.....	155-184
5.1. Introduction.....	157
5.2. Methods and Principle	158
5.2.1. Classification of systems.....	159
5.2.2. Self-driven assembly (system without fuel)	159
5.2.3. Fuel-driven assembly	159
5.2.3.1. Monovalent fuel-mediated assembly	160
5.2.3.2. Divalent fuel-mediated assembly.....	160
5.2.3.3. Trivalent fuel-mediated assembly.....	160
5.2.4. Incorporation of enzyme E.....	161
5.2.4.1. Trivalent fuel (T) with E.....	161
5.2.4.2. T mediated assembly in the presence of E.....	161
5.2.5. Mechanistic study of single-step assembly formation.....	162
5.2.5.1. A ₃ T assembly	162
5.2.5.2. A ₃ T formation in the absence of E.....	162
5.2.5.3. A ₃ T formation in the presence of E	165
5.3. Results and Discussion	168
5.4. Summary	179
5.5 References.....	179

Chapter 6	185-208
6.1. Introduction.....	187
6.2. Methods.....	188
6.2.1 Temporal evolution of assembly via numerical modeling.....	188
6.2.2. Spatiotemporal study of assembly formation using fluid dynamics.....	191
6.4 Summary.....	203
6.5 References.....	204
Chapter 7	209-214

CHAPTER 1

Multivalent Interactions and their Cross-Domain Utility

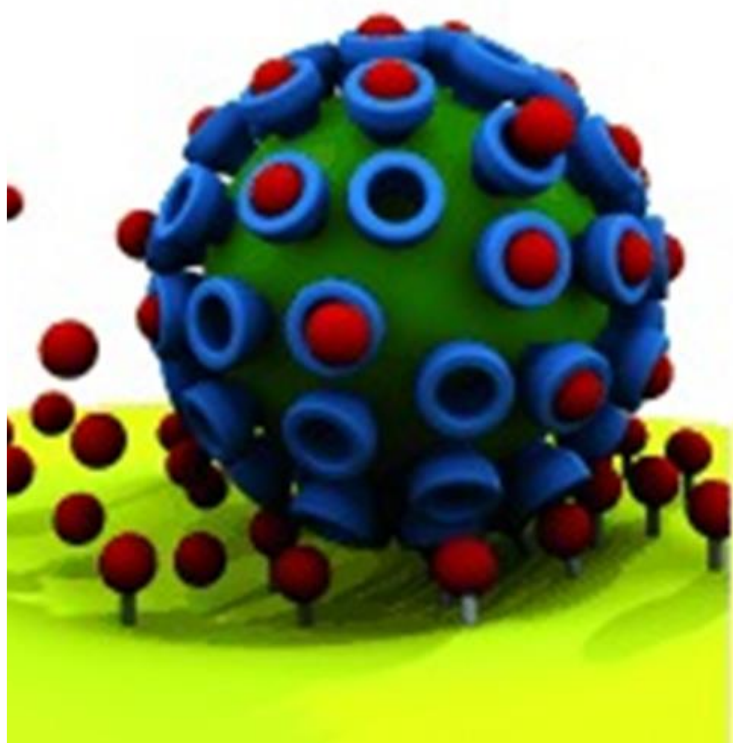


Image Reference. Fasting, C.; Schalley, C. A.; Weber, M.; Seitz, O.; Hecht, S.; Kokschi, B.; Dervedde, J.; Graf, C.; Knapp, E.-W.; Haag, R. Multivalency as a Chemical Organization and Action Principle. *Angew. Chem. Int. Ed.* **2012**, *51* (42), 10472–10498.

1.1 General aspects of multivalency

Multivalent interaction refers to the ability of a molecule or a compound to interact with multiple sites or targets simultaneously.¹ In other words, a multivalent interaction occurs when a molecule has multiple binding sites that can interact with different molecules or receptors. One of the key aspects of multivalency is the ability of a multivalent compound to exhibit increased binding strength or avidity compared to a monovalent compound.²⁻⁵ This is due to the fact that the multiple binding interactions between the multivalent compound and its targets can work together to create a stronger overall interaction (Figure 1.1).⁶ As a result, the implications of multivalent interactions are broad and far-reaching, impacting everything from drug design to materials science to fundamental chemistry research (Figure 1.2). For example, multivalent interactions can increase the affinity and specificity of a molecule to its target, leading to improved drug efficacy.⁵⁻⁹ Multivalent interactions can be achieved through various means, such as the use of dendrimers, polymers, or multivalent ligands.⁷⁻⁸ Additionally, multivalent interactions can be achieved through the use of nanoparticles, which can have multiple ligands on their surface that can interact with multiple receptors.⁹⁻¹¹ Multivalent interactions play a crucial role in biological systems. One example

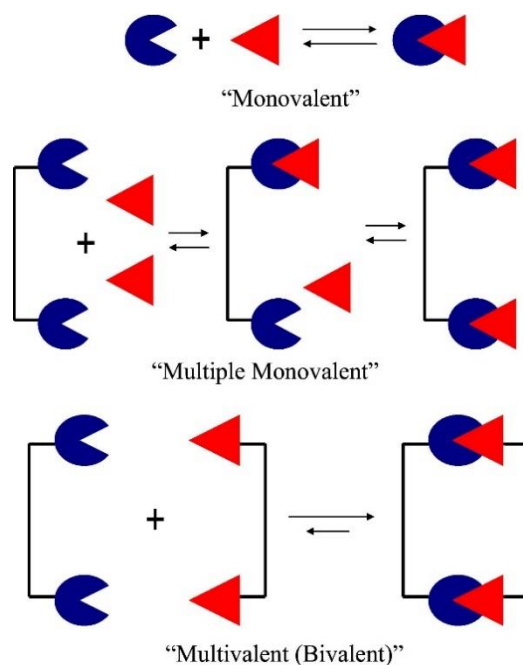


Figure 1.1. Schematic and nomenclature for monovalent and bivalent interaction systems. Adapted from reference [6] with permission.

of multivalent interactions in biological systems is the interaction between antibodies and antigens. Antibodies are proteins that can bind to specific antigens, such as viruses or bacteria, with high specificity and affinity. Antibodies have multiple binding sites, which allows them to interact with multiple antigens simultaneously, leading to the formation of antigen-antibody complexes.¹¹⁻¹³ These interactions can activate various immune responses, such as complement activation and phagocytosis, leading to the elimination of the antigen.¹⁴ Another example of multivalent interactions in biological systems is the interaction between lectins and carbohydrates. Lectins are proteins that can bind to specific carbohydrates with high affinity and specificity.³⁶ Many lectins have multiple binding sites, which allows them to interact with multiple carbohydrates simultaneously, leading to the formation of multivalent complexes.¹⁵⁻¹⁷ Multivalent interactions are also important in the interactions between cells and their extracellular matrix (ECM). The ECM is a complex network of proteins and carbohydrates that surrounds cells and provides structural support. Many ECM proteins, such as fibronectin and collagen, have multiple binding sites that allow them to interact with multiple receptors on the cell surface simultaneously, leading to the formation of multivalent complexes.¹⁸⁻²¹ These interactions can activate various signaling pathways, leading to changes in cell behavior, such as cell adhesion, migration, and differentiation.²²⁻²³ Apart from this, multivalent interactions

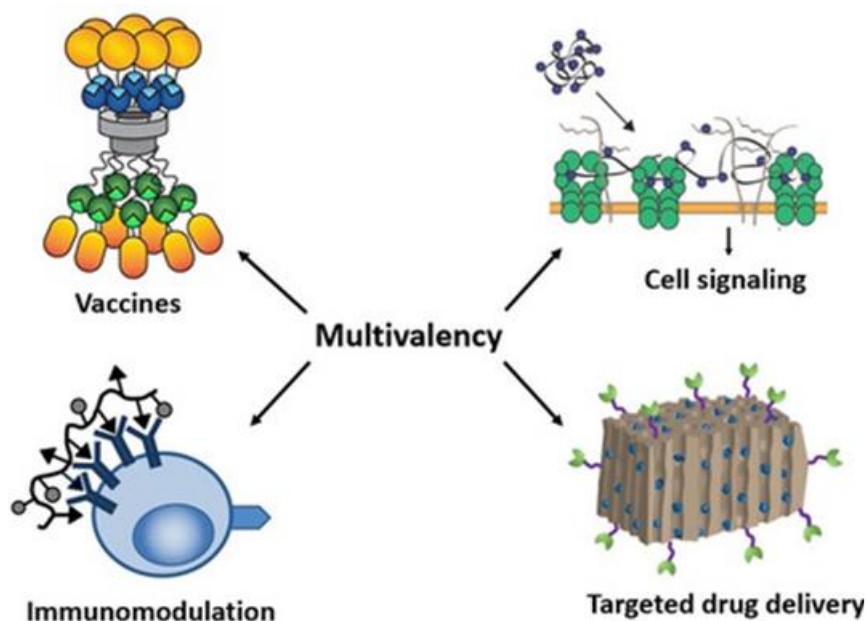


Figure 1.2. Multivalent interactions are frequently observed in nature, there is considerable enthusiasm in creating multivalent ligands to manipulate biological interactions. These ligands have diverse applications, including the development of vaccines, immunomodulators, cell signaling effectors, and vehicles for precise drug delivery. Adapted from reference [40] with permission.

play a significant role in the binding mechanisms of a virus to a cell surface as viruses often utilize multiple binding sites to establish strong and specific interactions with host cells. By understanding the multivalent nature of these interactions, researchers can gain insights into the complex interplay between viruses and cell surfaces, enabling the development of targeted strategies for preventing viral attachment, designing antiviral therapies, and enhancing the efficacy of drug delivery systems.²⁴ Figure 1.3 illustrates a comparison between different binding mechanisms of a virus to a cell surface. It highlights three scenarios: (a) multivalent binding of the virus to the cell surface, (b) noncompetitive binding using monovalent ligands which represents the classical drug approach, and (c) multivalent binding with polyvalent ligands.¹²⁶ The figure demonstrates that multi- and polyvalent ligands are significantly more efficient in both binding to and protecting the surface of the virus compared to monovalent ligands. As a result, the enhanced binding capability of multi- and polyvalent ligands effectively prevents viral adhesion. This finding reinforces the importance of multivalent interactions in designing strategies to control viral infections and develop more effective therapeutic interventions.²²⁻²⁴ As our understanding of multivalent interactions continues to grow, we can expect to see new and exciting applications emerge across a wide range of fields.

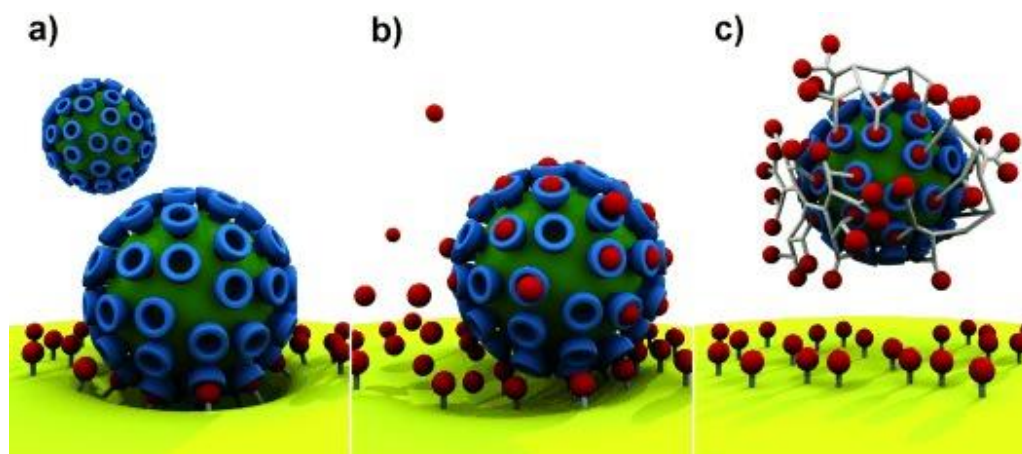


Figure 1.3. The figure illustrates a comparison between the binding mechanisms of a virus to a cell surface. When the virus exhibits (a) multivalent binding to the cell surface, (b) a non-competitive binding using monovalent ligands, which represents the classical drug approach; (c) Multivalent binding with polyvalent ligands. The figure demonstrates that multi- and polyvalent ligands are significantly more efficient in both binding to and protecting the surface of the virus compared to monovalent ligands. Consequently, this enhanced binding capability of multi- and polyvalent ligands effectively prevents viral adhesion. Taken from reference [126] with permission.

1.2 Multivalency or Cooperativity?

Multivalency and cooperativity are two concepts often encountered in the context of molecular interactions, particularly in the fields of biochemistry and supramolecular chemistry.²⁶ While they both involve the binding or interaction of multiple entities, they are distinct phenomena with different underlying mechanisms. Multivalency refers to the simultaneous binding or interaction of multiple ligands (small molecules) with multiple binding sites on a receptor (macromolecule). In other words, both the ligands and the receptor possess multiple binding sites, allowing for multiple interactions to occur concurrently. The binding affinity between a ligand and a receptor in a multivalent system can be significantly enhanced compared to a monovalent interaction. This enhanced binding arises from the cooperative effects of multiple binding events occurring simultaneously, leading to stronger overall binding.¹⁻³ Cooperativity, on the other hand, refers to the phenomenon where the binding or activity of one ligand at a binding site influences the binding or activity of another ligand at a different binding site on the same receptor or a different receptor.²⁶ Cooperativity can be positive or negative, depending on whether the binding of one ligand enhances or inhibits the binding or activity of another ligand. This phenomenon arises from allosteric interactions between the binding sites, where the conformational changes induced by the binding of one ligand affect the binding affinity or activity at other sites.²⁷ Briefly, multivalency involves the simultaneous binding or interaction of multiple ligands with multiple binding sites, leading to enhanced binding affinity. Cooperativity, on the other hand, refers to the influence of one ligand's binding or activity on the binding or activity of another ligand, either positively or negatively. While multivalency relies on the presence of multiple binding sites, cooperativity is a result of allosteric interactions between binding sites.²⁸⁻³¹

1.3 Self-assembled multivalency

1.3.1 Role of multivalency in assembly formation

Multivalent interaction is a key driving force for the formation of self-assembled materials/structures.³⁸⁻³⁹ Self-assembly is the process by which individual components come together spontaneously to form a larger, ordered structure. This process is driven by the interactions between the individual components, which can include hydrogen bonding, electrostatic interactions, and van der Waals forces.³² Multivalent interactions play a particularly important role in self-assembly because they allow for multiple weak interactions

between the individual components. This leads to the formation of more stable and complex structures than would be possible with single, strong interactions. Multivalent interactions can also lead to the formation of structures with high selectivity and specificity, as each component can interact with multiple complementary components.^{3,41} One example of multivalent interaction in self-assembly is the formation of supramolecular polymers which are linear or branched structures formed by the self-assembly of individual monomers through multivalent interactions.³³⁻³⁵ These monomers can have multiple functional groups that can interact with other monomers through non-covalent interactions. As a result, the monomers can come together to form a larger, ordered structure that is stabilized by the multivalent interactions between the monomers. Another example of multivalent interaction in self-assembly is the formation of micelles. Micelles are spherical structures formed by the self-assembly of amphiphilic molecules in aqueous solutions. These molecules have a hydrophilic head and a hydrophobic tail, which can interact with other

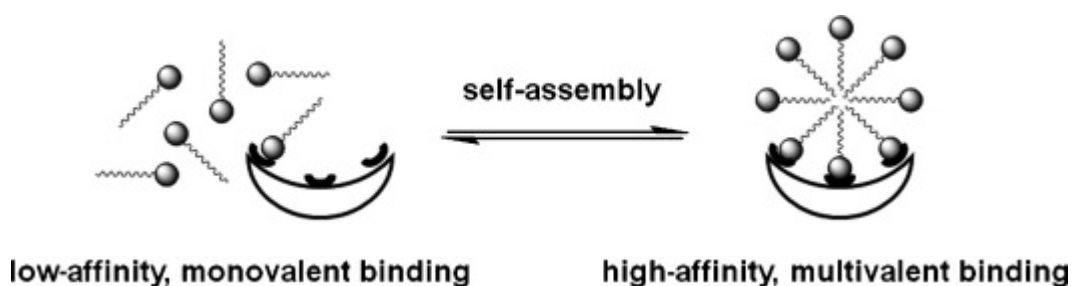


Figure 1.4. This scheme illustrates multivalency as a powerful tool for high-affinity molecular recognition in a system rather than focusing on covalent scaffold synthesis to organize multiple ligands. Taken from reference [25] with permission.

amphiphilic molecules through hydrophobic interactions. As more and more amphiphilic molecules come together, they can form a micelle structure, with the hydrophobic tails in the interior of the structure and the hydrophilic heads facing outward.³ Apart from this, multivalent interaction is a key concept in the formation of interfacial assemblies using dendrimers and polymers.⁴⁶⁻⁴⁸ Interfacial assemblies are structures that form at the interface between two different materials or phases, such as the interface between a solid and a liquid or between two immiscible liquids while dendrimers are highly branched, synthetic polymers that have multiple reactive sites on their surface. These reactive sites can be used to interact with complementary functional groups on other molecules or surfaces, leading to the formation of

stable interfacial assemblies. Polymers are another class of materials that can be used for the formation of interfacial assemblies.^{27,33} Like dendrimers, polymers can also have multiple reactive sites or functional groups on their surface, which can be used to interact with other molecules or surfaces.⁵² Polymers can be designed with specific chemical and physical properties, such as molecular weight, chain architecture, and degree of branching, which can influence their interaction with other molecules or surfaces. In the formation of interfacial assemblies, multivalent interaction is crucial for the stability and specificity of the assembly. The use of dendrimers or polymers with multiple reactive sites allows for the formation of multiple intermolecular interactions, which leads to the formation of stable and specific assemblies. The multivalent interaction can also provide increased binding affinity and selectivity, as multiple interaction sites can interact with complementary functional groups on other molecules or surfaces. Applications of interfacial assemblies formed using multivalent interaction include the design of functionalized surfaces, biosensors, and drug delivery systems.⁴² By controlling the properties of the dendrimers or polymers used in the assembly formation, researchers can tailor the interfacial assembly for specific applications, such as selective binding of biomolecules or controlled release of drugs. In this way, multivalent interaction can be used in the formation of a wide range of assemblies, including supramolecular structures, nanoparticles, and biomolecules.^{37,43} The use of multivalent interactions in the design of assemblies allows for the creation of structures with specific sizes, shapes, and functionality, which can be used for a wide range of applications, such as drug delivery, catalysis, and sensing.⁴³⁻⁴⁴

1.3.2. Role of increasing valency in assemblies

The role of increasing valency in assemblies is particularly exemplified by the unique properties and versatility of dendrimers. Dendrimers offer a versatile approach to modulating binding valency by functionalizing different generations with interaction sites.⁷ These highly branched macromolecules provide precise control over the number and spatial arrangement of binding groups. However, their spherical nature imposes steric constraints, particularly for higher generations, due to the exponential growth of end groups compared to the limited outer area of the dendrimer structure.¹ As a result, the accessibility of binding sites on the dendrimer surface becomes restricted, leading to steric hindrance effects.⁵³ For example, when studying the binding of a monotopic β -CD (β -cyclodextrin) to 1,4-butanediamino poly(propylene imine) (PPI) dendrimers, it was observed that higher generation dendrimers experienced steric

hindrance at the periphery due to the high density of guest groups.^{45,125} This steric hindrance limited the full occupancy of binding sites by β -CD, resulting in partial binding. Despite these steric effects, dendrimers functionalized with guest groups have demonstrated their utility in introducing functionality at β -CD-functionalized surfaces. They serve as powerful tools for creating multivalent interactions and manipulating interfacial properties. Early studies using guest-functionalized dendrimers revealed qualitative aspects of multivalent binding, with lower generations exhibiting reversible binding while higher generations displayed irreversible adsorption. A breakthrough in understanding the quantitative aspects of binding was achieved using ferrocenyl (Fc)-functionalized dendrimers.⁴⁶ Fc, which binds weaker to β -CD than other guest groups, allowed for a wider range of generations that could bind reversibly. Importantly, the redox-active nature of Fc facilitated the quantitative assessment of surface binding using electrochemical techniques. By comparing the coverage of adsorbed Fc and the coverage of β -CD in the monolayer, integer numbers representing the binding valency of dendrimers on the surface were determined. This correlation between dendrimer dimensions, the number of accessible β -CD sites, and binding valency provided a quantitative understanding of the steric effects and binding stoichiometry (Figure 1.4). Further studies confirmed the relationship between steric match and binding stoichiometry using dendrimers with longer linkers, different scaffolds (including the commonly used poly(amido amine), PAMAM, dendrimers), and different redox-active guest moieties.⁴⁷⁻⁴⁸ The insights gained from these studies have expanded our understanding of how steric hindrance, dendrimer size, and binding valency influence multivalent interactions at interfaces. In summary, dendrimers offer a versatile platform for modulating binding valency and introducing functionality at surfaces. While steric effects can limit the accessibility of binding sites, the precise control over dendrimer structure allows for systematic investigations and the design of multivalent interactions. The combination of electrochemical techniques and steric considerations has provided quantitative insights into the binding stoichiometry, intrinsic affinity, and effective molarity of dendrimer-surface interactions, paving the way for the rational design of advanced materials, and tailored interfacial properties.⁴⁴⁻⁴⁸

1.4 Multivalency in catalyst development

Multivalency also plays a crucial role in catalyst development, where it can enhance catalytic efficiency, selectivity, and stability.⁵¹ Catalysts are substances that increase the rate of chemical

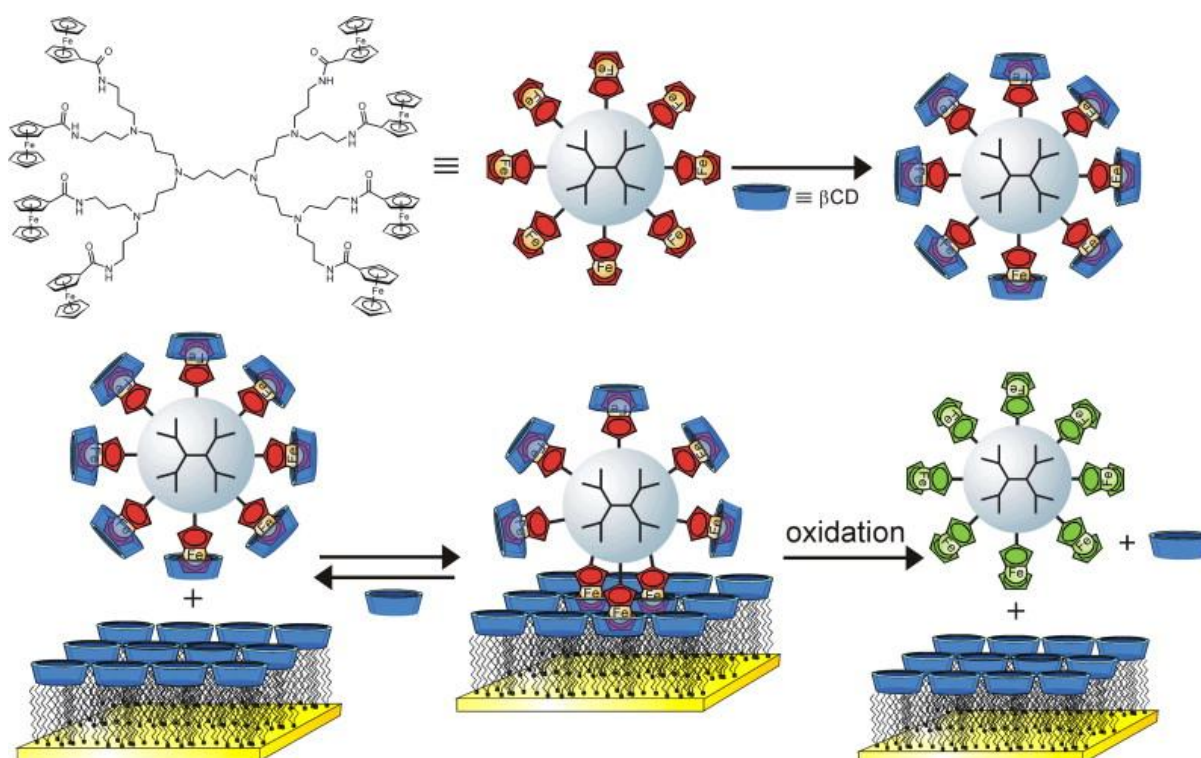


Figure 1.4. Formation of a dendrimer- β -cyclodextrin assembly (top) and the electrochemically controlled adsorption at the β -cyclodextrin host surface. Taken from reference [125] with permission.

reactions without being consumed in the process.⁵¹ Multivalent catalysts have multiple active sites that can interact with reactants and intermediates, leading to more efficient and selective catalysis. The multivalent effect arises from the cooperative interactions between the active sites, which can enhance the binding affinity and reaction rate of the reactants. Additionally, multivalent catalysts can exhibit increased stability and resistance to deactivation, as the presence of multiple active sites can compensate for the loss of individual sites. One example of multivalent catalysis is the use of multivalent metal complexes as homogeneous catalysts.⁴³⁻
⁴⁴ These complexes consist of a central metal ion coordinated to multiple ligands, which can interact with reactants and intermediates to facilitate various chemical transformations. Multivalent metal complexes have been used in a range of catalytic applications, including hydrogenation, oxidation, and polymerization. Another example of multivalent catalysis is the use of multivalent nanoparticles as heterogeneous catalysts.⁵⁴ These nanoparticles have multiple active sites on their surfaces, which can interact with reactants and intermediates to catalyze various chemical reactions. In one of the examples, catalytically active peptide-nanoparticle complexes were achieved by assembling short peptide sequences onto the surface

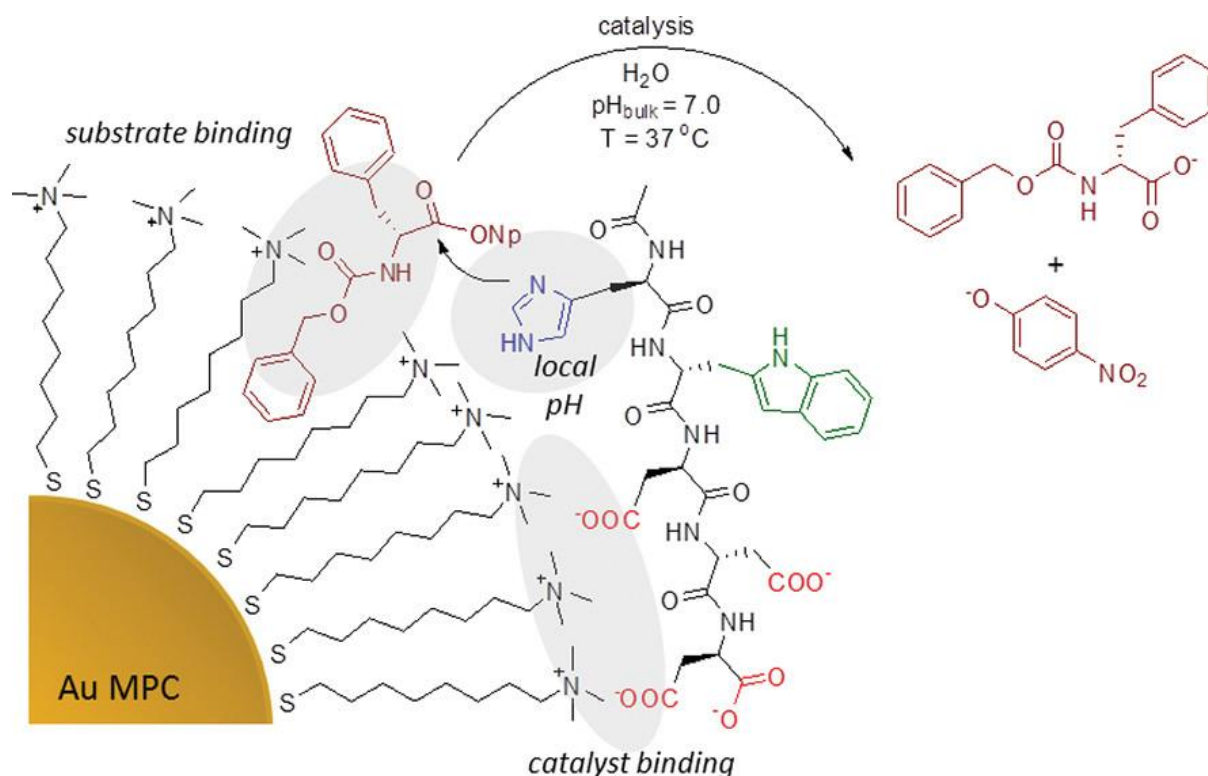


Figure 1.5. Self-assembly of peptides on the nanoparticle surface, resulting in the formation of catalytic multivalent peptide–nanoparticle complex that can catalyze the transesterification of the substrate. Taken from reference [49] with permission.

of cationic self-assembled monolayers on gold nanoparticles.⁴⁹⁻⁵⁰ This peptide functionalization resulted in a remarkable acceleration of the transesterification reaction involving the p-nitrophenyl ester of N-carboxybenzyl phenylalanine, surpassing a two-order-of-magnitude rate enhancement. The gold nanoparticle not only acted as a multivalent scaffold to bring the catalyst and substrate into proximity but also created a local microenvironment that further augmented the catalytic activity (Figure 1.5). The supramolecular nature of this ensemble allowed for in-situ modulation of the catalytic performance of the system. Multivalent nanoparticles have also been used in a range of catalytic applications, including environmental remediation, energy conversion, and chemical synthesis.⁵⁵⁻⁵⁶ The cooperativity of functional groups is another important aspect of multivalent catalysis, where the interaction between the active sites can lead to enhanced catalytic activity and selectivity.²⁶⁻²⁸ In multivalent catalysis, the functional groups of the ligands or the active sites of the nanoparticles can work together to facilitate various chemical transformations. The cooperative effect arises from the synergistic interactions between the functional groups, which can influence the electronic and steric properties of the active sites and enhance the binding affinity and reactivity

of the reactants.²⁸⁻³¹ Additionally, the cooperative effect can also facilitate the regeneration of the catalysts and prevent their deactivation by promoting the release of the products. The design of multivalent catalysts with cooperative functional groups requires careful consideration of various factors, such as the spatial arrangement and orientation of the groups, the electronic properties of the ligands and active sites, and the nature of the reactants and products.⁵⁸ Computational simulations and experimental data can provide valuable insights into the optimal design parameters for multivalent catalysts with cooperative functional groups.^{55-56,59-60}

1.5 Kinetics of multivalent systems

Multivalent systems can exhibit several types of kinetic behavior, including enhanced association rates, slower dissociation rates, and longer-lived complexes, compared to monovalent systems.⁶¹ One of the important aspects of multivalent kinetics is the effect of ligand density and spacing on the overall reaction rates and equilibrium constants.⁶² The optimal ligand density and spacing can vary depending on the specific system and the desired outcome, such as enhanced binding affinity or selectivity. In addition to ligand density, other factors that can affect the kinetics of multivalent systems include the size and shape of the interacting particles, the nature and strength of the binding interactions, and the solution conditions such as pH and ionic strength.⁶³⁻⁶⁴ Due to these factors, the kinetics of multivalent interaction-driven systems can be complex, as the binding of multiple ligands to multiple receptors can occur cooperatively or competitively.⁶⁵ Cooperative binding occurs when the binding of one ligand enhances the binding of another ligand, while competitive binding occurs when the binding of one ligand inhibits the binding of another ligand.^{65,71} Kinetic modeling of multivalent interaction-driven binding involves the development of mathematical models that describe the rates of binding and dissociation of multiple ligands to multiple receptors.⁶⁶⁻⁶⁹ These models can help to predict the binding behavior of these systems and can be used to optimize their design for specific applications. The most common approach for modeling multivalent interaction-driven binding involves the use of the Hill equation, which describes the cooperative binding of ligands to receptors and it can be used to model the binding of multiple ligands to multiple receptors and can be extended to include competitive binding as well. The Hill equation can be fit to experimental binding data to determine the affinity and cooperativity of the binding interactions.⁷⁰ For cooperative binding the equation is as follows:

$$\theta = \frac{[\mathbf{L}]^n}{K_d + [\mathbf{L}]^n}$$

where θ is the fractional saturation of the receptors (i.e. the proportion of receptors bound to ligands), $[\mathbf{L}]$ is the concentration of ligands, K_d is the dissociation constant, and n is the Hill coefficient, which describes the degree of cooperativity in the binding interactions. When $n = 1$, the Hill equation reduces to the standard binding equation.

Also, in the case of competitive binding between ligands, the Hill equation can be extended to include an additional term:

$$\theta = \left(\frac{[\mathbf{L}_1]^n}{[\mathbf{L}_1]^n + K_{d1}^n} \right) / \left(1 + \frac{[\mathbf{L}_2]^n}{K_{d2}^n} \right)$$

where $[\mathbf{L}_1]$ and $[\mathbf{L}_2]$ are the concentrations of the competing ligands, and K_{d1} and K_{d2} are the dissociation constants for each ligand. The Hill coefficient, n , describes the degree of cooperativity between ligands.⁶⁹⁻⁷¹

The stepwise process of multivalent binding and unbinding is illustrated in Figure 1.6. First, there is an initial intermolecular binding, followed by subsequent intramolecular steps where the inherent binding affinity remains constant. This particular model accounts for the improved binding affinity by considering a high local effective concentration (C_{eff}) of the host, which becomes available for the divalent guest molecule when it binds through only one of its guest moieties (referred to as divalent-single). Consequently, there is no assumed cooperativity in terms of an increase in intrinsic binding affinity from the first to the second binding. The expected equilibrium constant for a multivalent complex can be related to the corresponding monovalent constant using this proposed scheme. To ensure clarity, the trivalent rates and equilibrium constants are denoted by the subscript "T," while their monovalent and divalent counterparts are indicated by the subscripts "M" and "D," respectively, as shown in the equation below.

$$K_{eq-D} = \frac{2k_{on-M} \cdot k_{on-M} C_{eff}}{k_{off-M} \cdot 2k_{off-M}} = K_{eq-M}^2 C_{eff}$$

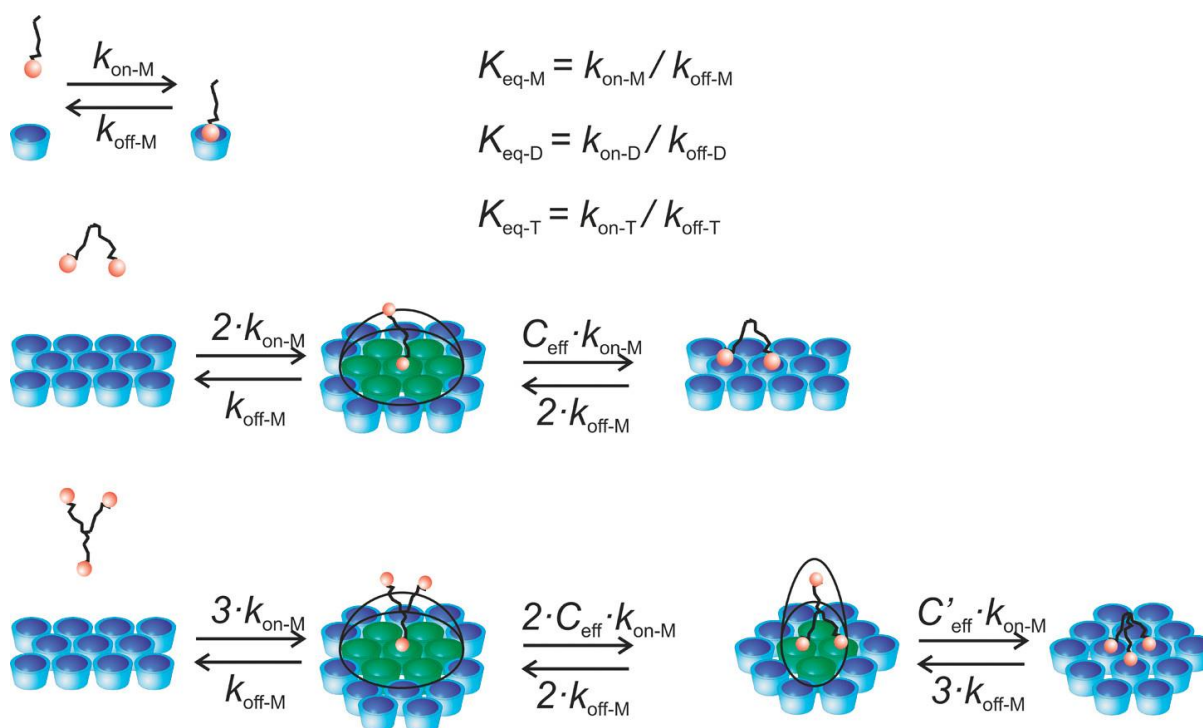


Figure 1.6. Scheme of multivalent equilibrium and stepwise kinetics. Taken from reference [61] with permission.

1.6 Rate law as modeling principle of multivalent systems

Another common approach that can be used to describe the kinetics of multivalent interaction-driven binding is to use the law of mass action which relates the rate of a chemical reaction to the concentrations of the reactants involved.⁷² However, in multivalent systems, modifications are made to the traditional rate laws to account for the presence of multiple ligands and multiple binding sites. For example, in a bivalent interaction where two ligands must bind simultaneously to a receptor to form a complex, the rate law equation can be written as:

$$\frac{d[P]}{dt} = k_{\text{on}} [L_1][L_2] - k_{\text{off}} [P]$$

Here, [P] represents the concentration of the bound complex, [L₁] and [L₂] represent the concentrations of the two ligands, k_{on} is the association rate constant, and k_{off} is the dissociation rate constant. This equation describes the rate of change of the complex

concentration over time, considering the contributions of both association and dissociation processes. The rate constants, k_{on} and k_{off} , reflect the specific molecular interactions and binding kinetics between the ligands and the receptor. These rate constants can be determined experimentally or estimated through computational approaches.⁷³ It's important to note that the rate law approach provides a simplified representation of multivalent interactions and assumes certain assumptions, such as independence of binding events and negligible rebinding effects.⁷⁰ In reality, multivalent interactions can be more complex, with factors like cooperativity, ligand-receptor stoichiometry, and spatial arrangements influencing the binding kinetics.⁷² Advanced modeling techniques, including statistical mechanics or Monte Carlo simulations, can be employed to capture these complexities and provide a more detailed understanding of multivalent interactions.⁷⁴ In these simulations, the binding and dissociation of ligands to receptors are modeled as a series of random events, with the probabilities of these events determined by the binding kinetics and the concentration of ligands and receptors. Kinetic Monte Carlo simulations can provide a detailed understanding of the binding behavior of these systems and can be used to predict the binding behavior under different experimental conditions.⁷⁵ Other approaches to modeling multivalent interaction-driven binding include the use of differential equations and stochastic models. These models can incorporate additional factors, such as the effects of receptor clustering and the influence of the local environment on binding interactions. Nonetheless, the rate law approach serves as a foundational principle for studying the kinetics of multivalent systems and offers valuable insights into the binding behavior between multiple ligands and multiple binding sites on a receptor.⁷²

1.7 Spatial patterning of dissipative self-assemblies

Dissipative self-assembly involves the formation of self-assembled structures in systems that are far from thermodynamic equilibrium. These systems are driven out of equilibrium through the continuous input of energy or the removal of energy, and the self-assembled structures are maintained through a balance of energy input and dissipation (Figure 1.7).⁷⁶ One important example of dissipative self-assembly is the formation of self-assembled gels through reversible chemical reactions. Self-assembled gels are formed through the aggregation of molecules or nanoparticles that are capable of undergoing reversible chemical reactions, such as acid-base reactions or redox reactions. The input of energy can be provided by light, heat, or an external chemical stimulus, and can drive the continuous formation and breakdown of the self-assembled structures.⁷⁷ The formation of self-assembled gels through dissipative self-assembly

can be modeled mathematically using reaction-diffusion equations, which describe the time-dependent evolution of the concentration of reacting species and the spatial distribution of the self-assembled structures.⁷⁸⁻⁸⁰

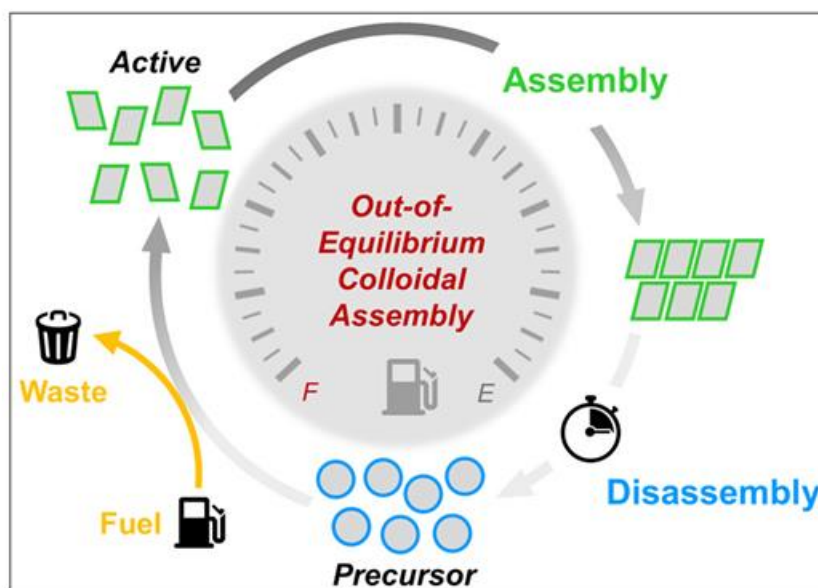


Figure 1.7. Scheme of dynamic self-assembly operating under out-of-equilibrium conditions. Taken from reference [114] with permission.

One such equation is the Belousov-Zhabotinsky (BZ) reaction, which is a classic example of a reaction-diffusion system that exhibits dissipative self-assembly.⁸¹ The BZ reaction is a chemical oscillator that involves the autocatalytic oxidation of malonic acid by bromate ions in the presence of a catalyst, such as cerium ions (Figure 1.8). The reaction produces a periodic oscillation in the concentration of a colored species, such as the ruthenium catalyst or the bromomalonic acid intermediate, which can be visualized by spectroscopic or imaging techniques. The dynamics of the BZ reaction can be described mathematically by a set of reaction-diffusion equations that involve the diffusion of the reacting species and the autocatalytic production and consumption of the intermediates.⁸²⁻⁸³ These equations can be solved numerically to generate spatiotemporal patterns of the oscillating concentration of the reacting species, which can exhibit complex structures such as spirals, waves, and Turing patterns.⁸⁴⁻⁸⁵ Apart from this, BZ-AOT (sodium bis(2-ethylhexyl) sulfosuccinate) system is a well-known example of dissipative self-assembly that exhibits spatiotemporal patterning. The BZ-AOT system consists of a mixture of the BZ reactants (e.g., malonic acid, bromate ion, and cerium(IV) ion) and the surfactant AOT in a water/organic solvent (e.g., toluene) mixture. When this system is stirred, it can exhibit a range of spatiotemporal behaviors, such as waves,

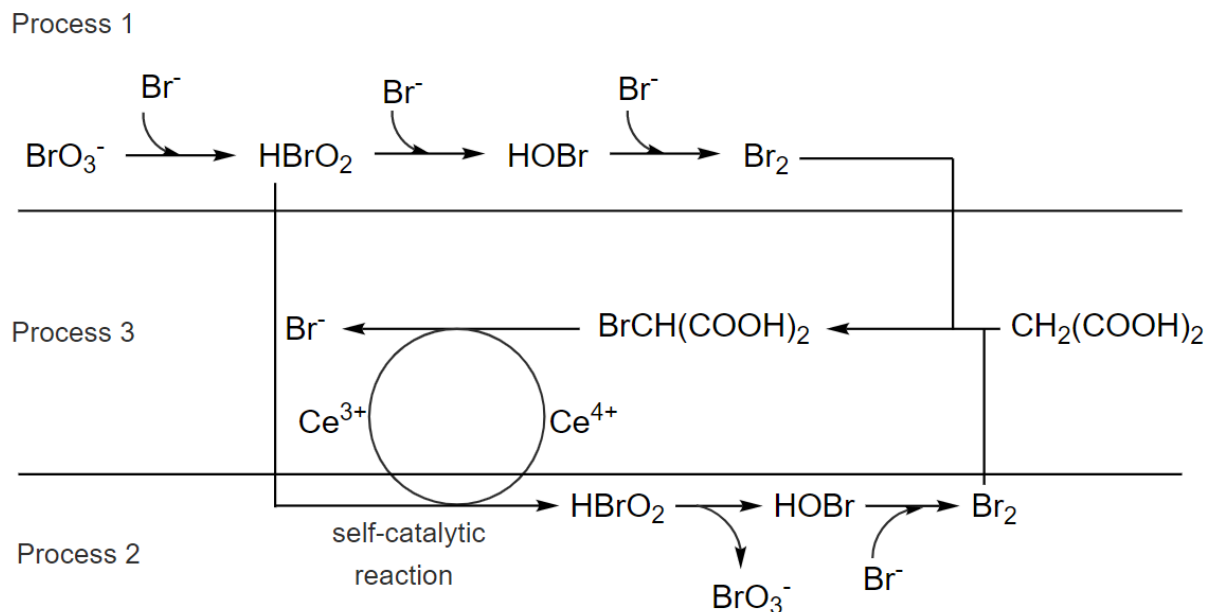


Figure 1.8. Reaction mechanism for BZ reaction showing oxidation of malonic acid catalyzed by cerium with the reduction of bromate. Taken from reference [123] with permission.

spots, and oscillations. Figure 1.9 shows an example of the spatiotemporal patterns observed in the BZ-AOT system. The spatiotemporal patterns in the BZ-AOT system arise from the interplay between the chemical reactions (the BZ reaction) and the physical properties of the surfactant AOT. The AOT molecules can self-assemble into micelles in the organic solvent phase, and the formation and dissolution of these micelles can affect the local concentration of the BZ reactants and the rates of the BZ reaction. This can give rise to complex spatiotemporal patterns in the reaction mixture.

The spatiotemporal behavior of the BZ-AOT system can be described by a set of coupled reaction-diffusion equations and transport equations for the BZ reactants and the AOT micelles, respectively.⁸⁶⁻⁸⁷ Here is an example set of equations that can be used to model the system:

Reaction-diffusion equations for the BZ reaction:

Equation 1.
$$\frac{\partial u}{\partial t} = D_u \nabla^2 u + f(u, v, w)$$

Equation 2.
$$\frac{\partial v}{\partial t} = D_v \nabla^2 v + g(u, v, w)$$

Equation 3.
$$\frac{\partial w}{\partial t} = D_w \nabla^2 w + h(u, v, w)$$

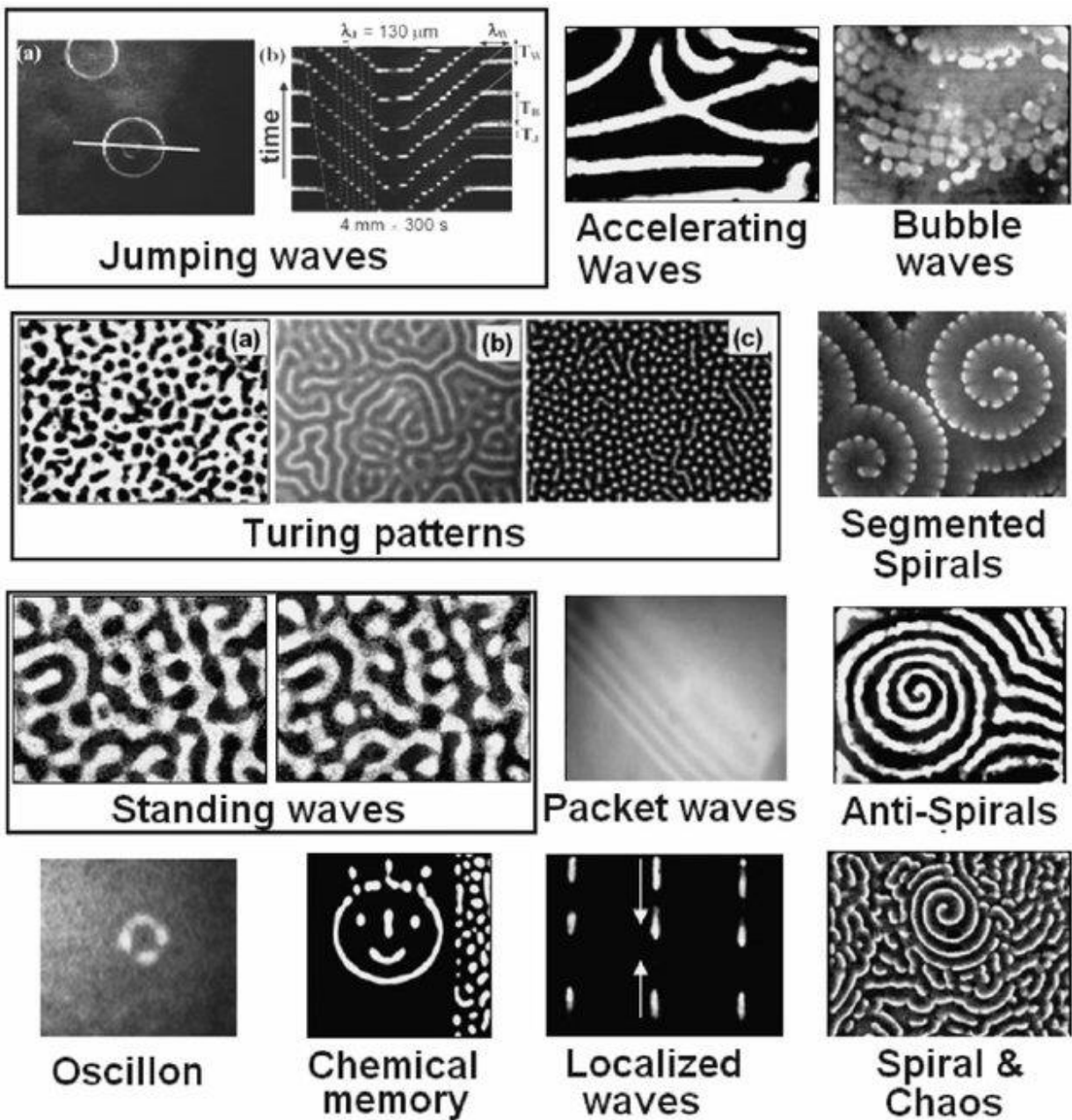


Figure 1.9. The BZ-AOT system exhibits various patterns, including jumping waves, Turing patterns, standing waves, and localized structures. (a) Jumping waves are depicted in a snapshot, while (b) shows a space-time plot along the white line indicated in (a), illustrating the wave propagation. Turing patterns are characterized by three distinct structures: 'black spots', 'labyrinth', and 'white spots'. Standing waves are represented by two anti-phase snapshots. Localized structures include 'oscillon', 'chemical memory', and 'localized waves' (wave propagation direction indicated by arrows). Taken from reference [124] with permission.

where u , v , and w are the concentrations of the BZ reactants, D_u , D_v , and D_w are the diffusion coefficients of the reactants, and $f(u, v, w)$, $g(u, v, w)$, and $h(u, v, w)$ are the reaction terms that describe the chemical reactions of the BZ system. These equations are based on the standard FitzHugh-Nagumo model for excitable media, and can describe a wide range of spatiotemporal behaviors, including waves, spots, and oscillations.

Transport equations for the AOT micelles

Equation 4.
$$\frac{\partial c}{\partial t} = \nabla \cdot (D_c \nabla c - \mu c \nabla \phi)$$

Equation 5.
$$\frac{\partial \phi}{\partial t} = \nabla \cdot (D_\phi \nabla \phi - c \nabla \mu)$$

where c is the concentration of the AOT micelles, ϕ is the electrostatic potential, D_c and D_ϕ are the diffusion coefficients of the micelles and the electrostatic potential, respectively, μ is the chemical potential of the micelles, and the terms involving ∇_ϕ and $\nabla\mu$ represent the electrostatic and chemical driving forces for micelle transport, respectively. These equations describe the transport and self-assembly of the AOT micelles in the organic solvent phase, and can affect the local concentration and rates of the BZ reactants, leading to spatiotemporal patterning. The exact form of the reaction terms and transport coefficients in these equations can vary depending on the specific details of the BZ-AOT system being studied, and may need to be determined experimentally or through numerical simulations. Apart from reaction-diffusion system, another example of dissipative self-assembly is the formation of active matter systems, which are systems composed of self-propelled particles that are capable of converting energy into directed motion.⁸⁸ Active matter systems can be modeled using various theoretical frameworks, such as active Brownian particles, Vicsek models, or hydrodynamic theories.^{89,124}

1.8 Multivalency driven diffusiophoresis

Diffusiophoresis refers to the motion of a particle in a fluid due to gradients in the concentration of solute species in the surrounding solution.⁹⁰ This phenomenon is driven by the interaction between the particle surface and the solute molecules, which results in a concentration-dependent surface charge distribution that induces an electrokinetic force on the particle.

Diffusiophoresis can occur for both charged and uncharged particles, and its magnitude and direction depend on the physicochemical properties of the particle and the surrounding fluid, as well as the solute concentration gradient.⁹¹⁻⁹² In addition to being influenced by the particle size, shape, and surface chemistry, diffusiophoresis can also be affected by external factors such as temperature, pressure, and flow conditions. The understanding and control of diffusiophoresis have important implications in various fields, such as colloidal science, microfluidics, and biotechnology.⁹¹ For example, diffusiophoresis can be used to manipulate the transport and deposition of particles in microfluidic devices, enhance the separation and purification of biomolecules, and control the assembly of colloidal structures.⁹⁰ Multivalency can play an important role in diffusiophoresis, as the presence of multiple binding sites on a particle surface can lead to enhanced interactions with the surrounding solute species and,

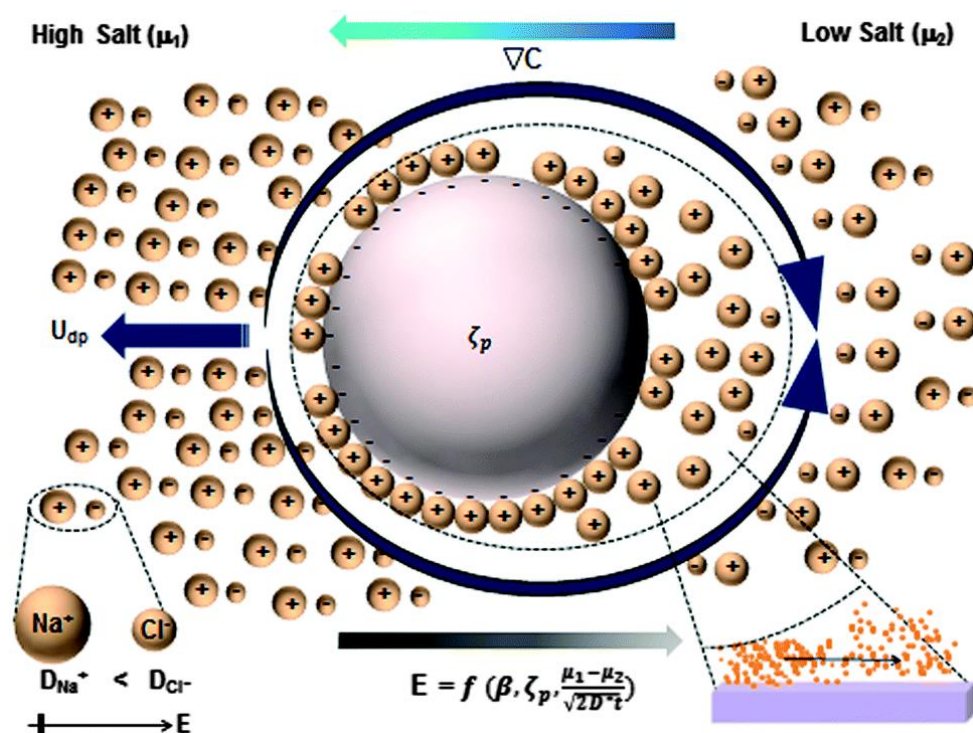


Figure 1.10. The figure depicts the essential mechanism of electrolyte diffusiophoresis, which involves two parallel additive phenomena. The first phenomenon is electrophoresis, which is triggered by an in situ electric field (E) generated by a concentration gradient (or more precisely, a chemical potential μ gradient) of NaCl. The second phenomenon is chemiphoresis, which occurs due to a gradient of NaCl concentration and, consequently, a pressure gradient within the electric double layer (EDL) tangential to the particle surface. This pressure gradient propels fluid flow along the particle surface inside the EDL. In the case of a negatively-charged salt like NaCl (β negative salt), both mechanisms contribute to the transportation of the negatively-charged particle toward regions of higher ionic concentration. Taken from reference [90] with permission.

therefore, stronger diffusiophoretic forces. For example, multivalent nanoparticles with functional groups such as carboxylic acids or amines can interact with oppositely charged solutes in the surrounding solution, leading to the formation of a diffuse layer of ions around the particle surface.⁹³ The density of this diffuse layer is proportional to the solute concentration gradient, and it can create an electrokinetic potential that drives the particle towards areas of higher or lower solute concentration, depending on the particle charge and solute species. In addition to electrostatic interactions, multivalent particles can also exhibit stronger hydrogen bonding or van der Waals interactions with solute molecules due to the presence of multiple binding sites.⁹⁰ This can lead to more complex diffusiophoretic behavior, where the particle motion is influenced by both electrokinetic and molecular-level interactions. The design and control of multivalent particles for diffusiophoresis applications require careful consideration of various factors, such as the particle size, surface chemistry, and ligand density, as well as the properties of the surrounding solution and solute species.⁹⁵ Computational simulations and experimental studies can provide insights into the optimal design parameters for multivalent particles with enhanced diffusiophoretic behavior.⁹⁶⁻⁹⁹

1.9 Diffusion and Gradient

Diffusion is a fundamental process that describes the movement of molecules or particles from an area of higher concentration to an area of lower concentration.¹⁰⁰ It plays a crucial role in various natural phenomena, including the formation of gradients.¹⁰¹ When a concentration gradient is present, it means that the concentration of a particular substance varies across space. Diffusion acts as a driving force to equalize this concentration gradient by allowing molecules or particles to move down the gradient, from regions of higher concentration to regions of lower concentration.¹⁰⁴ This process continues until equilibrium is reached, where the concentration becomes uniform throughout the system. The rate of diffusion is influenced by several factors, including the concentration gradient, the properties of the diffusing substance (such as its size and charge), the temperature, and the medium through which diffusion occurs. Generally, larger concentration gradients, higher temperatures, and a less viscous medium promote faster diffusion.¹⁰³ The presence of a concentration gradient can lead to various intriguing phenomena. For example, in the context of chemical reactions, diffusion plays a critical role in reaction-diffusion systems.^{83,110-113} These systems involve the interplay between chemical reactions and the diffusion of reactants and products. They can give rise to fascinating patterns

and structures, such as reaction-diffusion fronts, traveling waves, or stationary spatial patterns.⁸¹ Gradients formed by diffusing substances also have significant implications in fields such as biology and physiology. Cells often rely on concentration gradients to guide their behaviors. For instance, during embryonic development, gradients of signaling molecules play a crucial role in cell differentiation and tissue patterning.¹⁰⁵⁻¹⁰⁶ Cells can sense and respond to different concentrations of these molecules, leading to specific developmental outcomes. In experimental settings, researchers can create controlled concentration gradients using various techniques, including microfluidic devices, as mentioned earlier. By establishing spatial gradients of signaling molecules or other substances, researchers can investigate how cells respond to these cues, guiding processes like cell migration, proliferation, and differentiation.¹⁰⁴⁻¹⁰⁹

1.10 Flow-induced patterning

Flow-induced patterning refers to the formation of spatial patterns that arise as a result of fluid flow.¹¹⁴ When a fluid flows through a system, it can interact with other components, such as particles, solutes, or surfaces, leading to the emergence of intriguing patterns. One example of flow-induced patterning is observed in microfluidic systems.¹⁰⁶⁻¹⁰⁸ Microfluidics allows for precise control of fluid flow at small scales, enabling the creation of complex flow patterns. These patterns can interact with suspended particles or solutes in the fluid, causing them to arrange into specific spatial configurations. This phenomenon has been utilized to create ordered structures, such as particle chains, particle aggregation, or controlled deposition of particles onto surfaces (Figure 1.11). The flow-induced forces, such as drag, lift, or shear, play a crucial role in shaping the patterns.¹⁰³ One fascinating aspect of microfluidics is droplet-based systems. These systems allow researchers to generate and manipulate tiny droplets of fluids, each serving as a microreactor for studying chemical reactions and pattern formation.¹¹⁷ By carefully controlling the composition and arrangement of these droplets, researchers can investigate intriguing phenomena such as reaction-diffusion dynamics, Turing patterns, and spatial waves. It's like having a miniaturized laboratory where patterns emerge within individual droplets or across an array of them. Another remarkable capability of microfluidics lies in its ability to create well-defined concentration gradients of chemical species. By establishing gradients within microchannels, researchers can investigate how diffusion-driven processes give rise to pattern formation.¹¹⁵⁻¹¹⁶

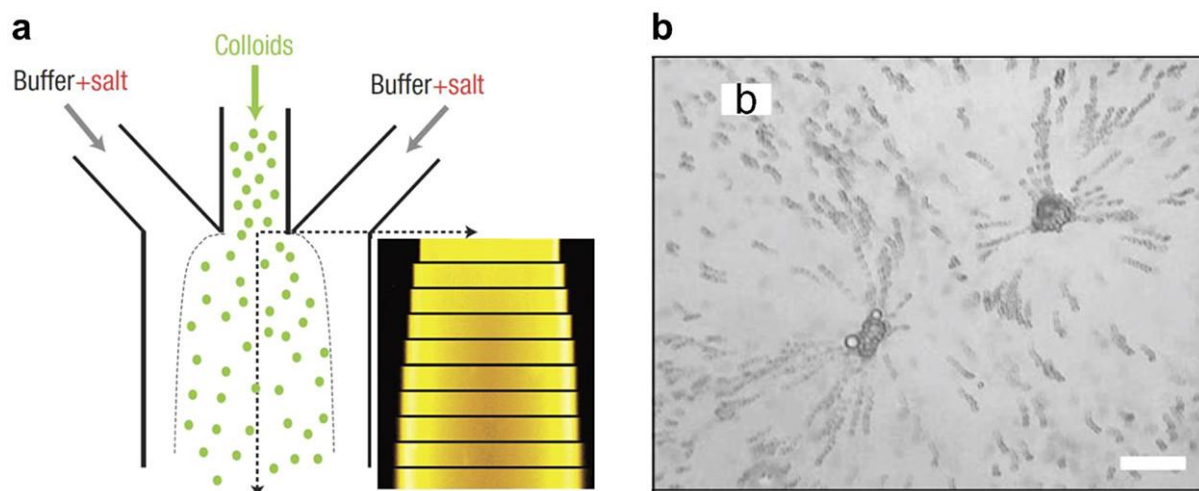


Figure 1.11. (a) The figure demonstrates the diffusiophoresis phenomenon of silica particles within a flow-focusing channel. The movement of the particles is caused by the combined effects of diffusion and electrophoresis in response to a concentration gradient. (b) The figure provides a visual representation of sulfate-modified polystyrene (s-PS) particles being transported via diffusioosmosis near two interacting micropumps made of CaCO_3 . This visualization highlights the interaction and transport dynamics between the particles and the micropumps. Taken from reference [91] with permission.

These gradients act as cues for cells, guiding their behaviors and influencing their organization. It's a powerful tool for unraveling the mechanisms behind cellular responses, tissue development, and pattern formation during biological processes.¹¹⁸⁻¹²⁰ In the realm of tissue engineering and cell patterning, microfluidics has revolutionized our ability to create precise spatial arrangements of cells.¹⁰⁷ By controlling fluid flow and channel geometries, researchers can position cells in desired patterns and guide their behavior. Techniques like droplet encapsulation and hydrogel-based patterning enable the formation of intricate cellular structures that mimic natural tissues.¹⁰⁸ Microfluidics provides a powerful toolbox for investigating cell-cell interactions, tissue morphogenesis, and the emergence of functional tissues. Furthermore, microfluidics allows researchers to generate biochemical gradients, which play a crucial role in pattern formation and cellular behavior.¹⁰⁹ By carefully manipulating the flow rates and mixing ratios of different solutions, researchers can create gradients of signaling molecules, growth factors, or nutrients. These gradients act as guidance cues, influencing cellular migration, differentiation, and the formation of complex patterns. It's a remarkable way to understand how cells sense and respond to their environment, leading to pattern formation.¹¹⁰⁻¹¹³

1.11 Catalysis under flow conditions

Microfluidic platforms offer several advantages for catalytic processes due to their precise control over fluid flow, reaction conditions, and surface interactions.¹¹⁴ One key advantage of microfluidics in catalysis is the ability to precisely manipulate reactant concentrations and flow rates. Microfluidic channels allow for precise control over the mixing of reactants, enabling rapid and efficient reactions.¹¹⁵ By precisely controlling flow rates, researchers can optimize residence times and diffusion rates, leading to enhanced catalytic performance. The fluid flow can enhance catalysis through several mechanisms. When a fluid flows over a catalytic surface, the flow-induced shear stress and mass transport can influence the reaction kinetics and improve the overall efficiency of the catalytic process.⁹¹ Firstly, the shear stress exerted by the flowing fluid can facilitate the transport of reactants to the catalytic surface, ensuring a higher concentration of reactants at the active sites. This enhanced mass transport helps overcome diffusion limitations, leading to increased reaction rates.¹¹⁶ Secondly, the fluid flow can modify the local environment at the catalytic surface. The flow-induced shear stress can induce conformational changes in the reactant molecules or disrupt adsorbate layers, promoting more favorable interactions with the catalytic surface.¹²¹ This alteration in the reactant-surface interactions can enhance the reaction rates and selectivity. Furthermore, the flow-induced fluid dynamics can promote the mixing of reactants, ensuring better contact between the reactants and the catalyst surface.¹¹⁷ This improved mixing enhances the likelihood of productive collisions between reactant molecules, further enhancing the reaction kinetics. Flow-induced catalysis has been observed in various systems, including microreactors, continuous flow reactors, and catalytic membranes. It offers several advantages, such as improved reaction selectivity, reduced reactant residence time, and enhanced control over reaction conditions. Flow-induced catalysis has found applications in various fields, including chemical synthesis, environmental remediation, and energy conversion processes.¹¹⁸⁻¹²¹ Visan et. Al reported experimental evidence of diffusiophoresis in catalytic particles, which is driven by the concentration field generated by the particles themselves (Figure 1.12). This framework introduces a general concept for heterogeneous catalysis, where the driving force relies on solute gradients arising from an uneven distribution of catalytic particles. In regions of higher particle density, the reactant concentration is reduced more significantly compared to the surrounding environment. This macroscopic concentration gradient propels the particles towards regions of higher reactant concentration through surface-driven flows. The underlying mechanism of this flow is attributed to osmotic pressure differences and diffusion potentials, particularly in the case of charged species. The concept of diffusiophoresis unveils an

additional transport mechanism in slurry reactors. To investigate this phenomenon, we examine the movement of particles induced by a photocatalytic degradation reaction using TiO₂ suspensions in a co-flow microchannel. This model highlights the significance of particle characteristics such as surface potential, interactions with reactants and products, and reaction kinetics in relation to catalyst particle migration.¹¹⁵

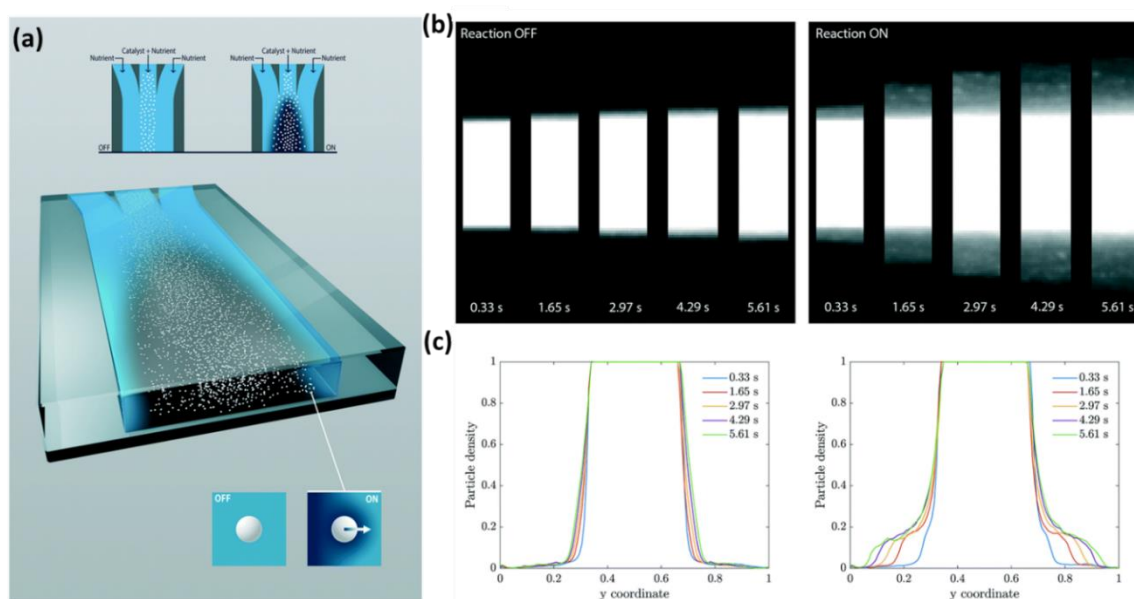


Figure 1.12. (a) In a coflow microchannel arrangement, the reactant is introduced into each inlet, whereas photocatalytic particles are solely present in the middle stream. As a result of this uneven distribution of particles, concentration gradients of the reactant occur during the process of photocatalytic degradation. These concentration gradients then propel the catalytic particles through diffusiophoresis. 2D and 1D profiles of particle density were examined for different residence times - (b) Optical microscopy images were captured at various positions in the downstream direction, corresponding to the specified residence time. On the left side of the images, the light was turned off, while on the right side, the light was turned on. (c) From the microscopy images, it can be observed that without the catalytic reaction, there is minimal diffusion of particles. However, during photocatalytic conversion, a broader shoulder of particles becomes apparent, indicating a more dispersed particle density profile. Taken from reference [115] with permission.

1.12 References

1. *Multivalency: Concepts, Research & Applications*; Huskens, J., Prins, L. J., Haag, R., Ravoo, B. J., Eds.; Wiley, 2018.
2. Choi, S.-K. *Synthetic Multivalent Molecules: Concepts and Biomedical Applications*; John Wiley & Sons: Nashville, TN, 2004.

3. Haag, R. Multivalency as a Chemical Organization and Action Principle. *Beilstein J. Org. Chem.* **2015**, *11* (1), 848–849.
4. Mahon, E.; Barboiu, M. Synthetic Multivalency for Biological Applications. *Org. Biomol. Chem.* **2015**, *13* (43), 10590–10599.
5. Kiessling, L. L.; Lamanna, A. C. Multivalency in Biological Systems. In *Chemical Probes in Biology Science at the Interface of Chemistry, Biology and Medicine*; Springer Netherlands: Dordrecht, 2003; pp 345–357.
6. Schug, K. A.; Joshi, M. D.; Frycák, P.; Maier, N. M.; Lindner, W. Investigation of Monovalent and Bivalent Enantioselective Molecular Recognition by Electrospray Ionization-Mass Spectrometry and Tandem Mass Spectrometry. *J. Am. Soc. Mass Spectrom.* **2008**, *19* (11), 1629–1642.
7. Smeijers, A. F.; Pieterse, K.; Hilbers, P. A. J.; Markvoort, A. J. Multivalency in a Dendritic Host-Guest System. *Macromolecules* **2019**, *52* (7), 2778–2788.
8. Wang, Z.; Yang, X.; Lee, N. Z.; Cao, X. Multivalent Aptamer Approach: Designs, Strategies, and Applications. *Micromachines (Basel)* **2022**, *13* (3), 436.
9. Dalal, C.; Saha, A.; Jana, N. R. Nanoparticle Multivalency Directed Shifting of Cellular Uptake Mechanism. *J. Phys. Chem. C Nanomater. Interfaces* **2016**, *120* (12), 6778–6786.
10. Wang, J.; Tian, S.; Petros, R. A.; Napier, M. E.; Desimone, J. M. The Complex Role of Multivalency in Nanoparticles Targeting the Transferrin Receptor for Cancer Therapies. *J. Am. Chem. Soc.* **2010**, *132* (32), 11306–11313.
11. Makhani, E. Y.; Zhang, A.; Haun, J. B. Quantifying and Controlling Bond Multivalency for Advanced Nanoparticle Targeting to Cells. *Nano Converg.* **2021**, *8* (1), 38.
12. Bell, G. I. Model for the Binding of Multivalent Antigen to Cells. *Nature* **1974**, *248* (5447), 430–431.
13. Goldberg, R. J. A Theory of Antibody—Antigen Reactions. II. Theory for Reactions of Multivalent Antigen with Multivalent Antibody. *J. Am. Chem. Soc.* **1953**, *75* (13), 3127–3131.
14. Jalil, A. R.; Hayes, B. H.; Andrechak, J. C.; Xia, Y.; Chenoweth, D. M.; Discher, D. E. Multivalent, Soluble Nano-Self Peptides Increase Phagocytosis of Antibody-Opsonized Targets While Suppressing “Self” Signaling. *ACS Nano* **2020**, *14* (11), 15083–15093.
15. Dam, T. K.; Brewer, C. F. Multivalent Lectin-Carbohydrate Interactions Energetics and Mechanisms of Binding. *Adv. Carbohydr. Chem. Biochem.* **2010**, *63*, 139–164.

16. Roy, R.; Murphy, P. V.; Gabius, H.-J. Multivalent Carbohydrate-Lectin Interactions: How Synthetic Chemistry Enables Insights into Nanometric Recognition. *Molecules* **2016**, *21* (5), 629.
17. Guo, Y.; Nehlmeier, I.; Poole, E.; Sakonsinsiri, C.; Hondow, N.; Brown, A.; Li, Q.; Li, S.; Whitworth, J.; Li, Z.; Yu, A.; Brydson, R.; Turnbull, W. B.; Pöhlmann, S.; Zhou, D. Dissecting Multivalent Lectin–Carbohydrate Recognition Using Polyvalent Multifunctional Glycan-Quantum Dots. *J. Am. Chem. Soc.* **2017**, *139* (34), 11833–11844.
18. Singh, P.; Carraher, C.; Schwarzbauer, J. E. Assembly of Fibronectin Extracellular Matrix. *Annu. Rev. Cell Dev. Biol.* **2010**, *26* (1), 397–419.
19. Reyes, C. D.; Petrie, T. A.; García, A. J. Mixed Extracellular Matrix Ligands Synergistically Modulate Integrin Adhesion and Signaling. *J. Cell. Physiol.* **2008**, *217* (2), 450–458.
20. Molina-Santiago, C.; de Vicente, A.; Romero, D. Bacterial Extracellular Matrix as a Natural Source of Biotechnologically Multivalent Materials. *Comput. Struct. Biotechnol. J.* **2021**, *19*, 2796–2805.
21. Nicolas, J.; Magli, S.; Rabbachin, L.; Sampaolesi, S.; Nicotra, F.; Russo, L. 3D Extracellular Matrix Mimics: Fundamental Concepts and Role of Materials Chemistry to Influence Stem Cell Fate. *Biomacromolecules* **2020**, *21* (6), 1968–1994.
22. Alberts, B.; Johnson, A.; Lewis, J.; Raff, M.; Roberts, K.; Walter, P. *Cell-Cell Adhesion*; Garland Science: London, England, 2002.
23. Basson, M. A. Signaling in Cell Differentiation and Morphogenesis. *Cold Spring Harb. Perspect. Biol.* **2012**, *4* (6), a008151–a008151.
24. Overeem, N. J.; van der Vries, E.; Huskens, J. A Dynamic, Supramolecular View on the Multivalent Interaction between Influenza Virus and Host Cell. *Small* **2021**, *17* (13), e2007214.
25. Barnard, A.; Smith, D. K. Self-Assembled Multivalency: Dynamic Ligand Arrays for High-Affinity Binding. *Angew. Chem. Int. E.* **2012**, *51* (27), 6572–6581.
26. Badjić, J. D.; Nelson, A.; Cantrill, S. J.; Turnbull, W. B.; Stoddart, J. F. Multivalency and Cooperativity in Supramolecular Chemistry. *Acc. Chem. Res.* **2005**, *38* (9), 723–732.
27. Lopez-Fontal, E.; Milanesi, L.; Tomas, S. Multivalence Cooperativity Leading to “All-or-Nothing” Assembly: The Case of Nucleation-Growth in Supramolecular Polymers. *Chem. Sci.* **2016**, *7* (7), 4468–4475.

28. Chen, L.; Wang, S. Multivalent Cooperativity Induced by Self-Assembly for f-Element Separation. *Commun. Chem.* **2021**, *4* (1), 78.
29. von Krbek, L. K. S.; Schalley, C. A.; Thordarson, P. Assessing Cooperativity in Supramolecular Systems. *Chem. Soc. Rev.* **2017**, *46* (9), 2622–2637.
30. Chung, M.-K.; Lee, S. J.; Waters, M. L.; Gagné, M. R. Self-Assembled Multi-Component Catenanes: The Effect of Multivalency and Cooperativity on Structure and Stability. *J. Am. Chem. Soc.* **2012**, *134* (28), 11430–11443.
31. Sevlever, F.; Di Bella, J. P.; Ventura, A. C. Discriminating between Negative Cooperativity and Ligand Binding to Independent Sites Using Pre-Equilibrium Properties of Binding Curves. *PLoS Comput. Biol.* **2020**, *16* (6), e1007929.
32. Han, S.; Kim, Y.-N.; Jo, G.; Kim, Y. E.; Kim, H. M.; Choi, J.-M.; Jung, Y. Multivalent-Interaction-Driven Assembly of Discrete, Flexible, and Asymmetric Supramolecular Protein Nano-Prisms. *Angew. Chem. Int. Ed.* **2020**, *59* (51), 23244–23251.
33. Mohammadi, E.; Kafle, P.; Huang, K.-Y.; Zhu, W.; Huang, J.; Jung, S.-H.; Lee, J.-K.; Evans, C. M.; Diao, Y. Role of Multivalent Interactions in Dynamic-Template-Directed Assembly of Conjugated Polymers. *ACS Appl. Mater. Interfaces* **2020**, *12* (2), 2753–2762.
34. Petkau-Milroy, K.; Sonntag, M. H.; Colditz, A.; Brunsveld, L. Multivalent Protein Assembly Using Monovalent Self-Assembling Building Blocks. *Int. J. Mol. Sci.* **2013**, *14* (10), 21189–21201.
35. Maiti, S.; Pezzato, C.; Garcia Martin, S.; Prins, L. J. Multivalent Interactions Regulate Signal Transduction in a Self-Assembled Hg²⁺ Sensor. *J. Am. Chem. Soc.* **2014**, *136* (32), 11288–11291.
36. Lim, Y.-B.; Lee, M. Self-Assembled Multivalent Carbohydrate Ligands. *Org. Biomol. Chem.* **2007**, *5* (3), 401–405.
37. Bakshi, A. K.; Haider, T.; Tiwari, R.; Soni, V. Critical Parameters for Design and Development of Multivalent Nanoconstructs: Recent Trends. *Drug Deliv. Transl. Res.* **2022**, *12* (10), 2335–2358.
38. Whitesides, G. M.; Boncheva, M. Beyond Molecules: Self-Assembly of Mesoscopic and Macroscopic Components. *Proc. Natl. Acad. Sci. U. S. A.* **2002**, *99* (8), 4769–4774.
39. Magdalena Estirado, E.; Aleman Garcia, M. A.; Schill, J.; Brunsveld, L. Multivalent Ultrasensitive Interfacing of Supramolecular 1D Nanoplatfoms. *J. Am. Chem. Soc.* **2019**, *141* (45), 18030–18037.
40. Arsiwala, A.; Castro, A.; Frey, S.; Stathos, M.; Kane, R. S. Designing Multivalent Ligands to Control Biological Interactions: From Vaccines and Cellular Effectors to Targeted Drug Delivery. *Chem. Asian J.* **2019**, *14* (2), 244–255.

41. Curk, T.; Dubacheva, G. V.; Brisson, A. R.; Richter, R. P. Controlling Superselectivity of Multivalent Interactions with Cofactors and Competitors. *J. Am. Chem. Soc.* **2022**, *144* (38), 17346–17350.
42. Mammen, M.; Choi, S.-K.; Whitesides, G. M. Polyvalent Interactions in Biological Systems: Implications for Design and Use of Multivalent Ligands and Inhibitors. *Angew. Chem. Int. Ed.* **1998**, *37* (20), 2754–2794.
43. Wang, H.; Koshi, Y.; Minato, D.; Nonaka, H.; Kiyonaka, S.; Mori, Y.; Tsukiji, S.; Hamachi, I. Chemical Cell-Surface Receptor Engineering Using Affinity-Guided, Multivalent Organocatalysts. *J. Am. Chem. Soc.* **2011**, *133* (31), 12220–12228.
44. Bagul, R. S.; Jayaraman, N. Multivalent Dendritic Catalysts in Organometallic Catalysis. *Inorganica Chim. Acta* **2014**, *409*, 34–52.
45. Huskens, J. Multivalent Interactions at Interfaces. *Curr. Opin. Chem. Biol.* **2006**, *10* (6), 537–543.
46. Nijhuis, C. A.; Huskens, J.; Reinhoudt, D. N. Binding Control and Stoichiometry of Ferrocenyl Dendrimers at a Molecular Printboard. *J. Am. Chem. Soc.* **2004**, *126* (39), 12266–12267.
47. Nijhuis, C. A.; Yu, F.; Knoll, W.; Huskens, J.; Reinhoudt, D. N. Multivalent Dendrimers at Molecular Printboards: Influence of Dendrimer Structure on Binding Strength and Stoichiometry and Their Electrochemically Induced Desorption. *Langmuir* **2005**, *21* (17), 7866–7876.
48. Nijhuis, C. A.; Dolatowska, K. A.; Ravoo, B. J.; Huskens, J.; Reinhoudt, D. N. Redox-Controlled Interaction of Biferrocenyl-Terminated Dendrimers with Beta-Cyclodextrin Molecular Printboards. *Chemistry* **2007**, *13* (1), 69–80.
49. Zaramella, D.; Scrimin, P.; Prins, L. J. Self-Assembly of a Catalytic Multivalent Peptide-Nanoparticle Complex. *J. Am. Chem. Soc.* **2012**, *134* (20), 8396–8399.
50. Pieters, G.; Prins, L. J. Catalytic Self-Assembled Monolayers on Gold Nanoparticles. *New J Chem* **2012**, *36* (10), 1931–1939.
51. Scrimin, P.; Cardona, M. A.; Prieto, C. M. L.; Prins, L. J. Multivalency as a Design Criterion in Catalyst Development. In *Multivalency*; John Wiley & Sons, Ltd: Chichester, UK, 2017; pp 153–176.
52. Zaupa, G.; Scrimin, P.; Prins, L. J. Origin of the Dendritic Effect in Multivalent Enzyme-like Catalysts. *J. Am. Chem. Soc.* **2008**, *130* (17), 5699–5709.

53. Zaupa, G.; Mora, C.; Bonomi, R.; Prins, L. J.; Scrimin, P. Catalytic Self-Assembled Monolayers on Au Nanoparticles: The Source of Catalysis of a Transphosphorylation Reaction. *Chemistry* **2011**, *17* (17), 4879–4889.
54. Argyle, M.; Bartholomew, C. Heterogeneous Catalyst Deactivation and Regeneration: A Review. *Catalysts* **2015**, *5* (1), 145–269.
55. Dutta, S.; Corni, S.; Brancolini, G. Molecular Dynamics Simulations of a Catalytic Multivalent Peptide-Nanoparticle Complex. *Int. J. Mol. Sci.* **2021**, *22* (7), 3624.
56. Salai Cheettu Ammal, S.; Takami, S.; Kubo, M.; Miyamoto, A. Integrated Computational Chemistry System for Catalysts Design. *Bull. Mater. Sci.* **1999**, *22* (5), 851–861.
57. Erlendsson, S.; Teilum, K. Binding Revisited-Avidity in Cellular Function and Signaling. *Front. Mol. Biosci.* **2020**, *7*, 615565.
58. Lanfranco, R.; Jana, P. K.; Tunesi, L.; Cicuta, P.; Mognetti, B. M.; Di Michele, L.; Bruylants, G. Kinetics of Nanoparticle-Membrane Adhesion Mediated by Multivalent Interactions. *Langmuir* **2019**, *35* (6), 2002–2012.
59. Errington, W. J.; Bruncsics, B.; Sarkar, C. A. Mechanisms of Noncanonical Binding Dynamics in Multivalent Protein-Protein Interactions. *Proc. Natl. Acad. Sci. U. S. A.* **2019**, *116* (51), 25659–25667.
60. Leunissen, M. E.; Frenkel, D. Numerical Study of DNA-Functionalized Microparticles and Nanoparticles: Explicit Pair Potentials and Their Implications for Phase Behavior. *J. Chem. Phys.* **2011**, *134* (8), 084702.
61. Gomez-Casado, A.; Dam, H. H.; Yilmaz, M. D.; Florea, D.; Jonkheijm, P.; Huskens, J. Probing Multivalent Interactions in a Synthetic Host-Guest Complex by Dynamic Force Spectroscopy. *J. Am. Chem. Soc.* **2011**, *133* (28), 10849–10857.
62. Schulte, C.; Soldà, A.; Spänig, S.; Adams, N.; Bekić, I.; Streicher, W.; Heider, D.; Strasser, R.; Maric, H. M. Multivalent Binding Kinetics Resolved by Fluorescence Proximity Sensing. *Commun. Biol.* **2022**, *5* (1), 1070.
63. Reader, P. P.; Shaw, A. M. Kinetic Analysis of the Multivalent Ligand Binding Interaction between Protein A/G and IgG: A Standard System Setting. *J. Phys. Chem. B* **2017**, *121* (38), 8919–8925.
64. Metzger, H. Receptors: Models for Binding, Trafficking, and Signaling. Douglas A. Lauffenburger, Jennifer J. Linderman. *Q. Rev. Biol.* **1995**, *70* (1), 72–73.

65. Klein, P.; Pawson, T.; Tyers, M. Mathematical Modeling Suggests Cooperative Interactions between a Disordered Polyvalent Ligand and a Single Receptor Site. *Curr. Biol.* **2003**, *13* (19), 1669–1678.
66. De Lean, A.; Rodbard, D. Kinetics of Cooperative Binding. In *General Principles and Procedures*; Springer US: Boston, MA, 1979; pp 143–192.
67. Parsons, D. L.; Vallner, J. J. Theoretical Models for Cooperative Binding—III. Positive and Negative Site-Site Cooperativity. *Math. Biosci.* **1978**, *41* (3–4), 231–240.
68. Douglass, E. F., Jr; Miller, C. J.; Sparer, G.; Shapiro, H.; Spiegel, D. A. A Comprehensive Mathematical Model for Three-Body Binding Equilibria. *J. Am. Chem. Soc.* **2013**, *135* (16), 6092–6099.
69. Faas, G. C.; Schwaller, B.; Vergara, J. L.; Mody, I. Resolving the Fast Kinetics of Cooperative Binding: Ca²⁺ Buffering by Calretinin. *PLoS Biol.* **2007**, *5* (11), e311.
70. Johnson, M. L. Mathematical Modeling of Cooperative Interactions in Hemoglobin. *Methods Enzymol.* **2000**, *323*, 124–155.
71. Stefan, M. I.; Le Novère, N. Cooperative Binding. *PLoS Comput. Biol.* **2013**, *9* (6), e1003106.
72. Savageau, M. A. Biochemical Systems Analysis. I. Some Mathematical Properties of the Rate Law for the Component Enzymatic Reactions. *J. Theor. Biol.* **1969**, *25* (3), 365–369.
73. Lasaga, A. C. Chapter 1. Rate Laws of Chemical Reactions. In *Kinetics of Geochemical Processes*; Lasaga, A. C., Kirkpatrick, J., Eds.; De Gruyter: Berlin, Boston, 1981; pp 1–68.
74. Violi, A.; Sarofim, A. F.; Voth, G. A. Kinetic Monte Carlo–Molecular Dynamics Approach to Model Soot Inception. *Combust. Sci. Technol.* **2004**, *176* (5–6), 991–1005.
75. Violi, A.; Kubota, A.; Truong, T. N.; Pitz, W. J.; Westbrook, C. K.; Sarofim, A. F. A Fully Integrated Kinetic Monte Carlo/Molecular Dynamics Approach for the Simulation of Soot Precursor Growth. *Proc. Combust. Inst.* **2002**, *29* (2), 2343–2349.
76. Tagliazucchi, M.; Szleifer, I. Dynamics of Dissipative Self-Assembly of Particles Interacting through Oscillatory Forces. *Faraday Discuss.* **2016**, *186* (0), 399–418.
77. De, S.; Klajn, R. Dissipative Self-Assembly Driven by the Consumption of Chemical Fuels. *Adv. Mater.* **2018**, *30* (41), e1706750.

78. Tagliazucchi, M.; Weiss, E. A.; Szleifer, I. Dissipative Self-Assembly of Particles Interacting through Time-Oscillatory Potentials. *Proc. Natl. Acad. Sci. U. S. A.* **2014**, *111* (27), 9751–9756.
79. Vriezema, D. M.; Comellas Aragonès, M.; Elemans, J. A. A. W.; Cornelissen, J. J. L. M.; Rowan, A. E.; Nolte, R. J. M. Self-Assembled Nanoreactors. *Chem. Rev.* **2005**, *105* (4), 1445–1489.
80. Mattia, E.; Otto, S. Supramolecular Systems Chemistry. *Nat. Nanotechnol.* **2015**, *10* (2), 111–119.
81. Vanag, V. K.; Epstein, I. R. Pattern Formation in a Tunable Medium: The Belousov-Zhabotinsky Reaction in an Aerosol OT Microemulsion. *Phys. Rev. Lett.* **2001**, *87* (22), 228301.
82. Carballido-Landeira, J.; Vanag, V. K.; Epstein, I. R. Patterns in the Belousov-Zhabotinsky Reaction in Water-in-Oil Microemulsion Induced by a Temperature Gradient. *Phys. Chem. Chem. Phys.* **2010**, *12* (15), 3656–3665.
83. Cassani, A.; Monteverde, A.; Piumetti, M. Belousov-Zhabotinsky Type Reactions: The Non-Linear Behavior of Chemical Systems. *J. Math. Chem.* **2021**, *59* (3), 792–826.
84. Vittadello, S. T.; Leyshon, T.; Schnoerr, D.; Stumpf, M. P. H. Turing Pattern Design Principles and Their Robustness. *Philos. Trans. A Math. Phys. Eng. Sci.* **2021**, *379* (2213), 20200272.
85. Henry, B. I.; Langlands, T. A. M.; Wearne, S. L. Turing Pattern Formation in Fractional Activator-Inhibitor Systems. *Phys. Rev. E Stat. Nonlin. Soft Matter Phys.* **2005**, *72* (2 Pt 2), 026101.
86. Vanag, V. K.; Epstein, I. R. Packet Waves in a Reaction-Diffusion System. *Phys. Rev. Lett.* **2002**, *88* (8), 088303.
87. Pao, C. V. On Nonlinear Reaction-Diffusion Systems. *J. Math. Anal. Appl.* **1982**, *87* (1), 165–198.
88. Landge, A. N.; Jordan, B. M.; Diego, X.; Müller, P. Pattern Formation Mechanisms of Self-Organizing Reaction-Diffusion Systems. *Dev. Biol.* **2020**, *460* (1), 2–11.
89. Bothe, D.; Hilhorst, D. A Reaction–Diffusion System with Fast Reversible Reaction. *J. Math. Anal. Appl.* **2003**, *286* (1), 125–135.
90. Velegol, D.; Garg, A.; Guha, R.; Kar, A.; Kumar, M. Origins of Concentration Gradients for Diffusiophoresis. *Soft Matter* **2016**, *12* (21), 4686–4703.

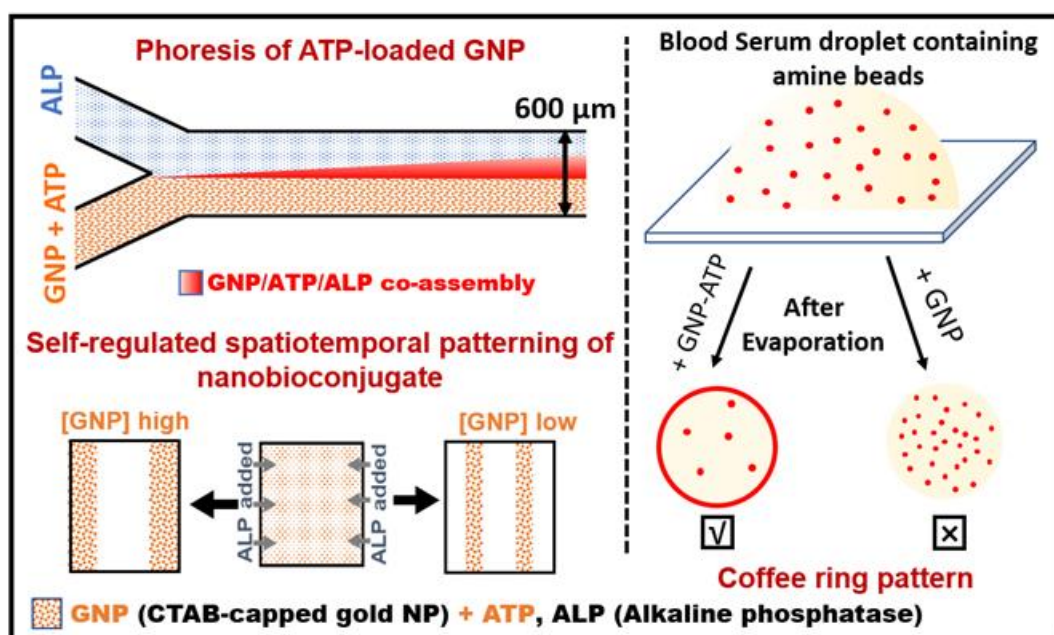
91. Shim, S. Diffusiophoresis, Diffusioosmosis, and Microfluidics: Surface-Flow-Driven Phenomena in the Presence of Flow. *Chem. Rev.* **2022**, *122* (7), 6986–7009.
92. Anderson, J. L.; Prieve, D. C. Diffusiophoresis: Migration of Colloidal Particles in Gradients of Solute Concentration. *Sep. Purif. Methods* **1984**, *13* (1), 67–103.
93. Ebel, J. P.; Anderson, J. L.; Prieve, D. C. Diffusiophoresis of Latex Particles in Electrolyte Gradients. *Langmuir* **1988**, *4* (2), 396–406.
94. Anderson, J. L.; Prieve, D. C. Diffusiophoresis Caused by Gradients of Strongly Adsorbing Solutes. *Langmuir* **1991**, *7* (2), 403–406.
95. Ault, J. T.; Shin, S.; Stone, H. A. Diffusiophoresis in Narrow Channel Flows. *J. Fluid Mech.* **2018**, *854*, 420–448.
96. Chiang, T.-Y.; Velegol, D. Multi-Ion Diffusiophoresis. *J. Colloid Interface Sci.* **2014**, *424*, 120–123.
97. Popescu, M. N.; Uspal, W. E.; Dietrich, S. Self-Diffusiophoresis of Chemically Active Colloids. *Eur. Phys. J. Spec. Top.* **2016**, *225* (11–12), 2189–2206.
98. Keh, H. J. Diffusiophoresis of Charged Particles and Diffusioosmosis of Electrolyte Solutions. *Curr. Opin. Colloid Interface Sci.* **2016**, *24*, 13–22.
99. Bian, X.; Kim, C.; Karniadakis, G. E. 111 Years of Brownian Motion. *Soft Matter* **2016**, *12* (30), 6331–6346.
100. Shewmon, P. Diffusion in a Concentration Gradient. In *Diffusion in Solids*; Springer International Publishing: Cham, 2016; pp 131–150.
101. Kinsey, S. T.; Locke, B. R.; Dillaman, R. M. Molecules in Motion: Influences of Diffusion on Metabolic Structure and Function in Skeletal Muscle. *J. Exp. Biol.* **2011**, *214* (Pt 2), 263–274.
102. Thompson, A. P.; Ford, D. M.; Heffelfinger, G. S. *Direct Molecular Simulation of Gradient-Driven Diffusion*. *J. Chem. Phys.* **1998**, *109* (15), 6406–6414.
103. Arnold, J. H. Studies in Diffusion. Ii. A Kinetic Theory of Diffusion in Liquid Systems. *J. Am. Chem. Soc.* **1930**, *52* (10), 3937–3955.
104. Tyrrell, H. J. V.; Harris, K. R. *Diffusion in Liquids: A Theoretical and Experimental Study*; Butterworth-Heinemann: Oxford, England, 2013.

105. Burridge, K. A.; Figa, M. A.; Wong, J. Y. Patterning Adjacent Supported Lipid Bilayers of Desired Composition to Investigate Receptor-Ligand Binding under Shear Flow. *Langmuir* **2004**, *20* (23), 10252–10259.
106. Fiddes, L. K.; Chan, H. K. C.; Lau, B.; Kumacheva, E.; Wheeler, A. R. Durable, Region-Specific Protein Patterning in Microfluidic Channels. *Biomaterials* **2010**, *31* (2), 315–320.
107. Nalayanda, D. D.; Kalukanimuttam, M.; Schmidtke, D. W. Micropatterned Surfaces for Controlling Cell Adhesion and Rolling under Flow. *Biomed. Microdevices* **2007**, *9* (2), 207–214.
108. Wu, X.; Moimas, S.; Hopf, R.; Giampietro, C.; Kourouklis, A.; Falk, V.; Mazza, E.; Ferrari, A. A Free-Form Patterning Method Enabling Endothelialization under Dynamic Flow. *Biomaterials* **2021**, *273* (120816), 120816.
109. Agarwal, U. S.; Dutta, A.; Mashelkar, R. A. Migration of Macromolecules under Flow: The Physical Origin and Engineering Implications. *Chem. Eng. Sci.* **1994**, *49* (11), 1693–1717.
110. Wojciak-Stothard, B. Endothelial Cell Migration under Flow. *Methods Mol. Biol.* **2011**, *769*, 137–147.
111. Lee, H.-W.; Shin, J. H.; Simons, M. Flow Goes Forward and Cells Step Backward: Endothelial Migration. *Exp. Mol. Med.* **2022**, *54* (6), 711–719.
112. *Computational Fluid Dynamics*; Wendt, J. F., Ed.; Springer Berlin Heidelberg: Berlin, Heidelberg, 2009.
113. Tu, J.; Yeoh, G. H.; Liu, C.; Tao, Y. *Computational Fluid Dynamics: A Practical Approach*; Elsevier, 2023.
114. van Ravensteijn, B. G. P.; Voets, I. K.; Kegel, W. K.; Eelkema, R. Out-of-Equilibrium Colloidal Assembly Driven by Chemical Reaction Networks. *Langmuir* **2020**, *36* (36), 10639–10656.
115. Visan, A.; Lammertink, R. G. H. Reaction Induced Diffusio-Phoresis of Ordinary Catalytic Particles. *React. Chem. Eng.* **2019**, *4* (8), 1439–1446.
116. Kirschning, A.; Solodenko, W.; Mennecke, K. Combining Enabling Techniques in Organic Synthesis: Continuous Flow Processes with Heterogenized Catalysts. *Chemistry* **2006**, *12* (23), 5972–5990.

117. Xu, B.-B.; Zhang, Y.-L.; Wei, S.; Ding, H.; Sun, H.-B. On-Chip Catalytic Microreactors for Modern Catalysis Research. *ChemCatChem* **2013**, *5* (8), 2091–2099.
118. Lee, M.-Y.; Srinivasan, A.; Ku, B.; Dordick, J. S. Multienzyme Catalysis in Microfluidic Biochips. *Biotechnol. Bioeng.* **2003**, *83* (1), 20–28.
119. Baraban, L.; Harazim, S. M.; Sanchez, S.; Schmidt, O. G. Chemotactic Behavior of Catalytic Motors in Microfluidic Channels. *Angew. Chem. Weinheim Bergstr. Ger.* **2013**, *125* (21), 5662–5666.
120. Luckarift, H. R.; Ku, B. S.; Dordick, J. S.; Spain, J. C. Silica-Immobilized Enzymes for Multi-Step Synthesis in Microfluidic Devices. *Biotechnol. Bioeng.* **2007**, *98* (3), 701–705.
121. Belder, D.; Ludwig, M.; Wang, L.-W.; Reetz, M. T. Enantioselective Catalysis and Analysis on a Chip. *Angew. Chem. Int. Ed.* **2006**, *45* (15), 2463–2466.
122. Kupitz, D.; Alonso, S.; Bär, M.; Hauser, M. J. B. Surfactant-Induced Gradients in the Three-Dimensional Belousov-Zhabotinsky Reaction. *Phys. Rev. E Stat. Nonlin. Soft Matter Phys.* **2011**, *84* (5 Pt 2), 056210.
123. Miyazaki, J. Belousov–Zhabotinsky Reaction. In *Pattern Formations and Oscillatory Phenomena*; Kinoshita, S., Ed.; Elsevier, 2013; pp 61–83.
124. Vanag, V. K.; Epstein, I. R. Cross-Diffusion and Pattern Formation in Reaction-Diffusion Systems. *Phys. Chem. Chem. Phys.* **2009**, *11* (6), 897–912.
125. Nijhuis, C. A.; Ravoo, B. J.; Huskens, J.; Reinhoudt, D. N. Electrochemically Controlled Supramolecular Systems. *Coord. Chem. Rev.* **2007**, *251* (13–14), 1761–1780.
126. Fasting, C.; Schalley, C. A.; Weber, M.; Seitz, O.; Hecht, S.; Kokschi, B.; Dornedde, J.; Graf, C.; Knapp, E.-W.; Haag, R. Multivalency as a Chemical Organization and Action Principle. *Angew. Chem. Int. Ed.* **2012**, *51* (42), 10472–1049.

CHAPTER 2

Self-regulatory Enzyme-actuated Micro/Macroscale Patterning of ATP- loaded Nanoparticle



This is adapted reproduction from Shandilya, E.; Maiti, S. Self-Regulatory Micro- and Macroscale Patterning of ATP-Mediated Nanobioconjugate. *ACS Nano* **2023**, *17* (5), 5108–5120.

2.1. Introduction

The demand for surface patterning technology, capable of controlling patterns on different length scales, has been increasing due to its wide range of applications in designing task-specific materials with tailored properties and functionalities.¹⁻³ By manipulating surface patterns, researchers can engineer materials optimized for applications in optoelectronics, plasmonic (bio)analysis, catalysis, and more.² In the realm of (bio)analytical techniques, surface patterning improves sensitivity, selectivity, and efficiency, benefiting biosensing, lab-on-a-chip devices, and microfluidics. Surface patterning can also optimize catalyst performance, leading to more efficient and sustainable chemical processes in energy production, environmental remediation, and pharmaceutical synthesis.⁴ However, achieving precise and periodic patterning often requires the utilization of techniques like lithography (optical, electron, or ion beam), contact printing, and soft lithography using a masked deposition.⁴⁻⁷ Despite their efficiency, these methods have certain drawbacks including the need for surface pre- or post-treatment, high costs, and reliance on skilled operators for optimal results.⁸ Researchers have recently turned their attention to molecular and supramolecular self-assembly strategies for surface patterning to overcome these challenges. These approaches offer a cost-effective and versatile alternative, particularly for various analysis purposes and large-area patterning.⁸⁻¹³ Notably, the biological world employs competitive and dynamic self-assembly processes driven by local microscale interactivity to achieve spatiotemporal patterning.¹⁴⁻¹⁶ In the realm of surface patterning, a variety of approaches have been employed, including surface-immobilized enzymes, specific protein-ligand binding affinity, complementary DNA strand or DNA origami-driven nanoparticle organization, as well as pH- or light-responsive molecular assembly.¹⁷⁻²⁰ Both non-template and template-assisted strategies have been utilized to create a gradient and localized patterning.²⁰ Additionally, diffusiophoresis, which involves utilizing a simple salt gradient, has emerged as an attractive strategy for segregating and spatially patterning colloidal particles.^{21,22} Chemical engineers have primarily adopted this process for filtration, separation, sedimentation, and the transport of different types of soft and hard nano/microparticles, including microorganisms.²¹

However, existing works in this area have mainly focused on gradients of commonly used inorganic salts such as NaCl, KCl, and MgCl₂.⁵⁰ Importantly, in this study, we demonstrate substrate-bound colloidal diffusiophoresis in the presence of an enzyme gradient. By harnessing the binding affinity between enzymes and substrates, along with the enzyme-driven

hydrolysis of the substrate, we generate an "in situ" salt (hydrolyzed product) gradient. This controlled propulsion event results in the aggregation and patterning of nanoparticles in different regions. Keeping these reports in mind, we asked the following questions –

- What will happen if the enzyme comes in contact with a surface-bound substrate? Will they still interact or will be able to form an assembly? If so, can we use this assembly for surface modification at different length scales?
- Can we utilize these enzyme-substrate interactions for modulating coffee ring pattern formation in serum samples for diagnostic purposes?

In response to the above questions, we investigate the sequestration and aggregation of anionic nucleotides (AMP/ADP/ATP) on the surface of cationic surfactant-bound gold nanoparticles (GNPs) in the presence of alkaline phosphatase (ALP) enzyme (Figure 2.1a). We also demonstrate the controlled patterning of the aggregating zone of GNP/ATP/ALP through a selective gradient of enzyme and substrate (Figure 2.1b). Additionally, we explore the formation of coffee ring patterns from evaporating droplets containing aqueous buffer and blood serum, facilitated by a specific GNP-ATP conjugate (Figure 2.1c). Moreover, our approach utilizes the inherent affinity between ALP and adenosine nucleotide-based substrates (AM/D/TP), which are noncovalently bound to the nanoparticle surface. This allows us to assemble the nanoparticle-enzyme ensemble in a controlled manner within the conditions of an enzyme gradient and during droplet evaporation. This approach offers two notable advantages: (i) it enables the simultaneous assembly and patterning of nanoparticles and enzymes at micro- and millimeter-scale regions using a diffusiophoretic process, and (ii) it allows for the manipulation of coffee ring patterns by incorporating ATP-loaded nanoparticles and enzymes, thereby offering potential applications in cost-effective disease diagnostics.²³⁻²⁹

The phenomenon of enzyme-substrate interactivity-driven colloidal chemotaxis-cum-phoresis, including the coffee ring effect, holds significant implications in the field of nanobiotechnology, providing insights into biomolecular phoresis and finding practical applications in various domains such as forensics and diagnostic assays.²³ Our study contributes to the understanding of controlled collective migratory behavior and precise positioning of nanoparticle-enzyme conjugates at different scales, further advancing the ongoing research on "enzyme/biocolloidal chemotaxis and clustering" inspired by physiological processes like purinosome or metabolon formation.³⁰⁻³⁵

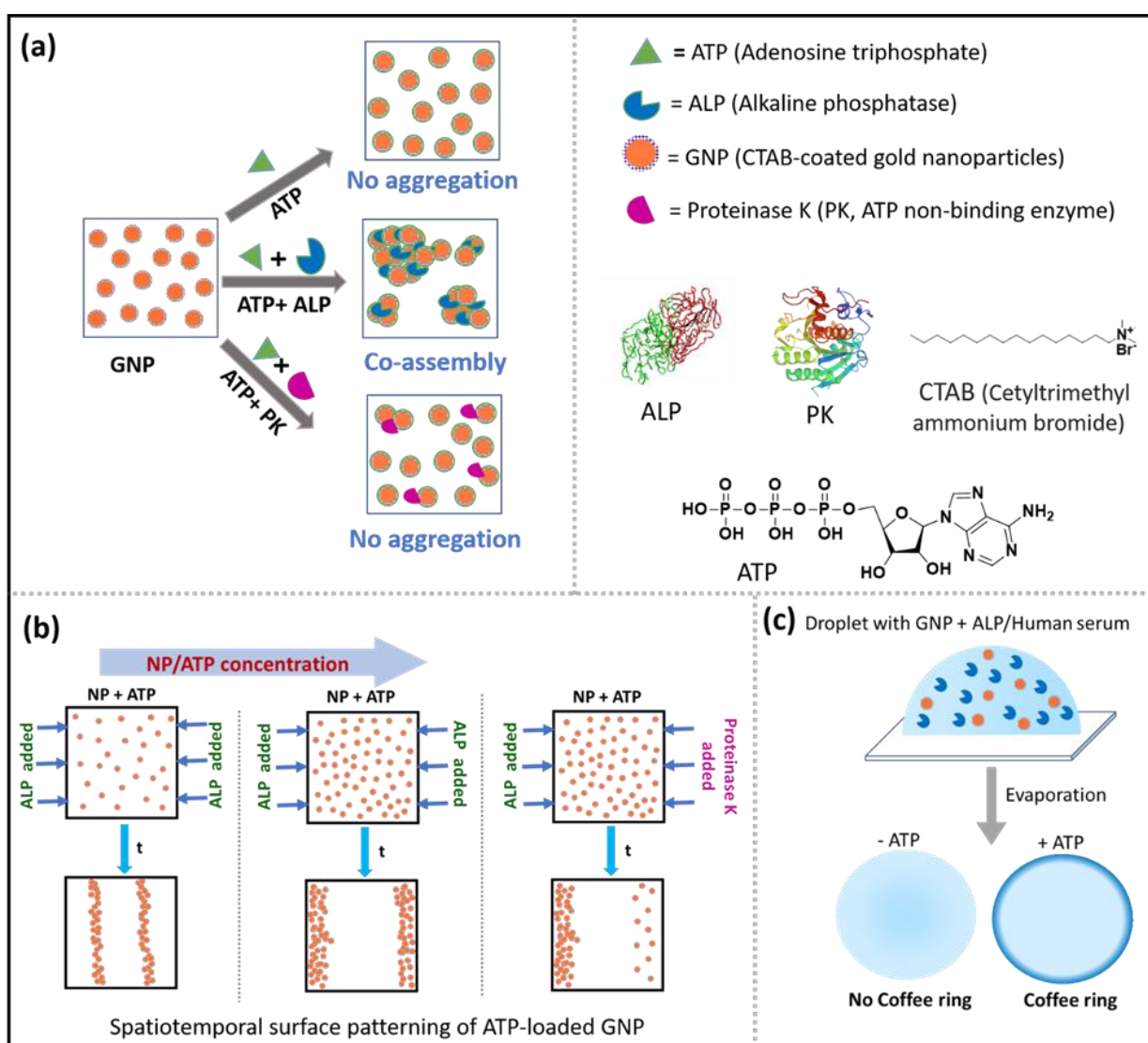


Figure 2.1. Schematic representation showing (a) specific aggregation of GNP in the simultaneous presence of ATP and ALP; (b) spatial aggregation pattern in the gradient of ALP; and (c) coffee ring effect upon evaporation of droplet due to evaporation of droplet containing blood serum with GNP-ATP conjugate.

2.2 Materials

All reagents used in the study were commercially available and used without further purification. Cetyltrimethylammonium bromide, silver nitrate, sodium borohydride, ascorbic acid, trisodium phosphate, Bovine Serum Albumin (BSA), FITC (Fluorescein isothiocyanate), proteinase K (PK), and Tris(hydroxymethyl)aminomethane (Tris base) were procured from Sisco Research Laboratory (SRL), India. Gold (III) Chloride trihydrate, adenosine triphosphate sodium salt (ATP), adenosine diphosphate (ADP), adenosine monophosphate (AMP), tetraspartic acid (DDDD), blood serum, Potato Apyrase (PA), and carboxylate and amine-

functionalized polystyrene beads were purchased from Sigma-Aldrich. Tetramethyl rhodamine isothiocyanate (RITC) was obtained from TCI chemicals. Throughout the study, we used milli-Q water. The hybridization chambers used had dimensions of 8-9 mm diameter \times 0.8 mm depth, 26 mm \times 51 mm OD, and 1.5 mm diameter ports, and were procured from GRACE Bio-Labs. The 2-inlet-2-outlet microfluidic chip (1.7 cm length \times 600 μ m width \times 100 μ m height) was obtained from Vena Delta.

2.3. Methods

2.3.1. Synthesis of Gold Nanoparticles (GNP)

Gold nanoparticles were synthesized following a previously reported seed-growth method.³⁹ In brief, a seed solution was prepared by adding HAuCl₄·4H₂O (0.25 mM) solution to a vial containing 0.75 mM CTAB solution. To this mixture, an ice-cold sodium borohydride solution was added, resulting in the formation of brown-colored seeds. For the growth solution, HAuCl₄·4H₂O (24 mM, 1.03 mL) solution was mixed with 5.22 mL of water, followed by the addition of CTAB (0.1 M, 10 mL) solution, causing the solution to change from light yellow to orange. Subsequently, l-ascorbic acid (0.1 M, 7.5 mL) was gently shaken into the solution, leading to its colorless appearance. To initiate growth, 62.5 μ L of aged seeds (2 hours) was vigorously blended with the growth solution for 20 seconds, resulting in a red color. The solution was then left undisturbed at 25 °C for 24 hours. The synthesized nanoparticles were subsequently purified using a Sephadex-G25 column and characterized prior to a further utilization.

2.3.2. Aggregation Kinetics

To investigate the aggregation of gold nanoparticles (GNP) in the presence of various nucleotides, peptides, enzymes, and salts, UV-vis spectroscopic measurements were conducted using an Agilent Cary 60 spectrophotometer. A 10 mm quartz cuvette from Optiglass was used, and the reaction volume was fixed at 1 mL with a nanoparticle concentration of 120 pM in most cases. Dynamic light scattering (DLS) studies and zeta potential measurements were also performed on the same samples using a Horiba Zetasizer SZ100-V2 to ensure aggregation.

2.3.3. Transmission Electron Microscopy (TEM) Imaging

JEOL JEM-F200 microscope was utilized to visualize the agglomeration of nanoparticles. TEM samples were prepared by incubating 120 pM of nanoparticles in the presence of ATP (0.3 mM), ALP (10 nM), or both for 1 hour. A small amount (5-7 μL) of the sample was cast onto a TEM grid and dried under vacuum before imaging.

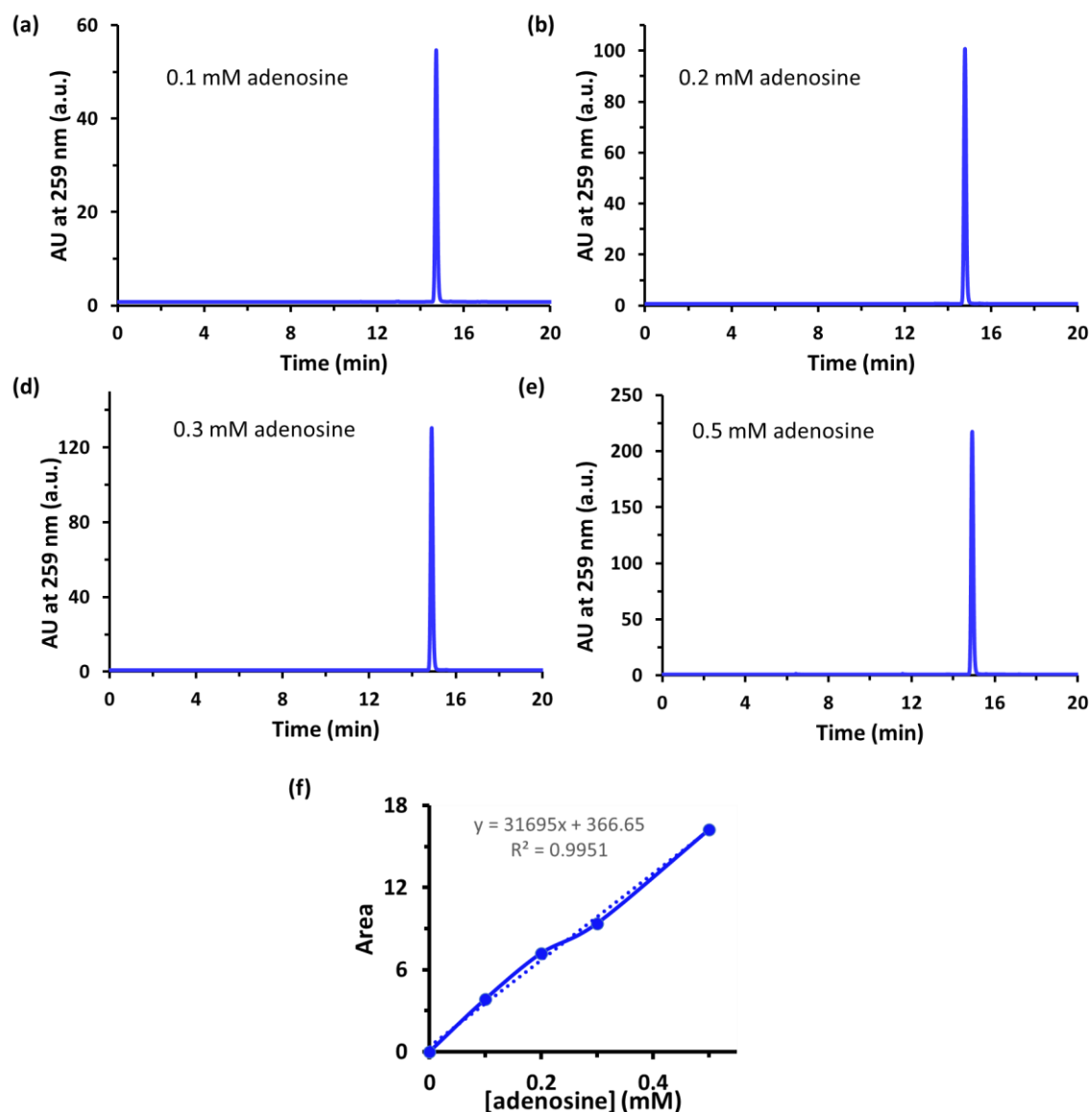


Figure 2.2. (a-e) HPLC Chromatogram of Adenosine (0.1 -0.5 mM) separated by C18 column using phosphate buffer/MeOH (97:3; v/v) (b) Calibration curve for adenosine.

2.3.4. Diffusion Coefficient Calculation

Mean square displacement (MSD) measurements were conducted to examine the impact of aggregation on the diffusion of nanoparticles. Carboxylate-modified polystyrene beads (diameter = 2 μm) were used to create a micron-sized replica of the nanoparticles (Bead-GNP).

The Bead-GNP complex was formed by mixing 25 $\mu\text{L}/\text{mL}$ bead solution with 0.45 nM GNP solution, followed by sonication for 12 minutes. MSD measurements were performed by pouring the sample solutions into a hybridization chamber on a glass slide and recording the motion of the micrometer-sized particles using a Zeiss Axio observer 7 microscopes with a 100 \times objective and AxioCam 503 Mono 3 Megapixel camera. The trajectories extracted from the recorded videos were used to calculate the average MSD plotted against Δt , from which the diffusion coefficient was determined using $\text{MSD} = 4D\Delta t$ for each sample.

2.3.5. HPLC measurements

HPLC analysis was performed on an Agilent 1260 Infinity II apparatus and chromatographic separations were carried out on a C18 4 μm , 150 \times 4.6mm column. The mobile phase consists of A:150 mM potassium phosphate buffer, pH7, and B: methanol (MeOH). The injection volume was 20 μL and the system was run iso-critically at 97% of A with a 0.2 ml/min flow rate. In order to investigate the hydrolytic activity of ALP on adenosine nucleotides in the presence and absence of GNPs, we conducted HPLC experiments to measure the amount of adenosine formed after a 60-minute reaction. The amount of ATP, ADP, and AMP was fixed at 0.3 mM. The calibration curve for adenosine is shown in Figure 2.2.

2.3.6. Phosphatase assay

Malachite Green (MG) probe solution was prepared according to the previously reported protocol (*J. Biol. Chem.* **2011**, 286, 30401-30408).

Alkaline phosphatase activity assay: For the assay, a reaction mixture containing 0.3 mM ATP/AMP with 0.5 μM ALP was prepared in 15 mM, pH 9 Tris-HCl buffer. After 10 minutes of the reaction period, 50 μl of the reaction mixture was added to 400 μl of MG probe solution, and after 1 minute 50 μl of citric acid was added to the mixture. After 1 minute, the absorption spectrum was recorded using a UV-Vis spectrometer between the range 400 - 700 nm. The peak was monitored at 620 nm. A similar procedure was followed after 20 minutes of reaction time.

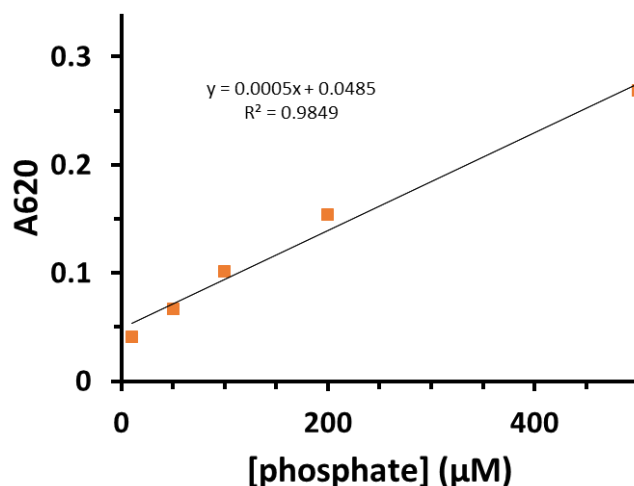


Figure 2.3. Calibration curve for the amount of phosphate present in the solution generated by using the malachite green assay.

2.3.7. Microfluidics Measurements

For visualization of the enzyme inside the microfluidic channel, ALP and BSA were labeled with FITC using a previously reported protocol.⁵⁰ For patterning under flow conditions, 2 inlet – 1 outlet microfluidic chip was used. From top and bottom inlets, GNP (120 pM) + 0.3 mM (ATP/AMP) or GNP + Adenosine (0.3 mM) + Pi (0.9 mM) and FITC-tagged ALP (50 % labeled) was injected respectively, at 300 μl/h flow rate using syringe pump bought from World Precision Instruments. Fluorescence microscope images using a 5x objective were taken across the channel (mostly near the inlet and outlet) and pixel intensity was calculated using ImageJ software and plotted against channel width. Next, to understand the migratory behavior of nanoparticles in response to adenosine and phosphate which are products of ALP activity over ATP. We used a two-inlet two-outlet microfluidics chip as shown in Figure 2.32. 120 pM GNP solution in buffer was injected from the bottom inlet, and buffer or 0.3 mM adenosine + 0.9 mM Pi (product of 0.3 mM ATP) in 15 mM tris-HCl, pH 9 buffer was injected from the top inlet at 0.3 ml/hr flow rate using a syringe pump. Then after, 30 minutes of run time solution from both outlets was collected and measured using a UV spectrophotometer.

2.3.8. Spatiotemporal Patterning of Nanoparticles over Glass Surface

To observe the spatiotemporal patterning of GNP assembly formation on a glass surface, ALP was labeled with FITC, and proteinase K was labeled with RITC using previously reported protocols.⁵⁰ A 15 μL solution of GNP (120 pM) with or without substrates like ATP or DDDD

was applied to a glass slide, and a square coverslip (2.2 cm × 2.2 cm) was placed over it. The coverslip was divided into five zones (A to E) for data interpretation. Then, 7 μL of enzyme solution (ALP or Proteinase K) was added from opposite edges, and images were taken at different time points using a 20× objective. ImageJ software was used for the analysis, and pixel intensity (labeled as Fl. Intensity) was plotted against the coverslip width. For the spatiotemporal patterning of Bead-GNP conjugates, a 15 μL solution of Bead-GNP containing 120 pM GNP and 0.005% carboxylate-modified beads in pH 9, 15 mM tris-HCl buffer was prepared. The solution was added to a glass slide, and a coverslip was placed over it. Microscopic images were captured in different zones. A similar experiment was conducted by adding ATP with the Bead-GNP complex and adding ALP (unlabeled) from opposite edges of the coverslip.

2.3.9. Theoretical evaluation of migration of nanoparticles under flow conditions

To understand the migratory behavior of nanoparticles, we modeled a square-shaped electrophoresis device (22 mm x 22 mm) having one inlet and one outlet using COMSOL Multiphysics (5.6 version) (Figure 2.37). This model uses electrophoretic transport and the laminar flow interfaces/modules. A laminar carrier stream of ATP-loaded nanoparticles was injected through an inlet with 0.3 ml/h fluid velocity and the components were separated by means of migratory transport in an electric field. The electrophoretic transport module connects the transport of ionic species by diffusion, convection, and migration in electric fields. The mass-balance equation used here to solve the nanoparticle migration is as follows:

$$\nabla \cdot (-D_i \nabla c_i - z_i u_{m,i} F c_i \nabla V) + u \cdot \nabla c_i = 0 \quad (2.1)$$

where C_i denotes the concentration of species, D_i is the diffusion coefficient of i^{th} species, u be the fluid velocity, F denotes Faraday's constant, V is the electric potential, z_i is the charge number of ionic species, and $u_{m,i}$ be the ionic mobility of species. Apart from this, we also used equations for the charge transport in the electrolyte by assuming electroneutrality condition, and a set of chemical equilibria for water self-ionization and dissociation reactions of weak acids and weak bases incorporated in the Electrophoretic module of COMSOL. The fluid flow set up includes solving Navier-Stokes equations along with Laminar flow. Herein, we considered the left and right wall of the device as the electrode having potential + 8 mV similar to the zeta potential of GNP + ATP + ALP system, while the top and bottom have no potential and serve as outlet and inlet, respectively. In addition to this, we considered a wall

having no potential at the center. For parameters, we used ATP-loaded nanoparticles (1 mM) from the inlet along with weak acid (pKa = 7, mobility = 2.4e-13 s.mol/Kg) and weak base (pKa = 7, mobility = 2.4e-13 s.mol/Kg) to maintain neutrality. The isoelectric point used for the ATP-loaded nanoparticle stream was considered 2. After solving-above mentioned equation, we observed that the concentration of ATP-loaded nanoparticles was higher on the left and right boundaries of the channel in comparison to the center of the channel showing the movement of nanoparticle laminar stream towards GNP+ATP+ ALP.

2.3.10. Phoretic velocity calculation

The generalized equation for the calculation of diffusiophoretic velocity is following:

$$U_{dp} = (\varepsilon kT / \eta Z e) \left\{ \beta \zeta - \frac{2kT}{Ze} \ln \left[1 - \tanh^2 \left(\frac{Ze\zeta}{4kT} \right) \right] \right\} \frac{\nabla C}{C} \quad (2.2)$$

This is a generalized equation combining both electrophoresis and chemiophoresis parts, where the first part is the electrophoretic component.⁵⁰ Here, U_{dp} = diffusiophoretic velocity; ε = permittivity of medium (6.9×10^{-10} F s⁻¹); $k_B = 1.38 \times 10^{-23}$ J K⁻¹, $T = 298$ K, $e = 1.6 \times 10^{-19}$ C and $\eta = 10^{-3}$ Pa.s, Z is the charge of the ions involved. Now, considering enzyme in a gradient of salt with different β -value, the diffusiophoretic velocity will mainly depend on $\beta \zeta$ -term. Now,

$$\beta = \frac{D_+ - D_-}{Z_+ D_+ - Z_- D_-} \quad (2.11)$$

and ζ is the zeta potential of the particle.⁵⁰ D_+ and D_- are the diffusion coefficient of cation and anion, respectively. Diffusion co-efficient of $\text{HPO}_4^{2-} = 1.9 \times 10^{-9}$ m² s⁻¹, $D_{\text{Na}^+} = 1.33 \times 10^{-9}$ m² s⁻¹ and thus β is 0.24.

Now, considering the ζ -potential of GNP-ATP conjugate is +20 mV, the diffusiophoretic velocity due to solely electrophoretic effect gained by the conjugate in a gradient of Pi (considering $\nabla C/C = 1 \mu\text{m}^{-1}$) will be around 42 $\mu\text{m/s}$. Therefore, we have observed the upgradient migration of GNP-ATP conjugate towards Pi (Figure 2.29). It also reflects migration and accumulation of GNP-ATP or GNP-AMP conjugate towards ALP gradient as in this case, Pi formed towards the enzyme side whereas, in the presence of only GNP-Pi conjugate (non-catalytic condition), we did not observe any notable migration of GNP-Pi-ALP aggregated band towards enzyme side (Figure 2.24, 2.28).

2.3.10. Coffee Ring Pattern Formation

A sample containing FITC labeled ALP (0.5 μM , 50 % labeled) was prepared with and without ATP, and GNP. 1 μl of this sample was drop cast over a glass slide. After air drying this sample, microscopic images were captured. Similarly, for observing the coffee ring formation ability of GNP in the presence of blood serum, samples with blood serum (0.1%) and 0.025% amine functionalized beads were prepared and analyzed. Apart from this, 10 nM ALP or 1 μM PK was added along with the above sample, and a coffee ring pattern was observed.

2.3.11. Calculation of capillary phoresis number

To explain the coffee ring pattern formation in different samples, the capillary phoresis number has been calculated.⁵⁸ The Capillary phoresy number (CP) can be expressed as the ratio of electrokinetic velocity (U_e) and velocity due to fluid capillary convection (U_c).

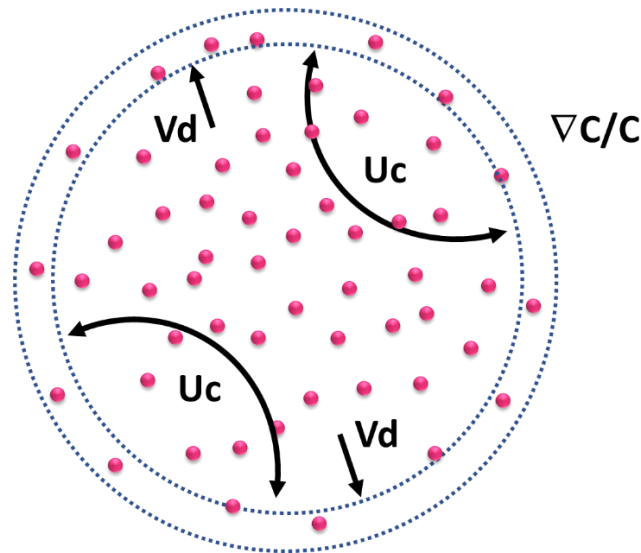


Figure 2.4. Top view of a droplet containing evenly distributed particles.

$$CP = \frac{U_e}{U_c} \quad (2.3)$$

where U_e is the net electrokinetic velocity comprising both particle diffusiophoretic (U_{dp}) and fluid diffusion-osmotic velocities (V_d), and can be given as follows:

$$U_e = \frac{\epsilon k T}{\eta_v Z e R} \beta \Delta \zeta \frac{\nabla C_{di}(\eta)}{C_{di}(\eta)} \quad (2.4)$$

where $\Delta\zeta$ is the difference between the zeta potential of particle and glass substrate, β is the dimensionless parameter denoting the diffusivity of a symmetric electrolyte, and can be expressed as follows:

$$\beta = \frac{D_+ - D_-}{D_+ + D_-} \quad (2.5)$$

Combining the above equations, we get

$$CP = \frac{\varepsilon k T t e}{\eta_v Z e R^2} \beta \Delta\zeta \quad (2.6)$$

where, $U_c \sim R/t_c$, $\nabla C_{di}(\eta)/C_{di}(\eta) \sim 1/R$ and $\frac{\varepsilon k T t e}{\eta_v Z e R^2} = K$

From here, CP can be written as

$$CP = K \beta \Delta\zeta \quad (2.7)$$

Where, $K = 0.0135$, $\beta = -0.4871$

For calculating K and β values, the values of the parameters chosen are as follows:

$D_+ = 0.7 \times 10^{-9} \text{ m}^2\text{s}^{-1}$, $D_- = 2.030 \times 10^{-9} \text{ m}^2\text{s}^{-1}$ are the diffusivity of ions since our system comprises Tris-HCl buffer. We used the diffusion coefficient of tris, and chloride ion in place of the diffusion coefficient of cation (D_+), and anion (D_-), respectively.

$R = 1.5 \text{ mm}$, radius of the drop.

$t_e = 30 \text{ min}$ (approx.), evaporation time of the drop (as per our experimental observation).

ε denotes the dielectric permittivity of the water

ζ_s is the zeta potential of the substrate (consisting of every component of the system).

ζ_{GS} is the zeta potential of the substrate (consisting of every component of the system) along with the glass surface (on which the drop was casted).

$\eta = 0.89 \times 10^{-3} \text{ Pa-s}$, viscosity of water.

$T = 25 \text{ }^\circ\text{C}$, room temperature.

The formation of particle patterns (banding/dispersion) is significantly influenced by diffusiophoresis and convection as explained in equations 2.3 to 2.7. The particles suspended in a droplet typically deposit in a ring-like pattern as it dries on a surface. The movement of

the particles is caused by three factors: (i) capillary convection within the droplet (U_{conv}); (ii) fluid diffusioosmotic transport along the substrate surface; and (iii) diffusiophoretic transport of the particles in the salt gradient (U_{dp}) in which U_{dp} and V_{do} affect by $\nabla C/C$ ratio.

2.4. Results and Discussion

Numerous biological processes involving self-assembly and patterning, such as cell-cell adhesion and viral infection, are influenced by multivalent interactions.³⁰⁻³⁵ This has motivated scientists from all domains to develop synthetic systems that mimic the dynamic behavior observed in biological systems.³⁶⁻⁴⁴ In line with this, we aimed to investigate the interaction and effectiveness of multiple charge counter-ions with a charged nanoparticle surface to induce aggregation. To accomplish this, we synthesized gold nanoparticles (GNP) capped with cetyltrimethylammonium bromide (CTAB), which imparted a positive surface charge to the nanoparticles. The synthesized GNP exhibited characteristic surface plasmon resonance absorption at 525 nm and had an average diameter of approximately 22 ± 3 nm (Figure 2.5).

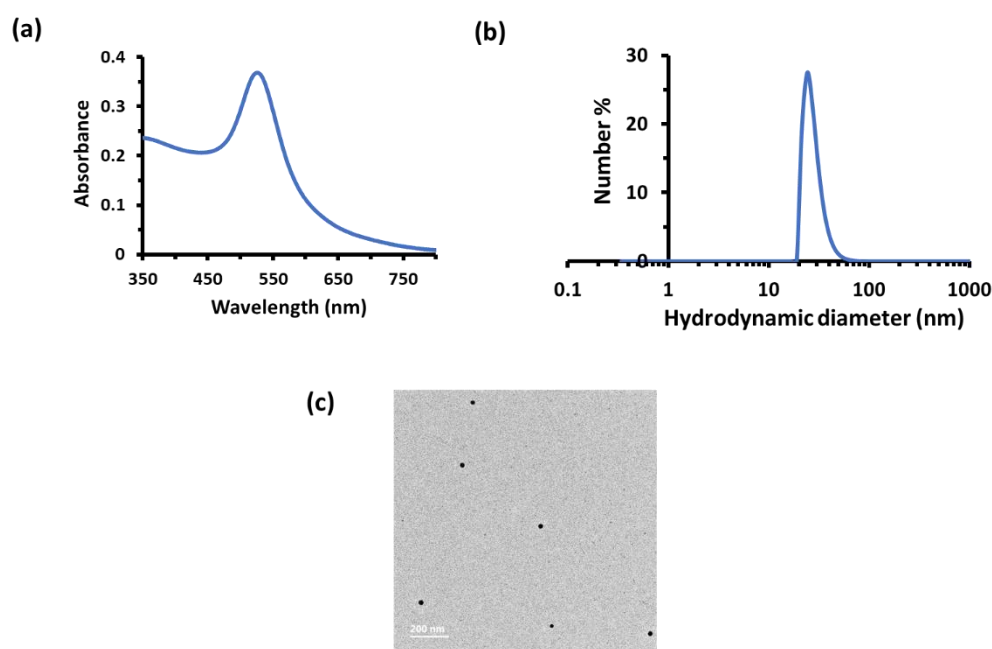


Figure 2.5 (a) UV-Vis scan of GNPs. (b) Size measurement of GNPs using (b) DLS (dynamic light scattering), (c) TEM (transmission electron microscopy) image.

We selected adenosine-based nucleotides, including adenosine triphosphate (ATP), adenosine diphosphate (ADP), and adenosine monophosphate (AMP), to examine their multivalent binding effects and the subsequent assembly of cationic GNP. The aggregation behavior of the nanoparticles was monitored using UV-vis spectroscopy by measuring the absorbance ratio at 620 nm and 520 nm (A_{620}/A_{520}).

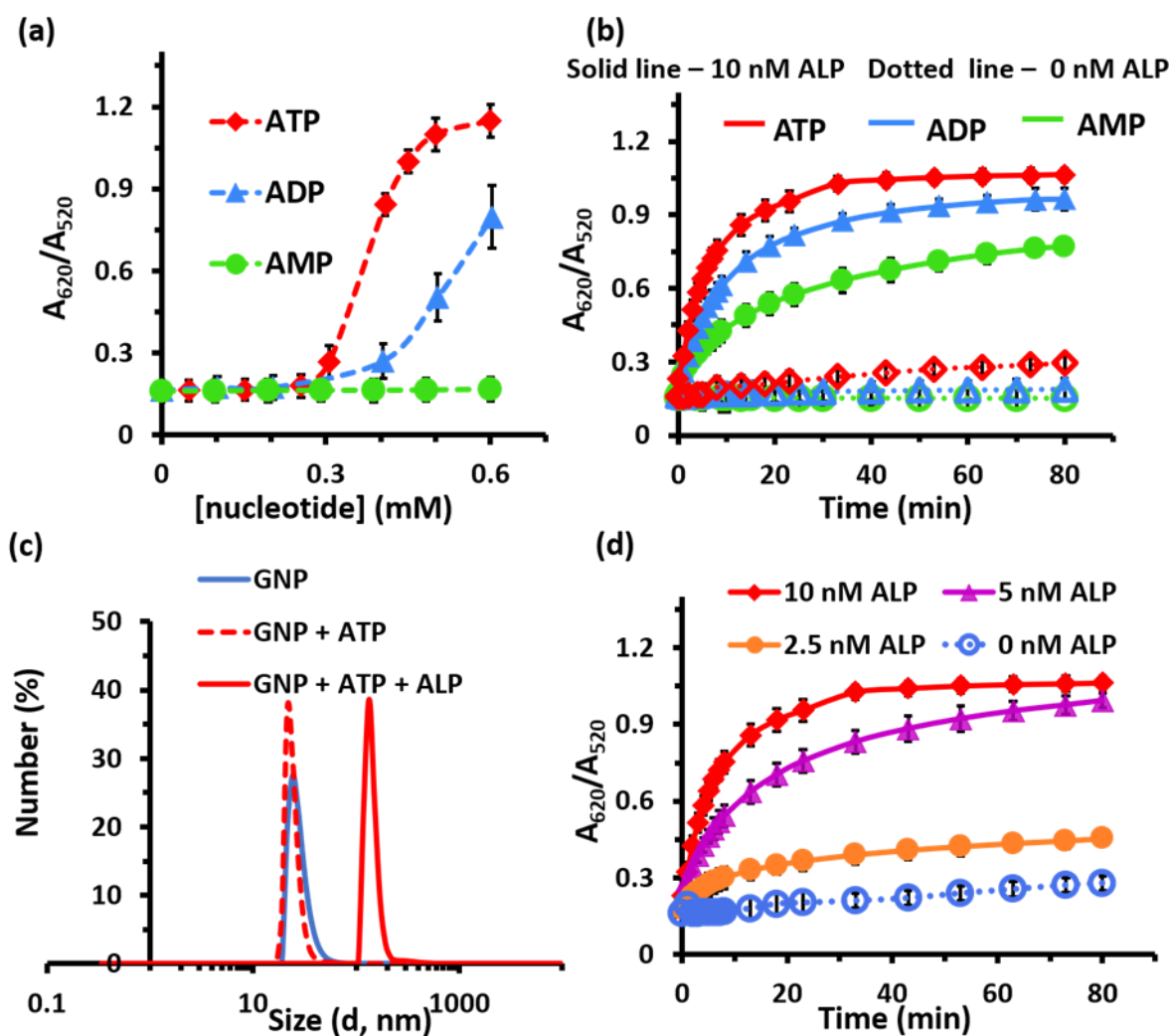


Figure 2.6. (a) Change in UV-vis absorbance ratio at 620 and 520 nm (A_{620}/A_{520}) ratio of CTAB-capped GNP in the presence of different concentrations of AMP, ADP, and ATP (0-0.6 mM). (b) Change in A_{620}/A_{520} ratio in the absence (dotted line) and presence (solid line) of a fixed concentration of alkaline phosphatase (ALP = 10 nM) with time keeping the fixed concentration of AMP or ADP or ATP (0.3 mM). (c) Hydrodynamic diameter (D_h) of the GNP in the absence and presence of only ATP and ATP+ALP after 60 min of their mixing. [ATP] = 0.3 mM, [ALP] = 10 nM (d) Change in UV-vis absorbance ratio (A_{620}/A_{520}) of GNP as a function of time in the presence of a fixed concentration of ATP (0.3 mM), but the different concentration of ALP (0-10 nM). [Tris] = 15 mM, pH = 9.

This ratio has been widely used in the literature to quantify the extent of GNP aggregation since the sharp surface plasmon peak at 520 nm broadens upon aggregation, resulting due to decrease in A_{520} accompanied by an increase in A_{620} .⁴⁵ To investigate the aggregation behavior, we kept the GNP concentration constant at 120 pM ($[Au] = 100 \mu\text{M}$) and titrated nucleotides into the solution at increasing concentrations. The values of A_{620}/A_{520} were recorded up to 1 hour after mixing. Our results showed that the rate of increase in the A_{620}/A_{520} ratio followed the

trend ATP>ADP>AMP, indicating the role of multiple charged interactions in triggering the assembly (Figure 2.6a). Specifically, significant GNP aggregation was observed after adding

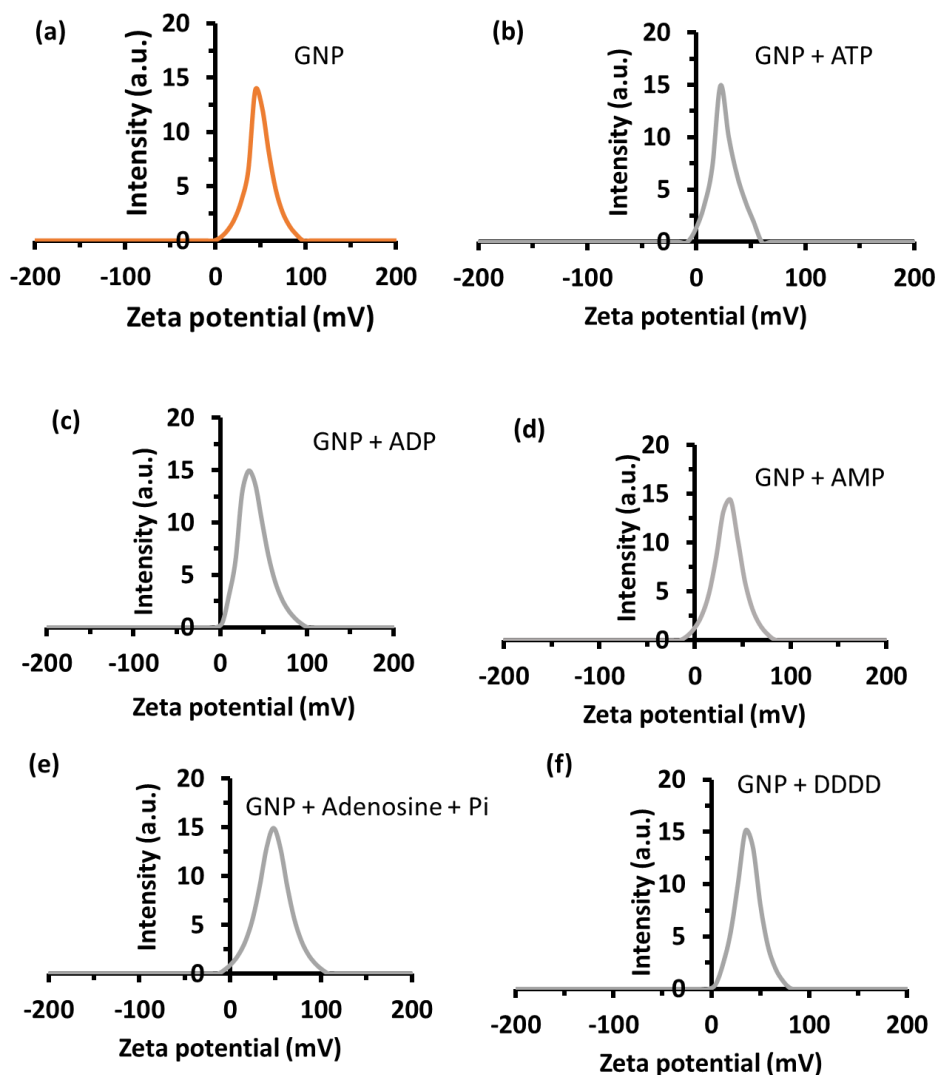


Figure 2.7. Zeta potential curve for (a) GNP, and GNP with (b) ATP, (c) ADP, (d) AMP, (e) Adenosine + phosphate, (f) DDDD. Experimental condition: [GNP] = 120 pM, [ATP] = 0.3 mM, [ADP] = 0.3 mM, [AMP] = 0.3 mM, [DDDD] = 0.2 mM, [Adenosine] = 0.3 mM, [Phosphate] = 0.9 mM, [tris-HCl] = 15 mM, pH 9 at 25 °C.

0.35 mM of ATP and 0.45 mM of ADP (at 0.3 mM and 0.4 mM of ATP and ADP, respectively, the aggregation was sufficiently stable), whereas minimal aggregation was observed in the case of AMP, even after adding 0.6 mM. We confirmed these findings using dynamic light scattering (DLS), which exhibited a similar trend (data not shown). The presence of nucleotides on the GNP surface was confirmed through zeta (ζ) potential measurements. The ζ -potential value for CTAB-capped cationic GNP was 40 ± 2 mV, which decreased to 20 ± 4 , 30 ± 3 , 35 ± 2 , and 34 ± 3 mV in the presence of 0.3 mM of ATP, ADP, AMP, and adenosine + Pi,

respectively, under our experimental conditions (Figure 2.7). This data suggests that the affinity of multiple phosphates towards the cationic surface is stronger compared to a single phosphate. We also determined the concentration of nucleotides bound to the GNP surface using the ultracentrifugation dialysis method, as depicted in Figure 2.8. In the presence of a fixed 0.3 mM concentration of ATP/ADP/AMP, the amounts of ATP, ADP, and AMP bound to the GNP surface were determined to be 0.26 mM, 0.18 mM, and 0.08 mM, respectively.

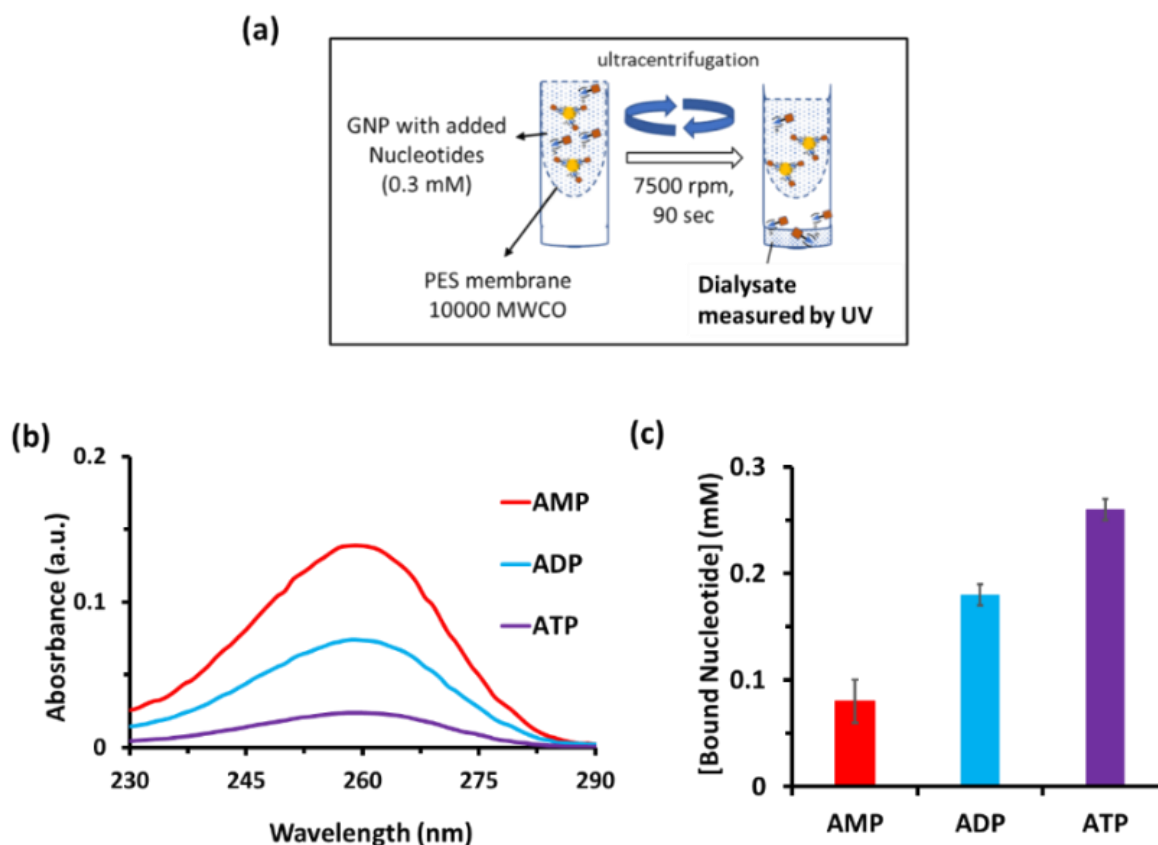


Figure 2.8. (a) Schematic representation for calculating surface-bound nucleotide. (b) UV-vis scan of dialysate in the presence of different nucleotides (25 times diluted). (c) Amount of nucleotide bound to GNP surface in our experimental condition.

Previous studies have reported in situ reversible assembly-disassembly processes of a surfactant or nanoparticle-based systems driven by multivalent interactions. These processes involve reducing the number of multivalent bonds through physicochemical processes, enzymatic reactions, or light stimulation.⁴⁸ Several dynamic assembly processes, such as programmed reactors or delivery vehicles, have utilized ATP to trigger surfactant assembly and subsequent dissociation to AMP or adenosine + inorganic phosphate (3Pi) using enzymes

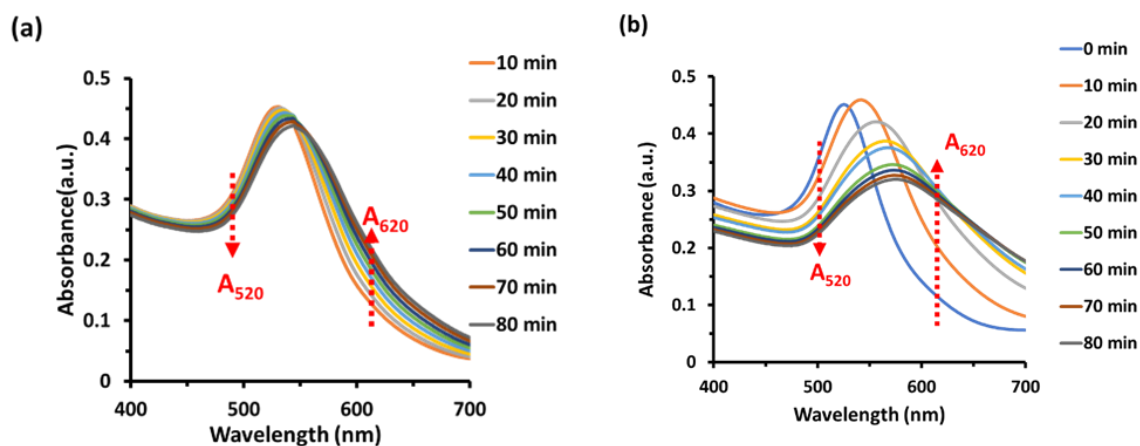


Figure 2.9. Scanning kinetics of GNP + ATP system (a) in the absence of ALP, (b) in the presence of ALP (10 nM) over time. Experimental condition: [GNP] = 120 pM ([Au] = 100 μ M), [ATP] = 0.3 mM, [tris-HCl] = 15 mM, pH 9 at 25 $^{\circ}$ C.

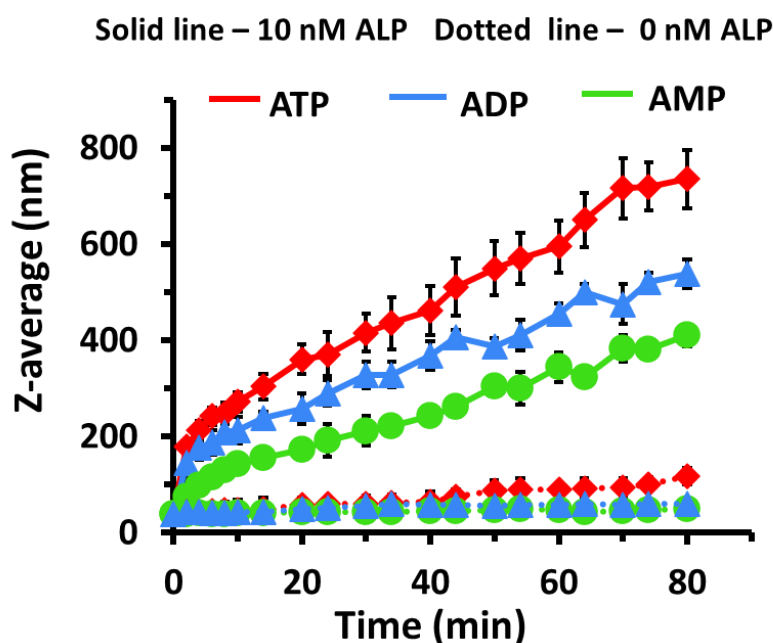


Figure 2.10. Size measurement of GNP system in the presence of different nucleotides, where dotted line and solid line denotes the absence of Alkaline phosphatase (ALP). Experimental condition: [GNP] = 120 pM ([Au] = 100 μ M), [nucleotide] = 0.3 mM, [ALP] = 10 nM, [tris-HCl] = 15 mM, pH 9 at 25 $^{\circ}$ C.

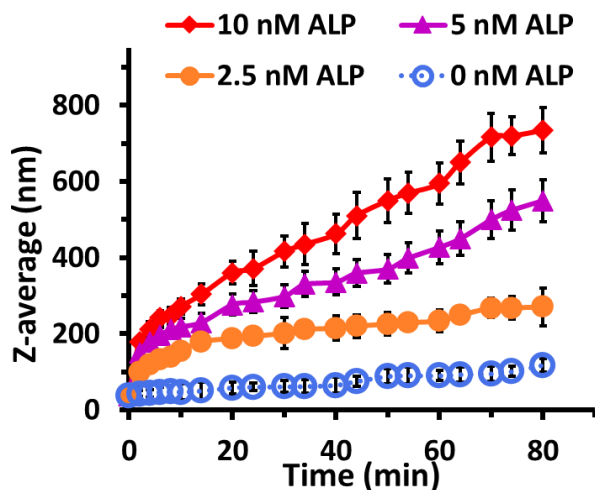


Figure 2.11. Size measurement of GNP system in the presence of fixed ATP concentration and varying ALP concentration, where dotted line and solid line denotes the absence of Alkaline phosphatase (ALP). Experimental condition: [GNP] = 120 pM ([Au] = 100 μ M), [ATP] = 0.3 mM, [ALP] = 0 - 10 nM, [tris-HCl] = 15 mM, pH 9 at 25 $^{\circ}$ C.

like ATPase or phosphatase.³⁶⁻³⁷ In our study, we aimed to investigate whether the enzyme alkaline phosphatase (ALP) would induce disassembly or decreased aggregation of gold nanoparticles (GNP) in the presence of ATP, as ALP is known to catalyze the dissociation of ATP into adenosine + 3Pi. To explore this, we monitored the aggregation kinetics by measuring the A620/A520 ratio over an 80-minute period in a 15 mM tris-HCl buffer at pH 9 and 25 $^{\circ}$ C. Surprisingly, we observed a significantly higher rate of GNP aggregation in the presence of ALP, rather than disassembly or decreased aggregation. Notably, the addition of ALP alone (0-10 nM) without ATP or ATP alone (0-0.3 mM) without ALP did not induce notable aggregation of the nanoparticle system (Figure 2.6b-d and Figure 2.9). Furthermore, GNP aggregation was observed when ADP (0.3 mM) was present simultaneously with ALP or when AMP (0.3 mM) was present with ALP (Figure 2.6b). Additionally, the rate of aggregation induced by ALP was higher in the presence of ATP compared to ADP and AMP (Figure 2.6b). These findings were further confirmed through dynamic light scattering (DLS) measurements. In the presence of ALP, the average sizes observed for ATP, ADP, and AMP were 735 ± 60 nm, 540 ± 30 nm, and 410 ± 22 nm, respectively, after 60 minutes of incubation, while sizes of 117 ± 17 nm, 62 ± 3 nm, and 52 ± 10 nm were observed in the absence of ALP (Figure 2.10). To investigate the role of ALP concentration, we varied the concentration of ALP while keeping the ATP concentration fixed at 0.3 mM. Interestingly, we observed an increase in both the A620/A520 ratio and size values, indicating an increased extent of aggregation with higher

ALP concentrations (Figure 2.6d and Figure 2.11). Transmission electron microscopy (TEM) images further supported these observations (Figure 2.12a-c). We also utilized GNP-tagged fluorescent beads ($\sim 2 \mu\text{m}$ diameter) to visualize the aggregation phenomenon, which showed

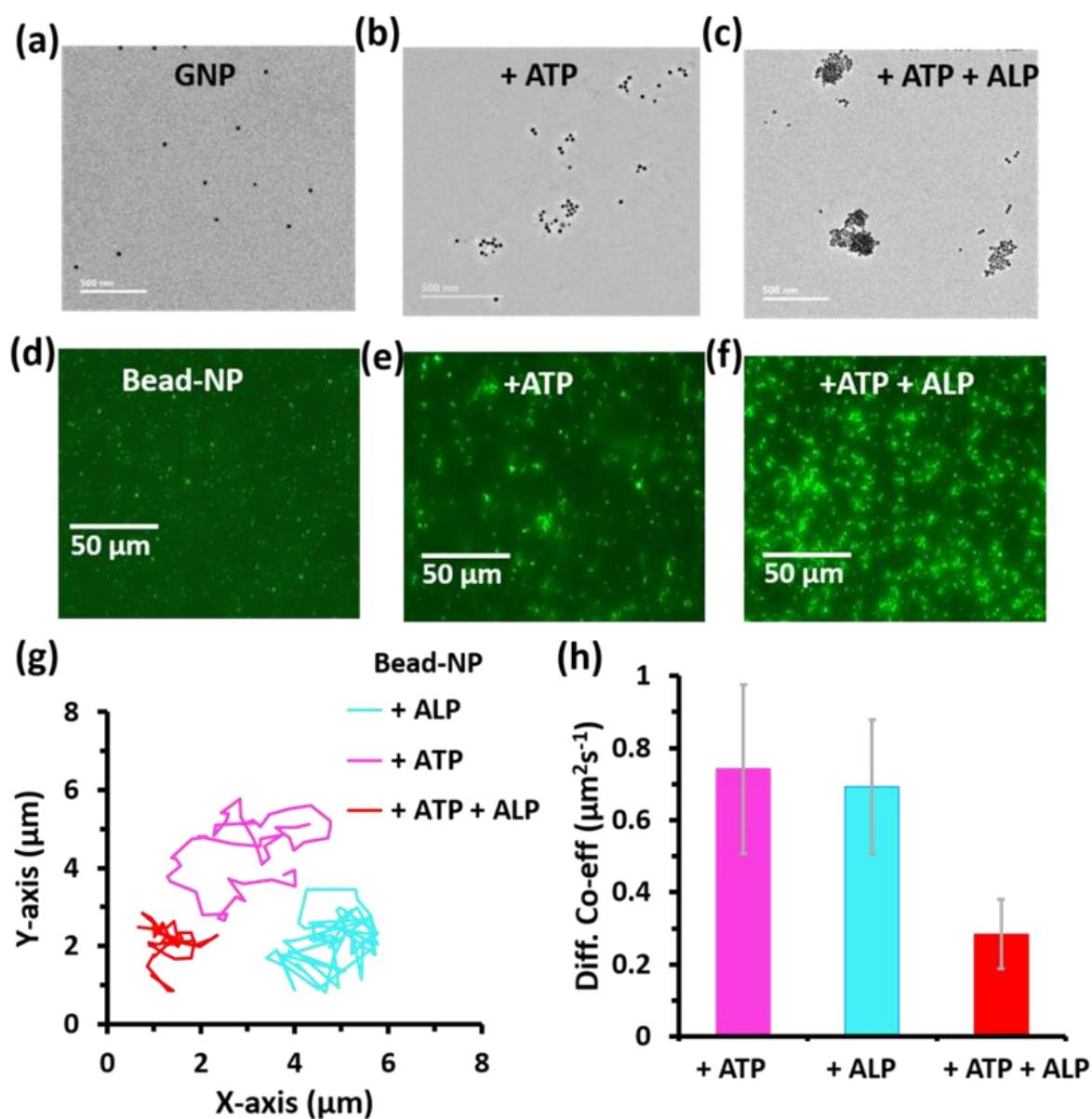


Figure 2.12. TEM images of (a) only GNP, (b) GNP + ATP (0.3 mM), (c) GNP + ALP (10 nM) + ATP (0.3 mM) after 60 min of mixing. Fluorescence microscopic images of fluorescent polystyrene bead-NP conjugate (d) without ATP and ALP, (e) with only ATP (0.3 mM) (f) with ATP (0.3 mM) and ALP (10 nM) after 60 min of mixing. (g) The trajectory of Bead-GNP conjugate in the presence of ATP (0.3 mM), ALP (10 nM), and (ATP+ALP) over 10 sec in the XY plane was observed under an optical microscope and analyzed using Tracker software. (h) Diffusion co-efficient of Bead- NP conjugate in those systems as obtained from the slope of the MSD curves using $\text{MSD}=4D\Delta t$. 10 Bead-NP conjugates from 5 sets of experiment has been taken for analysis.

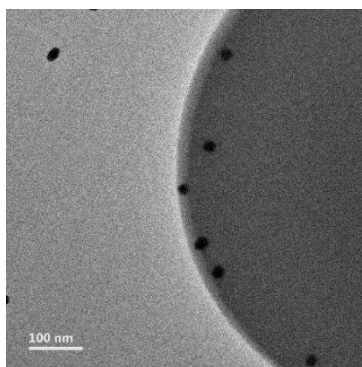


Figure 2.13. TEM image of bead-NP conjugate.

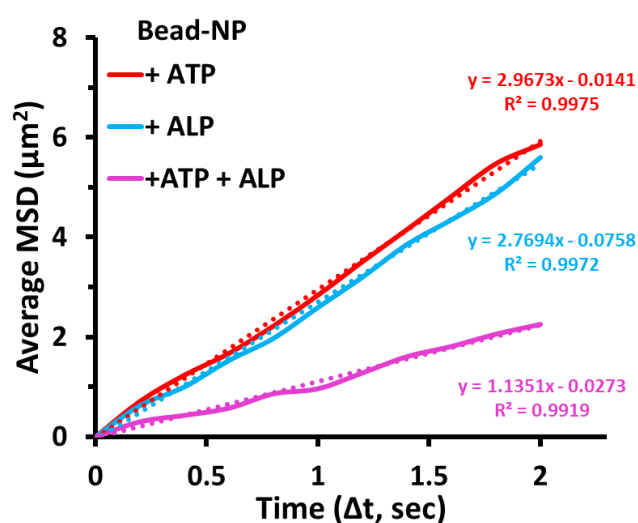


Figure 2.14. Mean square displacement versus time plot for bead-GNP conjugate with ATP, ALP, and ATP + ALP. Experimental condition: [bead-GNP] ([Au] = 100 μ M), [ATP] = 0.3 mM, [ALP] = 10 nM, [tris-HCl] = 15 mM, pH 9 at 25 $^{\circ}$ C.

enhanced aggregation only in the presence of ATP and ALP, as observed in fluorescence microscope images (Figure 2.12d-f, and Figure 2.13). By tracking their diffusion, we found that the diffusion of the beads in the presence of ATP and ALP together was approximately 2.5 times slower than when ALP and ATP were present separately with the beads, indicating the formation of larger aggregated structures (Figure 2.12g-h, and Figure 2.14). Overall, the extent and rate of GNP aggregation could be controlled by (i) fixing the ALP concentration and varying the ATP amount, (ii) fixing the ATP concentration and varying the ALP amount, and (iii) fixing the enzyme concentration and altering the extent of multivalent interaction by changing the ATP, ADP, or AMP concentrations. After observing the aggregation phenomenon of GNPs only in the simultaneous presence of ATP, other nucleotides (ADP and AMP), and

ALP, we became intrigued to gain further insights into this process. Firstly, we examined the zeta potential of the system. Surprisingly, in the presence of ALP (10 nM) and ATP (0.3 mM) after 1 hour, the zeta potential decreased to 10 ± 2 mV under our experimental conditions. We also measured the zeta potential of GNPs in the presence of AMP and ADP separately with ALP. In both cases, the zeta potential decreased to below 20 mV, and the rate of decrease in zeta potential over time followed the order: ATP > ADP > AMP (Figure 2.15). These findings suggest that the presence of nucleotides on the surface of GNPs also facilitates the binding of ALP to the nanoparticle surface, leading to a higher extent of aggregation with ALP in the presence of strongly-bound nucleotides. Since ALP is a negatively charged enzyme with a zeta potential of -30 ± 5 mV, it destabilizes the colloidal stability of the cationic GNP surface by specifically interacting with its substrate, resulting in aggregation.⁴⁶⁻⁴⁷

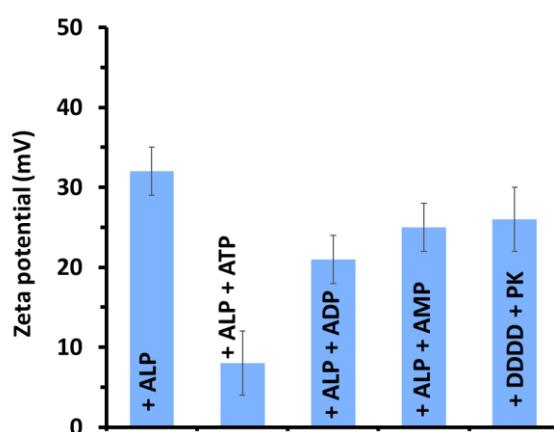


Figure 2.15. Zeta potential measurement of GNPs in the presence of enzymes with different nucleotides and peptides over time. Experimental condition: [GNP] = 120 pM ([Au] = 100 μ M), [nucleotide] = 0.3 mM, [DDDD] = 0.2 mM, [ALP] = 10 nM, [PK, Proteinase K] = 1 μ M, [tris-HCl] = 15 mM, pH 9 at 25 ° C.

In order to investigate the hydrolytic activity of ALP on these nucleotide phosphates in the presence and absence of GNPs, we conducted HPLC experiments to measure the amount of adenosine formed after a 60-minute reaction. Under the same experimental conditions, we examined the hydrolysis of AMP, ADP, and ATP, with each nucleotide used at a concentration of 0.3 mM as substrates for ALP. Surprisingly, we observed a similar concentration of free adenosine formed (~33% cleavage) with AMP both in the absence (0.10 ± 0.01 mM) and presence of GNPs (0.098 ± 0.015 mM), indicating that the presence of GNPs did not significantly alter the reaction rate. For ADP, the amount of adenosine formed (~15% cleavage) was lower than that of AMP, measuring 0.041 ± 0.003 mM and 0.038 ± 0.002 mM in the

absence and presence of GNPs, respectively. However, in the case of ATP, the amount of adenosine formed (~6% cleavage) was strikingly lower, measuring 0.021 ± 0.002 mM and 0.016 ± 0.002 mM in the absence and presence of GNPs, respectively (Figure 2.2, 2.16, 2.17). These results indicate a sharp decrease in the hydrolytic rate of ATP in the presence of GNPs compared to the other two nucleotides.

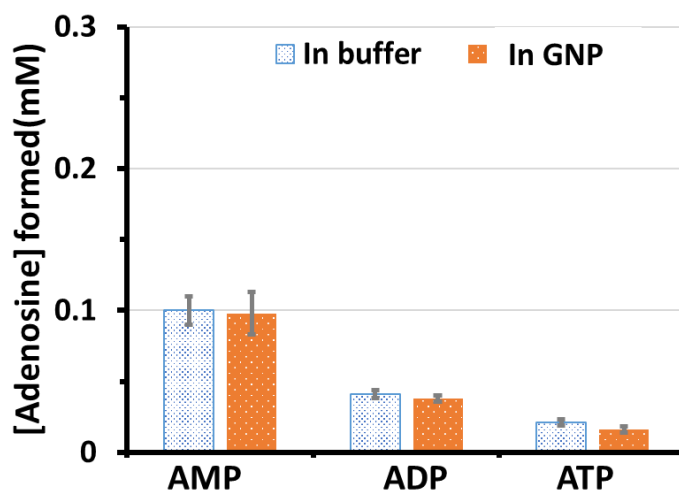


Figure 2.16. Amount of product (adenosine) formed for different nucleotides in the GNP system, and in buffer system (without nanoparticles) after 1 h of reaction. Experimental condition: [GNP] = 120 pM ([Au] = 100 μ M), [nucleotide] = 0.3 mM, [ALP] = 10 nM, [tris-HCl] = 15 mM, pH 9 at 25 $^{\circ}$ C.

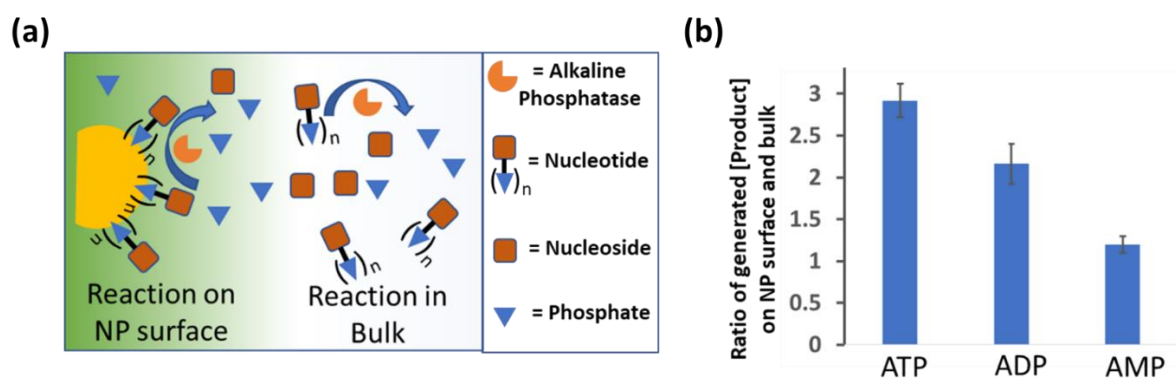


Figure 2.17. Schematic representation of reaction occurring on nanoparticle surface and bulk. (b) The ratio of concentration of product (Adenosine) formed on the GNP surface to product formed in bulk with different nucleotides after 1 h of reaction. Experimental condition: [GNP] = 120 pM ([Au] = 100 μ M), [nucleotide] = 0.3 mM, [ALP] = 10 nM, [tris-HCl] = 15 mM, pH 9 at 25 $^{\circ}$ C.

It is worth noting that ALP efficiently hydrolyzes monophosphoesters compared to di- and triphosphoesters, which is also reflected in its hydrolytic ability towards AMP, ADP, and ATP, despite their comparable binding affinities.⁴⁹⁻⁵¹ Additionally, ALP is known to bind to the product phosphates, which can act as competitive inhibitors.⁴⁹ Furthermore, we investigated the effect of the hydrolyzed product, adenosine (0.3 mM), and phosphates (0.9 mM) on the aggregation process (Figure 2.18). Interestingly, we observed aggregation of GNPs upon the addition of ALP, and the kinetics of aggregation were much lower compared to ATP but comparable to AMP. This can be attributed to the lower binding affinity of phosphates with GNPs compared to ATP. Overall, in our system, as the hydrolyzed product was also capable of forming aggregates, we were not able to observe any disassembly behavior of the GNPs under our experimental conditions. These findings suggest the following: (i) the hydrolysis of nucleotides by ALP is far from being completed within 1 hour, although complete aggregation and precipitation occur during that time interval, and (ii) the aggregation is higher with nucleotides that have a stronger binding affinity to the nanoparticle but lower hydrolytic ability with ALP. It is important to note that our experimental conditions, including the surface properties and concentration of nanoparticles, nucleotides, and reaction conditions, differ from other reported literature where the presence of ALP facilitated the generation of transient nanoparticle assemblies.⁵¹ In order to further investigate the enzyme-substrate selectivity in GNP aggregation, we conducted additional control experiments. Firstly, we utilized another enzyme, potato apyrase, which cleaves ATP to AMP + 2 Pi and has

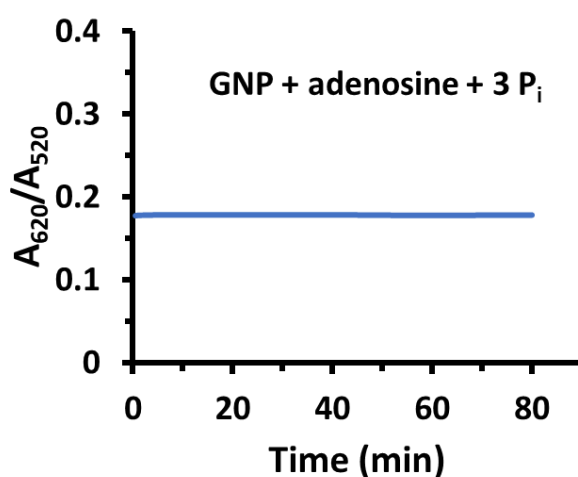


Figure 2.18. Aggregation kinetics of GNPs in the presence of product adenosine and phosphate over time. Experimental condition: [GNP] = 120 pM ([Au] = 100 μ M), [adenosine] = 0.3 mM, [Pi] = 0.9 mM, [tris-HCl] = 15 mM, pH 9 at 25 ° C.

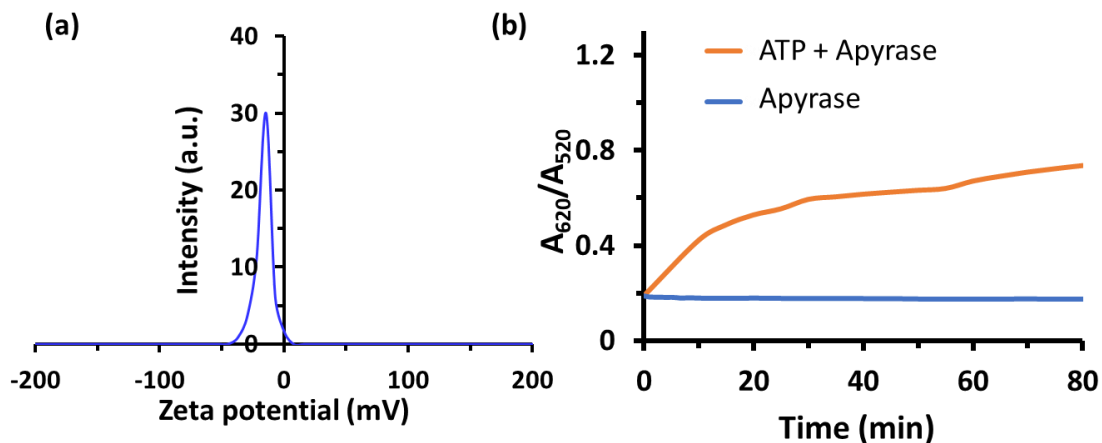


Figure 2.19. (a) Zeta potential curve for Apyrase. (b) Aggregation kinetics of GNPs in presence of potato apyrase in presence and absence of ATP over time. Experimental condition: [GNP] = 120 pM, [ATP] = 0.3 mM, [Apyrase] = 1 unit/ml, [tris-HCl] = 15 mM, pH 9 at 25 °C.

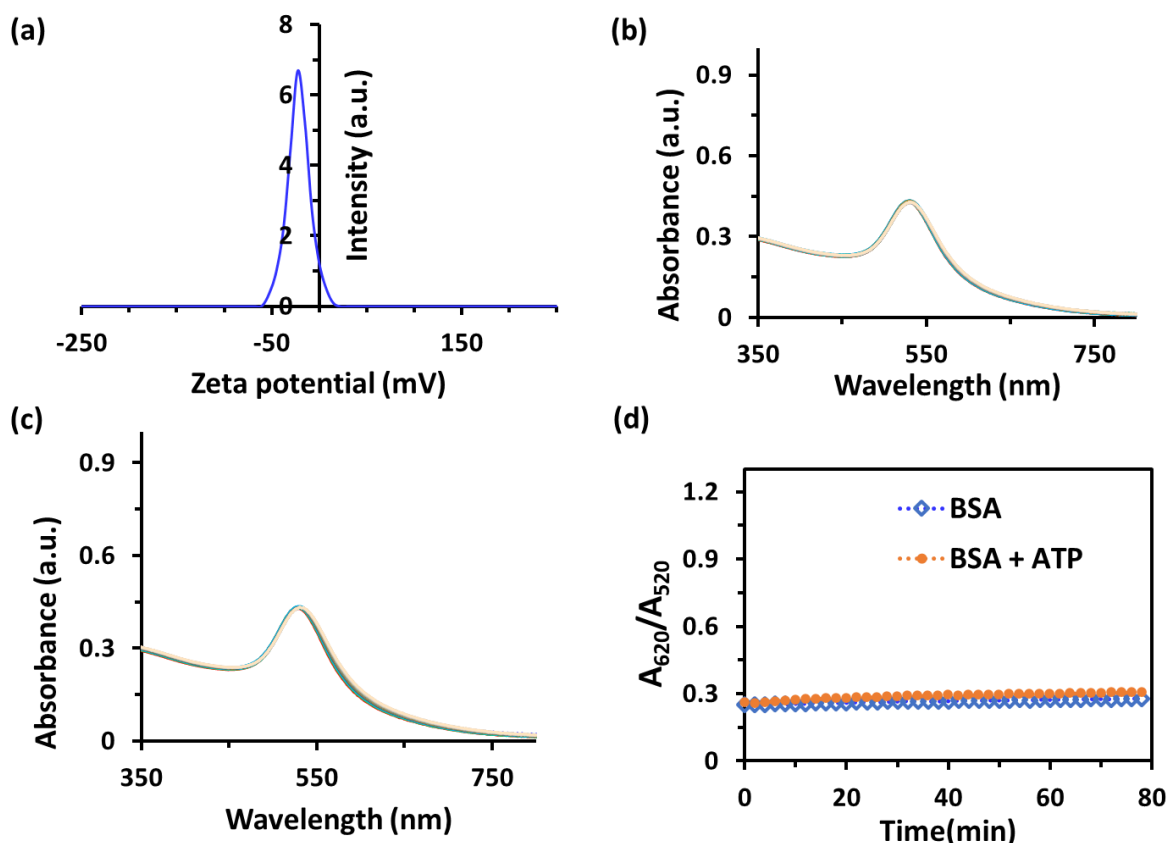


Figure 2.20. (a) Zeta potential of bovine serum albumin (BSA). (b) Scanning kinetics of GNP in the presence of (b) BSA, and (c) ATP and BSA. (d) Comparison of aggregation kinetics of GNP + BSA system in the presence and absence of ATP. Experimental condition: [GNP] = 120 pM ([Au] = 100 μ M), [BSA] = 5 μ M, [ATP] = 0.3 mM, [tris-HCl] = 15 mM, pH 9 at 25 °C.

a zeta potential of approximately -13 mV under our experimental conditions.³⁸ Remarkably, we observed aggregation of nanoparticles due to the interaction between the enzyme and substrate (Figure 2.19). To rule out the role of the negative potential of the enzyme in aggregation, we introduced an anionic protein, bovine serum albumin (BSA), which has a similar zeta potential (-25 ± 3 mV) to ALP under our experimental conditions but lacks the ability to cleave ATP. In the presence of ATP in the GNP-BSA system, no synergistic interaction between GNP, protein, and ATP occurred, and no further aggregation was observed (Figure 2.20). Furthermore, we explored the binding affinity of an anionic multivalent peptide substrate, tetraaspartate (DDDD), to the GNP surface. We found that at a concentration of 0.2 mM DDDD, the GNPs remained stable, but aggregation started to occur beyond that concentration. Interestingly, in a stable mixture of 0.2 mM DDDD and GNPs, the addition of ALP (10 nM) did not result in any aggregation under similar experimental conditions (Figure 2.21).

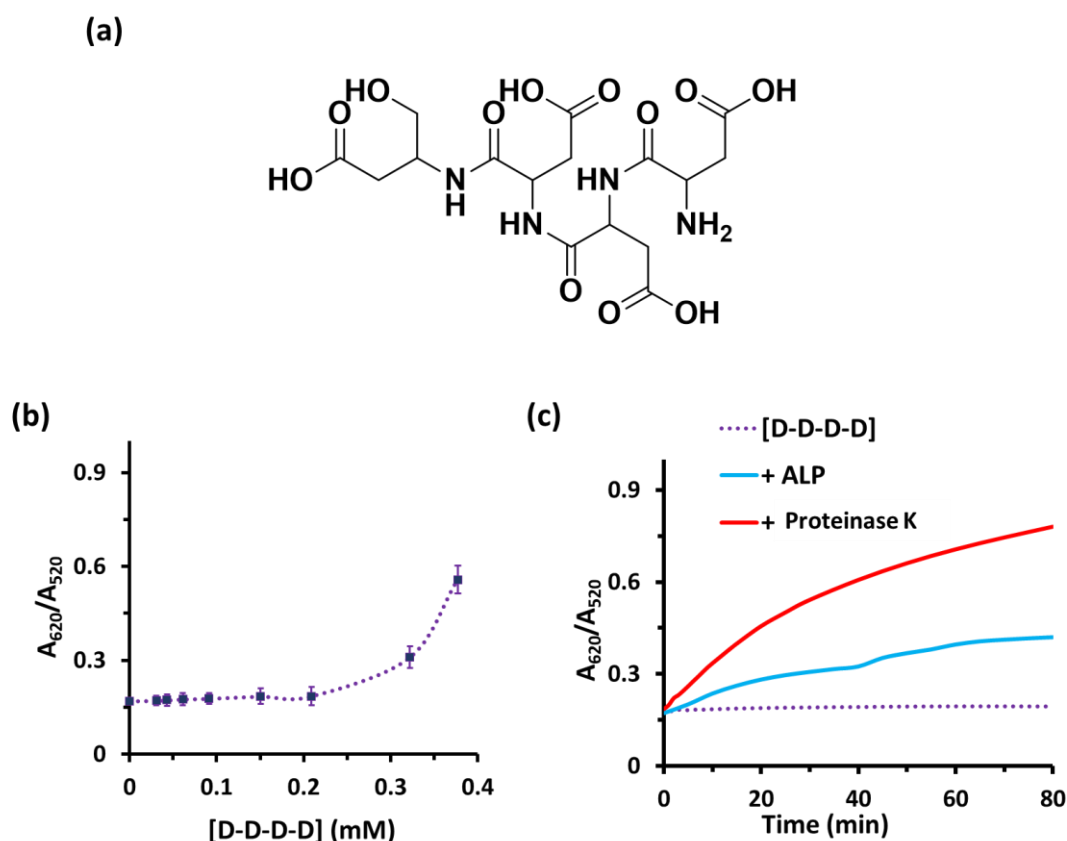


Figure 2.21. (a) Molecular structure of tetraaspartic acid (D-D-D-D). (b) GNP titration with peptide. (c) Aggregation kinetics of GNPs with peptide in the presence of ALP (blue curve) and in the presence of protease (red curve) over 80 minutes. Experimental condition: [GNP] = 120 pM ([Au] = 100 μ M), [D-D-D-D] = 0.2 mM, [ALP] = 10 nM, [proteinase K] = 1 μ M, [tris-HCl] = 15 mM, pH 9 at 25 $^{\circ}$ C.

Next, we examined the effect of using a protease enzyme, proteinase K (PK), which can act on DDDD as a substrate. PK is a non-specific peptidase with a zeta potential of -8 ± 2 mV, in contrast to the zeta potential of ALP, which is -28 ± 3 mV under our experimental conditions (pH = 9, Tris buffer).⁵² Upon the addition of PK to the mixture of GNP and DDDD, a slightly faster aggregation occurred, indicating that simultaneous and synergistic interactions among all three components—GNP, substrate, and substrate-specific enzyme—are necessary for aggregation to occur under these experimental conditions (Figure 2.21). However, the extent of aggregation was much lower than that observed in the GNP-ATP-ALP system. Importantly, no additional decrease in the zeta potential of the GNP-DDDD system was observed upon the introduction of PK, unlike ALP in the GNP-ATP/ADP/AMP system (Figure 2.15). These control experiments provide further insights into the enzyme-substrate selectivity and the interplay between GNPs, enzymes, and substrates in the aggregation process. The results demonstrate the specific requirements for synergistic interactions and the influence of zeta potential on GNP aggregation in the presence of different enzymes and substrates. Additionally, we investigated the potential of using proteinase K (PK) instead of ALP to induce aggregation of GNP-ATP conjugates. However, no significant aggregation was observed in the presence of PK (Figure 2.22). We also explored the use of carbonate solution instead of phosphate to induce GNP aggregation in the presence of ALP (Figure 2.23). Once again, no GNP aggregation was observed as carbonate, as an anion, does not exhibit affinity to ALP but only to the GNP surface, supporting our hypothesis of synergistic interactions.

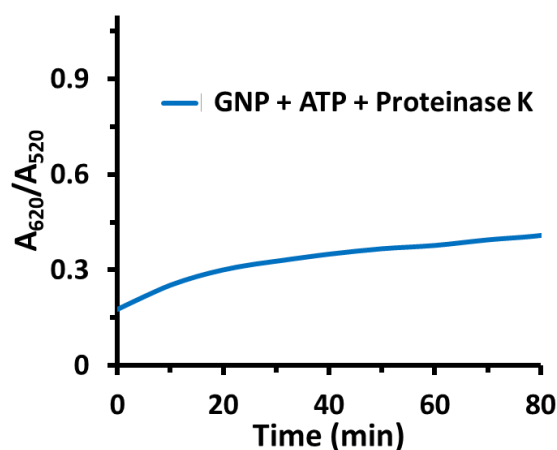


Figure 2.22. Aggregation kinetics of GNP + ATP system in the presence of protease over time. Experimental condition: [GNP] = 120 pM ([Au] = 100 μ M), [ATP] = 0.3 mM, [protease] = 1 μ M, [tris-HCl] = 15 mM, pH 9 at 25 $^{\circ}$ C.

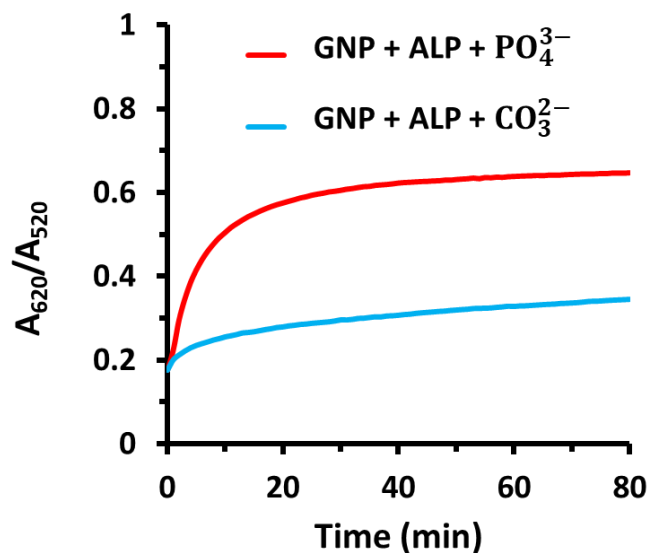


Figure 2.23. Aggregation kinetics of GNP with carbonate and phosphate ions in the presence of ALP. Experimental Conditions: [GNP] = 120 pM ([Au] = 100 μM), [ALP] = 10 nM, [PO_4^{3-}] = 1 mM, [CO_3^{2-}] = 1 mM [tris-HCl] = 15 mM, pH 9 at 25 ° C.

To investigate the formation and aggregation pattern of nanobioconjugates in microfluidic conditions, which holds potential for microfluidic-based nanobiodevices, we employed a two-inlet and one-outlet microfluidic channel with specific dimensions (height = 0.10 mm, width = 0.6 mm, length = 1.7 cm) as depicted in Figure 2.24a.¹² We introduced GNPs mixed with ATP, AMP, or Ade+3Pi through one inlet, while FITC-ALP was injected through the other inlet at a flow rate of 0.3 mL/h. We then observed the accumulation of ALP across the channel using fluorescence microscopy. Figure 2.24b displays the fluorescence intensity profiles at the end part of the microfluidic channel (1.6 mm from the inlet) for each case. Prior to the GNP experiment, we created a lateral substrate concentration gradient across the channel by injecting only ATP solution in buffer (0.3 mM) without GNPs through one inlet and FITC-ALP solution through the other. We tracked the movement of the fluorescently tagged enzyme by measuring the fluorescence at the terminal part of the channel, 1.6 cm away from the inlet (details provided in the Method Section). Interestingly, we observed that the enzyme slightly shifted towards higher ATP concentrations due to the expected propulsion of enzymes towards higher substrate concentrations (Figure 2.25).^{21,24}

However, when we conducted the GNP-bound ATP and enzyme experiment in the same manner, we noticed the gradual accumulation of fluorescent structures over time, primarily in the middle of the channel but closer to the enzyme side (Figure 2.24c, d). This accumulation

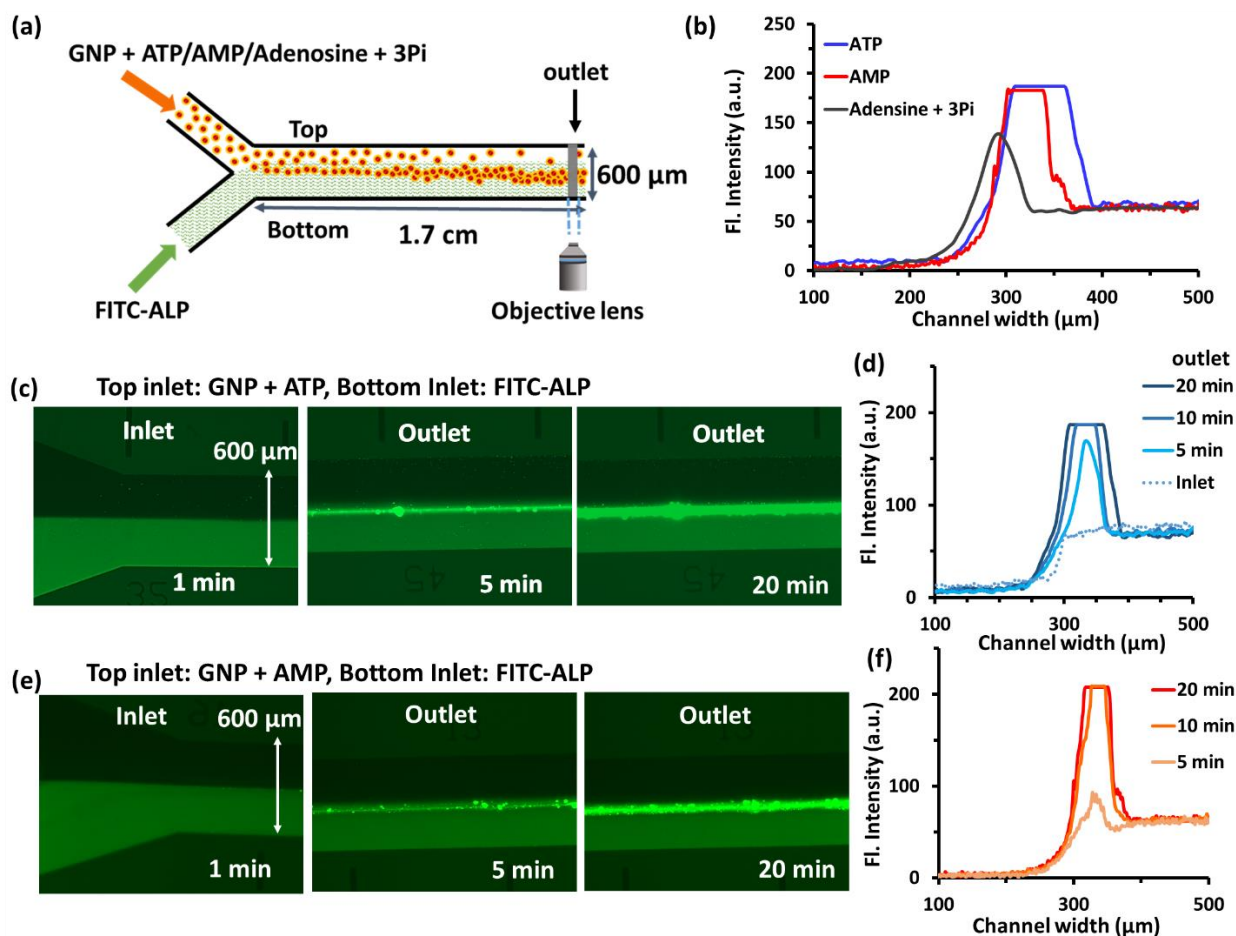


Figure 2.24. (a) Schematic image showing the setup of the 2-inlet-1-outlet microfluidic chip, where GNP+ATP/AMP conjugate has been passed through one inlet and FITC-ALP from the other and the fluorescence images were taken at the end of the channel at 1.6 cm apart. (b) Fluorescence intensity profile of outlet after 20 minutes when ATP/AMP/Adenosine+3 Pi was injected along with GNP from the top inlet and FITC-ALP from the bottom inlet. Representative image of the channel at the inlet, near outlet after 5 min, and 20 minutes when (c) ATP, and (e) AMP was injected with GNP from the top inlet showing accumulation of the fluorescent structures more towards enzyme side. Time-dependent fluorescence intensity profile at the outlet, from top to bottom end of the channel when (d) ATP and (f) AMP were injected along with GNP from the top inlet. The fluorescence is due to the accumulation of FITC-ALP.

of fluorescent structures indicates the aggregation of enzymes, nanoparticles, and ATP within the microfluidic channel. Notably, the accumulation does not occur at the GNP or substrate-rich zones, nor precisely at the center of the channel, but rather towards the enzyme side. This suggests that the enzymes do not actively propel toward the substrate-rich zone. Instead, the substrate, bound to GNPs, moves towards the enzyme-rich zone and initiates the formation of an agglomerate.

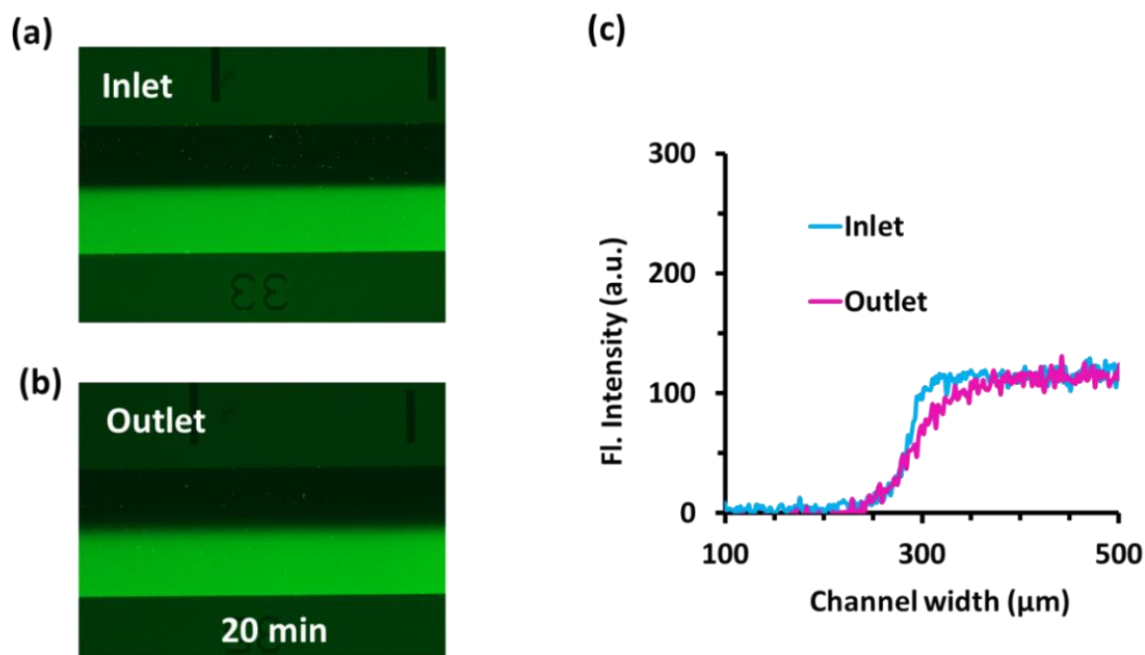


Figure 2.25. (a) Inlet and (b) outlet images, and (c) Intensity plot of Inlet and outlet of the microfluidic channel after 20 minutes of injecting ATP from the top inlet and FITC-ALP from the bottom inlet. Experimental condition: [ATP] = 0.3 mM, [ALP] = 0.5 μ M (50% labeled), [tris-HCl] = 15 mM (from both inlets), pH 9 at 25 $^{\circ}$ C.

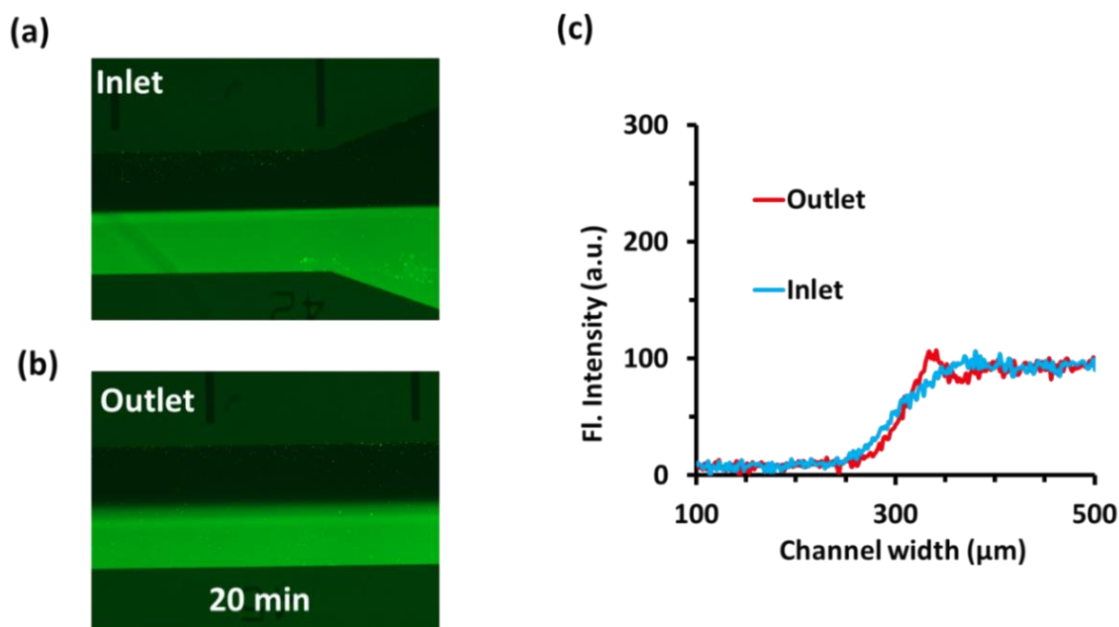


Figure 2.26. (a) Inlet and (b) outlet images, and (c) Intensity plot of Inlet and outlet of the microfluidic channel after 20 minutes of injecting GNP from the top inlet and FITC-ALP from the bottom inlet. Experimental condition: [GNP] = 120 pM ([Au] = 100 μ M, [ALP] = 0.5 μ M (50% labeled), [tris-HCl] = 15 mM (from both inlets), pH 9 at 25 $^{\circ}$ C.

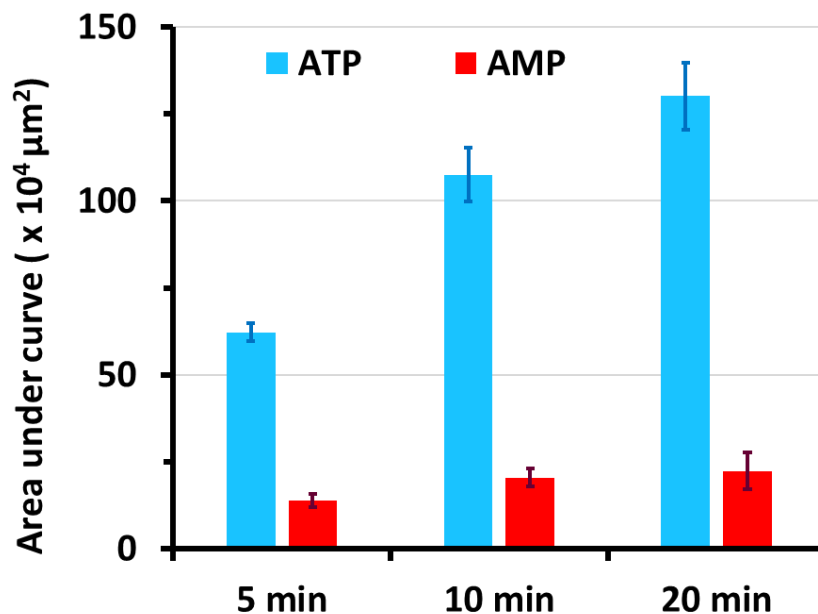


Figure 2.27. Amount of area covered under intensity curve across the channel width near an outlet (250 – 500 μm) while injecting GNP+ ATP from the top inlet (blue bars) or GNP + AMP from the top inlet (red bars), and FITC-ALP from the bottom inlet with time.

We repeated a similar experiment by injecting GNP-AMP from one side and FITC-ALP from the other, which resulted in a comparable trend of fluorescent aggregation towards the enzyme side. However, in this case, the rate of aggregated structure formation was slower compared to ATP (Figure 2.24e, f, and Figure 2.27). Intriguingly, when we passed GNP+Ade+Pi from the top inlet and FITC-ALP from the bottom, we did not observe aggregation towards the enzyme-rich zone. Instead, the aggregation occurred more at the interface or central zone, and the level of aggregation was significantly lower than in the AMP/ATP case (Figure 2.28a). It is worth noting that in the presence of Pi, where no further reaction product is formed, we can consider it a noncatalytic condition.

To further investigate, we conducted a control experiment under noncatalytic conditions by passing FITC-BSA through the bottom channel and GNP-ATP through the top (Figure 2.28b). Similar to the experiment discussed in Figure 2.20, no aggregation was observed inside the microfluidic channel. Additionally, we performed an experiment by passing GNPs from one side and FITC-ALP from the other inlet (Figure 2.26), but no significant fluorescent aggregation pattern was observed.

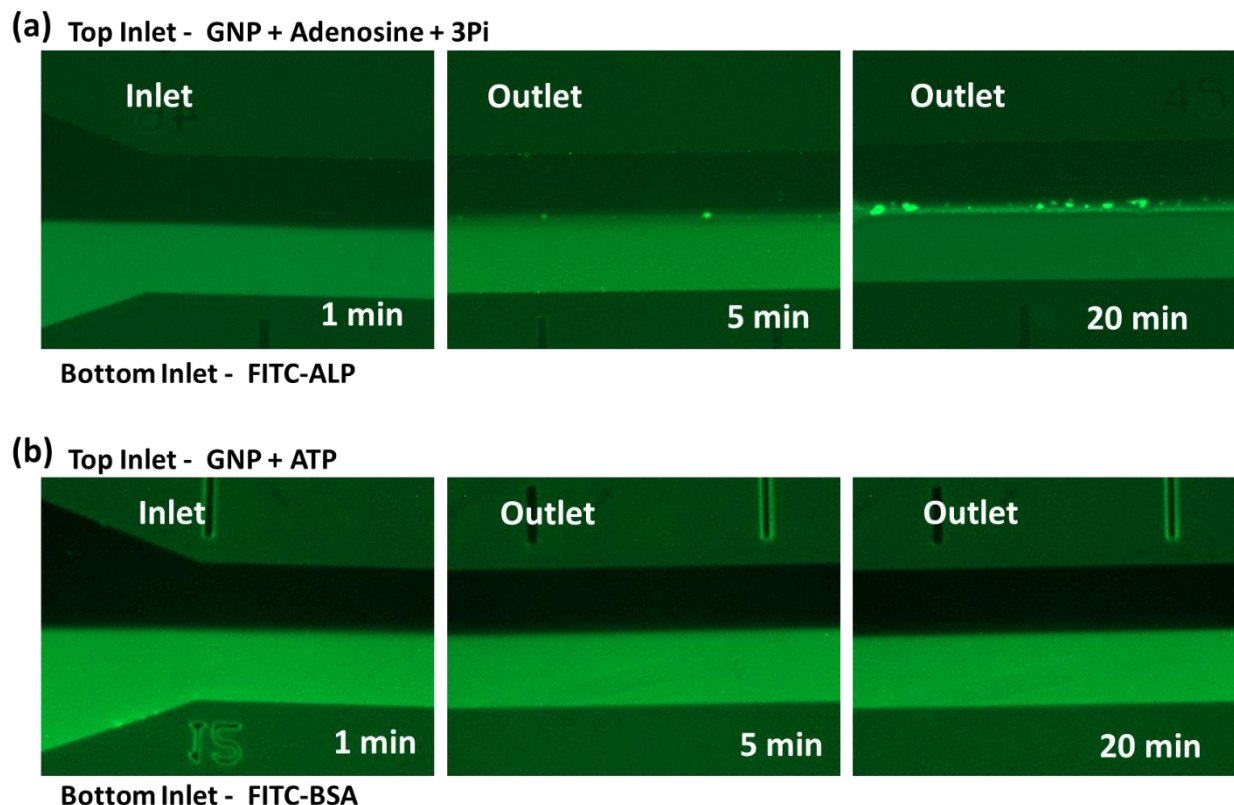


Figure 2.28. Inlet and outlet images of a microfluidic channel with time while injecting (a) GNP + Adenosine + Pi from the top inlet and FITC-ALP from the bottom inlet, and (b) GNP + ATP from the top inlet and FITC-BSA from the bottom inlet. Experimental condition: [GNP] = 120 pM, [Adenosine] = 0.3 mM, [Phosphate] = 0.9 mM, [FITC-ALP] = 0.5 μ M (50 % labeled), [BSA] = 5 μ M, [tris-HCl] = 15 mM (from both inlets), pH 9 at 25 $^{\circ}$ C.

These results indicate several important observations: (i) the aggregation is driven by synergistic interactions, as mentioned earlier; (ii) the zone of aggregation towards the enzyme-rich side is influenced by the diffusiophoretic effect, which will be discussed in the following paragraph; (iii) the rate of aggregation patterning follows the order: ATP > AMP > Ade+3Pi, as observed in the formation of aggregates in the aqueous mixture; (iv) notably, the zone of aggregated pattern differs in catalytic conditions (ATP and AMP) compared to noncatalytic conditions (Ade+Pi), with the former showing aggregation towards the enzyme side and the latter exhibiting aggregation at the central zone; and finally, (v) the rate of pattern formation can be controlled over time.

In our experimental conditions, as ALP can cleave both AMP and ATP, GNP-bound ATP or AMP generates adenosine and Pi towards the enzyme side, creating a gradient of Ade+Pi (Figure 2.3, Table 2.1). We also investigated the diffusiophoretic migration of GNP-ATP or

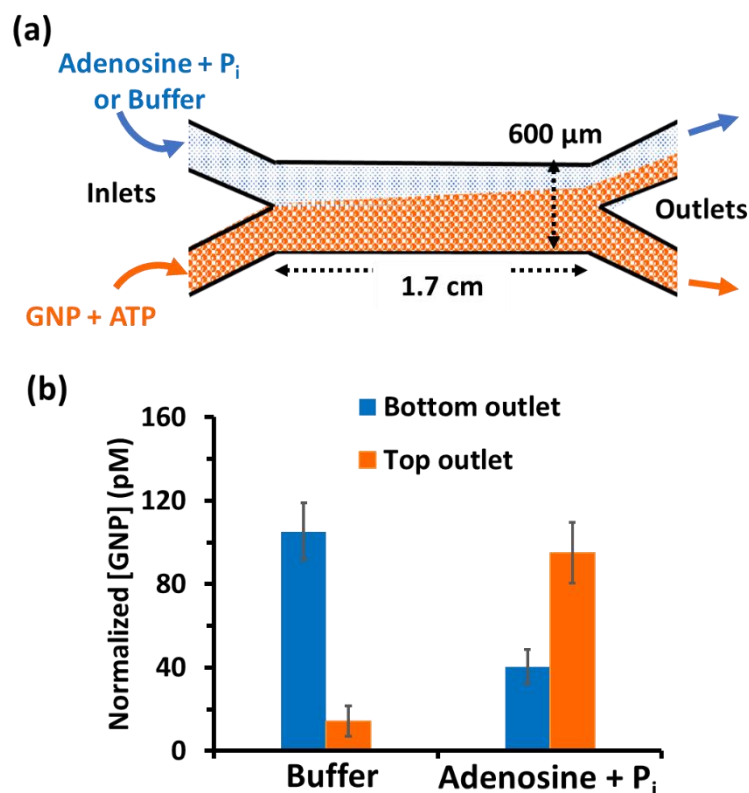


Figure 2.29. (a) Schematic of the 2-inlet-2-outlet microfluidic set up used in our experiment where from the top inlet adenosine+Pi solution or buffer and through the bottom inlet, GNP+ATP solution was injected. (h) Normalized concentration of GNP eluted through top and bottom outlets. Experimental condition: [Ade] = 0.3 mM, [Pi] = 0.9 mM, [ATP] = 0.3 mM, [GNP] = 120 pM, [tris] = 15 mM, pH = 9, Flow rate = 0.3 ml/h (for both experiments).

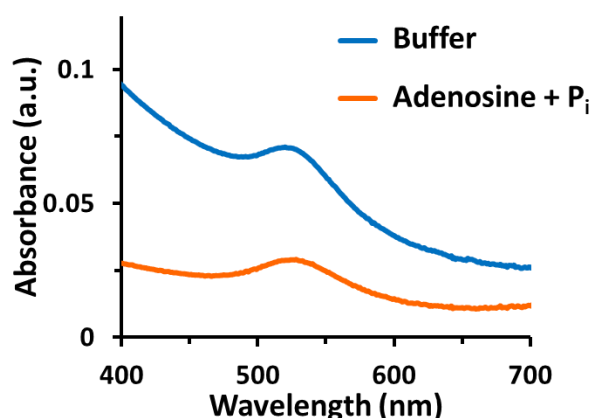


Figure 2.30. UV scan of sample collected from bottom outlet when buffer (Blue curve), or adenosine with Pi in buffer (Orange curve) was injected from the top inlet. Experimental condition: Bottom inlet – GNR in the buffer. [GNR] = 120 pM, [adenosine] = 0.3 mM, [Pi] = 0.9 mM, [tris-HCl] = 15 mM, pH 9, flow rate – 300 μl/h at 25 °C.

Table 2.1. Amount of phosphate formed in the presence of alkaline phosphatase after 10 and 30 minutes of reaction period. Experimental condition: [ATP] = 0.3 mM, [AMP] = 0.3 mM, [ALP] = 0.5 μ M, [Tris] = 15 mM, pH 9.

Time	Nucleotide	A ₆₂₀ (a.u.)	[Adenosine](μ M)	[Phosphate](μ M)
10 min	ATP	0.1316	55.4	166.2
	AMP	0.1102	123.4	123.4
30 min	ATP	0.2851	157.7	473.2
	AMP	0.1751	253.2	253.2

GNP-AMP towards the enzymatically formed Ade+Pi gradient in a two-inlet, two-outlet microfluidic channel, as illustrated in Figure 2.29 and Figure 2.30. Through one inlet, we introduced the GNP+ATP conjugate, while through the other inlet, Ade+Pi was injected. In a control experiment, only a buffer was passed through the channel. By analyzing the amount of GNP passing through both outlets, we observed that the GNP-ATP conjugate exhibited a 5-fold drift towards the adenosine+Pi side compared to the buffer. This phenomenon can be attributed to the diffusiophoretic migration, which combines electrophoresis and chemiphoresis, of the positively charged GNP-ATP conjugate towards the negatively charged enzyme.^{21,53-56} Calculations showed that the GNP-ATP conjugate could gain an additional 42 μ m/s of diffusiophoretic velocity due to the electrophoretic effect in the Ade+Pi gradient (detailed calculation provided in the Method Section). It is important to note that the diffusiophoresis-mediated formation of spatially controlled colloidal aggregates or bands in salt gradients has been reported in previous literature.⁵⁷⁻⁶⁰ However, in our case, we enzymatically generated this gradient, where the enzyme's gradient leads to the dissociation of ATP into adenosine and Pi in the enzyme-rich zone, resulting in a concentration gradient within the system. Importantly, we observed this effect in both microfluidic and macroscale experiments. These results sparked our interest in controlling aggregation patterns in a macroscale system by introducing a gradient of enzyme and GNP-ATP. Initially, we conducted an experiment on a glass slide by placing 15 μ l of GNP-ATP ([GNP] = 120 pM, [ATP] = 0 - 0.3 mM) and covering it with a square-shaped cover slip (2.2 cm). From two opposite ends, we added 7 μ l of FITC-ALP solution to generate an enzyme gradient inside the coverslip (Figure 2.31, 2.32a). The use of FITC-tagged ALP allowed us to visualize the aggregation pattern under

a microscope. Subsequently, we monitored the formation of fluorescent clusters across the coverslip in five different zones (A-E) as designated in Figure 2.32a. Interestingly, the fluorescent structures only formed at the edge of the coverslip (zones A and E) where FITC-ALP was added, but only in the presence of GNP-ATP. Figure 2.32c provides visual evidence of cluster formation at the two opposite ends under the coverslip, while the middle zone remains free from any fluorescent structures. In a control experiment without ATP but with GNPs, no fluorescent structures were observed (Figure 2.33). The agglomeration of fluorescent clusters at zones A and E was maximized when 0.3 mM of ATP was used. Intriguingly, when we performed experiments with 0.1 mM ATP and 40 pM GNP, the addition of ALP from both sides resulted in clusters specifically forming in zones B and D (Figure 2.32b+d). We also

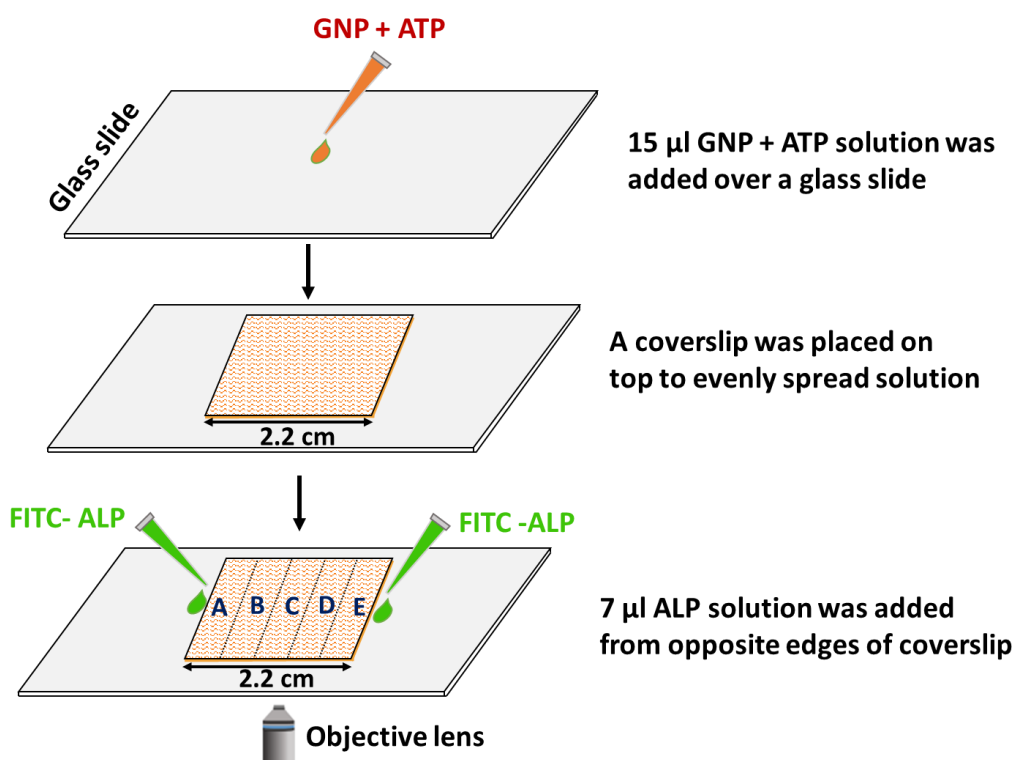


Figure 2.31. Schematic representation of the experimental set up for the zonal assembly formation over time in a space having a concentration gradient of the enzyme.

conducted an additional control experiment using GNP+DDDD conjugate and a gradient of ALP, which did not lead to notable clustering across the coverslip (Figure 2.34). Introducing an RITC-PK gradient in the GNP+ATP solution did not result in cluster formation (Figure

2.35). However, with an RITC-PK gradient in the GNP+DDDD solution, a lower concentration of clusters was observed at zones A and E (Figure 2.36). This experiment further indicated the requirement for synergistic interactivity among GNP, substrate, and enzyme for the formation of patterned clustering. To track the nanoparticles in this experiment, we attached them to carboxylate-modified beads, Bead-GNP (detailed procedure in the methods section), and performed an experiment by adding the Bead-GNP solution with ATP on a glass slide and injecting ALP from opposite edges. Once again, clusters of particles were observed specifically in zones A and E (data not shown).

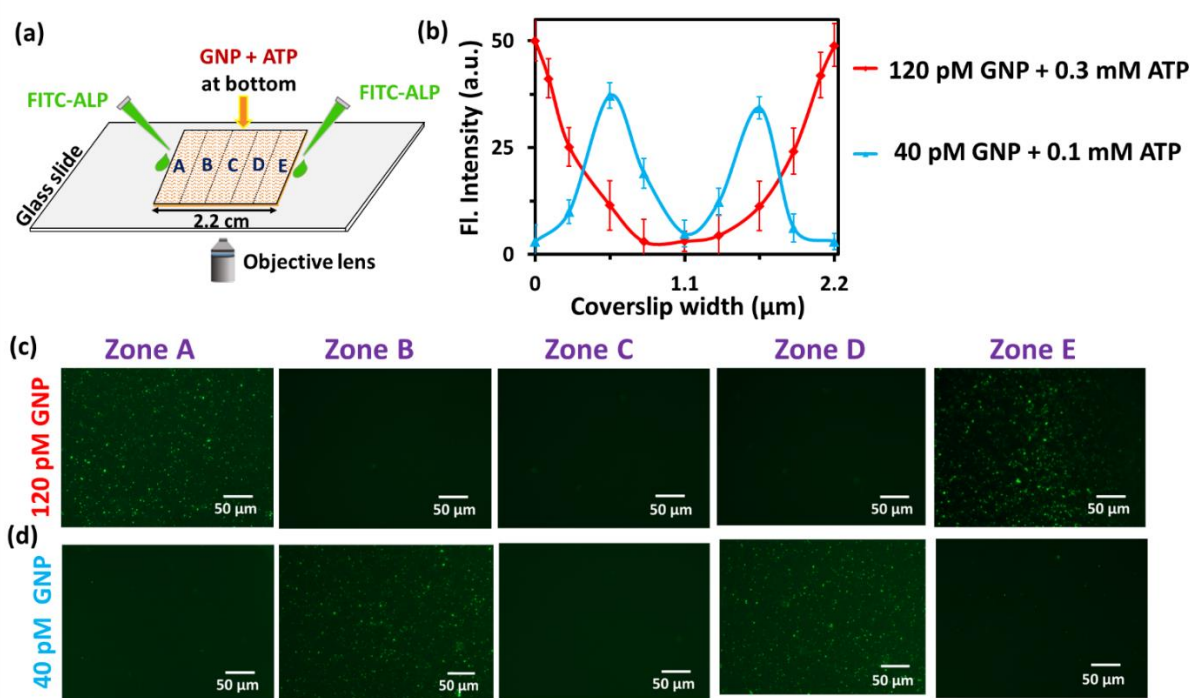


Figure 2.32. (a) Schematic representation of the experimental set up where GNP (40 or 120 pM) +ATP (0.1 or 0.3 mM) (15 μ l volume) solution was placed on a glass slide and a cover slip was placed over it. Then from two sides of the cover slip, FITC-tagged ALP was added (0.5 μ M, 7 μ l) was added and at different time intervals images were taken at zone A to E. (b) Fluorescence intensity profile across zone A to E at 10, 20 and 30 min when under the cover slip [GNP] = 120 pM and [ATP] = 0.3 mM and [GNP] = 40 pM and [ATP] = 0.1 mM. (c-d) Representative fluorescent image showing agglomeration of the fluorescent structure in a different zone in the presence of 120 and 40 pM of GNP after 30 minutes of reaction. Experimental condition: [Ade] = 0.3 mM, [Pi] = 0.9 mM, [ATP] = 0.3 mM, [GNP] = 120 pM, [tris] = 15 mM, pH = 9.

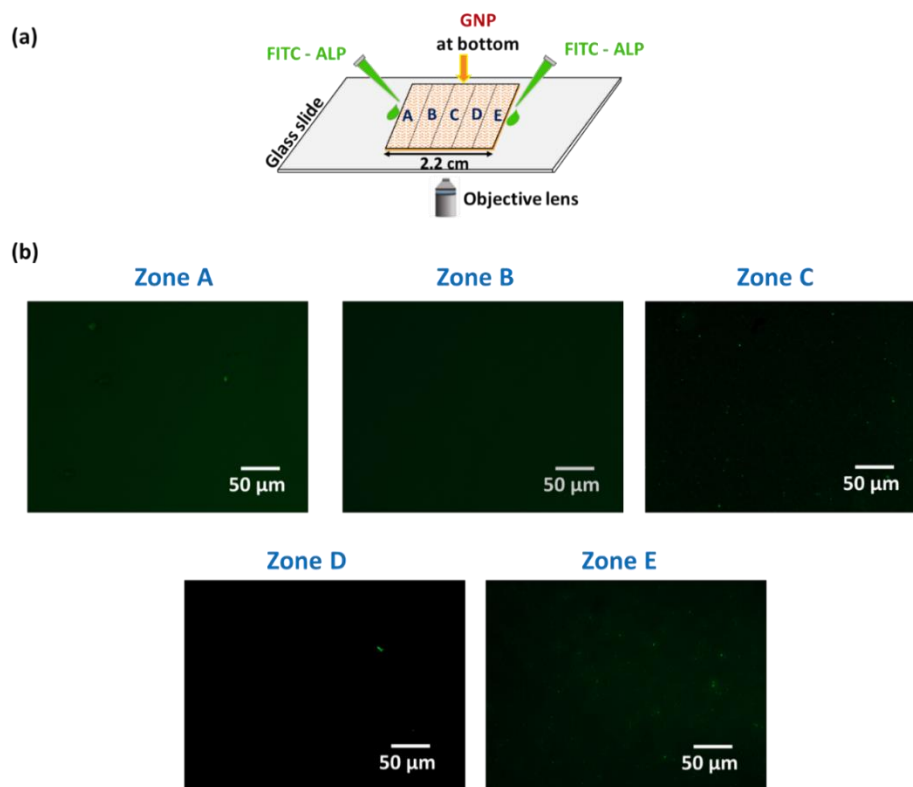


Figure 2.33. Fluorescence images of nanoparticle system in different zones when GNP only (without ATP) solution was added at bottom and ALP was added from opposite edges.

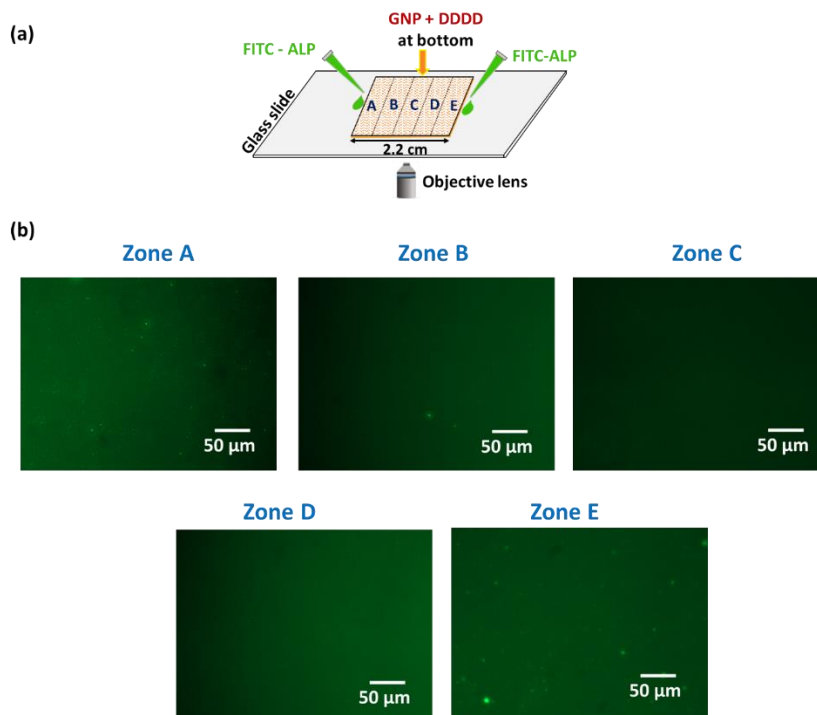


Figure 2.34. Zonal aggregation of nanoparticle system in different zones when GNP with DDDD solution was added at bottom and ALP was added from opposite edges.

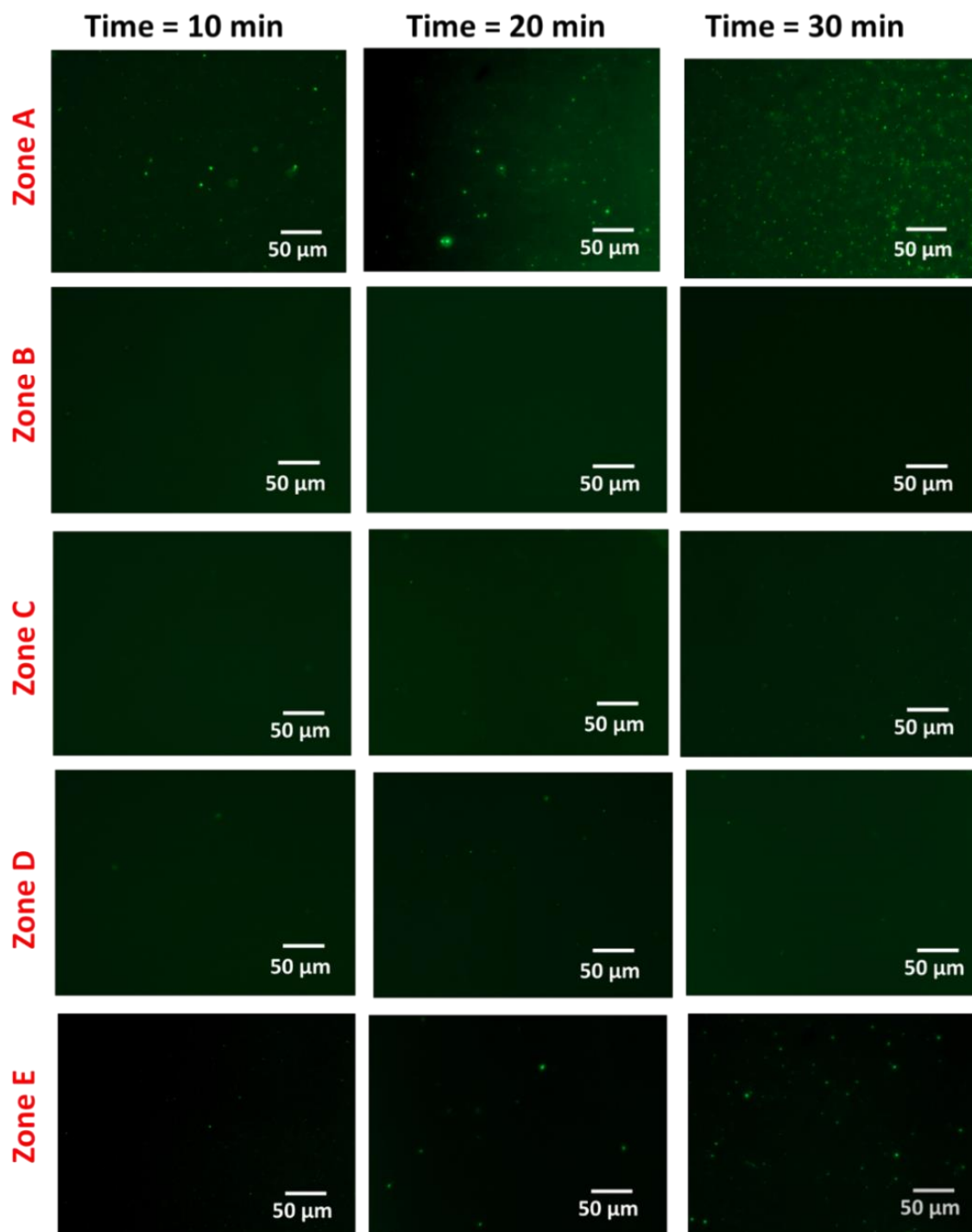


Figure 2.35. Zonal aggregation of nanoparticles with time when ATP solution was added at the bottom, ALP was added from zone A side, and Proteinase K was added from zone E side. Experimental condition: $[GNP] = 120 \text{ pM}$, $[ATP] = 0.3 \text{ mM}$, $[ALP] = 0.5 \text{ }\mu\text{M}$ (50% labeled), $[Proteinase \text{ K}] = 1 \text{ }\mu\text{M}$, $[\text{tris-HCl}] = 15 \text{ mM}$ at pH 9 at $25 \text{ }^\circ\text{C}$. Here also we observed much stronger aggregation at zone A and weaker at zone E. Absence of chemiphoresis in zone E as discussed in Figure 2.39 is the reason behind this. Whereas in zone A, both electrophoresis and chemiphoresis can happen (See Figure 2.37 to 2.39).

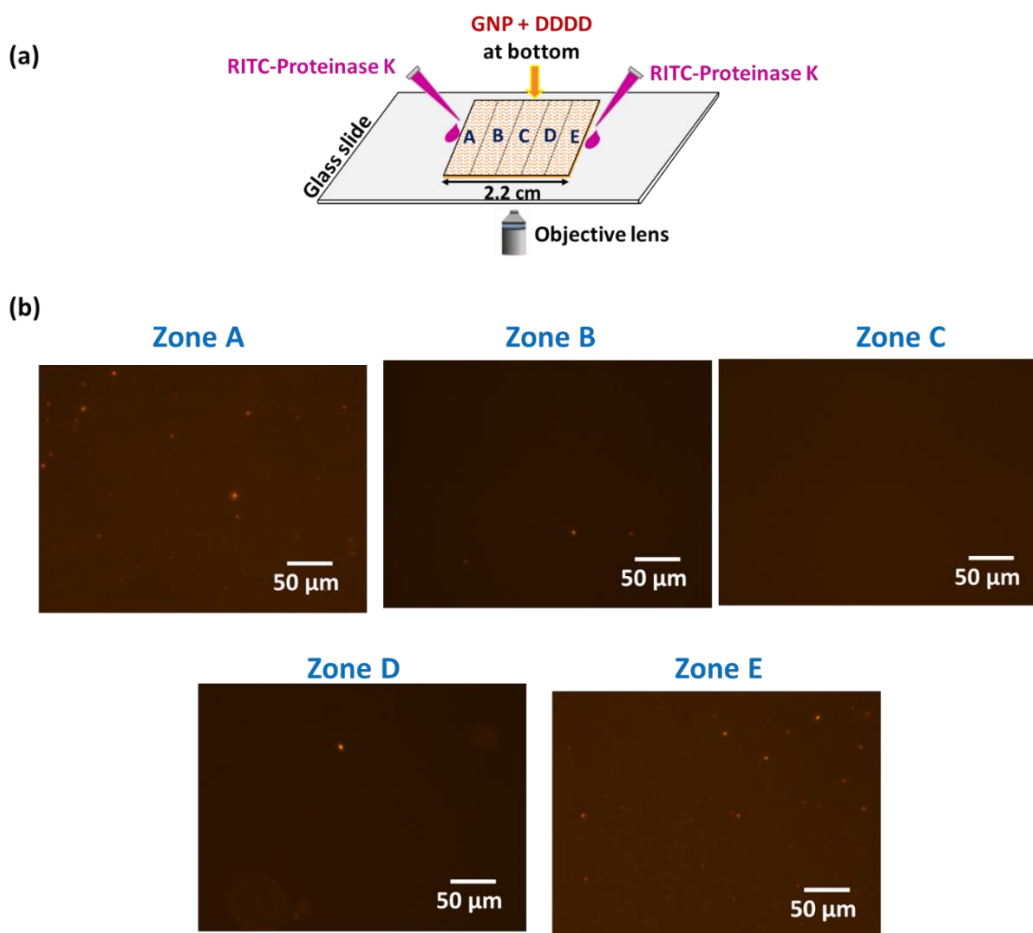


Figure 2.36. Zonal aggregation of nanoparticle system in different zones when GNP with DDDD solution was added at the bottom and RITC labeled Proteinase K was added from opposite edges. Experimental condition: $[GNP] = 120 \text{ pM}$, $[Proteinase K] = 1 \text{ μM}$ (50% labeled), $[DDDD] = 0.2 \text{ mM}$, $[tris-HCl] = 15 \text{ mM}$ at pH 9 at 25 °C . In this case, we observed more aggregation in zone A and E. Here both electrophoresis and chemiphoresis can happen. However, the extent of electrophoretic mobility will be much less as the negative charge of PK is only -8 mV (whereas for ALP it was -30 mV), thus having a much lower affinity towards positively charge GNP-substrate complex.

The observed clustering behavior can be attributed to the stronger chemiphoretic and electrophoretic contributions at higher GNP and ATP concentrations, leading to clustering at the terminal zones (A and E). On the other hand, weaker chemiphoresis and electrophoresis at lower GNP and ATP concentrations resulted in clustering in the inner zones B and D. This process can be attributed to the diffusiphoretic migration, which is a combined effect of both electrophoresis and chemiphoresis, where positively charged GNP-ATP conjugates migrate towards the negatively charged enzyme.⁵⁰⁻⁵⁴ We further verified the electrophoretic migration theoretically using COMSOL Multiphysics software (see Figure 2.37-2.39 and related discussion in the method section). The chemiphoretic contribution, in this case, arises from the

hydrolysis of ATP near ALP, which creates a solute gradient of high to low concentration across the surface of the nanoparticles (Figure 2.39).

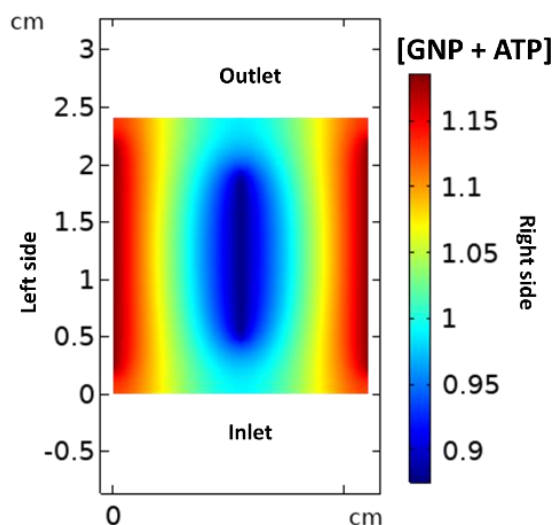


Figure 2.37. Concentration gradient of ATP-bound nanoparticles inside the electrophoresis chip, found theoretically after simulation, is similar to our experimental observation.

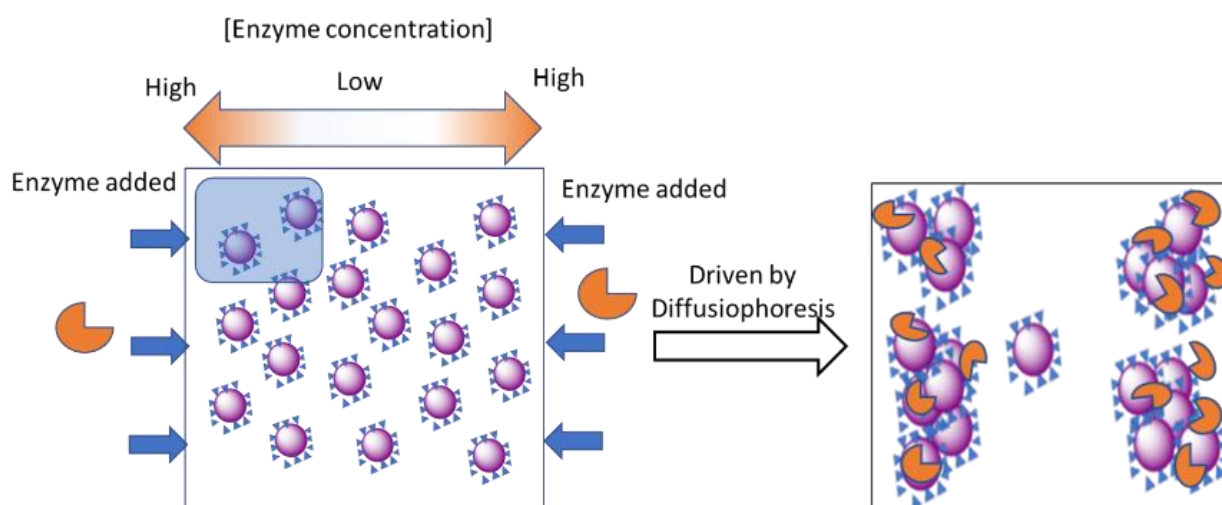


Figure 2.38. Schematic of the aggregation driven by enzyme-actuated diffusiophoretic mechanism only. The blue highlighted zone is elaborated in the next Figure.

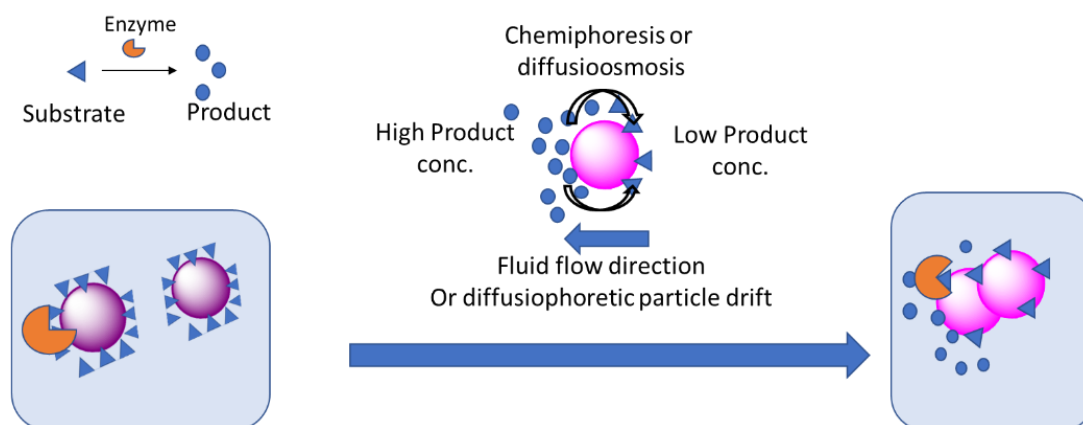


Figure 2.39. Due to the hydrolysis of GNP-bound substrate, there is a concentration gradient generated across the nanoparticle surface. This self-generated gradient will result in osmotic flow from low product concentration to high product concentration zone. Please see references 50-51 for more details about the diffusiophoretic process and specially diffusioosmosis or chemiphoresis.

Subsequently, we aimed to investigate the impact of the interaction and aggregation of GNP-ATP-ALP on the phenomenon known as the "coffee ring" effect during droplet evaporation. The coffee ring formation occurs when suspended or dispersed materials accumulate at the edges of a droplet after the liquid evaporates completely.⁵⁹⁻⁶² This effect arises due to the outward capillary flow from the center to the edge of the droplet, caused by faster evaporation at the edges compared to the center. The control and manipulation of the coffee ring phenomenon are of great interest due to their potential applications in surface coating, printing, and bioanalysis.^{27-29, 51-62}

Previous studies have primarily focused on investigating the coffee ring effect using nanoparticles of different sizes and shapes, surfactants, biomolecules, or cells. However, the presence of interactive particles (GNPs), enzymes (ALP), and small molecules (ATP) in a droplet introduces a different dynamic. This interaction has the potential to alter the pattern formation. To understand the coffee ring effect of the GNP-ATP-ALP conjugate, we initially labeled ALP with FITC and observed the enzyme deposition after the evaporation of the sample on a glass slide under a fluorescence microscope (Figure 2.40). In the presence of only buffer and ATP, a clear ring-like deposition formed at the periphery of the droplet (Figure 2.41). Interestingly, the presence of GNPs in the buffer significantly reduced the ring width, and FITC-ALP deposited almost uniformly across the droplet surface. When GNP+ATP+ALP was present, a much thicker ring width was observed. The formation probability and extent of the

ring pattern can be explained by calculating the electrokinetics-driven capillary phoresis (CP) number. A higher CP value indicates a higher propensity for coffee ring formation and vice versa.⁶¹ The CP number is determined by the diffusiophoretic velocity resulting from the salt buffer gradient upon evaporation, the diffusioosmotic-driven fluid transport along the surface, and the capillary convection within the droplet (Figure 2.4, see method section for detailed calculation).

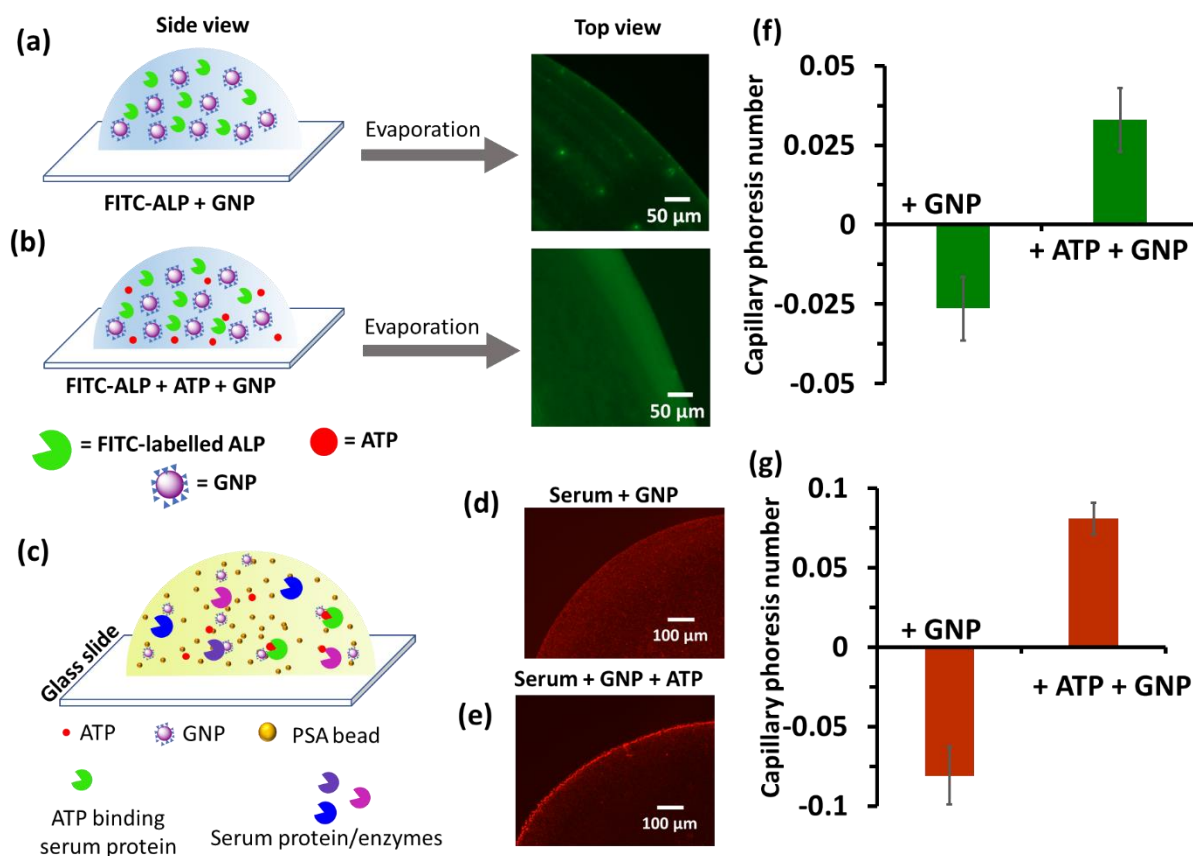


Figure 2.40. Fluorescence microscopic images of the spatiotemporal pattern of the ring-like structure formation after the evaporation of a droplet consisting of FITC-ALP uniformly mixed with (a) buffer + GNP, b) buffer + GNP + ATP. Experimental conditions: [GNP] = 120 pM, [ATP] = 0.3 mM, [FITC-ALP] = 500 nM, [Tris] = 15 mM, pH = 9. (c) Schematic representation showing human blood serum droplet with GNP, ATP, ALP together, (d-e) Fluorescence microscopic images of the spatiotemporal pattern of the ring-like structure formation after the evaporation of a serum droplet consisting of GNP, and GNP+ATP. (f-g) Plot for capillary phoresis number, for details about CP value calculation, please see method section).

Interestingly, despite the formation of aggregates due to the simultaneous presence of ALP and ATP, which, in principle, could further suppress the coffee ring pattern compared to the GNP+ALP system, a slightly higher ring width was observed. This can be attributed to the

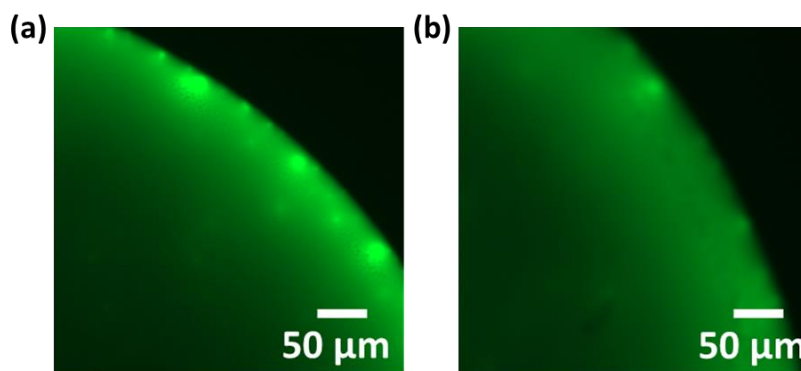


Figure 2.41. Fluorescence microscopic images of the spatiotemporal pattern of the ring-like structure formation after the evaporation of a droplet consisting of FITC-ALP uniformly mixed with (a) buffer, b) buffer + ATP. Experimental conditions: [ATP] = 0.3 mM, [FITC-ALP] = 500 nM, [Tris] = 15 mM, pH = 9.

higher electrokinetic effect resulting from the decrease in the net positive charge of the overall conjugate, reducing the frictional force from the negatively charged glass surface. Based on these observations, we further investigated the coffee ring pattern formation behavior in a complex biological fluid, blood serum. Unlike a simple buffer, blood serum contains numerous proteins (e.g., albumin, $\alpha/\beta/\gamma$ -globulin), enzymes, salts, and small molecules.⁶³ We used a diluted (0.1%) serum solution in pH = 9 Tris buffer for both ζ -potential measurement and coffee ring pattern formation. The ζ -potential value of the serum alone was found to be -28 mV, indicating the presence of mostly negatively charged proteins like albumin (50-60%) and α/β -globulin (30-40%) (among the globulin proteins, γ -globulin is positively charged in neutral conditions with a pI of 7.2, which constitutes only ~10% of the serum protein content). We also confirmed the presence of ATPase activity in the commercially procured blood serum solution, indicating the presence of ATP-binding proteins (Figure 2.41). To understand the coffee ring formation pattern in the serum in the absence and presence of GNP or ATP, we employed commercial negatively charged polystyrene amine (PSA) fluorescence beads (0.025 wt%, ζ -value = -30 mV, diameter ~1 μm) to track the deposition pattern during the evaporation of a droplet on a glass slide, as described earlier (Figure 2.40c). In the presence of only serum, clear coffee ring formation was observed, with the beads depositing at the edge of the droplet (Figure 2.42). However, in the presence of GNP alone in blood serum, the distinct coffee ring-like deposition of the fluorescent beads was not observed. This suppression of the coffee ring effect can be attributed to the high positive ζ -potential of GNPs (25 ± 2 mV), which counteracts the negative charge of the serum proteins, resulting in a net negative CP value due to stronger

inward-directed diffusiophoretic flow. This indicates that GNPs alone do not attract proteins from the blood serum to their surface under experimental conditions.

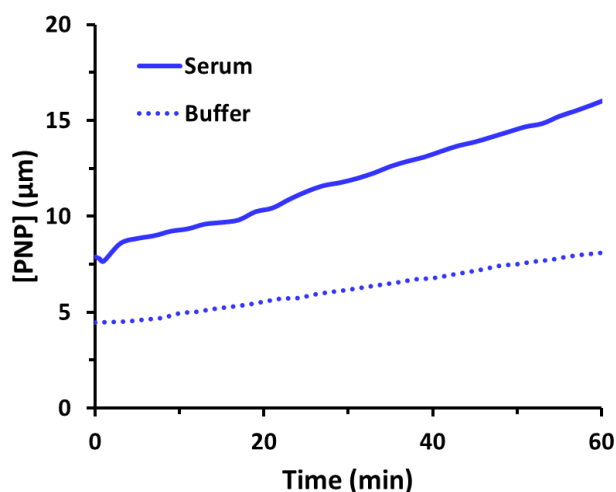


Figure 2.41. The amount of p-nitrophenol (PNP) formed due to hydrolysis of p-nitrophenyl phosphate (PNPP) in the presence and absence of blood serum. Experimental condition: [PNPP] = 1 mM, [serum] = 0.1 %, [tris] = 15 mM at pH 9. This experiment shows serum contains enzymes with phosphoesterase activity.

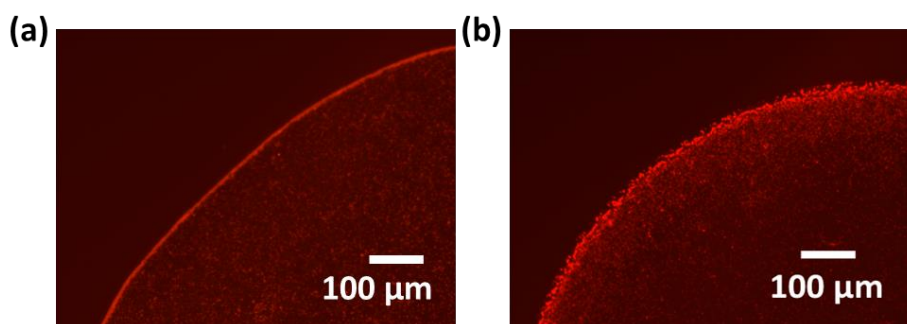


Figure 2.42. Fluorescence microscopic images of the pattern formation after the evaporation of a droplet consisting of PSA (amine-functionalized polystyrene beads) uniformly mixed with (a) buffer, b) buffer + serum. Experimental conditions: [PSA] = 0.025%, [Tris] = 15 mM, pH = 9.

Interestingly, by adding the GNP+ATP conjugate, the net positive ζ -potential decreased significantly to 4 ± 2 mV in the blood serum (Figure 2.40c-d). This suggests that serum proteins and enzymes are attracted to the GNP-ATP surface. Furthermore, we observed the restoration of the coffee ring pattern due to the suppression of the inward diffusiophoretic flow and the higher CP value (Figure 2.40f, Table 2.2). Therefore, the modulation of capillary phoresis by the GNP-ATP conjugate can serve as a sensor for identifying ATP-binding proteins (such as

heat shock protein (HSP90)) or phosphatase-like enzymes in complex environments like blood serum by observing the phoresis-mediated surface pattern formation on a glass slide.⁶⁴

Table 2.2. Zeta potential measurements of particle (ζ_s), and glass-substrate (ζ_{GS}) in the buffer. Experimental condition: [GNP] =120 pM, ALP = 0.5 μ M, [ATP] = 0.3 mM, [serum] =0.1 %, [PSA] = 0.025 %, [tris] = 15 mM at pH 9.

System	Components	ζ_s (mV)	ζ_{GS} (mV)
Buffer	GNP + ALP	28 \pm 1	32 \pm 2
	GNP + ATP + ALP	20 \pm 2	15 \pm 1
Serum in buffer	PSA + GNP	25 \pm 2	31 \pm 2
	PSA + GNP + ATP	4 \pm 2	-2 \pm 1

2.5. Summary

In summary, this study combines noncovalently bound GNP-substrate conjugates and enzymes to investigate various phenomena. Firstly, it explores the aggregation of nanoparticles in homogeneous conditions when exposed to nucleotides and alkaline phosphatase. Secondly, it examines the migratory and aggregation behavior of nanoparticles in response to enzymes, both catalytic and noncatalytic, under microfluidic conditions. Thirdly, it demonstrates the patterning of nanoparticle aggregation on a macroscale glass slide. Lastly, it explores the formation of coffee ring patterns from evaporating droplets and its potential application in analyzing clinically relevant samples such as blood serum. The results indicate that specific enzyme-substrate binding, combined with a strong affinity of the substrate to the nanoparticle surface, accelerates the aggregation process. Particularly, ATP exhibits a significantly higher binding affinity compared to its products (adenosine + Pi), leading to faster aggregation. Additionally, the study highlights the role of diffusiophoresis in governing the taxis and assembly formation of nanobioconjugates. Previous research has demonstrated dynamic self-assembly and patterning of nanoparticles using complementary charge interaction, light, lithography, and self-assembly approaches, which find applications in designing plasmonic or SERS-active substrates, dynamic nonlinear oscillatory systems, and catalytic materials.⁶⁵⁻⁷⁵

Furthermore, the study reports on the diffusiophoretic formation and accumulation of nanobioconjugates under microfluidic conditions, wherein the growth rate can be controlled by the enzyme-substrate gradients. While previous studies have observed "diffusiophoretic

banding" using polymer beads in gradients of NaCl, KCl, or LiCl, explaining enhanced particle migration in coastal aquifers and specific sedimentation zones relevant to oceanography and estuarine hydrodynamics, the present study specifically focuses on the use of nanoparticles and enzymes for catalytic surfaces and biosensors.²² Notably, the ability to modulate coffee ring formation patterns in blood serum samples using GNP-ATP conjugates demonstrates the potential of this approach in clinically relevant diagnostics.⁷⁶ Overall, this strategy shows promise for designing complex assembly patterns in microfluidic devices, involving heterogeneous nanobioconjugates or liposome-based systems.¹²

2.6. References

1. Kim, C.; Burrows, P. E.; Forrest, S. R. Micropatterning of Organic Electronic Devices by Cold-Welding. *Science* **2000**, *288*, 831–833.
2. Olive, A. G. L.; Abdullah, N. H.; Ziemecka, I.; Mendes, E.; Eelkema, R.; van Esch, J. H. Spatial and Directional Control over Self-Assembly Using Catalytic Micropatterned Surfaces. *Angew. Chem. Int. Ed.* **2014**, *53*, 4132–4136.
3. Heinrich, T.; Traulsen, C. H.-H.; Holzweber, M.; Richter, S.; Kunz, V.; Kastner, S. K.; Krabbenborg, S. O.; Huskens, J.; Unger, W. E. S.; Schalley, C. A. Coupled Molecular Switching Processes in Ordered Mono- and Multilayers of Stimulus-Responsive Rotaxanes on Gold Surfaces. *J. Am. Chem. Soc.* **2015**, *137*, 4382–4390.
4. Xu, H.; Huskens, J. Versatile Stamps in Microcontact Printing: Transferring Inks by Molecular Recognition and from Ink Reservoirs. *Chem -Eur. J.* **2010**, *16*, 2342–2348.
5. Huck, W. T. S. Self-Assembly Meets Nanofabrication: Recent Developments in Microcontact Printing and Dip-Pen Nanolithography. *Angew. Chem. Int. Ed.* **2007**, *46*, 2754–2757.
6. Kolodziej, C. M.; Maynard, H. D. Electron-Beam Lithography for Patterning Biomolecules at the Micron and Nanometer Scale. *Chem. Mater.* **2012**, *24*, 774–780.
7. Whitesides, G. M.; Ostuni, E.; Takayama, S.; Jiang, X.; Ingber, D. E. Soft Lithography in Biology and Biochemistry. *Annu. Rev. Biomed. Eng.* **2001**, *3*, 335–373.
8. Barad, H.-N.; Kwon, H.; Alarcón-Correa, M.; Fischer, P. Large Area Patterning of Nanoparticles and Nanostructures: Current Status and Future Prospects. *ACS Nano* **2021**, *15*, 5861–5875.
9. Pini, D.; Parola, A. Pattern Formation and Self-Assembly Driven by Competing Interactions. *Soft Matter* **2017**, *13*, 9259–9272.

10. Zhu, M.; Baffou, G.; Meyerbröcker, N.; Polleux, J. Micropatterning Thermoplasmonic Gold Nanoarrays to Manipulate Cell Adhesion. *ACS Nano* **2012**, *6*, 7227–7233.
11. Dorokhin, D.; Hsu, S.-H.; Tomczak, N.; Reinhoudt, D. N.; Huskens, J.; Velders, A. H.; Vancso, G. J. Fabrication and Luminescence of Designer Surface Patterns with Beta-Cyclodextrin Functionalized Quantum Dots via Multivalent Supramolecular Coupling. *ACS Nano* **2010**, *4*, 137–142.
12. Roling, O.; De Bruycker, K.; Vonhören, B.; Stricker, L.; Körsgen, M.; Arlinghaus, H. F.; Ravoo, B. J.; Du Prez, F. E. Rewritable Polymer Brush Micropatterns Grafted by Triazolinedione Click Chemistry. *Angew. Chem. Int. Ed.* **2015**, *54*, 13126–13129.
13. Klajn, R.; Gray, T. P.; Wesson, P. J.; Myers, B. D.; Dravid, V. P.; Smoukov, S. K.; Grzybowski, B. A. Bulk Synthesis and Surface Patterning of Nanoporous Metals and Alloys from Supraspherical Nanoparticle Aggregates. *Adv. Funct. Mater.* **2008**, *18*, 2763–2769.
14. Loescher, S.; Walther, A. Multivalency Pattern Recognition to Sort Colloidal Assemblies. *Small* **2021**, *17*, e2005668.
15. Koch, A. J.; Meinhardt, H. Biological Pattern Formation: From Basic Mechanisms to Complex Structures. *Rev. Mod. Phys.* **1994**, *66*, 1481–1507.
16. Maini, P. K.; Woolley, T. E.; Baker, R. E.; Gaffney, E. A.; Lee, S. S. Turing's Model for Biological Pattern Formation and the Robustness Problem. *Interface Focus* **2012**, *2*, 487–496.
17. Jiang, X.; Xu, Q.; Dertinger, S. K. W.; Stroock, A. D.; Fu, T.-M.; Whitesides, G. M. A General Method for Patterning Gradients of Biomolecules on Surfaces Using Microfluidic Networks. *Anal. Chem.* **2005**, *77*, 2338–2347.
18. Shelly, M.; Lee, S.-I.; Suarato, G.; Meng, Y.; Pautot, S. Photolithography-Based Substrate Microfabrication for Patterning Semaphorin 3A to Study Neuronal Development. *Methods Mol. Biol.* **2017**, *1493*, 321–343.
19. Dorsey, P. J.; Rubanov, M.; Wang, W.; Schulman, R. Digital Maskless Photolithographic Patterning of DNA-Functionalized Poly(Ethylene Glycol) Diacrylate Hydrogels with Visible Light Enabling Photodirected Release of Oligonucleotides. *ACS Macro Lett.* **2019**, *8*, 1133–1140.
20. Mahato, R. R.; Priyanka; Shandilya, E.; Maiti, S. Perpetuating Enzymatically Induced Spatiotemporal PH and Catalytic Heterogeneity of a Hydrogel by Nanoparticles. *Chem. Sci.* **2022**, *13*, 8557–8566.

21. Mohajerani, F.; Zhao, X.; Somasundar, A.; Velegol, D.; Sen, A. A Theory of Enzyme Chemotaxis: From Experiments to Modeling. *Biochemistry* **2018**, *57*, 6256–6263.
22. Agudo-Canalejo, J.; Adeleke-Larodo, T.; Illien, P.; Golestanian, R. Enhanced Diffusion and Chemotaxis at the Nanoscale. *Acc. Chem. Res.* **2018**, *51*, 2365–2372.
23. Li, J.; Lin, F. Microfluidic Devices for Studying Chemotaxis and Electrotaxis. *Trends Cell Biol.* **2011**, *21*, 489–497.
24. Mampallil, D.; Eral, H. B. A Review on Suppression and Utilization of the Coffee-Ring Effect. *Adv. Colloid Interface Sci.* **2018**, *252*, 38–54.
25. Li, H.; Buesen, D.; Williams, R.; Henig, J.; Stapf, S.; Mukherjee, K.; Freier, E.; Lubitz, W.; Winkler, M.; Happe, T.; *et al.* Preventing the Coffee-Ring Effect and Aggregate Sedimentation by in Situ Gelation of Monodisperse Materials. *Chem. Sci.* **2018**, *9*, 7596–7605.
26. Anyfantakis, M.; Baigl, D. Dynamic Photocontrol of the Coffee-Ring Effect with Optically Tunable Particle Stickiness. *Angew. Chem. Int. Ed.* **2014**, *53*, 14077–14081.
27. Shandilya, E.; Maiti, S. Deconvolution of Transient Species in a Multivalent Fuel-driven Multistep Assembly under Dissipative Conditions. *ChemSystemsChem* **2020**, *2*, e201900040.
28. Huskens, J. Multivalent Interactions at Interfaces. *Curr. Opin. Chem. Biol.* **2006**, *10*, 537–543.
29. Priyanka; Shandilya, E.; Brar, S. K.; Mahato, R. R.; Maiti, S. Spatiotemporal Dynamics of Self-Assembled Structures in Enzymatically Induced Agonistic and Antagonistic Conditions. *Chem. Sci.* **2021**, *13*, 274–282.
30. Overeem, N. J.; Hamming, P. H. E.; Tieke, M.; van der Vries, E.; Huskens, J. Multivalent Affinity Profiling: Direct Visualization of the Superselective Binding of Influenza Viruses. *ACS Nano* **2021**, *15*, 8525–8536.
31. Huskens, J.; Prins, L. J.; Haag, R.; Ravoo, B. J. *Multivalency: Concepts, Research and Applications*; Huskens, J.; Prins, L. J.; Haag, R.; Ravoo, B. J., Eds.; John Wiley & Sons: Nashville, TN, 2018.
32. Belitsky, J. M.; Nelson, A.; Hernandez, J. D.; Baum, L. G.; Stoddart, J. F. Multivalent Interactions between Lectins and Supramolecular Complexes: Galectin-1 and Self-Assembled Pseudopolyrotaxanes. *Chem. Biol.* **2007**, *14*, 1140–1151.
33. Astumian, R. D. Kinetic Asymmetry Allows Macromolecular Catalysts to Drive an Information Ratchet. *Nat. Commun.* **2019**, *10*, 3837.

34. Sharko, A.; Livitz, D.; De Piccoli, S.; Bishop, K. J. M.; Hermans, T. M. Insights into Chemically Fueled Supramolecular Polymers. *Chem. Rev.* **2022**, *122*, 11759–11777.
35. Maiti, S.; Fortunati, I.; Ferrante, C.; Scrimin, P.; Prins, L. J. Dissipative Self-Assembly of Vesicular Nanoreactors. *Nat. Chem.* **2016**, *8*, 725–731.
36. Mahato, R. R.; Shandilya, E.; Dasgupta, B.; Maiti, S. Dictating Catalytic Preference and Activity of a Nanoparticle by Modulating Its Multivalent Engagement. *ACS Catal.* **2021**, *11*, 8504–8509.
37. Mishra, A.; Dhiman, S.; George, S. J. ATP-driven Synthetic Supramolecular Assemblies: From ATP as a Template to Fuel. *Angew. Chem. Int. Ed.* **2021**, *60*, 2740–2756.
38. Jain, A.; Dhiman, S.; Dhayani, A.; Vemula, P. K.; George, S. J. Chemical Fuel-Driven Living and Transient Supramolecular Polymerization. *Nat. Commun.* **2019**, *10*, 450.
39. Grötsch, R. K.; Wanzke, C.; Speckbacher, M.; Angl, A.; Rieger, B.; Boekhoven, J. Pathway Dependence in the Fuel-Driven Dissipative Self-Assembly of Nanoparticles. *J. Am. Chem. Soc.* **2019**, *141*, 9872–9878.
40. Pezzato, C.; Prins, L. J. Transient Signal Generation in a Self-Assembled Nanosystem Fueled by ATP. *Nat. Commun.* **2015**, *6*, 7790.
41. Weißenfels, M.; Gemen, J.; Klajn, R. Dissipative Self-Assembly: Fueling with Chemicals versus Light. *Chem* **2021**, *7*, 23–37.
42. Wei, H.; Li, B.; Li, J.; Wang, E.; Dong, S. Simple and Sensitive Aptamer-Based Colorimetric Sensing of Protein Using Unmodified Gold Nanoparticle Probes. *Chem. Commun.* **2007**, 3735–3737.
43. Grzelczak, M.; Liz-Marzán, L. M.; Klajn, R. Stimuli-Responsive Self-Assembly of Nanoparticles. *Chem. Soc. Rev.* **2019**, *48*, 1342–1361.
44. Dhiman, S.; Jain, A.; Kumar, M.; George, S. J. Adenosine-Phosphate-Fueled, Temporally Programmed Supramolecular Polymers with Multiple Transient States. *J. Am. Chem. Soc.* **2017**, *139*, 16568–16575.
45. Grzybowski, B. A.; Huck, W. T. S. The Nanotechnology of Life-Inspired Systems. *Nat. Nanotechnol.* **2016**, *11*, 585–592.
46. Applebury, M. L.; Johnson, B. P.; Coleman, J. E. Phosphate Binding to Alkaline Phosphatase. *J. Biol. Chem.* **1970**, *245*, 4968–4975.

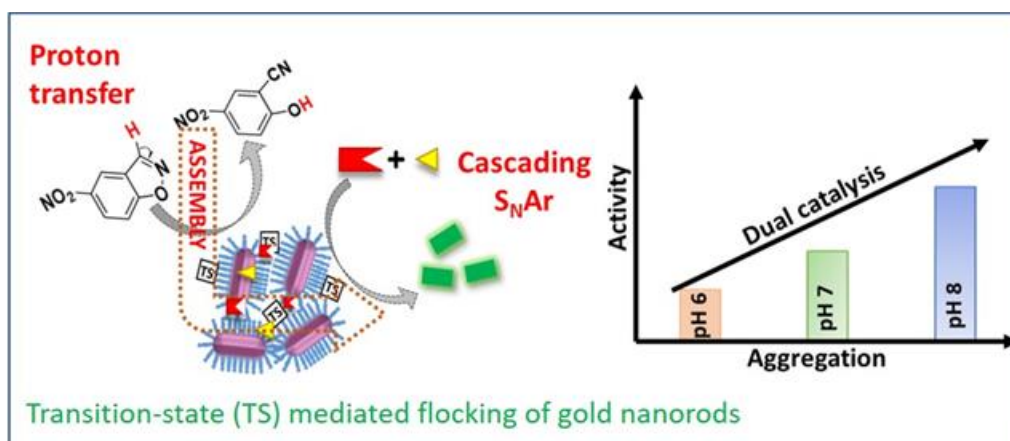
47. Deshwal, A.; Maiti, S. Macromolecular Crowding Effect on the Activity of Liposome-Bound Alkaline Phosphatase: A Paradoxical Inhibitory Action. *Langmuir* **2021**, *37*, 7273–7284.
48. Bian, T.; Gardin, A.; Gemen, J.; Houben, L.; Perego, C.; Lee, B.; Elad, N.; Chu, Z.; Pavan, G. M.; Klajn, R. Electrostatic Co-Assembly of Nanoparticles with Oppositely Charged Small Molecules into Static and Dynamic Superstructures. *Nat. Chem.* **2021**, *13*, 940–949.
49. Petrotchenko, E. V.; Serpa, J. J.; Hardie, D. B.; Berjanskii, M.; Suriyamongkol, B. P.; Wishart, D. S.; Borchers, C. H. Use of Proteinase K Nonspecific Digestion for Selective and Comprehensive Identification of Interpeptide Cross-Links: Application to Prion Proteins. *Mol. Cell. Proteomics* **2012**, *11*, M111.013524-1-M111.013524-13.
50. Velegol, D.; Garg, A.; Guha, R.; Kar, A.; Kumar, M. Origins of Concentration Gradients for Diffusiophoresis. *Soft Matter* **2016**, *12*, 4686–4703.
51. Anderson, J. L. Colloid Transport by Interfacial Forces. *Annu. Rev. Fluid Mech.* **1989**, *21*, 61–99.
52. Ault, J. T.; Warren, P. B.; Shin, S.; Stone, H. A. Diffusiophoresis in One-Dimensional Solute Gradients. *Soft Matter* **2017**, *13*, 9015–9023.
53. Palacci, J.; Abécassis, B.; Cottin-Bizonne, C.; Ybert, C.; Bocquet, L. Colloidal Motility and Pattern Formation under Rectified Diffusiophoresis. *Phys. Rev. Lett.* **2010**, *104*, 138302.
54. Shim, S. Diffusiophoresis, Diffusioosmosis, and Microfluidics: Surface-Flow-Driven Phenomena in the Presence of Flow. *Chem. Rev.* **2022**, *122*, 6986–7009.
55. Abécassis, B.; Cottin-Bizonne, C.; Ybert, C.; Ajdari, A.; Bocquet, L. Boosting Migration of Large Particles by Solute Contrasts. *Nat. Mater.* **2008**, *7*, 785–789.
56. Staffeld, P. O.; Quinn, J. A. Diffusion-Induced Banding of Colloid Particles via Diffusiophoresis. *J. Colloid Interface Sci.* **1989**, *130*, 69–87.
57. Ramm, B.; Goychuk, A.; Khmelinskaia, A.; Blumhardt, P.; Eto, H.; Ganzinger, K. A.; Frey, E.; Schwille, P. A Diffusiophoretic Mechanism for ATP-Driven Transport without Motor Proteins. *Nat. Phys.* **2021**, *17*, 850–858.
58. Guha, R.; Mohajerani, F.; Mukhopadhyay, A.; Collins, M. D.; Sen, A.; Velegol, D. Modulation of Spatiotemporal Particle Patterning in Evaporating Droplets: Applications to Diagnostics and Materials Science. *ACS Appl. Mater. Interfaces* **2017**, *9*, 43352–43362.

59. Shikha; Shandilya, E.; Priyanka; Maiti, S. Directional Migration Propensity of Calf Thymus DNA in a Gradient of Metal Ions. *Chem. Commun.* **2022**, *58*, 9353–9356.
60. Deegan, R. D.; Bakajin, O.; Dupont, T. F.; Huber, G.; Nagel, S. R.; Witten, T. A. Capillary Flow as the Cause of Ring Stains from Dried Liquid Drops. *Nature* **1997**, *389*, 827–829.
61. Hu, H.; Larson, R. G. Marangoni Effect Reverses Coffee-Ring Depositions. *J. Phys. Chem. B* **2006**, *110*, 7090–7094.
62. Leeman, M.; Choi, J.; Hansson, S.; Storm, M. U.; Nilsson, L. Proteins and Antibodies in Serum, Plasma, and Whole Blood-Size Characterization Using Asymmetrical Flow Field-Flow Fractionation (AF4). *Anal. Bioanal. Chem.* **2018**, *410*, 4867–4873.
63. Garnier, C.; Lafitte, D.; Tsvetkov, P. O.; Barbier, P.; Leclerc-Devin, J.; Millot, J.-M.; Briand, C.; Makarov, A. A.; Catelli, M. G.; Peyrot, V. Binding of ATP to Heat Shock Protein 90: Evidence for an ATP-Binding Site in the C-Terminal Domain. *J. Biol. Chem.* **2002**, *277*, 12208–12214.
64. Zhang, C. T.; Liu, Y.; Wang, X.; Wang, X.; Kolle, S.; Balazs, A. C.; Aizenberg, J. Patterning Non-Equilibrium Morphologies in Stimuli-Responsive Gels through Topographical Confinement. *Soft Matter* **2020**, *16*, 1463–1472.
65. Lagzi, I.; Kowalczyk, B.; Grzybowski, B. A. Liesegang Rings Engineered from Charged Nanoparticles. *J. Am. Chem. Soc.* **2010**, *132*, 58–60.
66. van der Weijden, A.; Winkens, M.; Schoenmakers, S. M. C.; Huck, W. T. S.; Korevaar, P. A. Autonomous Mesoscale Positioning Emerging from Myelin Filament Self-Organization and Marangoni Flows. *Nat. Commun.* **2020**, *11*, 4800.
67. Wang, W.; Duan, W.; Ahmed, S.; Sen, A.; Mallouk, T. E. From One to Many: Dynamic Assembly and Collective Behavior of Self-Propelled Colloidal Motors. *Acc. Chem. Res.* **2015**, *48*, 1938–1946.
68. Singh, D. P.; Choudhury, U.; Fischer, P.; Mark, A. G. Non-Equilibrium Assembly of Light-Activated Colloidal Mixtures. *Adv. Mater.* **2017**, *29*, 1701328.
69. Deshwal, A.; Shikha; Maiti, S. Trade-off between carbohydrates and metal ions regulates the chemotactic directionality of alkaline phosphatase. *Chem. Commun.* **2022**, *58*, 12851–12854.
70. Choi, S.; Mukhopadhyay, R. D.; Sen, S.; Hwang, I.; Kim, K. Out-of-equilibrium chemical logic systems: Light- and sound-controlled programmable spatiotemporal patterns and mechanical functions. *Chem.* **2022**, *8*, 2192–2203.

71. Matricardi, C.; Hanske, C.; Garcia-Pomar, J. L.; Langer, J.; Mihi, A.; Liz-Marzán, L. M. Gold Nanoparticle Plasmonic Superlattices as Surface-Enhanced Raman Spectroscopy Substrates. *ACS Nano* **2018**, *12*, 8531–8539.
72. Deng, J.; Walther, A. ATP-Responsive and ATP-Fueled Self-Assembling Systems and Materials. *Adv. Mater.* **2020**, *32*, e2002629.
73. Leira-Iglesias, J.; Tassoni, A.; Adachi, T.; Stich, M.; Hermans, T. M. Oscillations, Travelling Fronts and Patterns in a Supramolecular System. *Nat. Nanotechnol.* **2018**, *13*, 1021–1027.
74. Zhao, X.; Sen, A. Metabolon Formation by Chemotaxis. *Methods Enzymol.* **2019**, *617*, 45–62.
75. Yang, M.; Chen, D.; Hu, J.; Zheng, X.; Lin, Z.-J.; Zhu, H. The Application of Coffee-Ring Effect in Analytical Chemistry. *Trends Analyt. Chem.* **2022**, *157* (116752), 116752.

CHAPTER 3

Self-Assembly of Catalytically Active Gold Nanorods: Regulating Reactivity and Demonstrating Cascading Catalytic Phenomena



This is adapted reproduction from Shandilya, E.; Dasgupta, B.; Maiti, S. Interconnectivity between Surface Reactivity and Self-Assembly of Kemp Elimination Catalyzing Nanorods. *Chem. Eur. J.* **2021**, 27 (29), 7831–7836.

3.1 Introduction

Living systems, from bacteria to birds, exhibit various forms of communication and organization such as colonization, clustering, and flocking, enabling them to perform crucial functions for their sustainability.¹ These processes are facilitated by spatiotemporally organized catalytic reactions that play a central role in the emergence and properties of living beings.²⁻³ Understanding the behavior of catalysts is not only essential for gaining a deeper understanding of natural processes but also holds significant potential for developing synthetic systems with desirable functions.⁴⁻¹³ Recent pioneering reports have suggested that enhanced diffusion is a key phenomenon experienced by catalysts during their operation. Catalysts can also come into close proximity and form assemblies to efficiently utilize substrates. Natural examples of this include the formation of the purinosome and metabolon, which are dynamic assemblies of multi-enzyme complexes near mitochondria during purine starvation and sequential metabolic pathways, respectively.¹⁴⁻¹⁵ While assemblies resembling cellular systems have been observed in synthetically designed catalytically active nano/microparticles, such instances are relatively rare.¹⁶⁻²⁰ Assembly formation and gain-of-function have mainly been reported for amphiphilic or nanoparticle systems utilizing chemical fuel in a supramolecular fashion or physical energy sources such as light or electric signals, which induce configurational changes in building blocks.²¹⁻³⁰ Templated and cooperative assembly of catalytic building blocks using substrates have also been investigated.²⁸⁻³² In this study, we present an exciting example of synthetic nanocatalysts capable of forming functional self-assemblies, where the catalytic process plays a central role. Specifically, CTAB-functionalized gold nanorods catalyze the Kemp Elimination (KE) reaction, a widely used model for understanding mechanistic intricacies in biotransformation.³³⁻³⁹ This catalytic conversion process leads to the enhanced flocking behavior of nanorods during the transition state, resulting in the formation of larger assemblies. Furthermore, our research demonstrates that the hydrophobic nanocavities within the assembled nanorods can efficiently trap hydrophobic substrates, thereby enhancing the rate of aromatic nucleophilic substitution reactions. We also explore the dynamic nature of catalytic processes and investigate the role of enhanced diffusivity as a contributing factor. Additionally, we showcase a catalytic phenomenon where nanosized hydrophobic cavities of clustered nanorods accelerate the rate of reactions, leading to cascading effects even when the substrates and products of the initial reactions are not directly involved.

3.2 Materials

All reagents used in this study were obtained commercially and utilized as received, without any additional purification. The sourced materials included cetyltrimethylammonium bromide, silver nitrate, sodium borohydride, ascorbic acid monosodium phosphate, disodium phosphate, sodium hydroxide pellets, and HEPES (4-(2-hydroxyethyl)-1-piperazineethanesulfonic acid), diisopropyl ethyl amine, which were procured from Sisco Research Laboratory (SRL), India. Furthermore, 1,2-Benzisoxazole, 4-chloro-7-nitrobenzofuran, n-octylamine, Gold (III) Chloride trihydrate, and carboxylate and amine-functionalized polystyrene beads were purchased from Sigma-Aldrich. Throughout the study, milli-Q water was employed. The NMR spectra were procured using Bruker Avance-III 400 MHz spectrometer. ^1H NMR was recorded at an operation frequency 400 MHz and ^{13}C NMR at 100 MHz. The solvents used were CDCl_3 and DMSO-d₆ and the internal standard was tetramethylsilane (TMS) The chemical shift or delta (δ) values were reported in the units of parts per million (ppm). High-resolution mass spectra (HRMS) have been recorded on Waters Synapt G2-Si Q ToF Mass Spectrometer in positive and negative ESI) modes. The optical and fluorescence microscopic images were collected using Zeiss Axis Observer 7 microscope with AxioCam 503 Mono 3 Megapixel with ZEN 2 software. The Transmission Electron Microscopy images were taken using the JEOL JEM-F200 microscope. The Dynamic Light Scattering (DLS) data was recorded on Horiba Scientific Nano Particle Observer (SZ-100V2). The hybridization chambers were procured from GRACE Bio-Labs with product name SA8R-0.5-SecureSeal, with dimensions of 8-9mm Diameter \times 0.8mm Depth, 26mm \times 51mm OD, 1.5mm Diameter Ports.

3.3 Methods

3.3.1 Synthesis of Gold Nanoparticles

Gold nanoparticles were synthesized following a seed-growth method described in the literature.⁴¹ In brief, a seed solution was prepared by adding 0.25 mM $\text{HAuCl}_4 \cdot 4\text{H}_2\text{O}$ to a vial containing 75 mM CTAB. To this mixture, 6 mM ice-cold sodium borohydride solution was added, resulting in the formation of a brown-colored solution, indicating the formation of gold seeds. For the growth solution, 1.03 ml of 24 mM $\text{HAuCl}_4 \cdot 4\text{H}_2\text{O}$ solution was added to a vial containing 5.22 ml of water. Then, 10 ml of 0.1 M CTAB solution was added, causing the solution to change from light yellow to orange. Subsequently, 7.5 ml of 0.1 M L-ascorbic acid was gently added with shaking, leading to the solution becoming colorless. Next, 62.5 μl of the

seed solution, aged for two hours, was vigorously blended with the growth solution for 20 seconds, resulting in the appearance of red color. The resulting solution was then left undisturbed for 24 hours at 25°C. Before further use, the synthesized gold nanoparticles were filtered using Sephadex G-25 column chromatography.

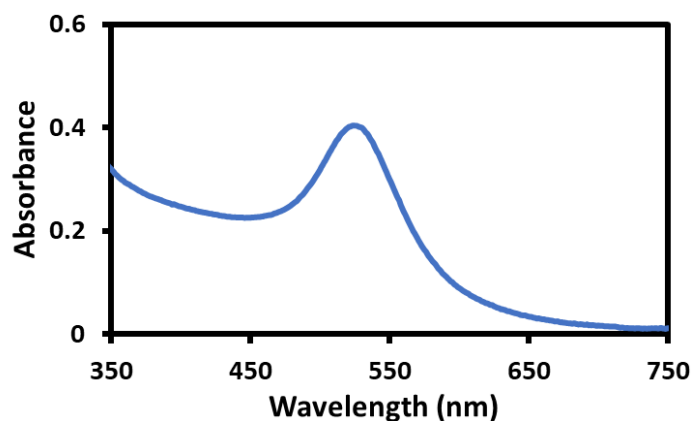


Figure 3.1. The UV-Vis spectrum of GNP at 25 °C.

3.3.2 Synthesis of Gold Nanorods

Gold nanorods have been synthesized as reported in the literature.⁴¹ A 5ml solution of 0.1M cetyltrimethylammonium bromide (CTAB) and 1 mM HAuCl_4 was prepared in milli-Q water, which gave a resultant golden-colored solution. To this, ascorbic acid was added (which made the solution colorless), followed by the addition of AgNO_3 . The final concentrations of ascorbic acid and AgNO_3 were 2 mM and 0.15 mM, respectively. Lastly, a solution of 1 mM NaBH_4 was prepared freshly, and 50 μL of it was added, which made the solution violet in color after some time. The violet color indicated the formation of gold nanorods. To remove unbound CTAB and other impurities, GNR solution was first filtered before using further. For this purpose, a Sephadex G-25 filter was used. Before using, the column was first equilibrated with an ample amount of water.

For initial confirmation, thus formed gold nanorods were characterized using a UV-Vis spectrophotometer. The obtained spectrum showed a characteristic peak at 750 nm and 523 nm, which confirmed the formation of gold nanorods.

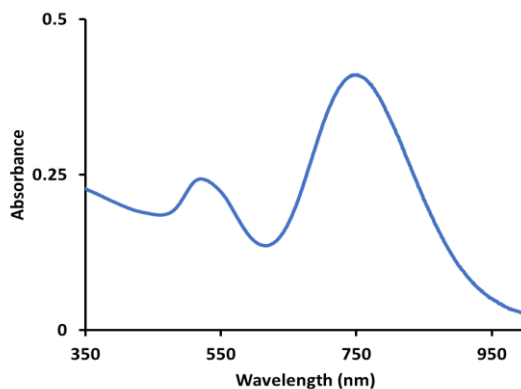


Figure 3.2. UV-Vis spectrum of GNR at 25 °C.

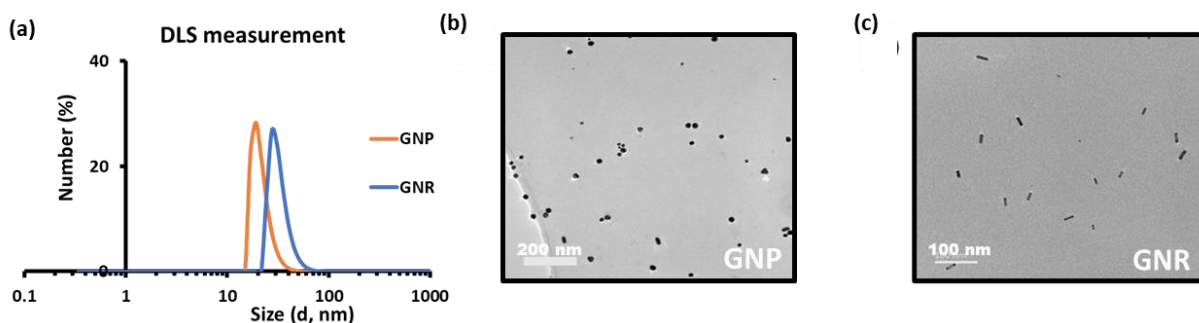


Figure 3.3. (a) Z-average of GNP and GNR; TEM images of (b) GNP, and (c) GNR in water at 25 °C.

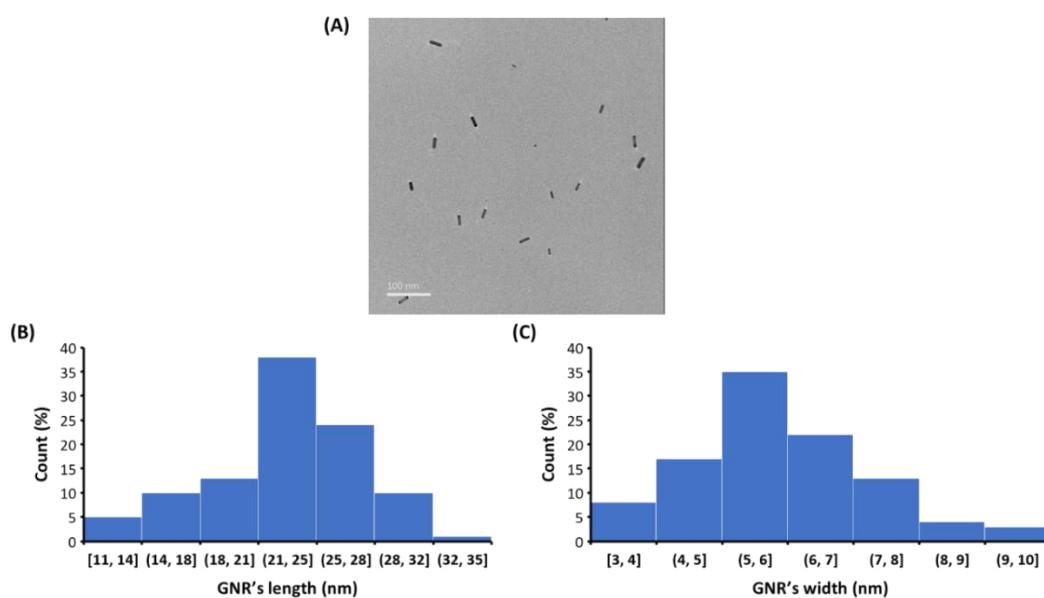


Figure 3.4. (A) TEM images of GNR; Histograms for evaluation of dimension of GNRs (A) for length (B) for width.

TEM-based analysis of GNR

Transmission electron microscopy also suggested the formation of gold nanorods. (Figure 3.4). From TEM images, we analyzed the dimensions of GNRs by using ImageJ software. Using ImageJ, we were able to get the exact length and width of gold nanorods. We collected data for more than 100 nanorods and obtained histograms for each dimension (Figure 3.4). From the collected data, the mean length and mean width are 23 ± 5 nm and 6 ± 1 nm, respectively. The mean aspect ratio for GNRs is 2.5 ± 0.5 nm.

The molar extinction coefficient of GNR

The molar extinction coefficient of GNR has been calculated using previous literature reports (*J. Phys. Chem. C* **2013**, *45*, 23950–23955). According to this, the volume of nanorods and its molar extinction coefficient are related by the relation

$$\epsilon = A + B * V$$

Where ϵ is the molar extinction coefficient of nanorod (in $10^9 \text{ M}^{-1}\text{cm}^{-1}$), V is the volume of nanorod (in 10^4 nm^3), and A and B are the constant whose values corresponds to $2.476 \times 10^9 \pm 3.99 \times 10^8$ and $1.667 \times 10^5 \pm 3.96 \times 10^4$, respectively. Following the above equation, the molar extinction for our gold nanorods will be around $2.57 \times 10^9 \text{ M}^{-1}\text{cm}^{-1}$. Mostly, we have used 0.15 nM gold nanorods, where the Au concentration is 100 μM .

3.3.2. Synthesis and Characterization of NBI, CNP, and NBD-C8 adduct

Synthesis of 5-nitrobenzisoxazole (NBI)

It has been synthesized as reported in the literature.³⁵ 1,2-Benzisoxazole (0.5g) was dissolved in conc. sulfuric acid (5ml) at room temperature. Next, a mixture of conc. nitric acid (0.6 ml) and conc. sulfuric acid (0.2 ml) was prepared and 0.5 ml of it was slowly added to the above solution and stirred for 40 minutes at room temperature. This mixture was poured into an ice-water mixture (20ml) with constant stirring and thawing for 10 min. The precipitate obtained was white, which was then filtered, washed using cold ethanol, dried under a high vacuum, and recrystallized in absolute ethanol to obtain a white, crystalline solid. Yield: 87.4%.

^1H NMR (400 MHz, CDCl_3): δ 7.79 (d, $J = 9.2$ Hz, 1H), 8.54 (d, $J = 9.2$ Hz, 1H), 8.75 (s, 1H), 8.93 (s, 1H). ^{13}C NMR (100 MHz, CDCl_3): δ 105.76, 114.51, 117.13, 120.89, 140.03, 142.34, and 159.64. HRMS (ESI): m/z calculated for $\text{C}_7\text{H}_3\text{N}_2\text{O}_3$ ($\text{M}+\text{H}$) $^+$: 165.0255, Found: 165.0233.

Synthesis of 2-cyano-4-nitrophenol

It has been synthesized as reported in the literature.³⁵ A solution of 5-nitrobenzisoxazole (0.1 g) was prepared in ethanol (2 ml) and water (1 ml) to which 3 ml of 2 M NaOH was added and the mixture was allowed to rest for 10 min. During this time, HCl was slowly added with constant stirring to bring the pH of the mixture to 1. The solution was then extracted with dichloromethane and dried under a high vacuum. The final product obtained was a light-yellow-colored solid. Yield: 66.78%.

^1H NMR (400 MHz, DMSO-d_6): δ 7.17 (d, $J = 9.2$ Hz, 1H), 8.36 (dd, $J = 7.6, 1.6$ Hz, 1H), 8.61 (d, $J = 1.6$ Hz, 1H). ^{13}C NMR (100 MHz, DMSO-d_6): δ 104.88, 120.36, 122.02, 135.55 (2C), 144.38, 171.05. HRMS (ESI): m/z calculated for $\text{C}_7\text{H}_3\text{N}_2\text{O}_3$ ($\text{M}+\text{H}$) $^+$: 165.0255, Found: 165.0230.

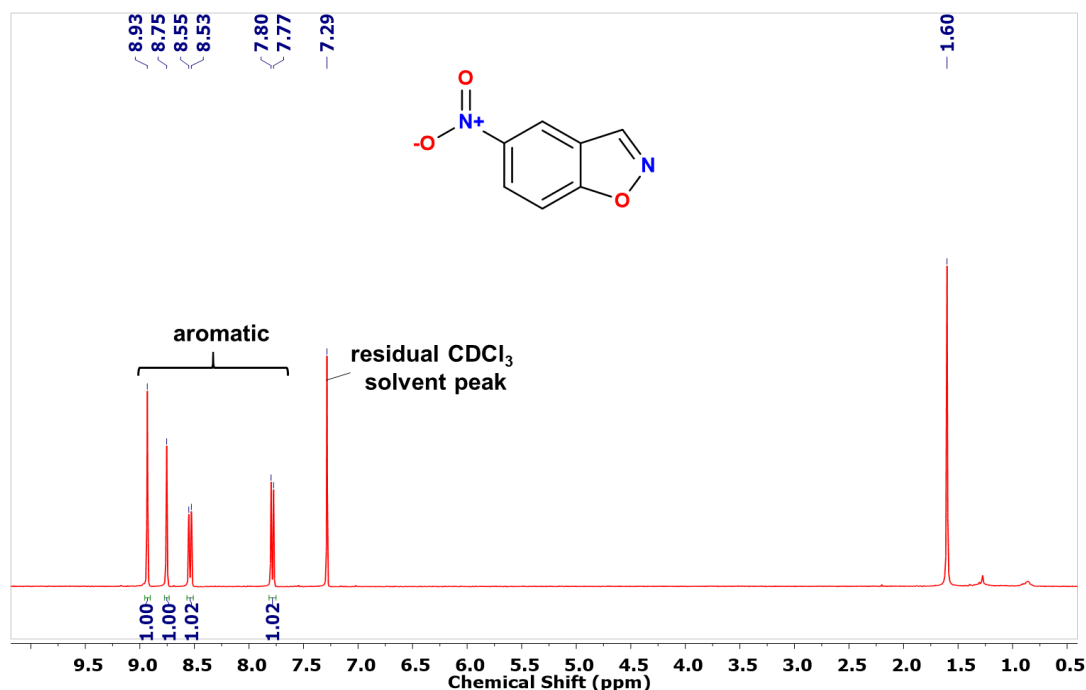


Figure 3.5. ^1H -NMR spectrum of 5-nitrobenzisoxazole (NBI).

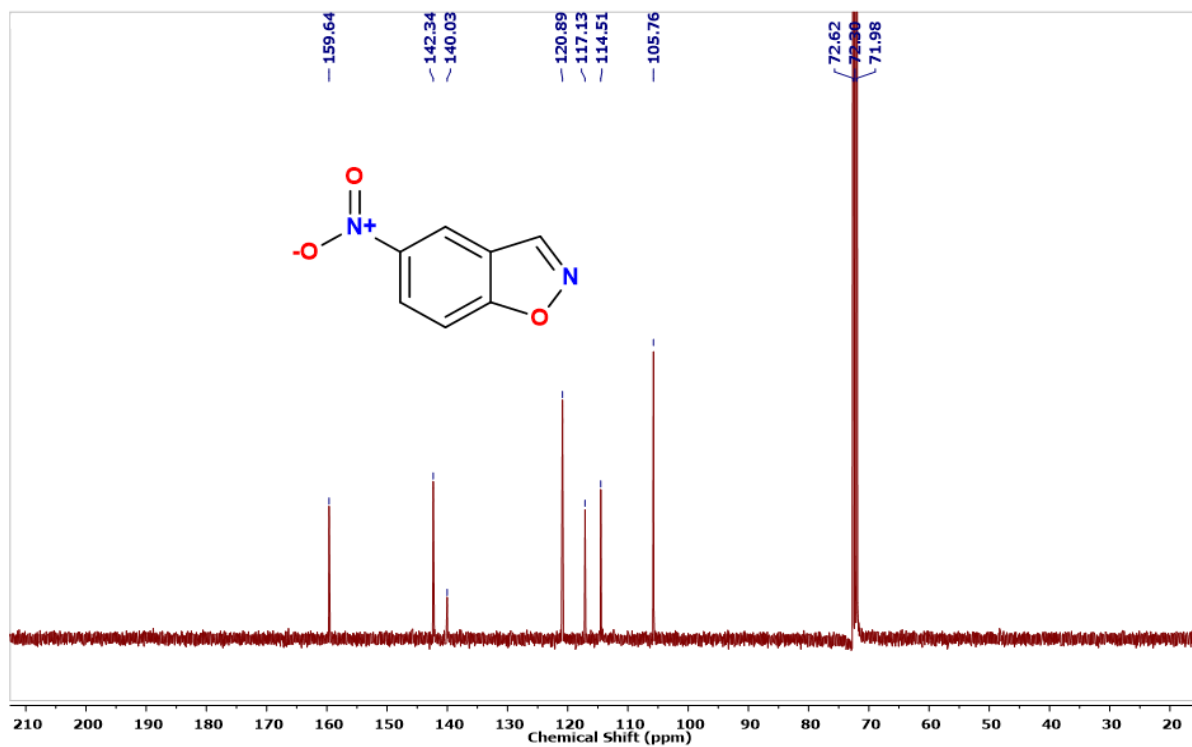


Figure 3.6. $^{13}\text{C-NMR}$ spectrum of 5-nitrobenzisoxazole (NBI).

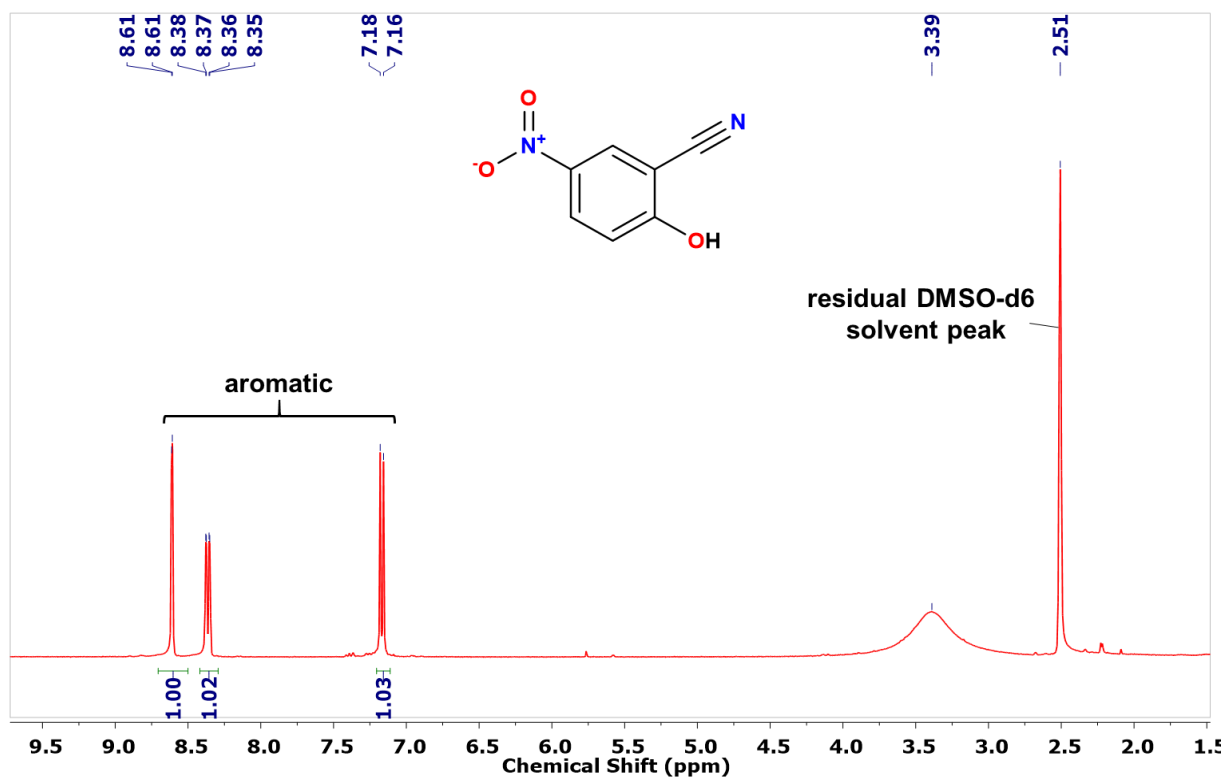


Figure 3.7. $^1\text{H-NMR}$ spectrum of 2-cyano-4-nitrophenol (CNP).

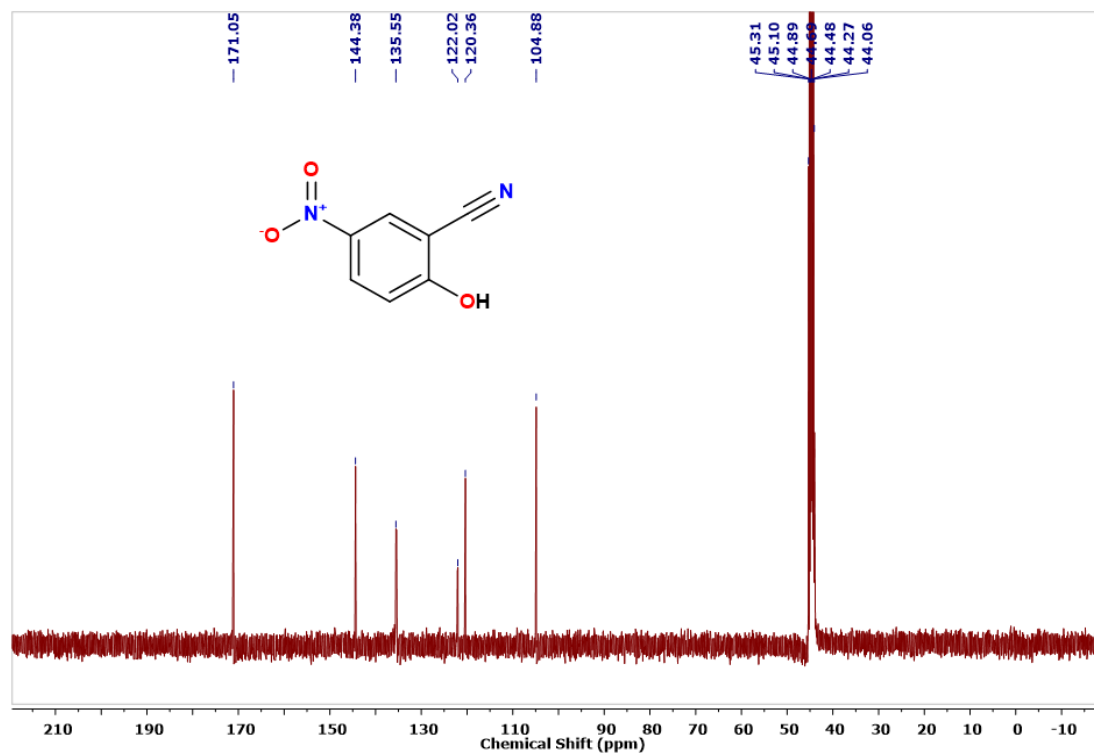


Figure 3.8. ^{13}C -NMR spectrum of 2-cyano-4-nitrophenol (CNP).

The UV-Vis spectrum of NBI and CNP

The CNP has absorbance maxima around 380 nm as shown in figure 3.9.

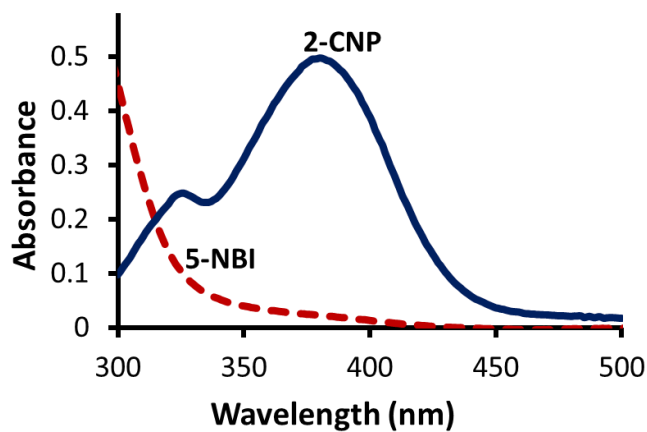


Figure 3.9. UV-Vis spectra of NBI and CNP, showing λ_{max} for CNP at 380 nm at 25 °C.

The UV-Vis spectrum of CNP in GNR system

To monitor the KE catalysis in the GNR system under a UV-Vis spectrophotometer, the characteristic peak of CNP was measured. Thus, obtained peak showed wavelength maxima at 380 nm (Figure 3.10), and in further studies, the product formation was measured at the same wavelength in the GNR system.

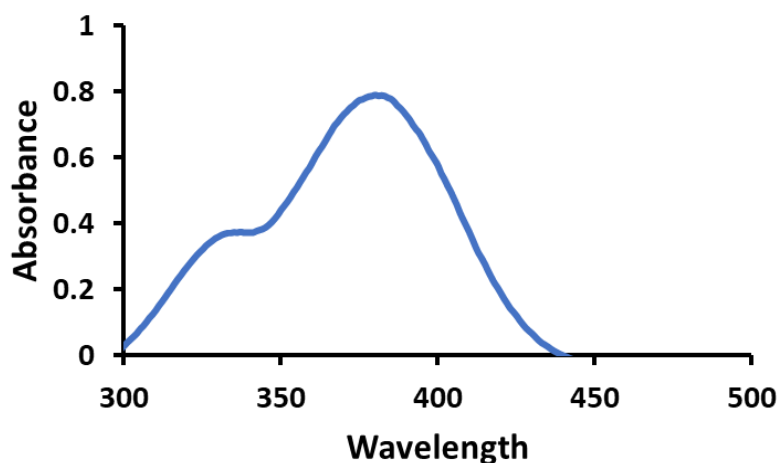


Figure 3.10. UV-Vis spectrum of CNP in the presence of GNR, showing λ_{max} at 380 nm (baseline with GNR) at 25 °C.

Synthesis of the compound NBD-C₈ (for analytical reference purposes)

It has been synthesized as reported in the literature.²¹ 100 mg of NBD-Cl (0.5 mmol), 180 μL of N, N-Diisopropylethylamine (1 mmol) 83 μL of n-octylamine was taken in a 25ml RB flask, and 10ml of methanol was added to it do dissolve all the materials. The reaction was stirred at room temperature for 15 h. The product was extracted using DCM-water, then purified using a DCM-hexane column and then dried under vacuum, and obtained a dark red solid. Yield: 90%.

^1H NMR (400 MHz, CDCl_3): δ 8.49 (d, $J = 8.4$ Hz, 1H), 6.47 (br-s, 1H), 6.19 (d, $J = 8.8$ Hz, 1H), 3.52 (dt, $J = 6.4, 6.0$, 2H), 1.83 (tt, $J = 7.2, 7.2$ Hz, 2H), 1.25-1.4 (m, 10H), 0.89 (t, $J = 6, 3$ H). ^{13}C NMR (100 MHz, DMSO-d_6): δ 14.07, 22.61, 26.95, 28.51, 29.18, 29.71, 31.73, 44.09, 98.57, 123.62, 136.69, 143.91, 144.07, 144.24. HRMS (ESI): m/z calculated for $\text{C}_{14}\text{H}_{21}\text{N}_4\text{O}_3$ ($\text{M}+\text{H}^+$): 293.1569, Found: 293.1604.

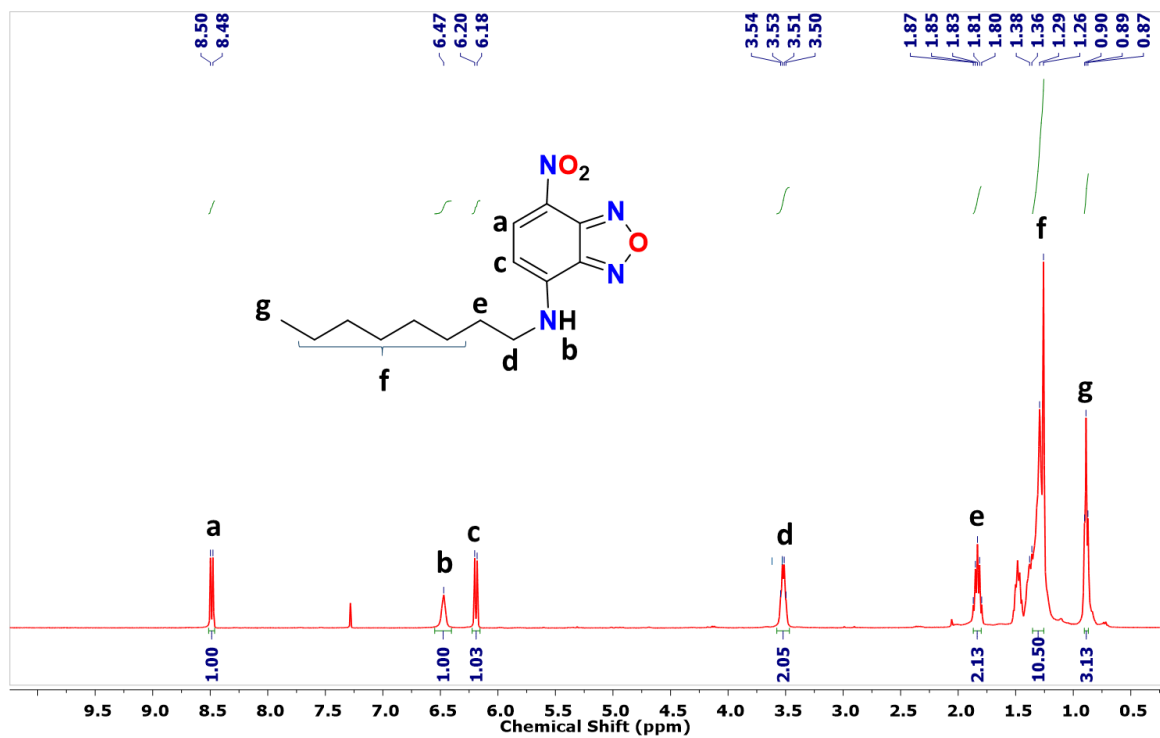


Figure 3.11. ¹H-NMR spectrum of NBD-C₈ adduct.

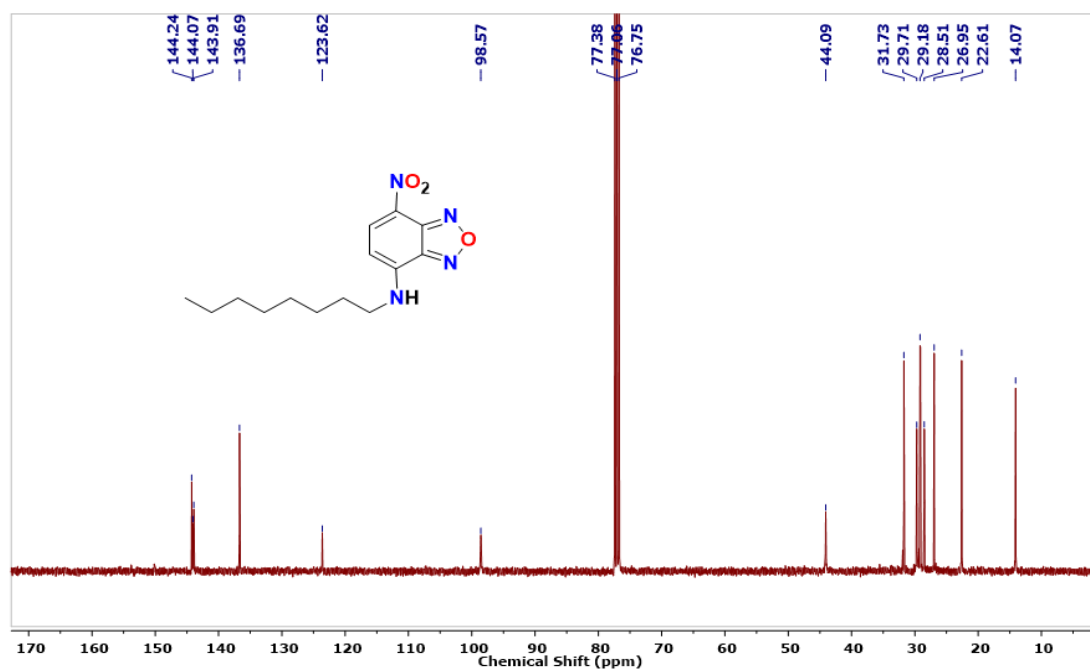


Figure 3.12. ¹³C-NMR spectrum of NBD-C₈ adduct.

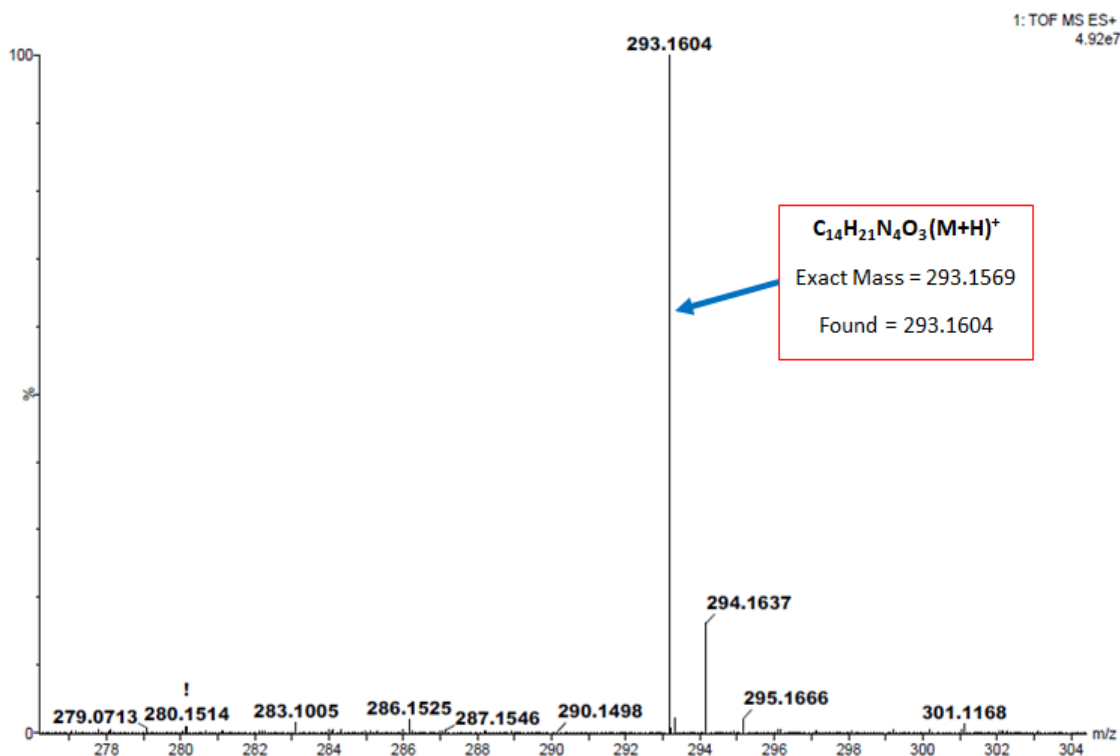


Figure 3.13. HRMS spectrum of compound NBD-C₈.

3.3.2. Fabrication of carboxylate modified polystyrene beads-gold nanorods (PS-GNR) conjugate

To form PS-GNR conjugate, carboxylate modified polystyrene beads having 2 μm mean particle diameter were procured from Sigma Aldrich and were used without further modifications. To fabricate the PS-GNR complex, 25 $\mu\text{l/ml}$ bead solution and 0.45 nM GNR solution were mixed and sonicated for 12 minutes. To confirm, thus formed conjugate was investigated using TEM, and obtained images are shown in Figure 3.14(A), and 3.14(B). Similarly, the PS_{amine}-GNR complex was formed using amine-modified polystyrene beads (with 2 μm diameter). PS_{amine}-GNR solution was then characterized using TEM as shown in Figure 3.14(C) and 3.14(D). The difference between the surface of PS-GNR and PS_{amine}-GNR clearly shows the binding of GNR with carboxylate modified polystyrene beads to form PS-GNR conjugate.

3.3.4. Optical tracking and MSD analysis

Sample preparation. For preparing samples, 20 μl of PS-GNR conjugate solution was taken into a vial, later 100 μm NBI was added and then the total volume was made up to 60 μl using

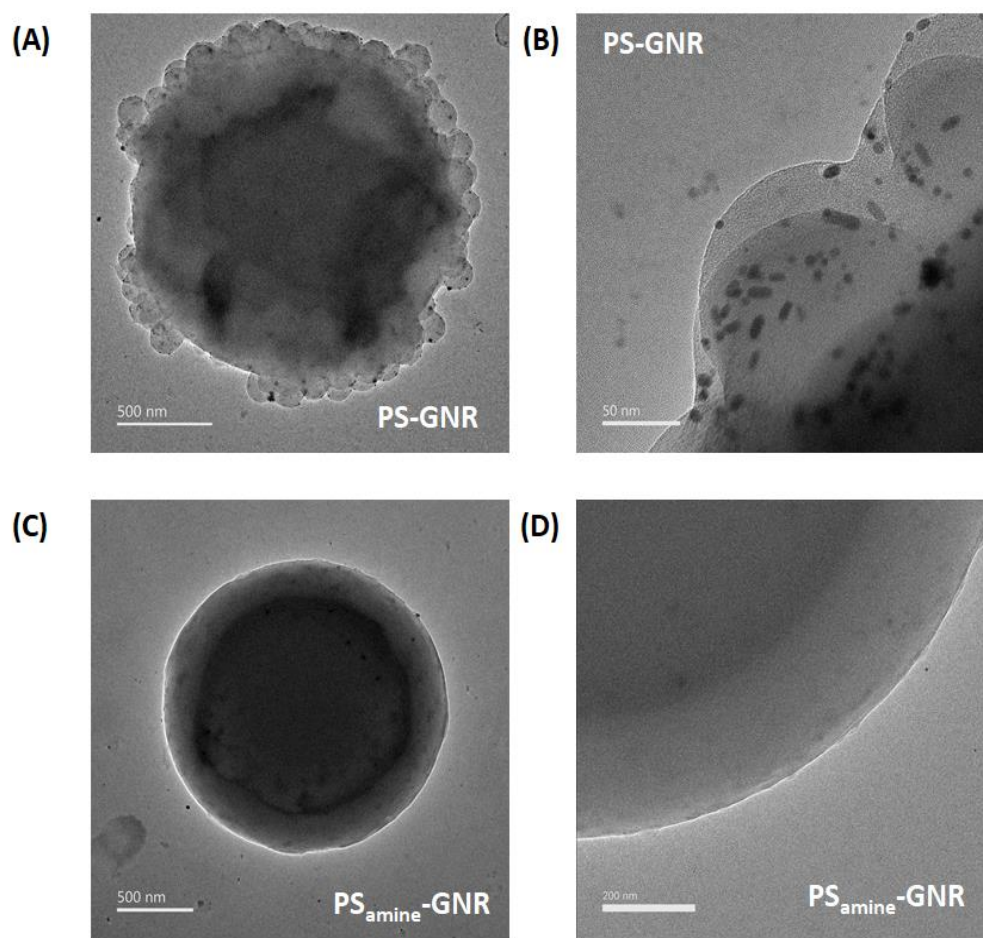


Figure 3.14. TEM images of PS-GNR conjugate with scale bar (a) 500 nm, (b) 50 nm, and TEM images of PS_{amine}-GNR solution (having amine-modified polystyrene beads (diameter = 2 μ m) + GNR solution) with scale bar (c) 500 nm (b) 200 nm, at 25 $^{\circ}$ C.

pH 8.0 phosphate buffer. While for control experiments, NBI was replaced with CNP and buffer, respectively. Thus, formed sample solutions were poured into a hybridization chamber (pasted on a glass slide) and sealed, a schematic representation of which is shown in Figure 3.24. The motion of the PS-GNR conjugate was recorded between 30 seconds to 2 minutes of time intervals after the addition of NBI or CNP. The motion of these micron-sized particles was recorded at the height of 200-250 μ m from the base of the hybridization chamber for 10 seconds at a rate of 10 frames per second by using Zeiss axio observer 7 microscopes with 100x objective and AxioCam 503 Mono 3 Megapixel camera. In all cases, at least 8 particles were recorded in each condition. Each recorded video was then analyzed using Tracker, a Video Analysis and Modeling Tool, which allowed the extraction of trajectories. Thus, extracted trajectories can be seen in Figure 3.24b. From these trajectories, MSD was calculated

by using a custom-made Python code and following equation (1) for two-dimensional analysis. (Figure 3.25)

$$MSD(\Delta t) = \langle \sum_i^n (x_i(t + \Delta t) - x_i(t))^2 \rangle \quad (3.1)$$

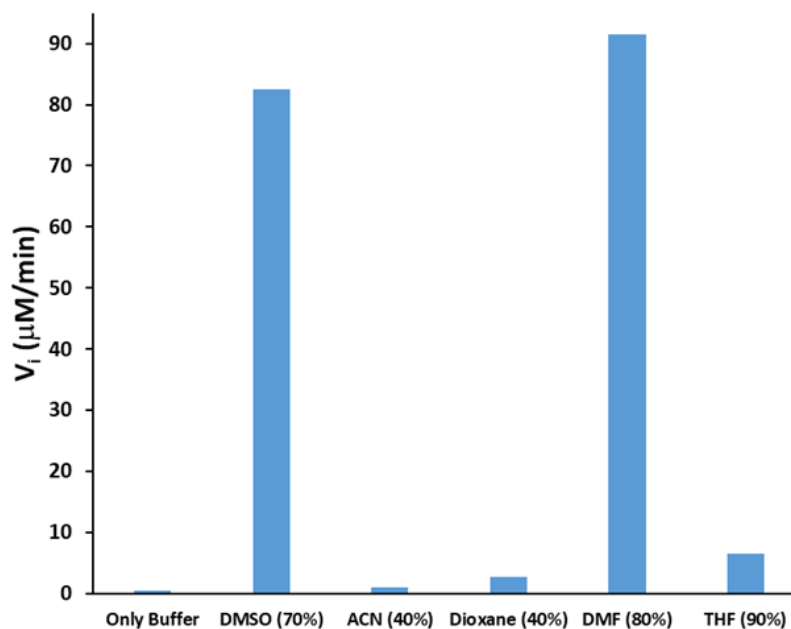
Where, t is the time, $x_i(t)$ is the position of the particle in the coordinate i at time t , $n = 2$ is the dimensions of MSD analysis, and $\langle . \rangle$ denotes ensemble and time average. The average MSD calculated as a function of the time interval for each case is shown in Figure 3.24. Interestingly, the mean MSD for PS-GNR conjugate with NBI is around 5 folds higher than with CNP or buffer. Furthermore, Linear MSD suggests Brownian motion among particles and can be understood from the equation $MSD(t) = at^\alpha$, curve fitting to suggest α close to 1 which again corresponds to the Brownian motion of micro-particles.⁴⁷⁻⁴⁸ Further, the diffusion coefficient was calculated by the slope of MSD curves using $MSD = 4D\Delta t$.⁴⁷⁻⁴⁸ (Figure 3.24)

3.4. Results and Discussion

Firstly, we synthesized the KE substrate, 5-nitrobenzisoazole (NBI), which was converted to 2-cyano-4-nitrophenol (CNP) under catalytic conditions. Product formation kinetics were monitored at 380 nm (Figure 3.9).³⁵ Initially, we have studied KE catalysis in the presence of both hydrophilic (solvents, salts, and buffers at different pH values) and hydrophobic (ranging from CTAB micelle to CTAB-capped gold nanoparticles (GNP), and gold nanorods (GNR)) environment. Generally, the presence of polar aprotic solvents, and basic salts, can increase catalytic efficiency by 2 to 4 orders of magnitude.³⁶ The initial rate of KE catalysis was examined for an increase in the percentage of different solvents [(Dimethyl Sulfoxide (DMSO), Acetonitrile (ACN), Dioxane, Dimethylformamide (DMF) and Tetrahydrofuran (THF)] in phosphate buffer (5mM, pH 8) (Figure 3.15). The percentage of each solvent was varied from 5% to 100%. The maximum rate was observed for DMSO (70%), ACN (40%), Dioxane (40%), DMF (80%), and THF (90%). Amongst them, maximum rates were observed for DMSO and DMF, with an enhancement of around 183-folds and 202-folds, respectively, in comparison with phosphate buffer. The effects of different salts, in 70% DMSO-H₂O, on the rate of KE catalysis were also studied.

Table 3.1. Molar extinction coefficient (at $\lambda = 380$ nm) of the product CNP

System	Molar Extinction Coefficient ($M^{-1}cm^{-1}$) (at 380 nm)
Phosphate Buffer (pH 6.0)	16000
Phosphate Buffer (pH 7.0)	16190
Phosphate Buffer (pH 8.0)	16500
70% DMSO + Phosphate Buffer (pH 8.0)	21390
80% DMF + Phosphate Buffer (pH 8.0)	16779
40% ACN + Phosphate Buffer (pH 8.0)	18579
40% Dioxane + Phosphate Buffer (pH 8.0)	16876
90% THF + Phosphate Buffer (pH 8.0)	14970

**Figure 3.15.** Initial rate of KE catalysis ($[NBI] = 100 \mu M$) in presence of different solvents in Phosphate Buffer (5mM, pH 8) at 25 °C.

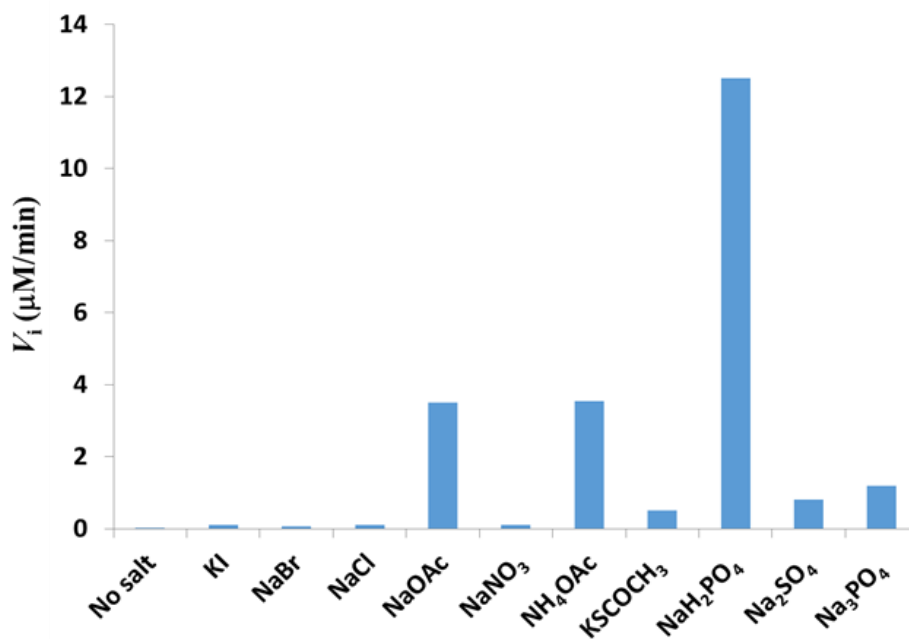


Figure 3.16. Initial rate of KE catalysis ($[\text{NBI}] = 100 \mu\text{M}$) in the presence of 15 mM concentration of different salts in 70% DMSO-water system at 25 °C.

Highest rates were observed for Acetates (OAc^-), thioacetate (AcS^-), phosphates ($\text{H}_2\text{PO}_4^{2-}$, PO_4^{3-}), and sulfate (SO_4^{2-}), with an enhancement of around 175-, 25-, 625-, 60- and 40-folds, respectively, in comparison with the rate in absence of any salt (Figure 3.16). However, maximal activity was observed for 70% DMSO- H_2O system and phosphates. (Figure 3.16)). The molar extinction coefficients used for different systems are given in Table 3.1. At nearly neutral pH (6 to 8), the KE reaction remains almost ineffective in aqueous media mainly because of the non-polarity of the substrate, NBI (Figure 3.17). However, the introduction of cationic micelle and vesicles in aqueous media can enhance the activity by 2-3 orders of magnitude due to – (i) enhanced solubility of substrate in the hydrophobic domain, (ii) higher concentration of reactive anionic base near the stern layer of the cationic micellar or vesicular system, and (iii) more than the 2-fold lower dielectric constant of micellar stern layer compared to bulk water.³⁸⁻³⁹ In fact, we also observed a similar scenario in a simple CTAB micellar system. While checking out the maximal observed activity, we increased the CTAB concentration while keeping the NBI concentration fixed at 100 μM . Here, we have observed the maximal activity at 8 mM CTAB (Figure 3.18). At higher CTAB concentrations unreactive bromide ion increases and thereby lead to a rate decrease as they replace reactive phosphate ions. Therefore, in the presence of CTAB micelles maximally an almost ~ 200 -fold enhanced activity was observed at 8 mM CTAB concentration (Figure 3.18)).

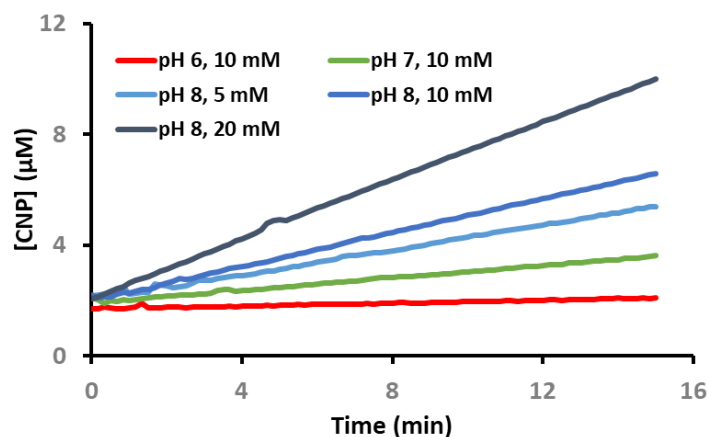


Figure 3.17. Amount of KE catalytic product formed as a function of time at pH 6.0 (10 mM Phosphate buffer), pH 7.0 (10 mM Phosphate buffer), and at pH 8.0 (5mM, 10 mM and 20 mM Phosphate buffer) at fixed [NBI] = 100 μ M, at 25 $^{\circ}$ C.

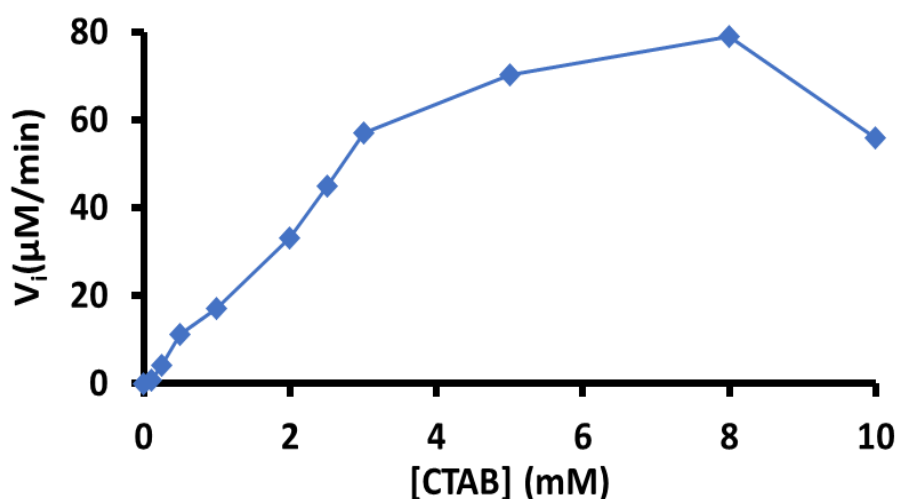


Figure 3.18. Initial rate of KE catalysis as a function of CTAB concentration at fixed [NBI] = 100 μ M in phosphate buffer (pH = 8, 5 mM) at 25 $^{\circ}$ C.

Encouraged by the above-mentioned facts and observations, we decided to utilize GNP (hydrodynamic diameter, $D_h = 25 \pm 2$ nm) and GNR with an aspect ratio of 2.5 ± 0.5 having a width of 6 ± 1 nm synthesized using reported protocols (Figure 3.2-3.4).⁴⁰⁻⁴¹ Highest initial rate (V_i) in KE catalysis was observed with GNR by almost 50, 200, and 500 -fold in pH = 6, 7, and 8, respectively while comparing with buffer only, at our experimental condition ([NBI] = 100 μ M, [GNR] = 0.15 nM ([Au] = 100 μ M), [Phosphate] = 10 mM) (Figure 3.19a+b, 3.20). Additionally, the observed activity in GNR is \sim 2-fold higher than CTAB micellar system and

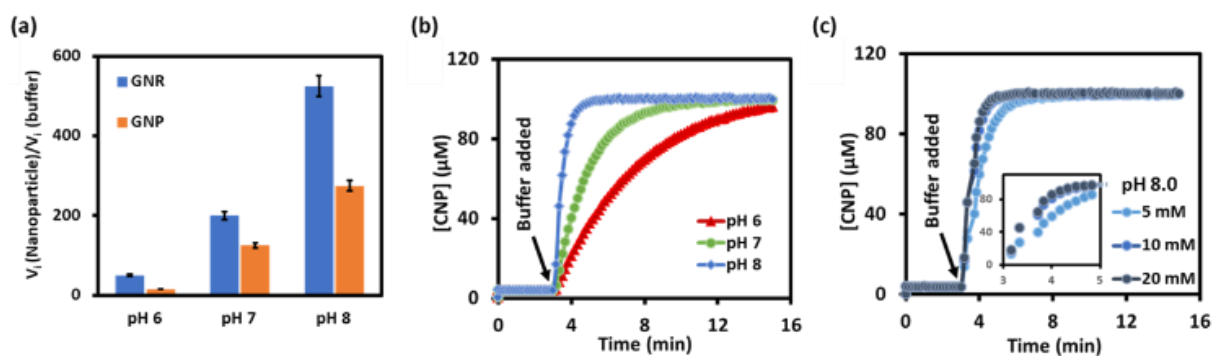


Figure 3.19. (a) Comparison of V_i (Nanoparticle)/ V_i (buffer) at pH 6, 7, and 8 for GNP and GNR. Amount of KE catalytic product formed as a function of time in GNR system at (b) pH 6 to 8, 10 mM phosphate buffer, and (c) 5, 10, and 20 mM of phosphate buffer at pH 8. Experimental condition: $[GNP] = 0.14$ nM ($[Au] = 100$ μ M), $[GNR] = 0.15$ nM ($[Au] = 100$ μ M), buffer = phosphate, $[NBI] = 100$ μ M, $T = 25$ $^{\circ}$ C.

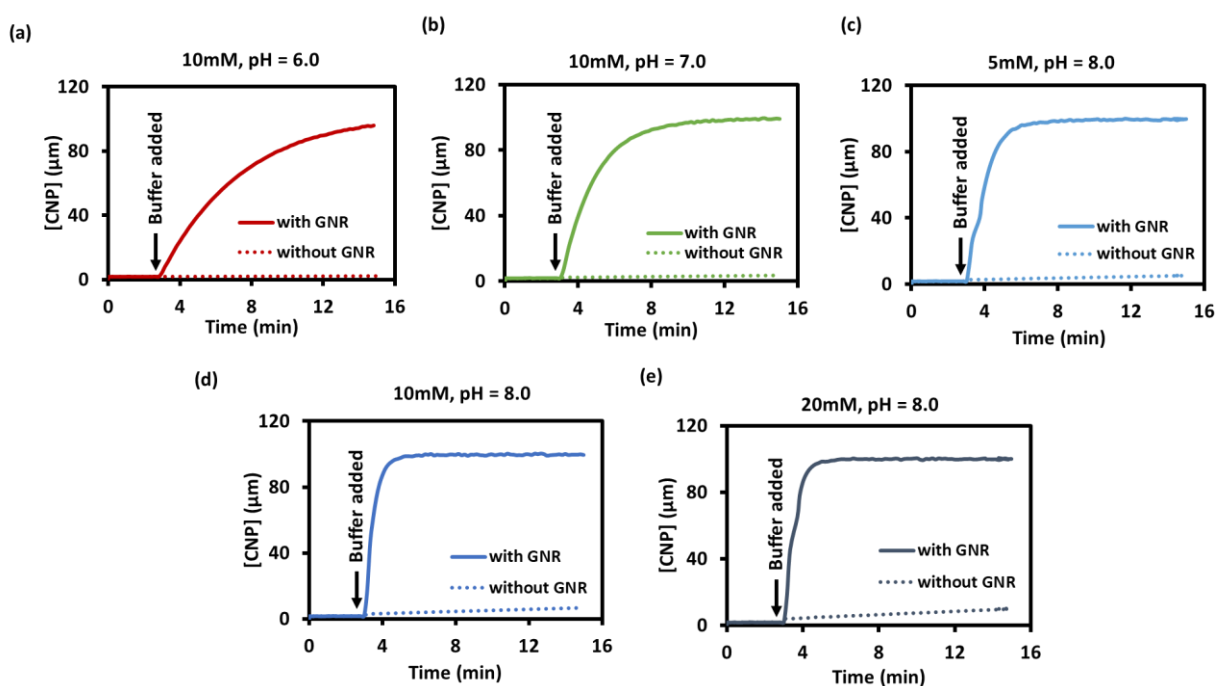


Figure 3.20. Product formation kinetics in absence and presence of GNR (0.15 nM, ($[Au] = 100$ μ M)), while adding (a) pH 6, 10 mM phosphate buffer, (b) pH 7, 10 mM phosphate buffer, (c) pH 8, 5 mM phosphate buffer, (d) pH 8, 10 mM phosphate buffer, and (e) pH 8, 20 mM phosphate buffer, after 3 minutes of additions of 100 μ M NBI at 25 $^{\circ}$ C.

GNP. Also, the activity was increased with an increase in the concentration of phosphate buffer from 5 – 20 mM, pH 8 with GNR at our experimental conditions (Figure 3.19c). The observed

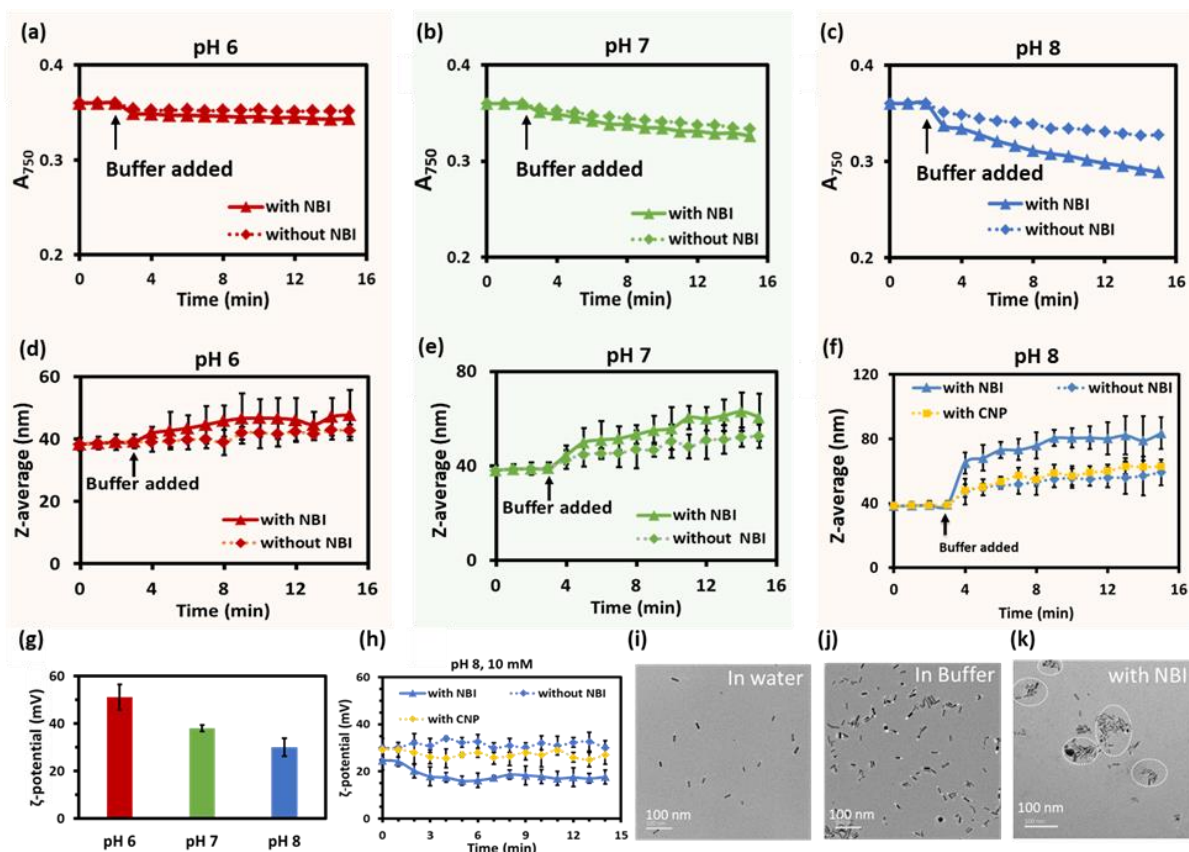


Figure 3.21. Change in A_{750} in the presence and absence of NBI at (a) pH 6, (b) pH 7, and (c) pH 8 with time. Change in hydrodynamic diameter in the absence and presence of NBI at (d) pH 6, (e) pH 7, and (f) pH 8 with time. (g) Zeta potential values of GNR system in the buffer from pH 6 to 8. (h) Change in zeta potential with time in the absence and presence of the reactant (NBI) and the product (CNP) at pH 8. TEM image of GNR (i) in water, (j) without NBI in pH 8, 10 mM phosphate buffer, (k) with NBI at pH 8, 10 mM phosphate buffer. The TEM samples were drop-casted in the TEM grid exactly after 2 minutes of the addition of buffer with or without NBI solution. Experimental condition: [GNR] = 0.15 nM ([Au] = 100 μ M), buffer = phosphate, [NBI] = 100 μ M, T = 25 $^{\circ}$ C.

higher activity in GNR is probably due to – (i) the presence of sharp edges which are known to show pronounced catalytic effects compared to isotropic ones,²¹ (ii) bilayer attachment of CTAB around the nanoparticle also provide added benefits as mentioned in preceding paragraph.⁴²⁻⁴⁴ Next, we performed time-dependent UV-Vis spectroscopic measurements to observe the change in the surface plasmon resonance pattern of GNR under catalytic conditions. For this purpose, we monitored absorbance at 750 nm (characteristic peak of GNR) during KE catalysis.⁴⁵ For this, we firstly added GNR (0.15 nM, [Au] = 100 μ M) and water mixture with and without NBI, then after 3 minutes phosphate buffer was added to the system and observed an instant decrease in absorbance value (Figure 3.21a-c). At pH 7, a slightly higher decrease in absorbance value was observed than at pH 6 in both presence and absence of NBI. While at pH 8, a decrease of 0.035 and 0.01 units in absorbance was observed

in the presence and absence of NBI, respectively, after only one minute of addition of buffer at our experimental condition. This difference in A750 increased during catalytic activity, suggesting the clustering of GNR over time. Again, we have observed a continuous decrease in A750 with an increase in buffer concentration from 5 mM to 20 mM (Figure 3.22). While maximum deviation in A750 from the initial value was observed for pH 8, 20 mM phosphate buffer at our experimental condition. Furthermore, we performed dynamic light scattering (DLS) experiments to find out the size of the particles present inside the system with respect to time. Here also, we observed an increase in the size of GNR in the presence of NBI with an increase in pH from 6 to 8. The observed z-average size of the GNR system, after one minute of buffer addition was 39 ± 2 nm, 43 ± 3 nm, and 48 ± 5 nm in the absence of NBI, which increased to 42 ± 4 , 45 ± 5 , and 65 ± 8 nm in presence of NBI at pH 6, pH 7, and pH 8 respectively at our experimental condition (Figure 3.21d-f). The difference between the average size of the GNR system in absence and presence of NBI increased with time at all pH values, with a maximal difference at pH 8 as the catalytic rate is highest in this case. In addition to this, we further observed an increase in average size with an increase in the concentration of phosphate buffer from 5 mM to 20 mM (data not shown). This corroboration of UV-Vis spectroscopic data and DLS measurements suggests the interconnectivity of catalytic activity and aggregation kinetics. This enhancement in size and KE catalysis in the GNR system can be clarified via zeta potential measurements.⁴⁶ Zeta potential of our reaction system ([GNR] = 0.15 nM, [Au] = 100 μ M) decreased from 51 ± 5 mV, 38 ± 1 mV, and 30 ± 3 mV, as we increased pH from 6, 7, and 8 respectively for 10 mM phosphate buffer (Figure 3.21g). The rate of decrease in zeta potential is significantly higher in the presence of NBI and during the period of catalytic conversion rather than in the product itself (Figure 3.21h). These outcomes made us postulate that the negatively charged transition state (TS) formed during KE catalysis resides on the nanorod surface and results in a decrease of GNR surface potential. This decrease in zeta potential value continued as we increased the strength of pH 8, phosphate buffer from 5 mM to 20 mM (data not shown). In addition to this, TEM (transmission electron microscopy) images also suggested the formation of a higher degree of self-assembled GNR upon the addition of NBI (Figure 3.21i-k). We have also studied the reusability of GNR for KE catalysis. For this purpose, we added NBI in batches of 50 μ M and looked at the changes in the size of the GNR system by using DLS measurements and product formation kinetics by using UV-Vis spectroscopy (Figure 3.23). The efficiency of KE catalysis in the repetitive cycle decreased after the addition of each batch, presumably because of the product inhibition effect. It suggests that the product also has affinity on the cationic GNR surface owing to its negative

charge along with the hydrophobic residue. Further, we did motion analysis by optical video recording and MSD (mean squared displacement) calculations to understand the catalytic effect in diffusion.⁴⁷⁻⁴⁸ For this, we have used a micro-sized replica of our system formed by using a carboxylate modified polystyrene bead ($d = 2 \mu\text{m}$)- GNR conjugate (PS-GNR) (Figure 3.14).

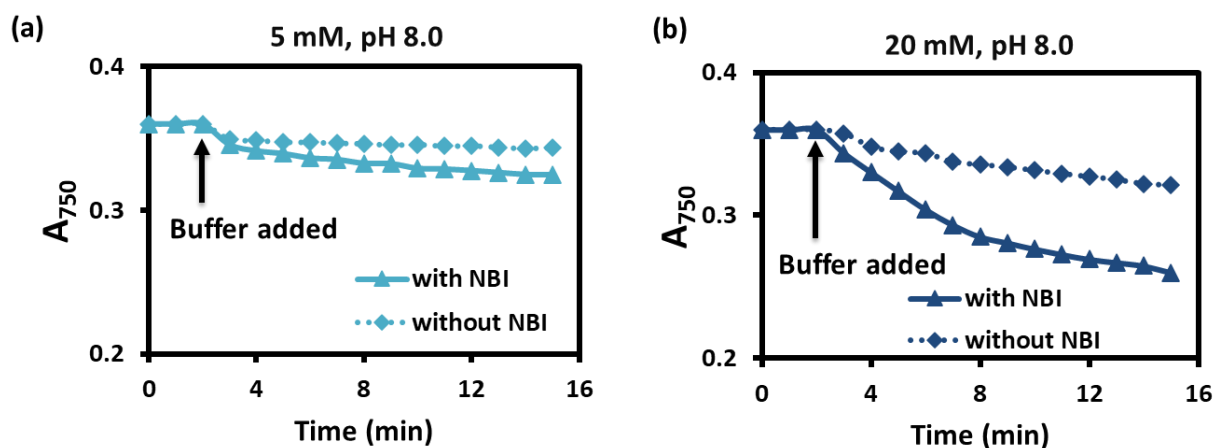


Figure 3.22. Decrease in absorbance at 750 nm of GNR (0.15 nM, [Au] = 100 μM) in the presence and absence of NBI over time at pH 8 (a) 5 mM phosphate buffer, and (b) 20 mM phosphate buffer at 25°C.

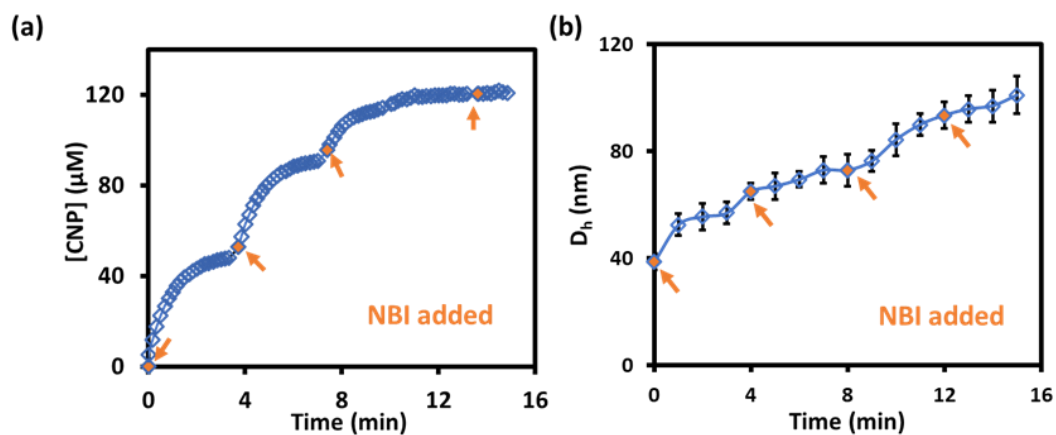


Figure 3.23. (a) Amount of product formation, and (b) Change in hydrodynamic diameter following four repetitive additions of NBI (50 μM) to a solution of GNR (0.15 nM, [Au] = 100 μM) in the presence of 10 mM phosphate at pH 8, at 25°C.

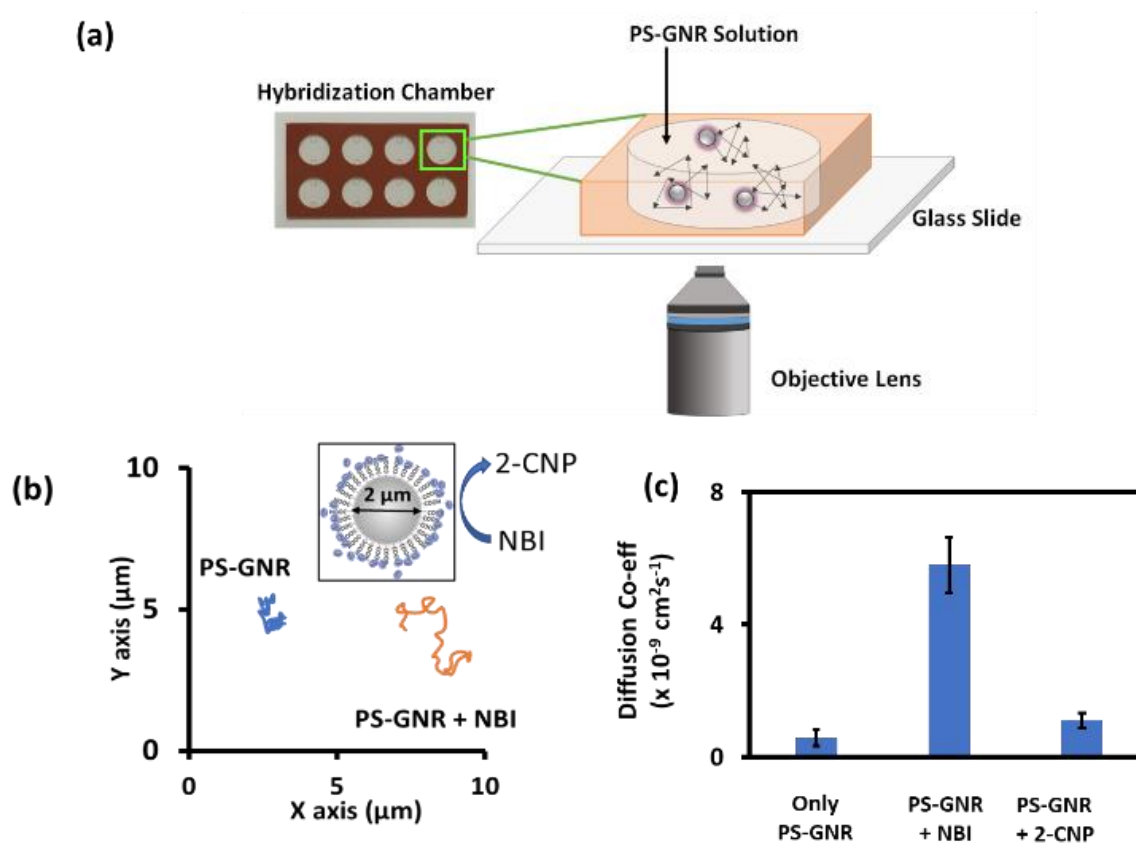


Figure 3.24. (a) Schematic representation of hybridization chamber (containing eight units in one strip) containing PS-GNR solution with microscope setup. The movement of the PS-GNR conjugate was observed under the optical microscope at a resolution of 100× and a scan rate of 10 frames/second. (b) The trajectory of PS-GNR conjugate in the absence and presence of NBI over 10 sec in the XY plane was observed under a microscope and analyzed using Tracker software. (b) Diffusion coefficient of PS-GNR conjugate in the absence and presence of NBI (100 μM) and the catalyzed product, CNP (100 μM) as obtained from the slope of the MSD curves using $MSD = 4D\Delta t$. CI = 95% with 8 PS-GNR conjugates from 4 sets of experiments.

In addition to this, we have checked if the replica made by us (PS-GNR conjugate) is the correct representation of our GNR system. For this purpose, we monitored the product formation kinetics of the same sample which has been used for optical tracking and MSD calculation using a UV-Vis spectrophotometer. So obtained plots for KE catalysis in the presence of PS-GNR conjugate and PS (polystyrene bead) only, can be seen in Figure 3.26, which suggests that PS-GNR conjugate has the same activity as that of GNR (can be compared with Figure 3.19) while the beads individually do not show any catalysis. Encouragingly, we have observed significantly enhanced diffusion (~5-7 fold) of GNR-bead conjugated particles in the presence of NBI in comparison with CNP and only buffer (Figure 3.24c+d, 3.25). It is noteworthy that a micron-sized bead which initially remained catalytically inactive can enhance the diffusion

of the whole conjugate, just by its surface functionalization with active nanometer-sized GNR (can be seen in the video). We were able to visualize the formation of dimer/trimer of microbeads coated with GNR under catalytic conditions (Figure 3.27). We presume that faster diffusion under catalytic conditions can play an additional role in higher assembly under catalytic conditions as mentioned in earlier literature reports.⁴⁴⁻⁴⁷

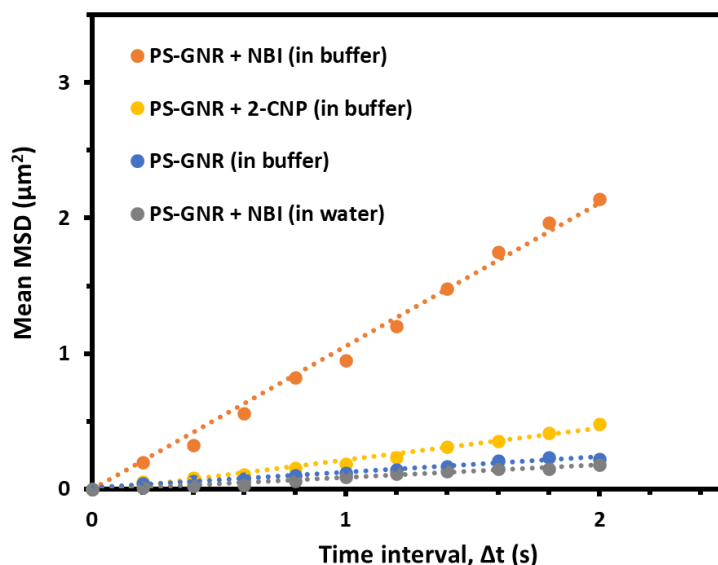


Figure 3.25. Plots showing the average of mean square displacement (MSD) of PS-GNR with 100 μM NBI, and 100 μM CNP in buffer, and in water, as a function of time interval. The motion of at least 8 PS-GNR conjugates from 4 sets of experiments was analyzed and averaged.

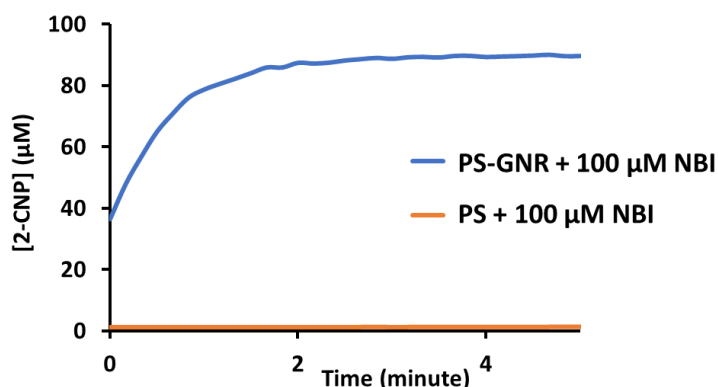


Figure 3.26. KE catalyzed product formation of 100 μM NBI in the presence of carboxylate modified polystyrene bead-GNR conjugate (PS-GNR, represented by blue curve) (experimental condition = 334 μl PS-GNR solution + 100 μM NBI + 10 mM phosphate buffer, pH 8.0 at 25°C) and carboxylate modified polystyrene beads only (PS, represented by orange curve) (8.5 μl PS solution + 100 μM NBI + 10 mM phosphate buffer, pH 8.0 at 25°C) (total volume = 1 ml, in cuvette).

Table 3.2: Average diffusion coefficient of PS-GNR conjugate in the presence of buffer with NBI (100 μM), CNP (100 μM), and in water with NBI (100 μM), obtained for 8 conjugates for 4 sets of experiments. Experimental Condition: [phosphate] = 10 mM, pH 8 at 25 $^{\circ}\text{C}$.

System	Experiment No.	Particle no.	Diffusion Coefficient (*10 ⁻⁹ cm ² s ⁻¹)	Average diffusion coefficient (*10 ⁻⁹ cm ² s ⁻¹)
PS-GNR + NBI (in 10 mM phosphate buffer)	1	1	6.7	5.7±0.7
		2	6.2	
	2	3	5.6	
		4	5.8	
	3	5	4.5	
		6	5.3	
	4	7	5.9	
		8	5.5	
PS-GNR + CNP (in 10 mM phosphate buffer)	1	1	1.2	1.1±0.2
		2	0.7	
	2	3	1.2	
		4	0.8	
	3	5	1.3	
		6	1.2	
	4	7	0.8	
		8	1.1	
PS-GNR (in 10 mM phosphate buffer)	1	1	0.6	0.5±0.1
		2	0.6	
	2	3	0.5	
		4	0.5	
	3	5	0.5	
		6	0.5	
	4	7	0.4	
		8	0.5	
PS-GNR + NBI (in water)	1	1	0.4	0.4±0.01
		2	0.4	
	2	3	0.4	

		4	0.4	
	3	5	0.3	
		6	0.5	
	4	7	0.5	
		8	0.4	

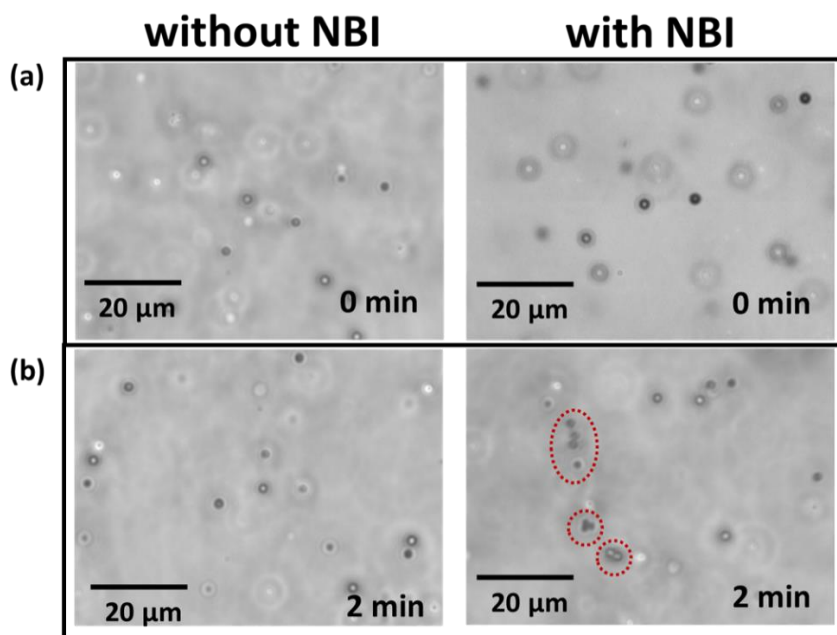


Fig 3.27. Microscopic image of PS-GNR conjugate in two different trials (a) before, (b) after 2 minutes of 100 μM NBI addition. Scale bar = 20 μm. (Images were taken from 200-250 μm height from the base of the hybridization chamber), at 25 °C.

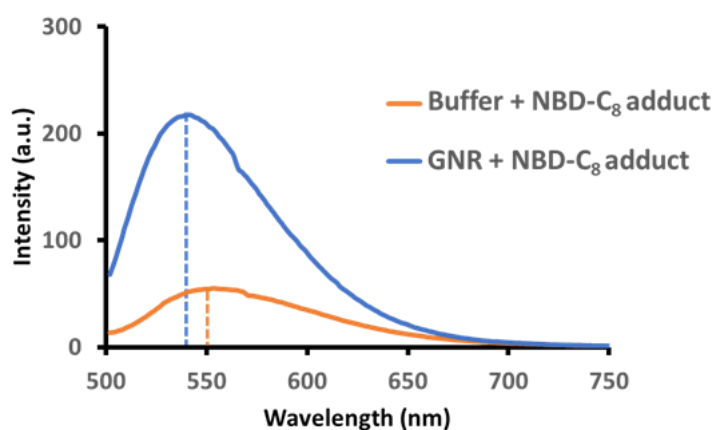


Figure 3.28. Emission spectra of NBD-C₈ adduct in the presence of 10 mM phosphate buffer ($\lambda_{\max} = 550$ nm), and the presence of GNR ($\lambda_{\max} = 535$ nm), at 25 °C.

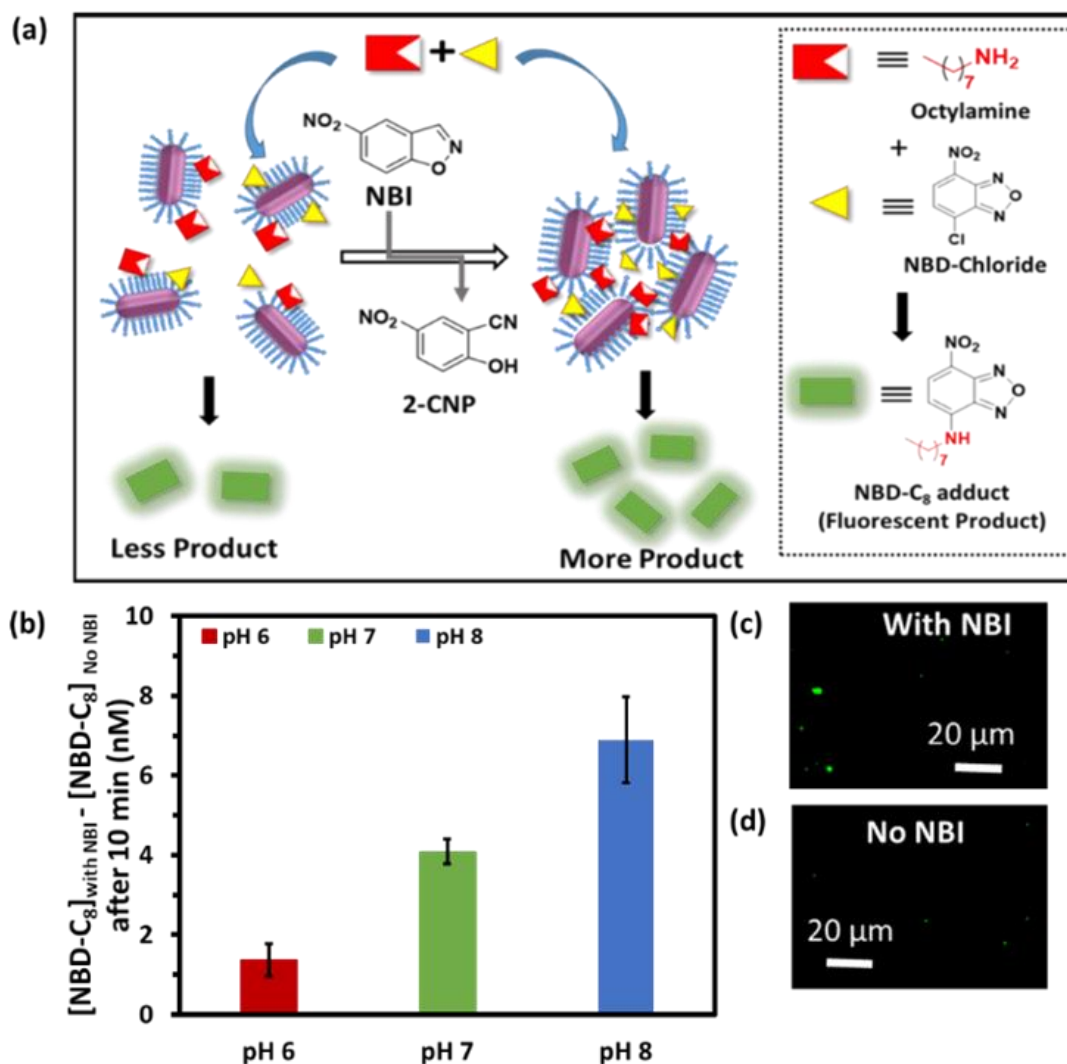


Figure 3.30. (a) Schematic representation of the aromatic nucleophilic substitution reaction to form a higher amount of fluorescent adduct (NBD-C₈) [excitation/emission maxima = 480/550 nm in buffer and 465/535 nm in GNR containing buffer] inside GNR cluster in the presence and absence of NBI. (b) NBD-C₈ formation in the absence and after 10 minutes of addition reaction of NBI (100 μM) in GNR system at pH 6, pH 7, and pH 8. Experimental condition: [NBI] = 100 μM , [GNR] = 0.15 nM ([Au] = 100 μM), [Phosphate] = 10 mM, T = 25 $^{\circ}\text{C}$. Fluorescent microscopic images of the reaction mixture in the presence of pH 8, 10 mM phosphate buffer, and (c) presence and (d) absence of NBI.

Finally, we were curious to explore if this self-assembly of GNR during KE catalysis can lead to the emergence of additional functionality not directly related to the KE catalysis. We argue that the hydrophobic cavities formed during the assembly formation of gold nanorods can be utilized as a nanoreactor where hydrophobic reactants can be trapped and made to react.²⁵⁻²⁶ To study this dual catalytic behavior of gold nanorods, we chose an aromatic nucleophilic substitution reaction between octyl amine and 4-Chloro-7-nitrobenzofurazan (NBD-chloride)

which form a fluorescent adduct (NBD-C₈), where reaction can be monitored easily by fluorescence techniques (Figure 3.28, 3.29). This reaction does not proceed in an aqueous buffer system, however, in the presence of GNR substantial reactivity was observed as the hydrophobic bilayer zone of CTAB on its surface helped the solubilization of the substrates. Interestingly, the presence of NBI (100 μM) leads to more NBD-C₈ formation where the clustering of GNR is more (Figure 3.30a+b). Fluorescence microscopic images also showed more and larger sized. fluorescent particles (NBD-C₈ adduct formed inside GNRs or in the cavity of its aggregates) in the presence of NBI (Figure 3.30c+d). Interestingly, here also, we have observed an increase in adduct formation with an increase in pH from 6 to 8. (Figure 3.32). Maximum NBD-C₈ adduct formation was observed for pH 8 in the presence of NBI, which again corroborates previous results of GNR aggregation. The formation of NBD-C₈ adduct in the presence of KE catalysis was also confirmed using mass spectrometry. For this purpose, the reaction mixture containing [GNR] = 0.15 nM ([Au] = 100 μM), [NBI] = 100 μM, [octylamine] = 1 μM, and [NBD-Cl] = 1 μM at pH 8.0 was prepared. In order to remove any metal impurities, the reaction mixture was filtered using an AMICON membrane filter with a 10 kDa cutoff. Thus, a filtered reaction mixture was observed using HRMS. The obtained spectrum confirmed the formation of the NBD-C₈ adduct with a characteristic peak at 293.1569 (Figure 3.31).

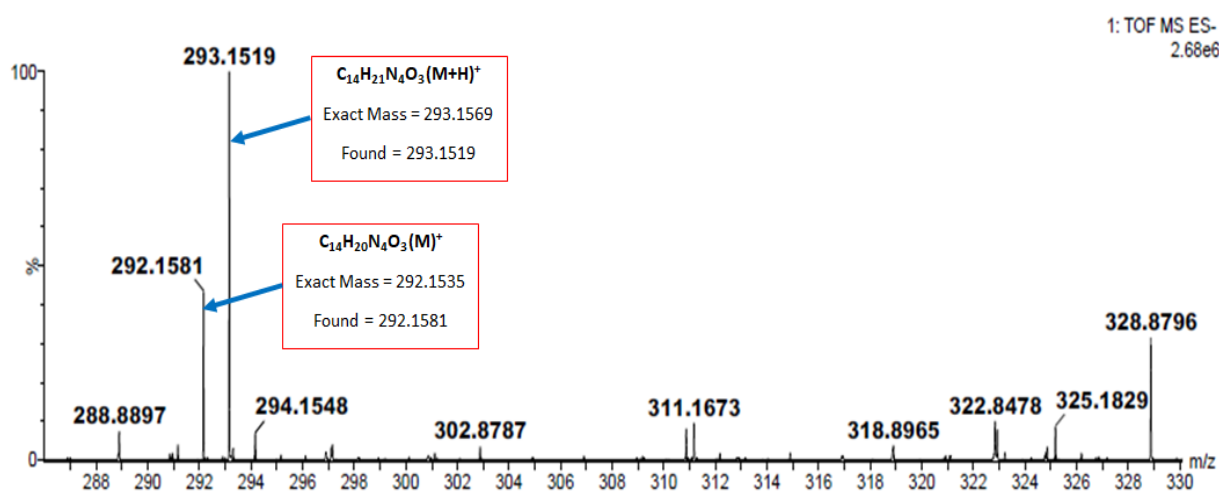


Figure 3.31. HRMS spectrum of the reaction mixture, confirming the formation of NBD-C₈ adduct. Experimental condition: [GNR] = 0.15 nM ([Au] = 100 μM), [NBI] = 100 μM, [octylamine] = 1 μM and [NBD-Cl] = 1 μM, [phosphate] = 10 mM at pH 8 and 25°C.

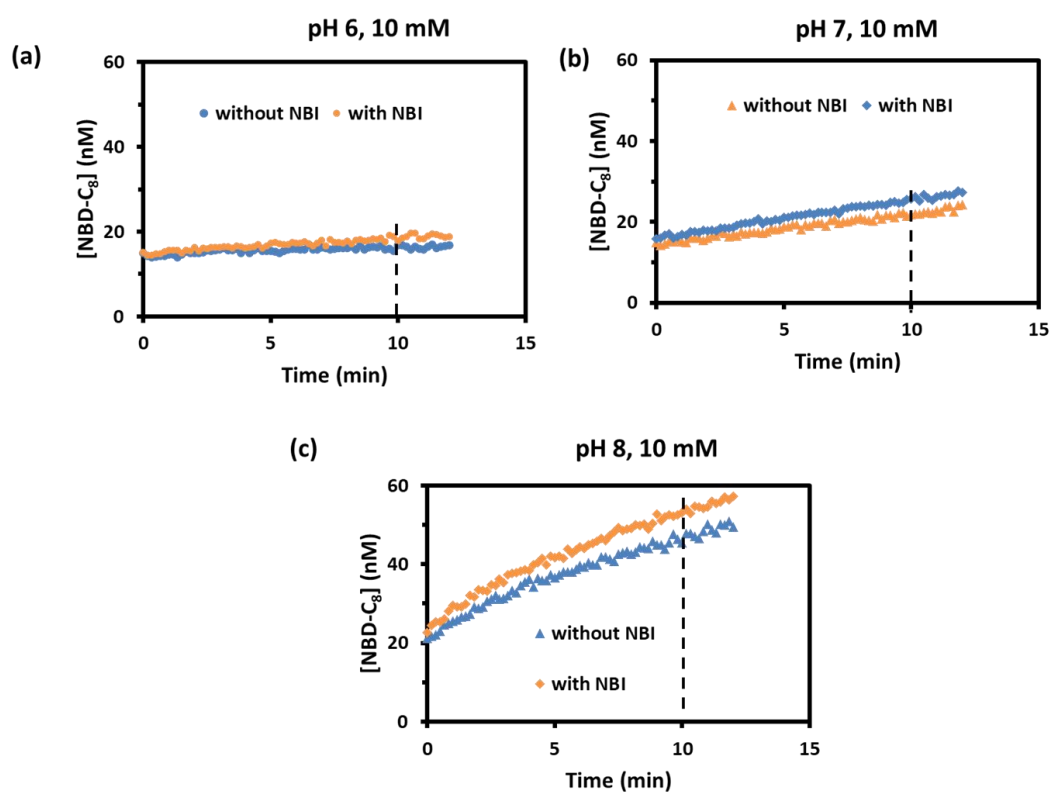


Figure 3.32. Amount of NBD-C₈ adduct formation in GNR system, in the presence and absence of NBI (100 μ M) system, monitored by fluorescence kinetics mode. Experimental condition: [GNR] = 0.15 nM ([Au] = 100 μ M), [octylamine] = 1 μ M, [NBD-Cl] = 1 μ M, and [phosphate] = 10 mM, pH = 6.0, 7.0 and 8.0 at 25°C.

3.5. Summary

In summary, we have shown that synthetic catalysts can show enhanced assembly which is driven by the formation of transition state during catalytic conversion. In KE catalysis, an uncharged reactant leads to anionic TS and thereby product on the cationic nanocatalyst (GNR) surface leading to a decrease in surface potential which results in loss of dispersibility of the colloidal system inducing the aggregation phenomenon. Notably, here neither substrate nor product plays any direct interactive role toward aggregation. Additionally, we have demonstrated a catalytic phenomenon occurring at the surfactant bilayer of the nanoparticle surface can lead to cascading of other reactions, absolutely unrelated to the original catalytic reaction (KE). We believe apart from unraveling the fundamental behavior of catalysts; these results can also potentially lead to the emergence of more life-like complex and dynamic chemical systems with unique multi-dimensional functionality as it showed a completely different approach to generate the assembly of a catalytic system that gets fueled during catalytic processes enabling new possibilities for next-generation dynamic materials.⁴⁸⁻⁵⁵

Overall, this study addresses the longstanding quest to understand the fundamental facts behind the dynamicity of catalytic processes. We report on the self-assembly of catalytically active gold nanorods, regulated by tuning their reactivity towards proton transfer reactions at different pH levels. Unlike substrate-induced templating and co-operativity, the enhanced aggregation rate is attributed to the alteration of catalytic surface charge only during reactivity. This research broadens our knowledge of catalytic behavior, introduces new insights into self-assembly phenomena, and showcases the potential of these systems in catalysis and beyond.

References

1. Sneyd, J.; Theraula, G.; Bonabeau, E.; Deneubourg, J.-L.; Franks, N. R. *Self-Organization in Biological Systems*; Princeton University Press, 2001.
2. Aubert, S.; Bezagu, M.; Spivey, A. C.; Arseniyadis, S. Spatial and Temporal Control of Chemical Processes. *Nat. Rev. Chem.* **2019**, *3* (12), 706–722.
3. Kroiss, D.; Ashkenasy, G.; Braunschweig, A. B.; Tuttle, T.; Ulijn, R. V. Catalyst: Can Systems Chemistry Unravel the Mysteries of the Chemical Origins of Life? *Chem* **2019**, *5* (8), 1917–1920.
4. Ye, R.; Hurlburt, T. J.; Sabyrov, K.; Alayoglu, S.; Somorjai, G. A. Molecular Catalysis Science: Perspective on Unifying the Fields of Catalysis. *Proc. Natl. Acad. Sci. U. S. A.* **2016**, *113* (19), 5159–5166.
5. Patiño, T.; Arqué, X.; Mestre, R.; Palacios, L.; Sánchez, S. Fundamental Aspects of Enzyme-Powered Micro- and Nanoswimmers. *Acc. Chem. Res.* **2018**, *51* (11), 2662–2671.
6. Altemose, A.; Harris, A. J.; Sen, A. Autonomous Formation and Annealing of Colloidal Crystals Induced by Light-powered Oscillations of Active Particles. *ChemSystemsChem* **2020**, *2* (1), e1900021.
7. Sánchez-Farrán, M. A.; Borhan, A.; Sen, A.; Crespi, V. H. Coupling between Colloidal Assemblies Can Drive a Bistable-to-oscillatory Transition. *ChemSystemsChem* **2020**, *2* (3), e1900036.
8. Wang, H.; Park, M.; Dong, R.; Kim, J.; Cho, Y.-K.; Tlusty, T.; Granick, S. Boosted Molecular Mobility during Common Chemical Reactions. *Science* **2020**, *369* (6503), 537–541.
9. Jee, A.-Y.; Cho, Y.-K.; Granick, S.; Tlusty, T. Catalytic Enzymes Are Active Matter. *Proc. Natl. Acad. Sci. U. S. A.* **2018**, *115* (46), E10812–E10821.
10. MacDonald, T. S. C.; Price, W. S.; Astumian, R. D.; Beves, J. E. Enhanced Diffusion of Molecular Catalysts Is Due to Convection. *Angew. Chem. Int. Ed.* **2019**, *58* (52), 18864–18867.
11. Muddana, H. S.; Sengupta, S.; Mallouk, T. E.; Sen, A.; Butler, P. J. Substrate Catalysis Enhances Single-Enzyme Diffusion. *J. Am. Chem. Soc.* **2010**, *132* (7), 2110–2111.

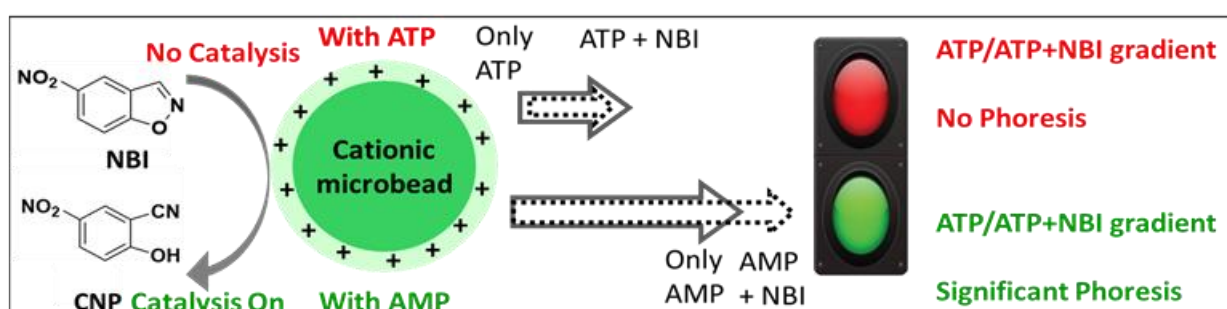
12. Weistuch, C.; Pressé, S. Spatiotemporal Organization of Catalysts Driven by Enhanced Diffusion. *J. Phys. Chem. B* **2018**, *122* (21), 5286–5290.
13. Zhang, Y.; Hess, H. Enhanced Diffusion of Catalytically Active Enzymes. *ACS Cent. Sci.* **2019**, *5* (6), 939–948
14. An, S.; Kumar, R.; Sheets, E. D.; Benkovic, S. J. Reversible Compartmentalization of de Novo Purine Biosynthetic Complexes in Living Cells. *Science* **2008**, *320* (5872), 103–106.
15. Møller, B. L. Plant Science. Dynamic Metabolons. *Science* **2010**, *330* (6009), 1328–1329.
16. Wang, W.; Duan, W.; Sen, A.; Mallouk, T. E. Catalytically Powered Dynamic Assembly of Rod-Shaped Nanomotors and Passive Tracer Particles. *Proc. Natl. Acad. Sci. U. S. A.* **2013**, *110* (44), 17744–17749.
17. Soto, R.; Golestanian, R. Self-Assembly of Active Colloidal Molecules with Dynamic Function. *Phys. Rev. E Stat. Nonlin. Soft Matter Phys.* **2015**, *91* (5), 052304.
18. Kokot, G.; Kolmakov, G. V.; Aranson, I. S.; Snezhko, A. Dynamic Self-Assembly and Self-Organized Transport of Magnetic Micro-Swimmers. *Sci. Rep.* **2017**, *7* (1), 14726.
19. Jewell, E. L.; Wang, W.; Mallouk, T. E. Catalytically Driven Assembly of Trisegmented Metallic Nanorods and Polystyrene Tracer Particles. *Soft Matter* **2016**, *12* (9), 2501–2504.
20. Zhao, X.; Palacci, H.; Yadav, V.; Spiering, M. M.; Gilson, M. K.; Butler, P. J.; Hess, H.; Benkovic, S. J.; Sen, A. Substrate-Driven Chemotactic Assembly in an Enzyme Cascade. *Nat. Chem.* **2018**, *10* (3), 311–317.
21. Maiti, S.; Fortunati, I.; Ferrante, C.; Scrimin, P.; Prins, L. J. Dissipative Self-Assembly of Vesicular Nanoreactors. *Nat. Chem.* **2016**, *8* (7), 725–731.
22. Mishra, A.; Korlepara, D. B.; Balasubramanian, S.; George, S. J. Bioinspired, ATP-Driven Co-Operative Supramolecular Polymerization and Its Pathway Dependence. *Chem. Commun.* **2020**, *56* (10), 1505–1508.
23. Jain, A.; Dhiman, S.; Dhayani, A.; Vemula, P. K.; George, S. J. Chemical Fuel-Driven Living and Transient Supramolecular Polymerization. *Nat. Commun.* **2019**, *10* (1), 450.
24. Deng, J.; Walther, A. ATP-Responsive and ATP-Fueled Self-Assembling Systems and Materials. *Adv. Mater.* **2020**, *32* (42), e2002629.
25. Sawczyk, M.; Klajn, R. Out-of-Equilibrium Aggregates and Coatings during Seeded Growth of Metallic Nanoparticles. *J. Am. Chem. Soc.* **2017**, *139* (49), 17973–17978.
26. Zhao, H.; Sen, S.; Udayabhaskararao, T.; Sawczyk, M.; Kučanda, K.; Manna, D.; Kundu, P. K.; Lee, J.-W.; Král, P.; Klajn, R. Reversible Trapping and Reaction Acceleration within Dynamically Self-Assembling Nanoflasks. *Nat. Nanotechnol.* **2016**, *11* (1), 82–88.

27. Chandrabhas, S.; Maiti, S.; Fortunati, I.; Ferrante, C.; Gabrielli, L.; Prins, L. J. Nucleotide-Selective Templated Self-Assembly of Nanoreactors under Dissipative Conditions. *Angew. Chem. Int. Ed.* **2020**, *59* (49), 22223–22229.
28. Grötsch, R. K.; Wanzke, C.; Speckbacher, M.; Angi, A.; Rieger, B.; Boekhoven, J. Pathway Dependence in the Fuel-Driven Dissipative Self-Assembly of Nanoparticles. *J. Am. Chem. Soc.* **2019**, *141* (25), 9872–9878.
29. Pezzato, C.; Cheng, C.; Stoddart, J. F.; Astumian, R. D. Mastering the Non-Equilibrium Assembly and Operation of Molecular Machines. *Chem. Soc. Rev.* **2017**, *46* (18), 5491–5507.
30. Ragazzon, G.; Prins, L. J. Energy Consumption in Chemical Fuel-Driven Self-Assembly. *Nat. Nanotechnol.* **2018**, *13* (10), 882–889.
31. Fanlo-Virgós, H.; Alba, A.-N. R.; Hamieh, S.; Colomb-Delsuc, M.; Otto, S. Transient Substrate-Induced Catalyst Formation in a Dynamic Molecular Network. *Angew. Chem. Int. Ed.* **2014**, *53* (42), 11346–11350.
32. Ni, J.; Liu, H.-Y.; Tao, F.; Wu, Y.-T.; Xu, P. Innenrücktitelbild: Remodeling of the Photosynthetic Chain Promotes Direct CO₂ Conversion into Valuable Aromatic Compounds *Angew. Chem. Weinheim Bergstr. Ger.* **2018**, *130* (49), 16469–16469.
33. Li, A.; Wang, B.; Ilie, A.; Dubey, K. D.; Bange, G.; Korendovych, I. V.; Shaik, S.; Reetz, M. T. A Redox-Mediated Kemp Eliminase. *Nat. Commun.* **2017**, *8* (1), 14876.
34. Hollfelder, F.; Kirby, A. J.; Tawfik, D. S.; Kikuchi, K.; Hilvert, D. Characterization of Proton-Transfer Catalysis by Serum Albumins. *J. Am. Chem. Soc.* **2000**, *122* (6), 1022–1029.
35. Rani, S.; Dasgupta, B.; Bhati, G. K.; Tomar, K.; Rakshit, S.; Maiti, S. Superior Proton-Transfer Catalytic Promiscuity of Cytochrome c in Self-Organized Media. *Chembiochem* **2021**, *22* (7), 1285–1291.
36. Casey, M. L.; Kemp, D. S.; Paul, K. G.; Cox, D. D. Physical Organic Chemistry of Benzisoxazoles. I. Mechanism of the Base-Catalyzed Decomposition of Benzisoxazoles. *J. Org. Chem.* **1973**, *38* (13), 2294–2301.
37. Privett, H. K.; Kiss, G.; Lee, T. M.; Blomberg, R.; Chica, R. A.; Thomas, L. M.; Hilvert, D.; Houk, K. N.; Mayo, S. L. Iterative Approach to Computational Enzyme Design. *Proc. Natl. Acad. Sci. U. S. A.* **2012**, *109* (10), 3790–3795.
38. Pérez-Juste, J.; Hollfelder, F.; Kirby, A. J.; Engberts, J. B. Vesicles Accelerate Proton Transfer from Carbon up to 850-Fold. *Org. Lett.* **2000**, *2* (2), 127–130.
39. Sanchez, E.; Lu, S.; Reed, C.; Schmidt, J.; Forconi, M. Kemp Elimination in Cationic Micelles: Designed Enzyme-like Rates Achieved through the Addition of Long-Chain Bases: Kemp Elimination in Cationic Micelles. *J. Phys. Org. Chem.* **2016**, *29* (4), 185–189.

40. Jana, N. R. Gram-Scale Synthesis of Soluble, near-Monodisperse Gold Nanorods and Other Anisotropic Nanoparticles. *Small* **2005**, *1* (8–9), 875–882.
41. Maiti, S.; Ghosh, M.; Das, P. K. Gold Nanorod in Reverse Micelles: A Fitting Fusion to Catapult Lipase Activity. *Chem. Commun.* **2011**, *47* (35), 9864–9866.
42. Mahmoud, M. A.; Narayanan, R.; El-Sayed, M. A. Enhancing Colloidal Metallic Nanocatalysis: Sharp Edges and Corners for Solid Nanoparticles and Cage Effect for Hollow Ones. *Acc. Chem. Res.* **2013**, *46* (8), 1795–1805.
43. Jiji, S. G.; Gopchandran, K. G. Shape Dependent Catalytic Activity of Unsupported Gold Nanostructures for the Fast Reduction of 4-Nitroaniline. *Colloids Interface Sci. Commun.* **2019**, *29*, 9–16.
44. Ni, B.; Wang, X. Face the Edges: Catalytic Active Sites of Nanomaterials. *Adv. Sci. (Weinh.)* **2015**, *2* (7), 1500085.
45. Kanjanawarut, R.; Yuan, B.; XiaoDi, S. UV-Vis Spectroscopy and Dynamic Light Scattering Study of Gold Nanorods Aggregation. *Nucleic Acid Ther.* **2013**, *23* (4), 273–280.
46. Hunter, R. J. *Zeta Potential in Colloid Science: Principles and Applications*; Academic Press: San Diego, CA, 2013.
47. Ma, X.; Jannasch, A.; Albrecht, U.-R.; Hahn, K.; Miguel-López, A.; Schäffer, E.; Sánchez, S. Enzyme-Powered Hollow Mesoporous Janus Nanomotors. *Nano Lett.* **2015**, *15* (10), 7043–7050.
48. Ghosh, S.; Mohajerani, F.; Son, S.; Velegol, D.; Butler, P. J.; Sen, A. Motility of Enzyme-Powered Vesicles. *Nano Lett.* **2019**, *19* (9), 6019–6026.
49. Mallory, S. A.; Valeriani, C.; Cacciuto, A. An Active Approach to Colloidal Self-Assembly. *Annu. Rev. Phys. Chem.* **2018**, *69*, 59–79.
50. Popescu, M. N. Chemically Active Particles: From One to Few on the Way to Many. *Langmuir* **2020**, *36* (25), 6861–6870.
51. Ottel , J.; Hussain, A. S.; Mayer, C.; Otto, S. Chance Emergence of Catalytic Activity and Promiscuity in a Self-Replicator. *Nat. Catal.* **2020**, *3* (7), 547–553.
52. Grzybowski, B. A.; Fitzner, K.; Paczesny, J.; Granick, S. From Dynamic Self-Assembly to Networked Chemical Systems. *Chem. Soc. Rev.* **2017**, *46* (18), 5647–5678.
53. Wanzke, C.; Jussupow, A.; Kohler, F.; Dietz, H.; Kaila, V. R. I.; Boekhoven, J. Dynamic Vesicles Formed by Dissipative Self-assembly. *ChemSystemsChem* **2020**, *2* (1), e1900044.
54. Merindol, R.; Walther, A. Materials Learning from Life: Concepts for Active, Adaptive and Autonomous Molecular Systems. *Chem. Soc. Rev.* **2017**, *46* (18), 5588–5619.
55. Shandilya, E.; Maiti, S. Deconvolution of Transient Species in a Multivalent Fuel-driven Multistep Assembly under Dissipative Conditions. *ChemSystemsChem* **2020**, *2* (2), e1900040.

CHAPTER 4

Spatiotemporal Mapping of Colloidal Phoresis and Population Dynamics during Downregulation of Multivalent Interactivity



This is adapted reproduction from Shandilya, E.; Rallabandi, B.; Maiti, S. Spatiotemporally Tuned Colloidal Phoretic Leap in an Altering Multivalent Interaction Field. *ChemRxiv*, 2023. DOI -10.26434/chemrxiv-2023-r1djt.

4.1. Introduction

The investigation of multivalent interactions and their impact on supramolecular processes has garnered considerable attention in both biological and synthetic systems.¹⁻³ Over the past two decades, pioneering work has provided valuable insights into the role of weak and cooperative binding, which plays a crucial role in establishing strong and specific affinity between entities, particularly on surfaces.⁴⁻⁷ These interactions have found diverse applications in fields such as sensing, catalysis, and drug design. By harnessing these interactions, viral infections can be inhibited, and biochemical pathways can be manipulated to achieve desired cellular responses.⁸⁻¹⁰ Building blocks like peptides, proteins, carbohydrates, nucleotides, and self-assembled monolayers, have been extensively studied in the context of multivalent interactions.¹¹⁻¹⁹ They serve as essential components for understanding binding mechanisms, assembly processes, sensing capabilities, and catalytic functions. The ability to regulate and control these interactions has facilitated the development of time-regulated dynamic self-assembled systems. In such systems, the interplay between multivalent chemical stimuli and building blocks can be precisely adjusted, allowing for simultaneous temporal control over associated functions.²⁰⁻²⁵ Despite the significant progress made in this field, there are still substantial gaps in our understanding of the spatial and temporal aspects of multivalent interactions and their influence on the motion, spatial distribution, and related functions of interacting species. These gaps present intriguing opportunities for further exploration and research. The recent study by Wilson et al. on the diffusiophoretic motion of anionic microbeads in response to gradients of divalent cations or anions is a step toward unraveling the complexities of multivalent interactions.²⁶ Nevertheless, the investigation of how multivalent interactions, in conjunction with their in-situ modulation, govern the diffusiophoresis of surface-interactive colloids in both spatial and temporal dimensions remain largely unexplored.²⁶⁻²⁷ The work of Derjaguin, followed by that of Anderson et al., established the physicochemical origin of diffusiophoretic transport of colloids in the gradient of salts.²⁸⁻³⁵ Past studies have been limited to common inorganic salts like NaCl, KCl, MgCl₂, etc., featuring mainly halides, nitrates, sulfates, and carbonates of group-I and II metal ions of the periodic table.²⁴⁻⁴⁰

Motivated by these gaps in knowledge, our study aims to investigate the role of multivalent interactions and their spatiotemporal control in governing diffusiophoresis, using biologically essential molecules as the driving force. By shifting the focus from common inorganic salts to gradients of nucleotides, such as adenosine mono/di/triphosphate (AMP/ADP/ATP), and their

mixtures, we seek to understand how these molecular gradients impact the phoretic drift of a fluorescent, cationic micron-sized bead.⁴¹ Notably, in cellular systems, diffusiophoretic transport of large molecules due to gradients of small molecules such as metabolites or ATP is ubiquitous and has recently gained attention.⁴²⁻⁴³ Additionally, we explore the catalytic activation behavior exhibited by nucleotides, analogous to the allosteric modulation observed in enzymes, and its influence on the overall phoretic drift of the bead under both catalytic and non-catalytic conditions.⁴⁴⁻⁴⁶ The findings from this study hold significant potential in advancing our understanding of multivalent interactions and their role in diffusiophoresis, as well as opening doors for the development of autonomous systems with spatiotemporal programming capabilities. By harnessing enzymatic in-situ downregulation of multivalent interactions, we aim to demonstrate the occurrence of colloidal phoretic leaps and showcase how particles can be precisely positioned and catalytic processes can be controlled in a programmable manner.

4.2. Materials

All commercially available reagents were used as received without any further purification. Cetyltrimethylammonium bromide, silver nitrate, sodium borohydride, ascorbic acid, malachite green, hydrochloric acid, calcium nitrate, and ammonium molybdate were procured from Sisco Research Laboratory (SRL), India. Gold (III) chloride trihydrate, adenosine triphosphate sodium salt (ATP), adenosine diphosphate (ADP) sodium salt, adenosine monophosphate (AMP) sodium salt, Potato Apyrase (PA), and carboxylate functionalized polystyrene beads were purchased from Sigma-Aldrich. Throughout the study, we have used milli-Q water. UV-Vis studies were performed using Varian Cary 60 (Agilent Technologies) spectrophotometer. The total reaction volume in the cuvette was fixed at 1 mL and a cuvette of path length 1 cm was used for the entire study. The fluorescence images of the microfluidic channel were collected using Zeiss Axis Observer 7 microscope with AxioCam 503 Mono 3 Megapixel with ZEN 2 software. The Transmission Electron Microscopy images were taken using the JEOL JEM-F200 microscope. The Dynamic Light Scattering (DLS) and zeta potential data were recorded on Horiba Scientific Nano Particle Observer (SZ-100V2). The 2-inlet-1-outlet microfluidic chip (1.7 cm length x 600 μm width x 100 μm height) was procured from Vena Delta. A demountable quartz cuvette having dimensions 40 \times 10 \times 0.05 mm³ (length \times width \times height) was procured from Lark Scientific.

4.3. Methods

4.3.1. Synthesis and Characterization of gold nanorods (GNR)

Gold nanorods were synthesized following a procedure described in the literature.⁴¹ Initially, a 5 mL solution containing 0.1 M cetyltrimethylammonium bromide (CTAB) and 1 mM HAuCl₄ was prepared in milli-Q water, resulting in a golden-colored solution. To this solution, ascorbic acid was added, causing the solution to become colorless. Subsequently, AgNO₃ was introduced with final concentrations of 2 mM for ascorbic acid and 0.15 mM for AgNO₃. Finally, a fresh solution of 1 mM NaBH₄ was prepared and 50 μ L of this solution was added, leading to a violet coloration over time. The appearance of the violet color confirmed the successful formation of gold nanorods. To remove unbound CTAB and other impurities, GNR solution was first filtered before using further. For this purpose, a Sephadex G-25 filter was used. Before use, the column was first equilibrated with an ample amount of water. For initial confirmation, thus formed gold nanorods were characterized using UV-Vis spectrophotometer. The obtained spectrum showed a characteristic peak at 750 nm and 523 nm, which confirmed the formation of gold nanorods.

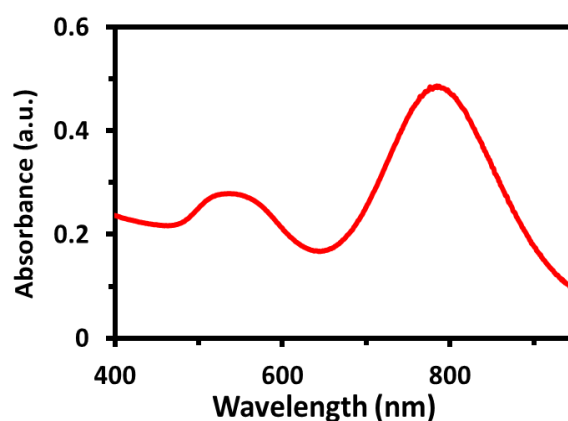


Figure 4.1. UV spectrum of GNR in water.

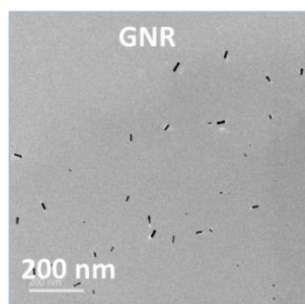


Figure 4.2. TEM image of GNR in water. Experimental condition: [GNR] = 150 pM in water at 25 °C.

4.3.2. Fabrication of Bead-GNR (CMB) conjugate

To prepare the Bead-GNR (CMB) conjugate, carboxylate-modified polystyrene beads with a mean particle diameter of 1 μm were obtained from Sigma Aldrich and used as received without any additional modifications. For the fabrication of the Bead-GNR complex, 4 μL (0.1 mg) of carboxylate-modified polystyrene beads ($d = 1 \mu\text{m}$) were dispersed in 896 μl of water, followed by the addition of 100 μL of gold nanorods at a concentration of approximately 150 pM. The mixture was sonicated for 15 minutes to ensure proper mixing. To remove any unbound gold nanorods, the solution containing the Bead-GNR conjugate was centrifuged at 6000 rpm for 3 minutes, allowing the conjugate to settle at the bottom. The settled conjugate was then collected and redispersed in water for further use. To confirm the formation of the conjugate, transmission electron microscopy (TEM) was employed for investigation. The zeta potential of the synthesized Bead-GNR conjugate, measured in water, was determined to be approximately $80 \pm 5 \text{ mV}$.

4.3.3. Activity of CMB over NBI

NBI (5-nitrobenzisoxazole) and CNP (2-cyano nitrophenol) were synthesized by following previously reported protocols.⁴¹ The activity of the above formed CMB complex was checked for NBI. For sample preparation, the above formed CMB complex was treated with NBI (100 μM) in the presence of both nucleotides and a mixture of nucleotides (whenever mentioned). The amount of CNP ($\epsilon_{380 \text{ nm}} = 8000 \text{ M}^{-1}\text{cm}^{-1}$) formation was quantified by measuring absorbance at 380 nm over time using a UV-vis spectrophotometer. The 10 mM stock solution of NBI and CNP were prepared in acetonitrile (ACN), and dimethyl sulfoxide (DMSO), respectively.

4.3.4. Stability of GNR in the presence of ATP

To ensure the stability of the Bead-GNR conjugate in the presence of ATP, 1 mM ATP was added to a 1.5 ml vial containing CMB. This sample was centrifuged for 5 minutes at 6500 rpm so that all the beads settled at the bottom. UV-vis scan of the supernatant showed the absence of GNR (Figure 4.8).

4.3.5. Microfluidic experiment and calculation of drift

For this purpose, we used a microfluidic experiment with a two-inlet and one-outlet channel with dimensions of $17 \times 0.6 \times 0.1 \text{ mm}^3$ (length \times width \times height) and injected fluorescent CMB solution from one inlet and nucleotide (AMP (1 mM) or ATP (1 mM) or χ_{ATP} at 0.01, 0.1, 0.25, 0.5, 0.75) from the other, each at a flow rate of $Q/2 = 0.16 \text{ ml/h}$, and observed the transverse drift of the CMB near the end of the channel (16 mm from the inlets merging) under a fluorescence microscope by scanning the zonal intensity (Figure 4.11a). The intensity was normalized with respect to its integral across the channel, which is a measure of the number of particles per area and is a conserved quantity at a steady state. The diffusiophoretic drift due to the presence of nucleotides was calculated by comparing the location where the normalized intensity is 0.1 (near the baseline) with that of the no-nucleotide condition i.e., only in the presence of milli-Q water. Similarly, during catalytic conditions, we passed the substrate, NBI (1 mM) with nucleotide AMP (1 mM) or ATP (1 mM) or χ_{ATP} at 0.25, 0.5, 0.75 from one channel, and the beads through the other (Figure 4.15a). We then measured the drift of CMB near the end of the channel ($x = 1.6 \text{ cm}$) under a fluorescent microscope.

4.3.6. Population dynamics study inside macroscale setup

Our macroscale experimental setup is shown in Figure 4.16a. Here, we added a $50 \mu\text{l}$ of either ATP or AMP or AMP + NBI through one arm and filled the chamber having dimensions $40 \times 10 \times 0.05 \text{ mm}^3$ (length \times width \times height). The concentrations of nucleotides were maintained at 1 mM as in the microfluidic study. Next, we added $5 \mu\text{l}$ of the CMB (0.025 mg/ml bead, 5 times more dilute than the concentration used in the microfluidic study) and followed the particle motion inside the chamber using the microscope. We followed the population dynamics at four zones, namely frames A, B, C, and D, each having length of 1.5 mm. Also, during the enzymatic reaction, the macroscale channel was filled with nucleotide solution with or without PA and NBI through one arm and CMB was added from another. And the population of CMB was monitored inside the channel using a fluorescence microscope.

4.3.7. Enzymatic activity

To estimate the amount of ATP cleaved during potato apyrase (PA) activity malachite green assay was used.⁵² Firstly, phosphate calibration was made using this assay (Figure 4.3). Then, ATP (0 - 100 μM) was incubated with 100 nM PA along with 0.25 mM Ca^{2+} , and the amount of phosphate formed was measured at different time points. After that, the initial activity rate for each set was plotted against ATP concentration and curve fitted into Michaelis–Menten

kinetics graph (Figure 4.4). Thus, obtained V_{max} , K_m values were 0.15 s^{-1} , $13.13 \text{ }\mu\text{M}$, respectively.

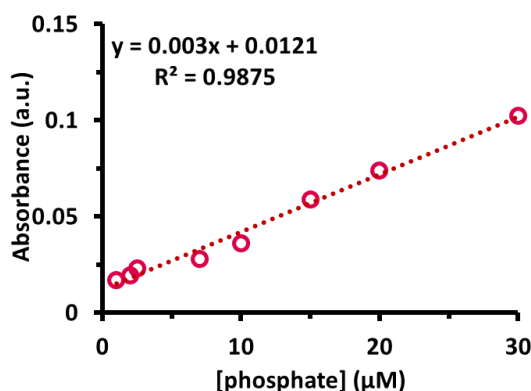


Figure 4.3. Phosphate calibration curve using Malachite green assay.

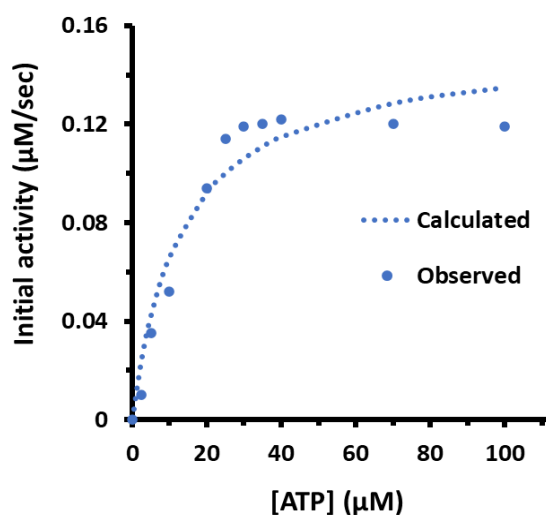


Figure 4.4. Initial activity measured for phosphate formation plotted against the amount of ATP. The Blue dotted line denotes Michaelis–Menten plot fitting. The obtained V_{max} and K_m values were 0.15 s^{-1} , and $13.13 \text{ }\mu\text{M}$, respectively.

4.4. Results and Discussion

We prepared a catalytically active CMB according to the procedure described in the literature (details in the method section).⁴¹ The carboxylate-functionalized polystyrene beads had a hydrodynamic diameter (D_h) of $1 \text{ }\mu\text{m}$ and a zeta potential of $-90 \pm 5 \text{ mV}$. Upon conjugation with cationic gold nanorods (GNR) (length: $23 \pm 5 \text{ nm}$, width: $6 \pm 1 \text{ nm}$, and $\zeta = 100 \pm 10 \text{ mV}$), the overall zeta potential of the fluorescent CMB changed to $+80 \text{ mV}$, indicating successful binding and reversal of the surface charge of the CMB (Figure 4.1, 4.2, 4.5b-c). Previous studies have demonstrated the catalytic efficiency of this type of CMB in facilitating the proton transfer reaction known as Kemp elimination (KE) in the presence of phosphate buffer.^{41,45}

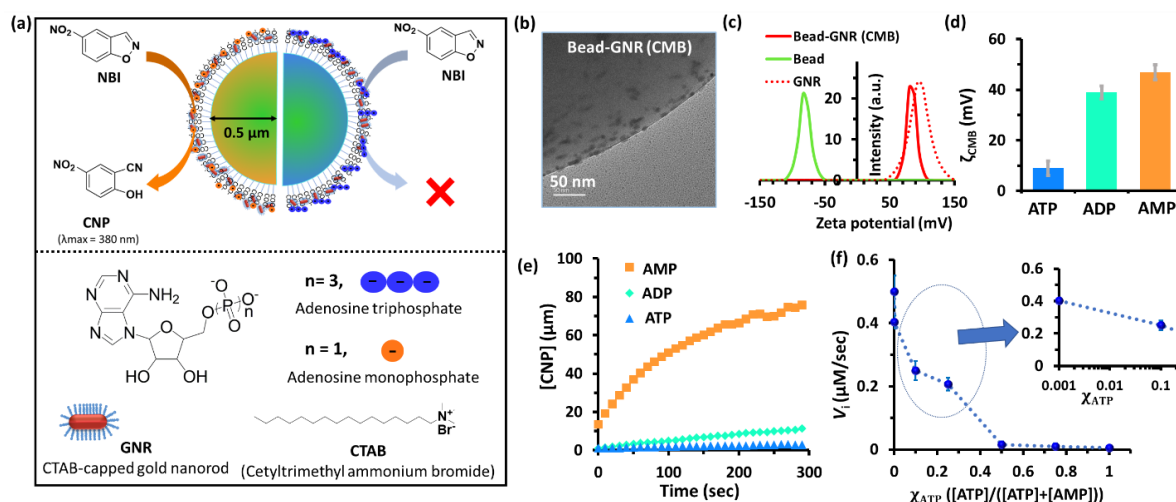


Figure 4.5. Characterization, nucleotide binding ability, and reactivity of the colloid. (a) Schematic representation of a carboxylate-functionalized polystyrene bead modified with gold nanorods (CMB) catalyzing the Kemp elimination reaction, (b) TEM image of CMB conjugate showing GNR-bound bead surface. (c) Zeta potential profile of CMB, only beads, and GNR in water at 25 °C. (d) Zeta potential of CMB in the presence of adenosine-based nucleotides (1 mM). (e) The amount of Kemp elimination product (CNP) formed after the addition of different nucleotides (1 mM) as a function of time. (f) Initial rate of CNP formation in the presence of different fractions of ATP in a mixture of ATP and AMP.

However, carboxylate beads without nanoparticles did not exhibit any activity (Figure 4.10). In a separate study, we showed that the KE catalysis over a cationic gold nanoparticle surface can be controlled by modulating its multivalent interaction with AMP, ADP, and ATP.⁴⁵ Before quantifying the impact of adenosine-based nucleotides on the CMB's ability to catalyze KE, we first examined the binding ability of these nucleotides on the surface of the CMB. As expected, in the presence of nucleotides at a concentration of 1 mM, the zeta potential of the CMB decreased to 47 ± 8 mV, 39 ± 5 mV, and 9 ± 4 mV with AMP, ADP, and ATP, respectively, indicating surface binding (Figure 4.5d, 4.6). Across a range of concentrations between 0.01 and 10 mM of nucleotides, the difference in the zeta potential of CMB in the presence of ATP and AMP is highest at 1 mM concentration (Figure 4.7). At 10 mM ATP, we observed lower stability of CMB as the zeta potential reaches only 3 ± 2 mV. Therefore, we used 1 mM concentration of nucleotides throughout, unless noted otherwise. Of all the nucleotides, ATP binds most strongly due to the simultaneous interaction of three phosphate groups with GNR placed on the CMB surface.¹³⁻¹⁴ The binding of ATP at a concentration of 1 mM did not affect the stability of the CMB, as no detachment of the GNR from the bead was

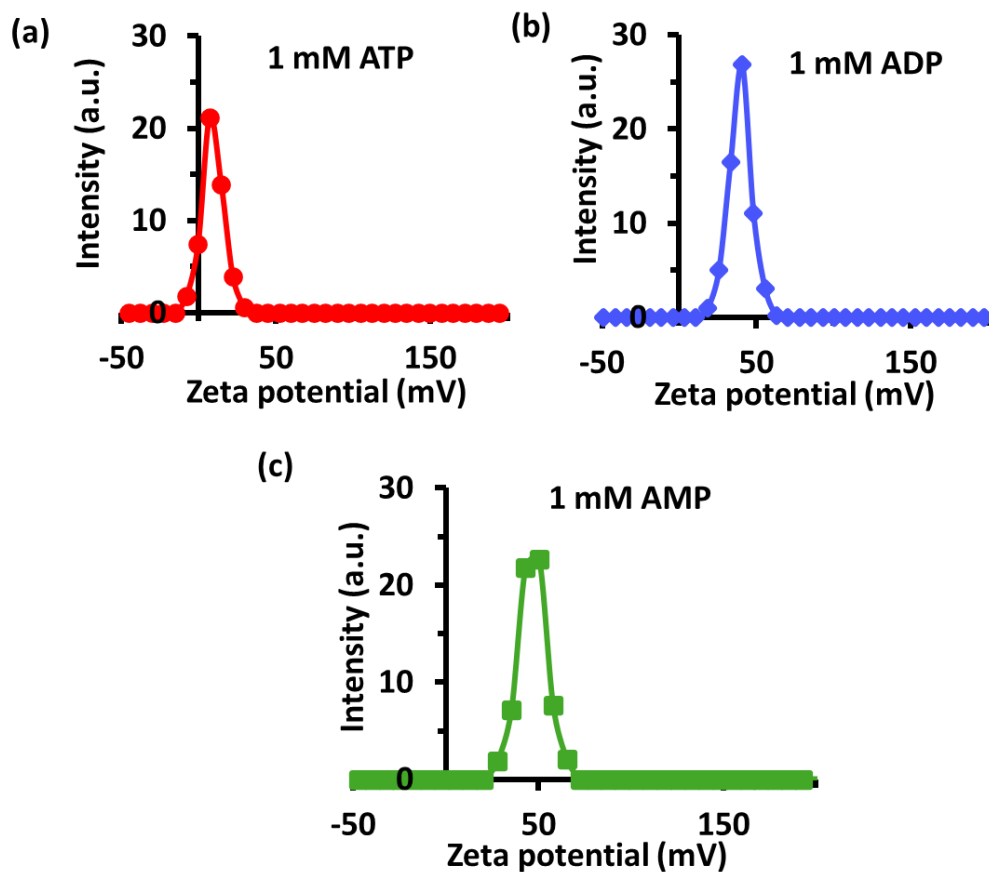


Figure 4.6. Zeta potential of CMB in the presence of (a) ATP, (b) ADP, (c) AMP. Experimental condition: 0.1 mg/mL bead, [GNR] = 150 pM, [nucleotide] = 1 mM at 25 °C.

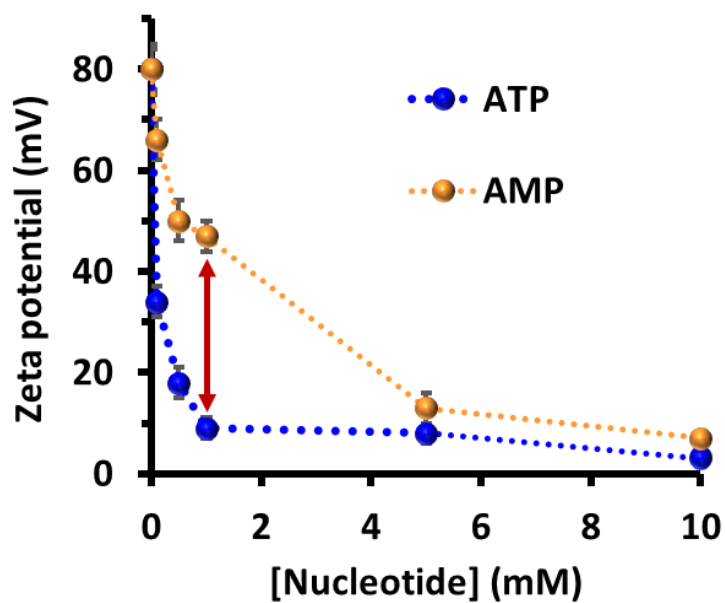


Figure 4.7. Zeta potential measurement of CMB conjugate in presence of different nucleotide concentrations. Experimental condition: 0.1 mg/mL bead, [GNR] = 150 pM, [nucleotide] = 1 mM at 25 °C.

observed (Figure 4.8). Subsequently, we evaluated the catalytic activity of the CMB in facilitating the KE reaction by monitoring the UV-scanning kinetics and tracking the change in absorbance of the product (2-cyano nitrophenol (CNP)) peak at 380 nm (Figure 4.9). In the absence of nucleotides, no activity was observed (Figure 4.10). Interestingly, the addition of 1 mM AMP to the system significantly enhanced the reaction rate by nearly 1000-fold (Figure 4.5e). However, the presence of an equivalent amount of ADP resulted in only a modest 10-fold increase in catalysis, while the addition of ATP did not improve the catalytic activity. We also investigated the catalysis in a mixed AMP/ATP system by varying the mole fraction of ATP from 0 to 1, while maintaining a total concentration of 1 mM (Figure 4.5f). The catalytic ability decreased significantly as the ATP content increased, and in the presence of 0.5 mM ATP and 0.5 mM AMP, almost no catalytic activity was observed. The pattern of catalytic activity in the presence of a mixed AMP/ATP nucleotide system was similar to what was previously observed with only cationic gold nanoparticles.⁴⁵ These findings indicate that the phenomenon of binding and nucleotide-mediated modulation of KE catalysis persists on the cationic surface of the GNR, even when it is bound to an anionic micron-sized polymer bead. This demonstrates the robustness and versatility of the multivalent interaction-mediated catalytic system involving the CMB-GNR conjugate.

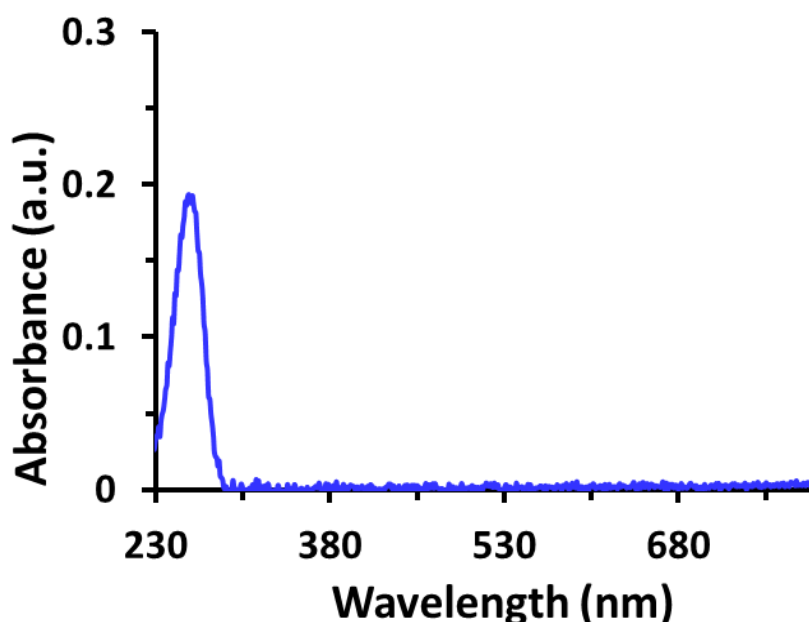


Figure 4.8. UV-vis scan of supernatant of ATP containing CMB solution. Experimental condition: 0.1 mg/mL bead, [GNR] = 150 pM, [ATP] = 1 mM at 25 °C.

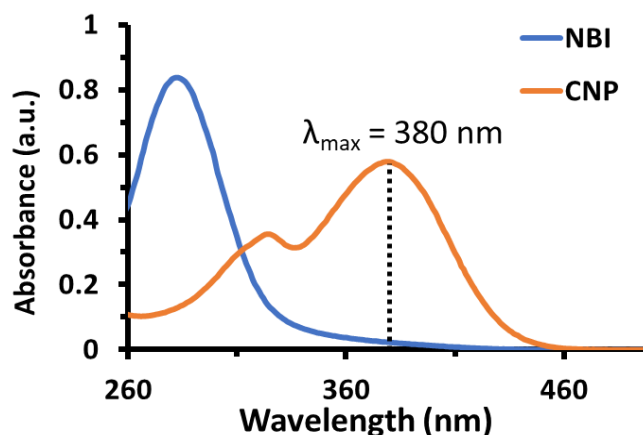


Figure 4.9. Scan spectra of (a) NBI, and (b) CNP in water.

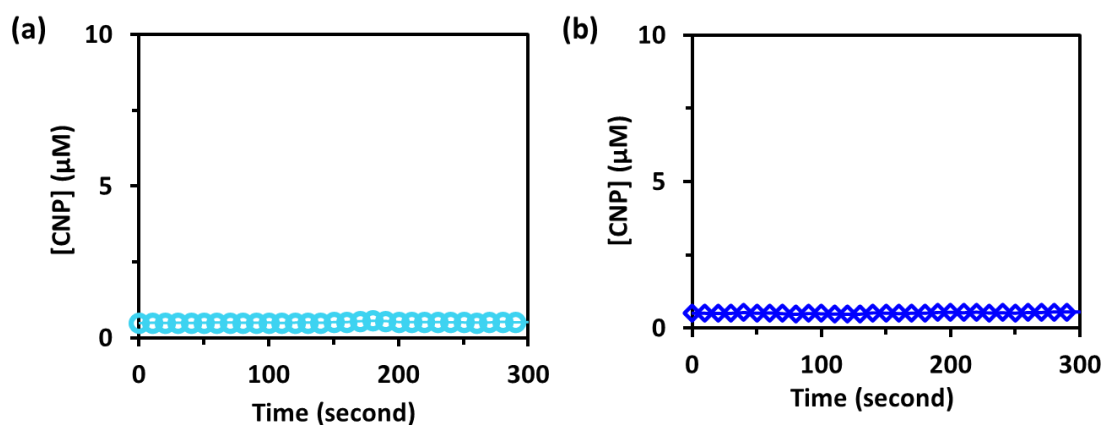


Figure 4.10. Amount of CNP formation with carboxylate beads (a) without GNR and (b) with GNR in water. Experimental condition: 0.1 mg/mL carboxylate beads, [NBI] = 100 μM in water at 25 $^{\circ}\text{C}$.

After characterizing the charge-neutralizing properties and nucleotide distribution on the cationic surface, our investigation turned towards understanding how these multivalent binding interactions can modulate the diffusiophoresis of the CMB in a gradient of adenosine nucleotides. We approached this by examining two aspects: (i) the individual phoretic effect of nucleotides with different charges and (ii) the phoretic response in the presence of mixed nucleotides competing for binding with the CMB surface. For this purpose, we first used a microfluidic experiment with a two-inlet and one-outlet channel with dimensions of $17 \times 0.6 \times 0.1 \text{ mm}^3$ (length \times width \times height). We injected fluorescent CMB solution from one inlet and nucleotide (1 mM) from the other, each at a flow rate of $Q/2 = 0.16 \text{ ml/h}$, and observed the transverse drift of the CMB near the end of the channel (16 mm from the inlets merging) under a fluorescence microscope by scanning the zonal intensity (Figure 4.11a). The intensity was normalized with respect to its integral across the channel, which is a measure of the number of

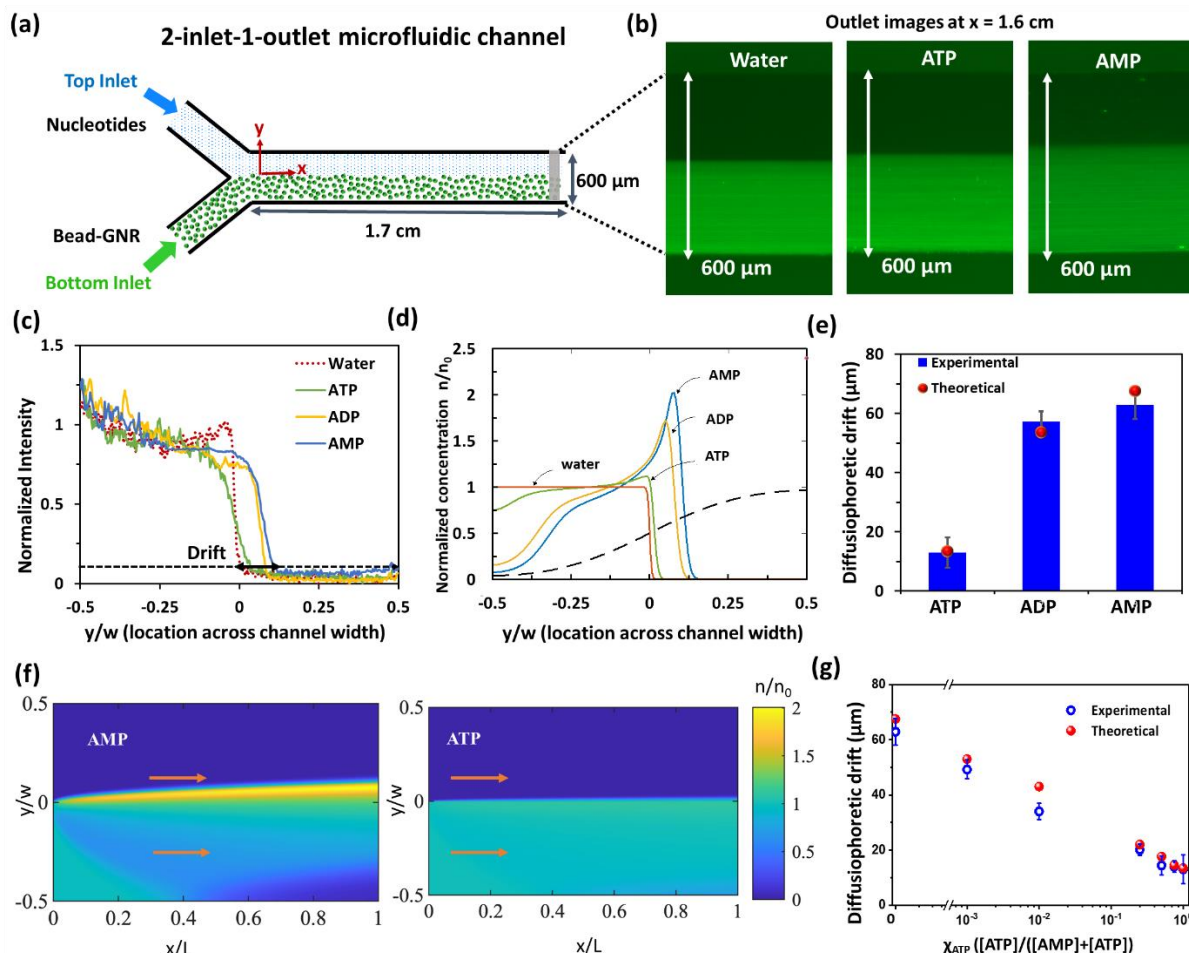


Figure 4.11. (a) Schematic image showing the setup of the 2-inlet-1-outlet microfluidic experiment, where CMB has been passed through one inlet and nucleotides from the other, and the fluorescence images were taken at the end of the channel at $L = 1.6$ cm apart. Flow speed = 0.32 ml/h. (b) A representative image of the channel at the outlet showing accumulation of the fluorescent CMB towards the AMP side is more than ATP and control. (c) Experimentally obtained fluorescence intensity profile at the outlet, from top to bottom end of the channel. The fluorescence is due to the presence of CMB (channel width = 600 μm). (d) Particle concentration profiles at the downstream end of the channel exposed to 1mM AMP, ADP, and ATP were obtained from the model. Concentrations are normalized in such a way that the integral across the channel width is conserved relative to the inlet. Particles drift due to diffusiophoresis towards higher concentrations of nucleotide (whose concentration is indicated as a dashed curve). The magnitude of drift follows the ordering AMP>ADP>ATP, consistent with experiments. (e) The experimental and theoretical diffusiophoretic drift of CMB towards AMP, ADP, and ATP when the concentration of nucleotides is 1 mM. Phoretic drift was calculated at a normalized intensity of 0.1 (near the baseline) as denoted by the dotted line in Figure 4.11c. (f) Maps of particle concentration within the channel for AMP and ATP. The particle drift under exposure to ATP is negligible (g) Experimental diffusiophoretic drift of CMB towards a gradient of nucleotides (AMP and ATP individually and in the mixture). χ_{ATP} is the mole fraction of ATP in a mixture of ATP and AMP i.e. $[ATP]/([AMP]+[ATP])$. In the case of 4.11e and 4.11g, phoretic drift was calculated at a normalized intensity of 0.1 (near the baseline) as denoted by the dotted line in Figure 4.11c. The error bar is the standard deviation of four independent sets of experiments.

particles per area and is a conserved quantity at a steady state. The diffusiophoretic drift due to the presence of nucleotides was calculated by comparing the location where the normalized intensity is 0.1 (near the baseline) with that of the no-nucleotide condition i.e., only in the presence of milli-Q water. Figure 4.11c shows the ratio of this drift to the channel width (width = 600 μm , constant across all experiments). Remarkably, we observed that particles exhibited drift towards the nucleotide in the cases of AMP and ADP, with drift values of $63 \pm 4 \mu\text{m}$ and $57 \pm 3 \mu\text{m}$, respectively. However, in the presence of an ATP gradient, we observed no significant drift, with a calculated value of only $13 \pm 5 \mu\text{m}$ (Figure 4.11b-d, Table 4.1).

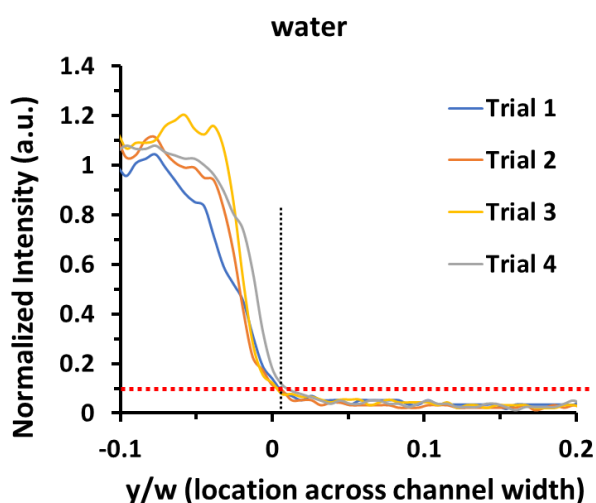


Figure 4.12. Intensity profile of CMB across the microfluidic channel for 4 individual experiments in the presence of water. Experimental condition: 0.1 mg/mL beads, [GNR] = 150 pM at 25 °C.

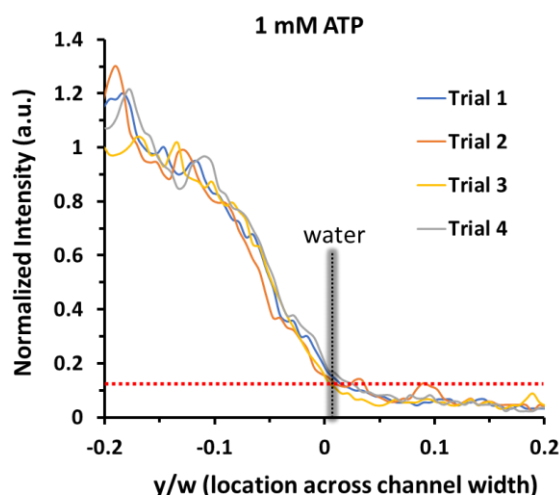


Figure 4.13. Intensity profile of CMB across the microfluidic channel for 4 individual experiments in the presence of ATP. Experimental condition: 0.1 mg/mL beads, [GNR] = 150 pM, [ATP] = 1 mM at 25 °C. The black dotted line serves as a guideline to the eye for comparison with the control (water case).

Table 4.1. The diffusiophoretic drift of CMB inside a microfluidic chip while calculated at 1.6 cm distance from an inlet in the presence of different nucleotides. The noted drift of CMB in the presence of nucleotide is after subtracting from water. Experimental condition: 0.1 mg/mL bead, [GNR] = 150 pM, [nucleotide] = 1 mM in water at 25 °C.

S. No.	Sample	Diffusiophoretic drift from 4 trials (y/w)	Average \pm S.D. (μm)
1.	Water	0.006	
		0.006	
		0.005	
		0.007	
2.	1 mM ATP	0.027	13.01 \pm 5.18
		0.034	
		0.034	
		0.015	
3.	1 mM ADP	0.107	57.15 \pm 3.54
		0.094	
		0.105	
		0.099	
4.	1 mM AMP	0.102	62.89 \pm 4.82
		0.113	
		0.120	
		0.110	

To gain a deeper understanding of the observed drift in the experiments, we developed a model that describes the diffusiophoretic motion of particles in a co-flow geometry, mimicking the experimental setup. The model incorporates a height-averaged description of fluid flow and the transport of nucleotides and particles (Figure 4.11f). By comparing with experimental results, we determined that the positively charged particles indeed drift towards the nucleotide, consistent with the experimental observations. Furthermore, the model accurately captures the varying degrees of drift induced by different nucleotides, with AMP producing the highest drift, followed by ADP, and ATP resulting in a weak drift. The extent of drift is primarily controlled by the differences in ζ -potential among these nucleotides, while the ionic charge and diffusivities of the nucleotides play a secondary role. The model's predictions align well with the experimentally measured drift values for AMP, ADP, and ATP (Figure 4.11e). Importantly, the model parameters are directly extracted from experimental measurements without involving any fitting parameters. Additionally, we analyzed the contributions of chemiphoresis

and electrophoresis to the particle motion in each case (Table 4.2) based on well-established theoretical frameworks.^{28,34,35}

In practical systems, mixtures of nucleotides are often encountered. Considering the significant disparities in the ability of different nucleotides to drive phoretic drift, we investigated the phoretic drift in mixed nucleotide systems with varying molar compositions of AMP and ATP. Our aim was to evaluate the amount of ATP needed to counteract the diffusiophoretic motion induced by AMP. We introduced a fraction of ATP, $\chi_{\text{ATP}} = [\text{ATP}]/([\text{ATP}]+[\text{AMP}])$, ranging from 0 to 1 (Figure 4.11g, Table 4.3). Interestingly, we observed a sharp decrease in drift after the addition of as little as 10 μM ATP (with 990 μM AMP; $\chi_{\text{ATP}}=0.01$). At $\chi_{\text{ATP}}=0.25$, the drift became almost negligible, reducing from 66 μm to 14 μm . These findings clearly demonstrate that even minute amounts of ATP can effectively mediate interactions on the cationic surface, with a 10% ATP fraction suppressing AMP-mediated drift by 50%. To further understand the effect of mixed ATP and AMP systems, we employed the same modeling framework as before, incorporating experimentally measured zeta potentials (Figure 4.14). This time, we tracked the transport of individual nucleotides and related their concentration gradients to the diffusiophoretic particle velocity, \mathbf{u}_{dp} , using a well-established theoretical framework for mixtures.^{31,35} Similar to the experimental results, the modeled drift decreased rapidly in the presence of a mixture, even with a small amount of ATP, and decreased further with increasing χ_{ATP} . The theoretical predictions for the drift aligned excellently with the experimental measurements across all mixture compositions (Figure 4.11g).

Table 4.2. Calculated ambipolar diffusivities and diffusiophoretic mobilities, showing the relative contributions of electrophoresis and chemiophoresis to the mobility.

	AMP	ADP	ATP
ζ (mV)	47	40	9
D (10^{-10} m ² /s)	7.27	8.06	8.42
Γ_p (10^{-10} m ² /s)	5.67	4.06	0.656
% Electrophoresis	66.7	69.2	89.5
% Chemiophoresis	33.3	30.8	10.5

Table 4.3. The diffusiophoretic drift of CMB inside the microfluidic chip while calculated 1.6 cm distant from the inlet in the presence of different ratios of ATP and AMP while keeping total nucleotide concentration constant. The noted drift of CMB in the presence of nucleotide is after subtracting from water. Experimental condition: 0.1 mg/mL bead, [GNR] = 150 pM in water at 25 °C.

S. No.	χ_{ATP} ([ATP]/([AMP]+[ATP]))	Diffusiophoretic drift from 4 trials (y/w)	Average \pm S.D. (μ m)
1.	0	0.102	62.89 \pm 4.82
		0.113	
		0.120	
		0.110	
2.	0.001	0.082	49.2 \pm 3.43
		0.085	
		0.090	
		0.095	
3.	0.01	0.064	33.72 \pm 2.05
		0.058	
		0.061	
		0.065	
4.	0.25	0.037	20.10 \pm 1.50
		0.039	
		0.039	
		0.043	
5.	0.5	0.031	14.4 \pm 3.46
		0.023	
		0.029	
		0.037	
6.	0.75	0.033	13.95 \pm 2.1
		0.031	
		0.025	
		0.028	
7.	1	0.027	13.01 \pm 5.18
		0.034	
		0.034	
		0.015	

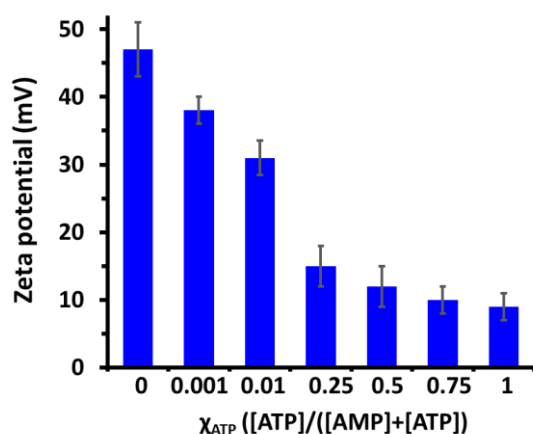


Figure 4.14. Zeta potential of CMB in a gradient of different compositions of AMP and ATP (total nucleotide concentration = 1 mM). Experimental condition: 0.1 mg/mL bead, [GNR] = 150 pM, [nucleotide] = 1 mM at 25 °C.

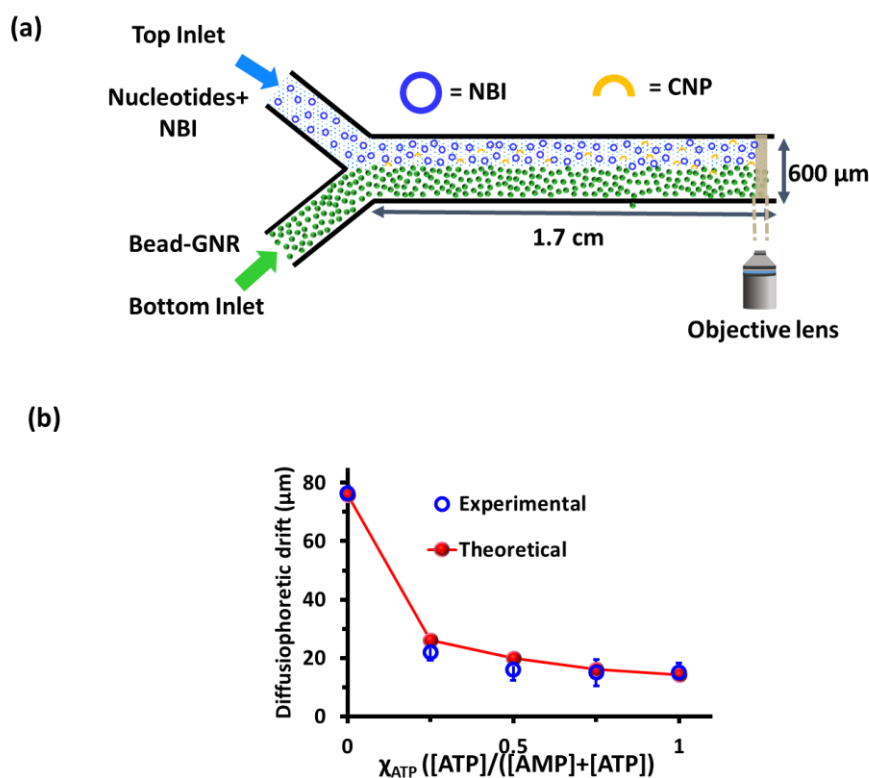


Figure 4.15. (a) Schematic representation of microfluidic setup while injecting Nucleotide with NBI from the top inlet and Bead-GNR from the bottom inlet. (b) The diffusiophoretic drift of Bead-GNR was obtained both experimentally and theoretically. Experimental condition: 0.1 mg/mL beads, [GNR] = 150 pM, [ATP] = 0 – 1 mM, [AMP] = 0 – 1 mM, [NBI] = 0.1 mM at 25 °C.

Table 4.4. The diffusiophoretic drift of CMB inside a microfluidic chip while calculated at 1.6 cm distance from an inlet in the presence of different ratios of ATP and AMP during catalysis. The noted drift of CMB in the presence of nucleotide is after subtracting from water + NBI. Experimental condition: 0.1 mg/mL bead, [GNR] = 150 pM, [Nucleotide] = 1 mM, [NBI] = 0.1 mM in water at 25 °C.

S. No.	χ_{ATP} ([ATP]/([AMP]+[ATP]) + NBI	Diffusiophoretic drift from 4 trials (y/w)	Average \pm S.D. (μm)
1.	Water + NBI	0.004	
		0.005	
		0.003	
		0.004	
2.	0	0.132	76.35 \pm 2.60
		0.137	
		0.129	
		0.127	
3.	0.25	0.040	22.05 \pm 2.74
		0.046	
		0.042	
		0.035	
4.	0.5	0.039	16.05 \pm 3.74
		0.031	
		0.024	
		0.029	
5.	0.75	0.025	15.15 \pm 4.51
		0.021	
		0.038	
		0.032	
6.	1	0.025	15.15 \pm 1.85
		0.032	
		0.029	
		0.031	

In recent studies, it has been demonstrated that catalysts, whether enzymes or micro/nanoparticles, exhibit drift in the direction of a substrate gradient, with the extent of migration dependent on their catalytic activity and other factors such as the presence of a cofactor (48-49). The direction and magnitude of this drift are primarily governed by phoretic effects. Inspired by these findings, we explored the diffusiophoretic drift of the CMB in the microfluidic channel during proton transfer reactivity, specifically by introducing the substrate NBI with nucleotides as a gradient. To achieve this, we passed the NBI substrate with nucleotides ($\chi_{\text{ATP}} = 0$ to 1) through one channel while allowing the beads to flow through the other (Figure 4.15a), and we measured the resulting drift, similar to the previous experiment. As depicted in Figure 4.5(f), the CMB exhibited KE catalysis only in the presence of a large fraction of AMP, while remaining inactive in both ATP and AMP + ATP (0.5 mM each) systems. With the addition of NBI, we expected to observe an additional shift of the CMB towards the AMP + NBI side due to catalytic effects. Indeed, with AMP alone, the drift was measured at $63 \pm 4 \mu\text{m}$, and with AMP + NBI, it increased to $76 \pm 3 \mu\text{m}$ (Figure 4.15b, Table 4.4). However, in non-catalytic conditions (ATP and AMP + ATP systems with NBI), only minimal additional drift was observed. We hypothesize that the extra drift of the CMB is due to the slight increase in the zeta potential of the CMB during the catalysis of the uncharged NBI on its surface (in the presence of AMP).³¹⁻³⁵ The calculated additional drift resulting from the presence of NBI in combination with a mixture of AMP or ATP closely matched the experimental observations (Figure 4.15b). This further supports our hypothesis, indicating that the effect of catalysis on the extent and direction of colloidal drift is primarily determined by its influence on the substrate polarity and, consequently, the overall colloidal charge.

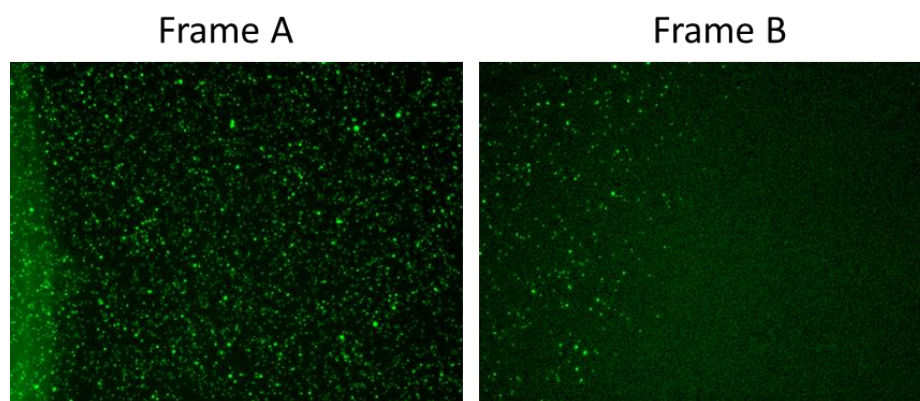


Figure 4.16. Migration of CMB inside Macroscopic chamber in milli-Q only. Experimental condition: 0.025 mg/mL bead, [GNR] = 37.5 pM at 25 °C. The X-axis of each image is 1.5 mm.

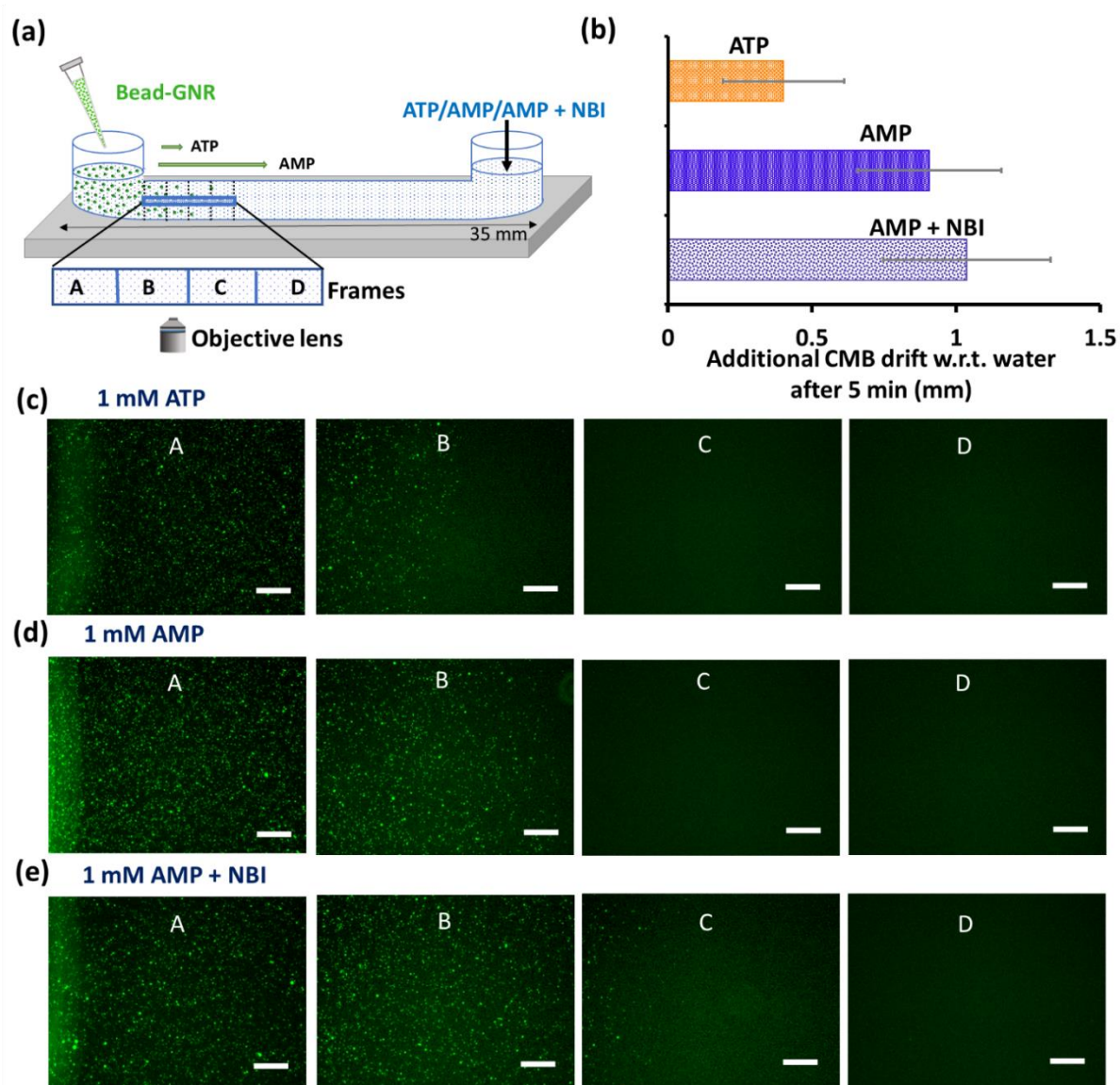


Figure 4.17. Macroscale manifestation of diffusiophoretic drift in a gradient of nucleotides. (a) Schematic representation of the experimental setup. 50 μl of nucleotide solution with and without NBI solution was added from one end of the channel and 5 μl CMB solution was added from another end. (b) Additional distance covered by CMB when the channel was filled with ATP or AMP (1 mM) with and without NBI solution with respect to only water after 5 min. Fluorescence images of channels in different frames when (c) ATP, (d) AMP, (e) AMP + NBI solution was added. The scale bar of each image is 200 μm .

Spatial cues play a crucial role in natural systems, where signaling gradients like the extracellular matrix contribute to processes such as bone and cartilage development. These cues have also been harnessed in synthetic systems to investigate reaction-diffusion kinetics, spatially segregated chemistry, and morphogenesis. Building upon this knowledge, we sought to explore the potential of nucleotide gradients in driving diffusiophoretic motion on a macroscale, without the need for continuous flow. Our experimental setup at the macroscale,

as depicted in Figure 4.17a, allowed us to investigate the dynamics of colloidal microbeads (CMB) in response to nucleotide gradients. We introduced nucleotides with or without NBI (Nucleotide-Binding Indicator) through one arm of the setup, while CMB solution was introduced through the other arm. We then tracked the population dynamics at four distinct zones within the chamber, namely frames A, B, C, and D, each spanning a length of 1.5 mm (refer to the method section for detailed information).

To isolate the phoretic effects resulting from nucleotide gradients, we conducted a control experiment using only milli-Q water. This allowed us to observe the natural motion behavior of the CMB inside the chamber, driven by particle diffusion, gravity, and inertial effects (Figure 4.16). Subsequently, we performed experiments in the presence of nucleotides to investigate the influence of nucleotide gradients on particle motion. Notably, we observed that the CMB traveled a greater distance in the presence of nucleotides, specifically moving against the nucleotide gradient (up the gradient) as depicted in Figure 4.17. Moreover, the drift exhibited a more pronounced effect with AMP compared to ATP. Intriguingly, the combination of NBI and AMP resulted in an additional 10% migration against the gradient compared to using AMP alone (Figure 4.17).

In all cases, our measurements were conducted for a duration of up to 5 minutes, as beyond that timeframe, we observed particles settling at the bottom of the glass channel. This settling behavior can be attributed, at least in part, to the interactivity between the cationic beads and the anionic glass surface (Figure 4.18). Despite this limitation, we consistently observed similar trends in phoretic drift within this macroscale setup compared to our microfluidic experiments. One particularly intriguing finding is that we achieved a nearly 0.5 mm difference in the diffusiophoretic drift of the CMB in the macroscale setup, which is almost one order of magnitude greater than what was observed in the microfluidic flow setup, by utilizing AMP instead of ATP (Figure 4.17b). This substantial difference highlights the significant impact of nucleotide choice on the magnitude of the phoretic drift at the macroscale. We have previously demonstrated, both experimentally and theoretically, that multivalent interactions with ATP significantly alter diffusiophoretic motion in ATP/AMP mixtures (Figures 4.11g). Building on this finding, we now aim to investigate the in situ degradation of this multivalent interactivity and its implications for the temporal modulation of phoresis and zone-specific population dynamics of the CMB. To achieve in situ downregulation of multivalent interactivity, we utilize the potato apyrase enzyme (PA), which cleaves ATP into AMP + 2 Pi. It is worth noting that this approach has been employed in recent studies to create

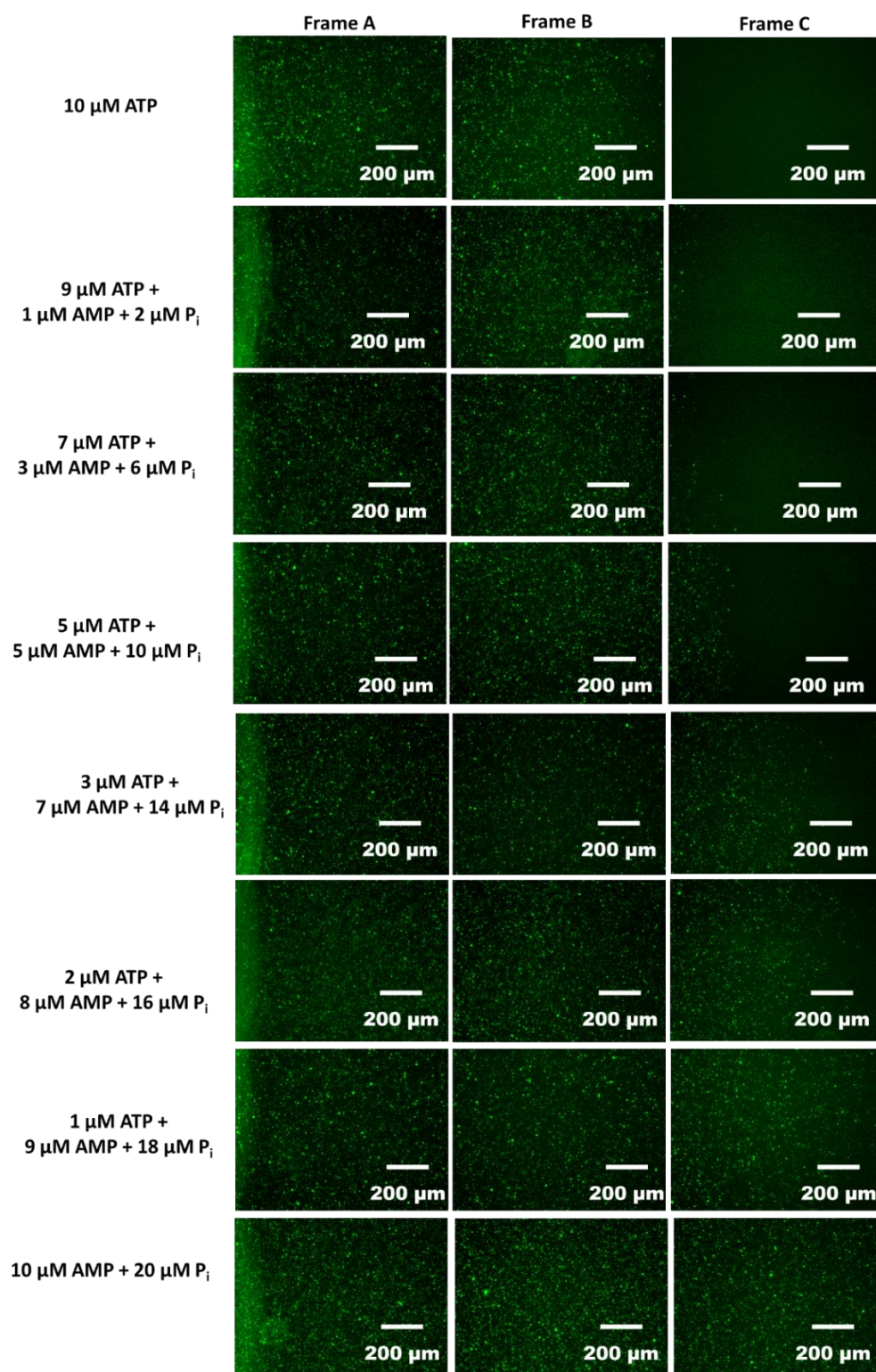


Figure 4.21. Migration of CMB inside macroscopic channel while varying concentrations of ATP, AMP, and P_i while keeping total concentration constant, that is, 10 μM . Experimental condition: 0.025 mg/mL bead, $[\text{GNR}] = 37.5 \text{ pM}$, $[\text{Nucleotide}] = 10 \text{ }\mu\text{M}$, $[\text{P}_i] = 2 \times [\text{AMP}]$, $[\text{Ca}^{2+}] = 0.25 \text{ mM}$ at 25 $^\circ\text{C}$.

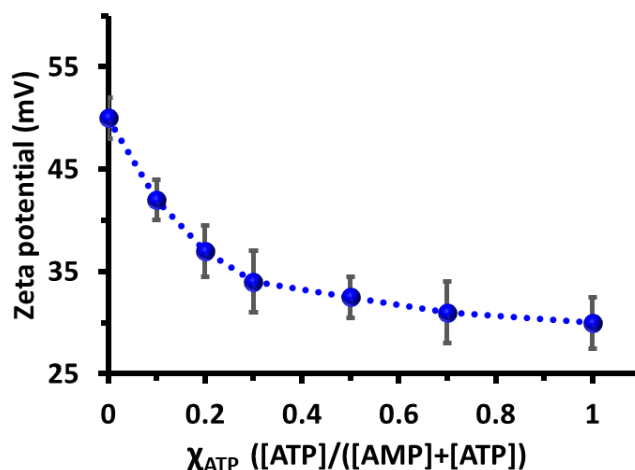


Figure 4.19. Zeta potential of CMB in gradient of different compositions of AMP + 2 Pi and ATP (total nucleotide concentration = 10 μM). Experimental condition: 0.025 mg/mL bead, [GNR] = 37.5 pM, $[\text{Ca}^{2+}] = 0.25 \text{ mM}$ at 25 $^{\circ}\text{C}$.

transient and dynamic self-assembled systems with applications ranging from programmed reactors to switchable catalysts.^{20,55} However, the influence of this effect on modulating complex non-equilibrium phoretic processes has not been explored before. Uncovering this behavior across different length scales offers intriguing opportunities for controlling transport and spatiotemporal localization dynamics in diffusion-driven systems. For our experiments, we utilized the macroscale setup described earlier (schematically shown in Figure 4.17). In this case, we used a concentration of only 10 μM ATP since complete hydrolysis of ATP occurs within 5 minutes at a PA concentration of 100 nM (refer to method section) for enzyme kinetics, k_{cat} , and K_{m} values, Figure 4.3, 4.4). At any given time, the hydrolysis reaction produces a solution containing $10 \chi_{\text{ATP}} \mu\text{M}$ ATP + $10 (1 - \chi_{\text{ATP}}) \mu\text{M}$ AMP + $20 (1 - \chi_{\text{ATP}}) \mu\text{M}$ Pi, where the fraction of ATP, χ_{ATP} , defined as $\chi_{\text{ATP}} = [\text{ATP}]/([\text{ATP}] + [\text{AMP}])$, continually decreases over time. Before directly measuring the temporal dynamics of CMB due to ATP hydrolyzed by PA, we conducted steady-state control experiments (without the enzyme) to replicate the chemical composition of the solution that would be present during the reaction. This approach facilitates a clearer understanding of the spatiotemporal dynamics observed in the reaction conditions with PA. In our control experiments, we employed compositions of ATP + AMP + Pi as described earlier (without PA) with ATP fractions, χ_{ATP} , ranging from 0.1 to 0.9. As observed in previous experiments with mixtures, we noted significant differences in the ζ -potential of the CMB with 10 μM ATP ($\chi_{\text{ATP}} = 1$; $\zeta = 30 \pm 3 \text{ mV}$) compared to 10 μM AMP + 20 μM Pi ($\chi_{\text{ATP}} = 0$; $\zeta = 50 \pm 2 \text{ mV}$) (Figure 4.19). The additional drift of the CMB (compared to milliQ water alone) observed at χ_{ATP} values of 0 and 1 was 3 ± 0.5 and $1.2 \pm 0.3 \text{ mm}$, respectively (Figure 4.20). Interestingly, this drift remained roughly constant as the

χ_{ATP} value was decreased from 1 to 0.4, and a sudden increase in drift was observed when χ_{ATP} dropped below 0.3 (Figure 4.20). This experiment highlights the role of multivalent binding in driving diffusiophoretic effects, as the number of phosphate units (covalently linked for ATP or free phosphate in the case of AMP + 2Pi) remains constant in all cases.

Subsequently, we investigated how the sensitivity of phoresis to the ATP fraction could be utilized to modulate the spatiotemporal dynamics of CMB by dynamically changing the interaction valency through enzymatic hydrolysis of ATP. To accomplish this, we filled the chamber with ATP (0.01 mM) and PA (150-200 nM), followed by the addition of CMB solution from one arm (Figure 4.22). The population of particles in frame C was monitored over time since, in the absence of PA, no particles were present in that frame throughout the experimental duration, while it became densely populated in the presence of AMP + 2Pi. Remarkably, with 150 nM PA, frame C started to exhibit particle presence after just 1 minute (Figure 4.22b). By using 200 nM PA instead, we observed an increase in the density of CMB particles in frame C after 1 minute (data not shown), confirming the role of ATP hydrolysis in controlling particle motion. Furthermore, we measured the diffusiophoretic velocity in the same experiment by tracking particle motion in frame A. In the presence of ATP without PA, the drift velocity was approximately $15 \pm 3 \mu\text{m/s}$ during the recording period (Figure 4.22).

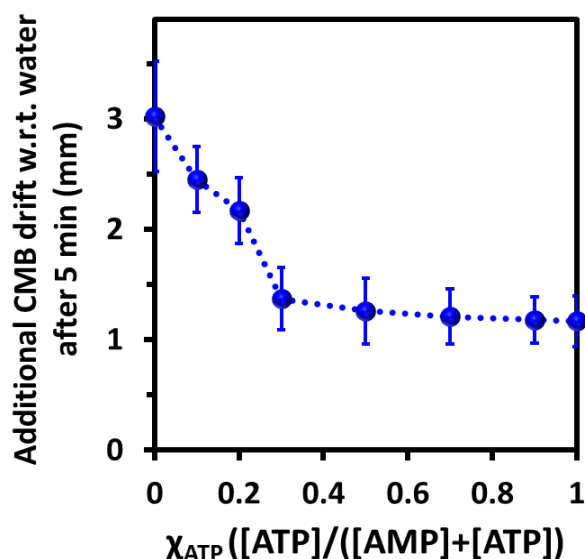


Figure 4.20. Additional CMB drift in reference to water in the presence of different ratios of ATP and AMP + 2Pi while keeping total nucleotide concentration constant, that is, 10 μM . Experimental condition: 0.025 mg/mL bead, [GNR] = 37.5 pM, [Nucleotide] = 10 μM , [Pi] = 2 x [AMP], [Ca²⁺] = 0.25 mM at 25 °C.

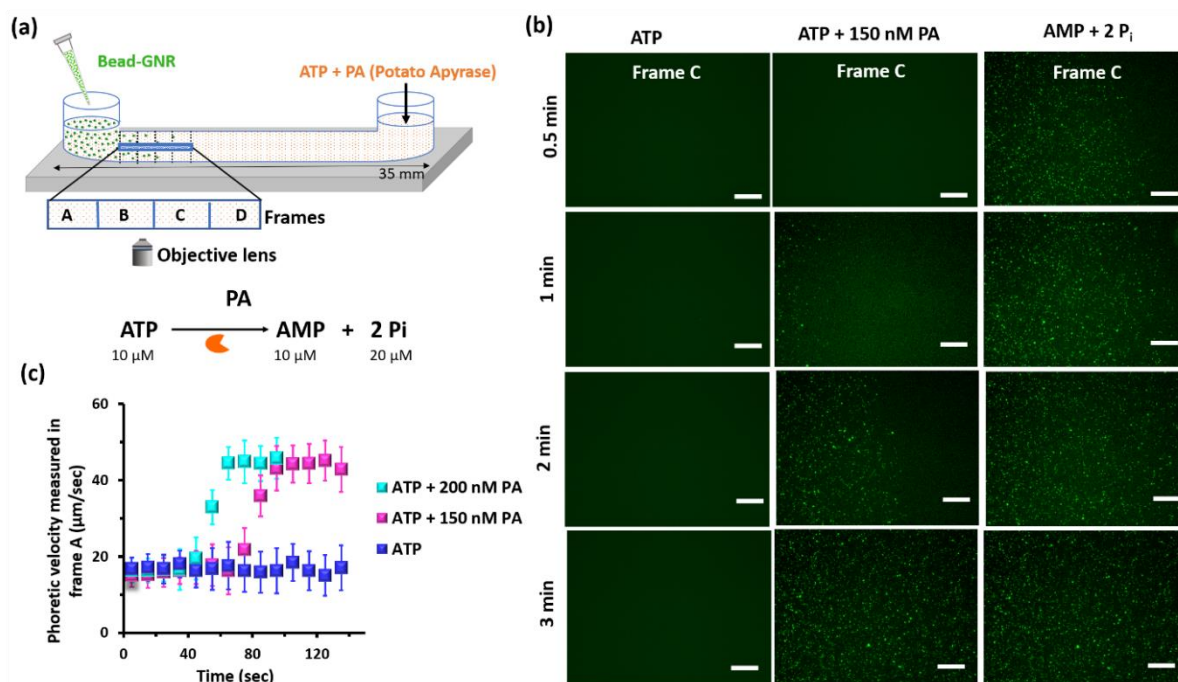


Figure 4.22. Spatiotemporal evolution of colloidal population dynamics during enzymatic hydrolysis of ATP. (a) Schematic representation of the experimental setup. ATP-containing potato apyrase was filled inside the channel and CMB solution was added from another end. (b) Temporal evolution of migration of CMB in frame C with time when ATP or AMP + 2P_i or ATP + PA (150 nM, ATP hydrolysis condition) was added inside the channel. (c) The phoretic velocity of CMB was measured in frame A during ATP hydrolysis at different PA concentrations. The calculation was performed from the recorded videos. Experimental condition: 0.025 mg/mL bead, [GNR] = 37.5 pM, [ATP] = 10 μM, [PA] = 150 nM, [Ca(NO₃)₂] = 0.25 mM at 25 °C.

Interestingly, in the presence of PA, the velocity initially resembled the ATP-only case and then rapidly increased (i.e., "leaped") to over 40 μm/s after some time, maintaining a constant velocity for the remainder of the experiment. For instance, in the presence of 200 nM PA, the drift velocity of CMB increased to 45 μm/s from an initial velocity of 17 μm/s within a span of only 40 seconds (Figure 4.22c). A similar trend was observed for 150 nM, where the phoretic jump took approximately 85 to reach the maximum velocity (Figure 4.22c). Based on our kinetic parameters, the sudden leap in phoretic velocity was found to occur after the dissociation of approximately 70% of ATP. These observations demonstrated that (i) a phoretic leap of colloids can be achieved by downregulating the multivalent interactivity with external counterparts and (ii) by adjusting the drift velocity, the population density of colloid particles at a specific frame and time interval can be modulated. Controlling the position of a catalyst both spatially and temporally is not only important for industrial applications involving integrated catalysis with synchronized or tandem reactions but also for generating non-

equilibrium chemical reaction networks.⁵⁰ Previously, such systems have been reported using immobilized or confined catalysts on solid or gel matrices. In this study, we demonstrated that phoresis can be employed to control the position of a catalyst and, consequently, the spatiotemporal catalytic activity. The experimental setup was designed as depicted in Figure 4.23a, b, analogous to the system discussed in the previous section. We monitored the activity in Zone 1 and Zone 2 using a plate reader. Zone 1 was chosen in a manner that facilitated rapid

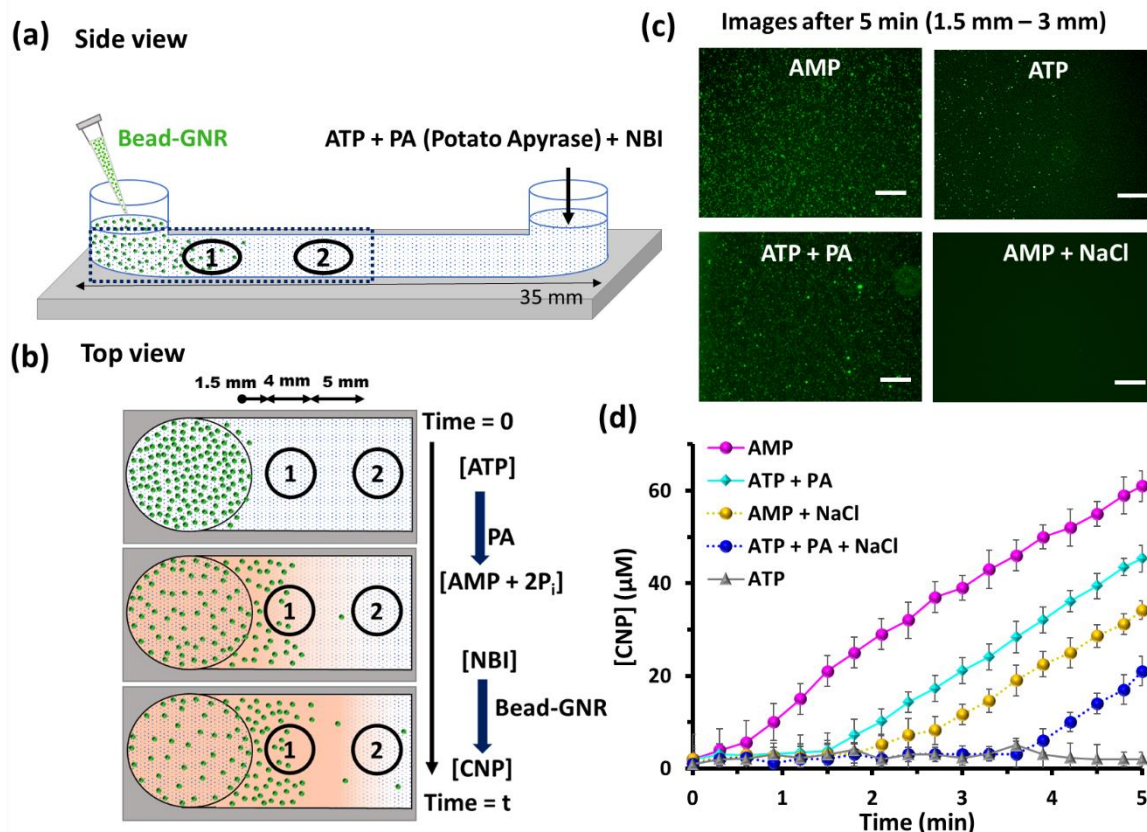


Figure 4.23. Spatiotemporal control over the catalytic process by tuning the phoresis of CMB. (a) Schematic representation of macroscopic channel while filling channel with ATP, PA, and NBI from one arm and adding Bead-GNR(CMB) solution from another arm so that both ATP to AMP conversion and NBI to CNP conversion occur simultaneously. The dotted rectangle marks the area of experimental observation where absorbance is recorded in Zone 1 and Zone 2. (b) Schematic for top view of the area of interest showing phoresis and conversion of both ATP and NBI inside channel over time. The distances between Zone 1 and the armhole, and Zone 1 and Zone 2 are 1.5 mm, and 5 mm, respectively. The diameter of each zone is 4 mm. In zone 2, product CNP traveled solely by diffusion effect and the product accumulation rate is given in Figure 4.25. (c) Microscopic images of CMB in the presence of different conditions are 1.5 mm distant from the armhole. Scale bar = 200 μm. (d) The amount of CNP formed in the presence of ATP (no catalysis) only, AMP only (catalysis), ATP + PA (enzymatic conversion and phoresis), and AMP + NaCl (catalysis but no phoresis) in zone 1. Experimental condition: [AMP] = 0.1 mM, [ATP] = 0.1 mM, [NaCl] = 0.1 mM, [PA] = 500 nM, [Ca(NO₃)₂] = 0.25 mM at 25 °C.

travel of CMB in the presence of AMP (which activates NBI to CNP conversion). To confirm that the reactivity in Zone 1 was solely due to diffusiophoretic effects, we utilized a mixture of AMP + NaCl to inhibit the phoresis of CMB. NaCl was selected as it is a β -negative salt that does not impede the reactivity (Figure 4.24). As expected, we observed the absence of particles in Zone 1 even after 5 minutes in the presence of AMP + NaCl. Notably, product formation in Zone 1 commenced after 30 seconds of mixing in the case of AMP alone, whereas with AMP + NaCl, it started after 4 minutes, highlighting the role of diffusiophoresis. Since ATP inhibits the reaction, enzymatically hydrolyzing ATP can generate AMP + 2Pi, activating both the reaction and phoresis. In this context, we observed an enhancement in product concentration in Zone 1 in the presence of 500 nM PA, starting around 1.5 minutes, whereas in the mixture of ATP + PA + NaCl, product formation occurred after approximately 4 minutes (Figure 4.23d, 4.25). Overall, we demonstrated that both phoresis and phoretic leap can be exploited to finely tune catalytic processes in a spatiotemporal manner.

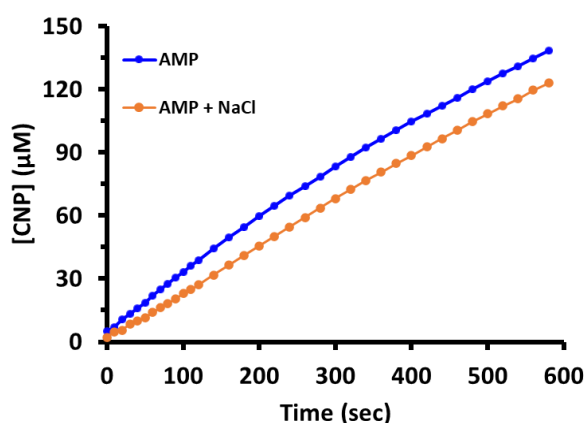


Figure 4.24. Amount of CNP formation with AMP, and AMP + NaCl. Experimental condition: 0.025 mg/mL bead, [GNR] = 37.5 pM, [AMP] = 100 μ M, [NaCl] = 100 μ M, [NBI] = 1 mM at 25 $^{\circ}$ C.

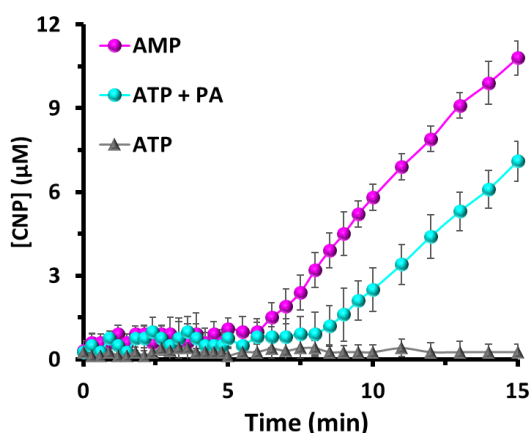


Figure 4.25. The amount of CNP traveled to Zone 2 of the macroscale channel solely due to diffusion with only nucleotide (ATP and AMP), and during enzymatic action (ATP to AMP conversion by PA).

4.5. Summary

In our comprehensive investigation, we have delved into the fascinating interplay between multivalent chemical fuel-driven interactions, catalytic microbeads, and adenosine nucleotides. Through a combination of theoretical modeling and meticulous experimentation, we have not only explored the intricate dynamics of diffusiophoretic drift but also shed light on the profound impact of nucleotide-mediated catalytic processes on colloidal behavior and the spatiotemporal organization of particles. By unraveling the complex interplay between catalytic microbeads and adenosine nucleotides, we have observed remarkable phenomena that shape colloidal transport and functionality. One notable phenomenon is the colloidal phoretic leap, a remarkable occurrence that manifests during the in situ downregulation of multivalent interactions. Importantly, we have found that the timing of these phoretic leaps can be precisely regulated by manipulating the enzymatic hydrolysis of ATP. This intriguing observation opens up new avenues for controlling and manipulating colloidal motion with exquisite precision. Moreover, our research has unveiled the potential for leveraging colloidal transport to exert spatiotemporal control over catalytic processes. By modulating the transport properties of colloidal particles, we can regulate the spatial and temporal distribution of catalytic activity. This breakthrough finding holds significant promise for the development of synthetic systems capable of generating spatiotemporally controlled micron-sized colloidal patterns.⁵⁶ Through fine-tuning multivalent interactions with small molecules, we can program the delivery of colloids for specific chemical processes, such as catalysis or controlled release of drugs and chemicals. This programmable control over colloidal motion provides a powerful tool for designing synthetic systems that emulate the defining properties of living matter. In summary, our study opens up exciting prospects for the creation of synthetic spatiotemporally controlled complex integrative catalytic systems.⁵⁰⁻⁵⁶ These systems, inspired by chemical gradient-sensing driven signaling mechanisms observed in living organisms, exhibit motility behavior and offer potential applications in a wide range of fields. From designing advanced catalytic processes with synchronized or tandem reactions to developing non-equilibrium chemical reaction networking systems, the possibilities are vast.

4.6. References

1. Krishnamurthy, V. M.; Estroff, L. A.; Whitesides, G. M. *Multivalency in Ligand Design'' in Fragment-Based Approaches in Drug Discovery*; Wiley-VCH: Weinheim, 2006.

2. Dervede, J. *Multivalency in Biosystems*; John Wiley & Sons Ltd, 2017.
3. Fasting, C.; Schalley, C. A.; Weber, M.; Seitz, O.; Hecht, S.; Koks, B.; Dervede, J.; Graf, C.; Knapp, E.-W.; Haag, R. *Angew. Chem. Int. Ed* **2012**, *51*, 10472–10498.
4. Scheepers, M. R. W.; van IJendoorn, L. J.; Prins, M. W. J. Multivalent Weak Interactions Enhance Selectivity of Interparticle Binding. *Proc. Natl. Acad. Sci. U. S. A.* **2020**, *117* (37), 22690–22697.
5. Kane, R. S. Thermodynamics of Multivalent Interactions: Influence of the Linker. *Langmuir* **2010**, *26* (11), 8636–8640.
6. Di Iorio, D.; Verheijden, M. L.; van der Vries, E.; Jonkheijm, P.; Huskens, J. Weak Multivalent Binding of Influenza Hemagglutinin Nanoparticles at a Sialoglycan-Functionalized Supported Lipid Bilayer. *ACS Nano* **2019**, *13* (3), 3413–3423.
7. Overeem, N. J.; van der Vries, E.; Huskens, J. A Dynamic, Supramolecular View on the Multivalent Interaction between Influenza Virus and Host Cell. *Small* **2021**, *17* (13), e2007214.
8. Zaramella, D.; Scrimin, P.; Prins, L. J. Self-Assembly of a Catalytic Multivalent Peptide-Nanoparticle Complex. *J. Am. Chem. Soc.* **2012**, *134* (20), 8396–8399.
9. Chan, C. W.; Smith, D. K. Pyrene-Based Heparin Sensors in Competitive Aqueous Media - the Role of Self-Assembled Multivalency (SAMul). *Chem. Commun.* **2016**, *52* (19), 3785–3788.
10. Curk, T.; Dubacheva, G. V.; Brisson, A. R.; Richter, R. P. Controlling Superselectivity of Multivalent Interactions with Cofactors and Competitors. *J. Am. Chem. Soc.* **2022**, *144* (38), 17346–17350.
11. Zaupa, G.; Prins, L. J.; Scrimin, P. Resin-Supported Catalytic Dendrimers as Multivalent Artificial Metallonucleases. *Bioorg. Med. Chem. Lett.* **2009**, *19* (14), 3816–3820.
12. Badjić, J. D.; Nelson, A.; Cantrill, S. J.; Turnbull, W. B.; Stoddart, J. F. Multivalency and Cooperativity in Supramolecular Chemistry. *Acc. Chem. Res.* **2005**, *38* (9), 723–732.
13. Mulder, A.; Huskens, J.; Reinhoudt, D. N. Multivalency in Supramolecular Chemistry and Nanofabrication. *Org. Biomol. Chem.* **2004**, *2* (23), 3409–3424.
14. Shandilya, E.; Maiti, S. Deconvolution of Transient Species in a Multivalent Fuel-driven Multistep Assembly under Dissipative Conditions. *ChemSystemsChem* **2020**, *2* (2), e1900040.
15. Das, K.; Gabrielli, L.; Prins, L. J. Chemically Fueled Self-Assembly in Biology and Chemistry. *Angew. Chem. Int. Ed.* **2021**, *60* (37), 20120–20143.

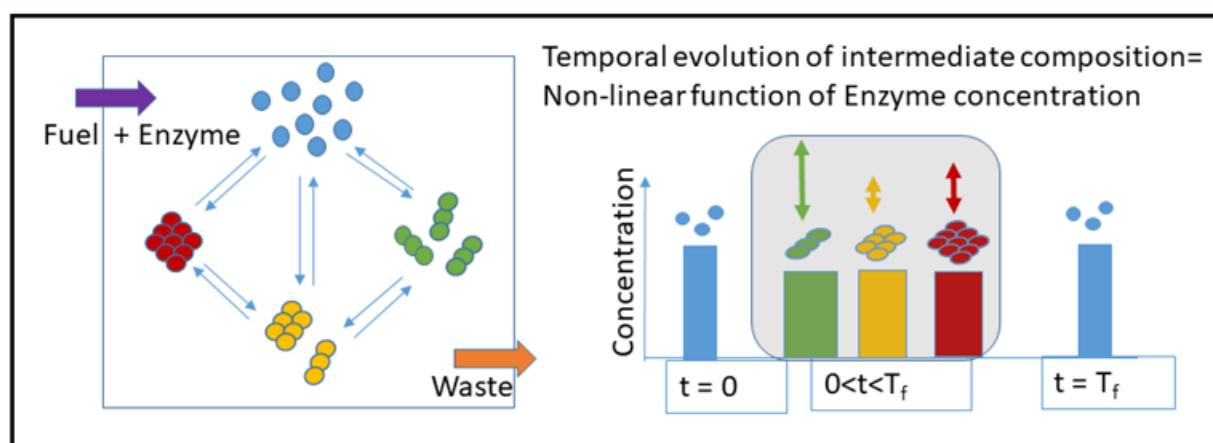
16. Fialkowski, M.; Bishop, K. J. M.; Klajn, R.; Smoukov, S. K.; Campbell, C. J.; Grzybowski, B. A. Principles and Implementations of Dissipative (Dynamic) Self-Assembly. *J. Phys. Chem. B* **2006**, *110* (6), 2482–2496.
17. De, S.; Klajn, R. Dissipative Self-Assembly Driven by the Consumption of Chemical Fuels. *Adv. Mater.* **2018**, *30* (41), e1706750.
18. Corra, S.; Bakić, M. T.; Groppi, J.; Baroncini, M.; Silvi, S.; Penocchio, E.; Esposito, M.; Credi, A. Kinetic and Energetic Insights into the Dissipative Non-Equilibrium Operation of an Autonomous Light-Powered Supramolecular Pump. *Nat. Nanotechnol.* **2022**, *17* (7), 746–751.
19. Pezzato, C.; Cheng, C.; Stoddart, J. F.; Astumian, R. D. Mastering the Non-Equilibrium Assembly and Operation of Molecular Machines. *Chem. Soc. Rev.* **2017**, *46* (18), 5491–5507.
20. te Brinke, E.; Groen, J.; Herrmann, A.; Heus, H. A.; Rivas, G.; Spruijt, E.; Huck, W. T. S. Dissipative Adaptation in Driven Self-Assembly Leading to Self-Dividing Fibrils. *Nat. Nanotechnol.* **2018**, *13* (9), 849–855.
21. Wilson, J. L.; Shim, S.; Yu, Y. E.; Gupta, A.; Stone, H. A. Diffusiophoresis in Multivalent Electrolytes. *Langmuir* **2020**, *36* (25), 7014–7020.
22. Majhi, S.; Bhattacharyya, S. Numerical Study on Diffusiophoresis of a Hydrophobic Nanoparticle in a Monovalent or Multivalent Electrolyte. *Colloids Surf. A Physicochem. Eng. Asp.* **2022**, *648* (129272), 129272.
23. Derjaguin, B.; Sidorenkov, G.; Zubashchenkov, E.; Kiseleva, E. Kinetic Phenomena in Boundary Films of Liquids. *Kolloidn. Zh* **1947**, *9*, 335–347.
24. Prieve, D. C.; Anderson, J. L.; Ebel, J. P.; Lowell, M. E. Motion of a Particle Generated by Chemical Gradients. Part 2. Electrolytes. *J. Fluid Mech.* **1984**, *148* (1), 247–269.
25. Ebel, J. P.; Anderson, J. L.; Prieve, D. C. Diffusiophoresis of Latex Particles in Electrolyte Gradients. *Langmuir* **1988**, *4* (2), 396–406.
26. Gupta, A.; Rallabandi, B.; Stone, H. A. Diffusiophoretic and Diffusioosmotic Velocities for Mixtures of Valence-Asymmetric Electrolytes. *Phys. Rev. Fluids* **2019**, *4* (4).
27. Ault, J. T.; Warren, P. B.; Shin, S.; Stone, H. A. Diffusiophoresis in One-Dimensional Solute Gradients. *Soft Matter* **2017**, *13* (47), 9015–9023.
28. Nery-Azevedo, R.; Banerjee, A.; Squires, T. M. Diffusiophoresis in Ionic Surfactant Gradients. *Langmuir* **2017**, *33* (38), 9694–9702.
29. Shim, S. Diffusiophoresis, Diffusioosmosis, and Microfluidics: Surface-Flow-Driven Phenomena in the Presence of Flow. *Chem. Rev.* **2022**, *122* (7), 6986–7009.

30. Velegol, D.; Garg, A.; Guha, R.; Kar, A.; Kumar, M. Origins of Concentration Gradients for Diffusiophoresis. *Soft Matter* **2016**, *12* (21), 4686–4703.
31. Abécassis, B.; Cottin-Bizonne, C.; Ybert, C.; Ajdari, A.; Bocquet, L. Boosting Migration of Large Particles by Solute Contrasts. *Nat. Mater.* **2008**, *7* (10), 785–789.
32. Shin, S.; Shardt, O.; Warren, P. B.; Stone, H. A. Membraneless Water Filtration Using CO₂. *Nat. Commun.* **2017**, *8* (1), 15181.
33. Prieve, D. C. Migration of a Colloidal Particle in a Gradient of Electrolyte Concentration. *Adv. Colloid Interface Sci.* **1982**, *16* (1), 321–335.
34. Staffeld, P. O. & Quinn, J. A. Diffusion-induced banding of colloid particles via diffusiophoresis. *J. Colloid Interface Sci.* **130**, 69–87 (1989).
35. Burkholder, E. W.; Brady, J. F. Tracer Diffusion in Active Suspensions. *Phys. Rev. E.* **2017**, *95* (5–1), 052605.
36. Shandilya, E.; Dasgupta, B.; Maiti, S. Interconnectivity between Surface Reactivity and Self-Assembly of Kemp Elimination Catalyzing Nanorods. *Chemistry* **2021**, *27* (29), 7831–7836.
37. Ramm, B.; Goychuk, A.; Khmelinskaia, A.; Blumhardt, P.; Eto, H.; Ganzinger, K. A.; Frey, E.; Schwille, P. A Diffusiophoretic Mechanism for ATP-Driven Transport without Motor Proteins. *Nat. Phys.* **2021**, *17* (7), 850–858.
38. Sear, R. P. Diffusiophoresis in Cells: A General Nonequilibrium, Nonmotor Mechanism for the Metabolism-Dependent Transport of Particles in Cells. *Phys. Rev. Lett.* **2019**, *122* (12), 128101.
39. Pizauro, J. M.; Ciancaglini, P.; Leone, F. A. Allosteric Modulation by ATP, Calcium and Magnesium Ions of Rat Osseous Plate Alkaline Phosphatase. *Biochim. Biophys. Acta* **1993**, *1202* (1), 22–28.
40. Mahato, R. R.; Shandilya, E.; Dasgupta, B.; Maiti, S. Dictating Catalytic preference and Activity of a Nanoparticle by Modulating Its Multivalent Engagement. *ACS Catal.* **2021**, *11* (14), 8504–8509.
41. Mortensen, N. A.; Okkels, F.; Bruus, H. Reexamination of Hagen-Poiseuille Flow: Shape Dependence of the Hydraulic Resistance in Microchannels. *Phys. Rev. E Stat. Nonlin. Soft Matter Phys.* **2005**, *71* (5).
42. Zhao, X. *et al.* Substrate-driven chemotactic assembly in an enzyme cascade. *Nat. Chem.* **10**, 311–317 (2018).
43. Agudo-Canalejo, J.; Illien, P.; Golestanian, R. Phoresis and Enhanced Diffusion Compete in Enzyme Chemotaxis. *Nano Lett.* **2018**, *18* (4), 2711–2717.

44. Aubert, S.; Bezagu, M.; Spivey, A. C.; Arseniyadis, S. Spatial and Temporal Control of Chemical Processes. *Nat. Rev. Chem.* **2019**, *3* (12), 706–722.
45. Chen, R.; Neri, S.; Prins, L. J. Enhanced Catalytic Activity under Non-Equilibrium Conditions. *Nat. Nanotechnol.* **2020**, *15* (10), 868–874.
46. Nguindjel, A.-D. C.; de Visser, P. J.; Winkens, M.; Korevaar, P. A. Spatial Programming of Self-Organizing Chemical Systems Using Sustained Physicochemical Gradients from Reaction, Diffusion and Hydrodynamics. *Phys. Chem. Chem. Phys.* **2022**, *24* (39), 23980–24001.
47. Shandilya, E.; Maiti, S. Self-Regulatory Micro- and Macroscale Patterning of ATP-Mediated Nanobioconjugate. *ACS Nano* **2023**, *17* (5), 5108–5120.
48. Bian, T.; Gardin, A.; Gemen, J.; Houben, L.; Perego, C.; Lee, B.; Elad, N.; Chu, Z.; Pavan, G. M.; Klajn, R. Electrostatic Co-Assembly of Nanoparticles with Oppositely Charged Small Molecules into Static and Dynamic Superstructures. *Nat. Chem.* **2021**, *13* (10), 940–949.
49. Dhiman, S.; Jain, A.; Kumar, M.; George, S. J. Adenosine-Phosphate-Fueled, Temporally Programmed Supramolecular Polymers with Multiple Transient States. *J. Am. Chem. Soc.* **2017**, *139* (46), 16568–16575.
50. Epstein, I. R.; Xu, B. Reaction-Diffusion Processes at the Nano- and Microscales. *Nat. Nanotechnol.* **2016**, *11* (4), 312–319.
51. Landge, A. N.; Jordan, B. M.; Diego, X.; Müller, P. Pattern Formation Mechanisms of Self-Organizing Reaction-Diffusion Systems. *Dev. Biol.* **2020**, *460* (1), 2–11.
52. Tian, L.; Li, M.; Liu, J.; Patil, A. J.; Drinkwater, B. W.; Mann, S. Nonequilibrium Spatiotemporal Sensing within Acoustically Patterned Two-Dimensional Protocell Arrays. *ACS Cent. Sci.* **2018**, *4* (11), 1551–1558.
53. Ragazzon, G.; Malferrari, M.; Arduini, A.; Secchi, A.; Rapino, S.; Silvi, S.; Credi, A. Autonomous Non-Equilibrium Self-Assembly and Molecular Movements Powered by Electrical Energy. *Angew. Chem. Int. Ed.* **2023**, *62* (5), e202214265.
54. Qiu, Y.; Feng, Y.; Guo, Q.-H.; Astumian, R. D.; Stoddart, J. F. Pumps through the Ages. *Chem* **2020**, *6* (8), 1952–1977.
55. Kathan, M.; Crespi, S.; Thiel, N. O.; Stares, D. L.; Morsa, D.; de Boer, J.; Pacella, G.; van den Enk, T.; Kobauri, P.; Portale, G.; Schalley, C. A.; Feringa, B. L. A Light-Fuelled Nanoratchet Shifts a Coupled Chemical Equilibrium. *Nat. Nanotechnol.* **2022**, *17* (2), 159–165.
56. Grzybowski, B. A. *Chemistry in Motion: Reaction-Diffusion Systems for Micro- and Nanotechnology*; Wiley-Blackwell: Hoboken, NJ, 2009.

CHAPTER 5

Kinetic Insights into Enzymatically Controlled Transiency in Multivalent Fuel-Driven Multistep Assembly



This is adapted reproduction from Shandilya, E.; Maiti, S. Deconvolution of Transient Species in a Multivalent Fuel-driven Multistep Assembly under Dissipative Conditions. *ChemSystemsChem* **2020**, 2 (2), e1900040.

5.1. Introduction

Systems chemistry offers a unique opportunity to unravel the intricate mechanisms underlying emergent properties resulting from the complex interactions among multiple entities.¹⁻² By understanding and formulating these emergent properties, we can gain valuable insights into the chemical origins and evolutionary processes of species from the ground up.³⁻⁵ Furthermore, exploring how different interacting and inter-converting species alter their compositions in a spatiotemporal manner holds tremendous potential. Multivalent interactions between molecules play a crucial role in various biological processes, such as lectin-carbohydrate binding, cell surface adhesion, and host-pathogen interactions.⁶⁻⁷ These interactions also regulate dynamic self-assembly processes within living systems, such as microtubule dynamics and the growth and contraction of actin filaments.⁸⁻¹¹ The use of chemical fuels, such as guanosine triphosphate (GTP) and adenosine triphosphate (ATP), further controls the assembly-disassembly processes of microtubules and actin filaments, respectively. It is important to note that the non-covalent binding interaction between the chemical fuel and associated building blocks is paramount in driving these processes, transcending the inherent rate of association of the building blocks themselves.¹² In recent years, supramolecular chemists have been captivated by the idea of designing transient synthetic systems driven by chemical fuels, as opposed to thermodynamically stable systems.¹³⁻²³ These transient systems offer distinct advantages, including programmability and renewability. The ability to pre-program and regenerate these fuel-responsive materials opens up possibilities in sustained and programmed drug delivery vehicles, as well as in the design of complex reaction networks that mimic advanced materials with life-like properties.

To create adaptable and controllable materials, utilizing chemical fuels with multivalent properties has emerged as an attractive approach.²⁴⁻²⁶ Notably, researchers have successfully employed the multivalent property of ATP as a chemical fuel to drive the formation of vesicles and pulsating polymer micelles. By introducing enzymes, such as potato apyrase, the system achieves transiency, leading to the formation of ATP-driven vesicular assemblies and functional nanoreactors.²⁴ This principle has also been extended to the transient assembly of nanoparticles and the generation of cooperative but self-destructive catalytic systems.²⁷⁻³³ Despite the progress made, the complexity and dynamic properties of these transiently assembled functional systems still fall short of those found in natural systems.³⁸⁻⁴¹ Therefore, a detailed understanding of how compositions of each assembled species in multivalent fuel-driven multi-step assemblies change over time, along with the overall strength of dissipation,

is essential. By investigating the kinetic parameters involved in the complex assembly/disassembly processes, we can further explore the full potential of fuel-responsive, transient self-assembly. To achieve this, our study at hand utilizes Python programming to quantitatively and qualitatively analyze the kinetic aspects of multistep assembly formation and examine how the dissipative strength modulates the intermediate compositions of each element within these assemblies.

5.2. Methods and Principle

To study the mechanism and kinetics of multistep assembly formation in transient conditions computational methods were employed. Firstly, a reaction system was devised and for that system, a set of chemical equations were formed and rate expressions were written according to the mass-action kinetics which gave us the rate of change of concentration of the species involved in the reaction system. Thus, formed ordinary differential equations (ODEs) were solved using Python programming. To solve ODEs, the **odeint** function from the “**Python 3**” directory was used and for plotting the concentration versus time graph for each component of the system, the **matplotlib** library function was used. We have employed a similar method to understand the role of the number of valent sites in fuel during assembly formation. As the previous reports suggest, the binding efficiency of a ligand depends on the number of valent sites available for interaction with the monomer.⁴⁷⁻⁴⁹ To understand the role of the stabilizing ligand (fuel) and the number of binding sites in stabilizing ligand during transient assembly formation, we have made the following assumptions:

Assembling and disassembling principle

All the assemblies formed throughout the present work are supposed to form only with monomer association or dissociation in a sequential manner.⁴² The association and dissociation rate constants are assumed to be the same throughout the aggregation. The association and dissociation reactions among the reaction components are assumed to have elementary order (to study kinetics). However, in some cases, we have also shown the effect in the case of overall second order i.e. first order with respect to both monomer and fuel. As the number of valent sites in fuel is decreased by one, the related kinetic constant is assumed to be reduced by 10-fold and vice-versa. The fuel being used in the system can be cleaved using an enzyme, E. When enzyme, E cleaves the multivalent fuel it forms a byproduct (P) which does not have any effect on the assembly of monomers and therefore towards assembly formation.

5.2.1. Classification of systems

Systems of our interest had a pool of all the components like monomers or surfactants (S), fuels i.e. stabilizing ligands [(trivalent (T), divalent (D), monovalent (M)] and Enzyme (E). Various types of systems were designed using different fuels (T, D, and M), S, and E. According to the number of valent sites or the number of interaction-prone sites, the fuels had been classified into three types: 1. Trivalent fuel (T, having three binding sites), 2. Divalent fuel (D, having two binding sites), 3. Monovalent fuel (M, fuel with only one binding site).

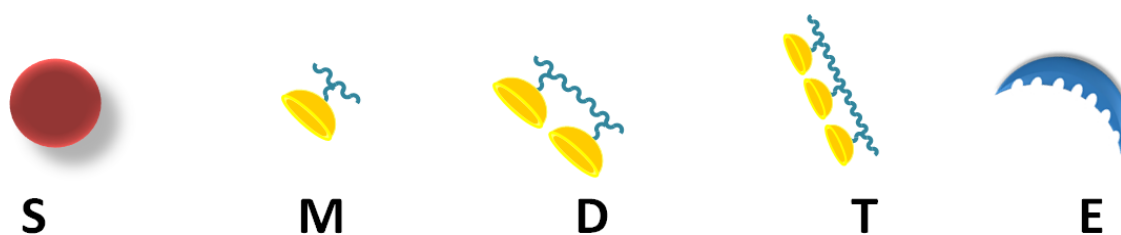


Figure 5.1. Graphical representation of monomer (S), fuels (M, D, and T), and enzyme (E)

5.2.2. Self-driven assembly (system without fuel)

This type of system had only S and the assembly was formed with the addition of one unit S to the former assembly. Using the above-mentioned assembling principle, the assembled states were such that $A_2, A_3, A_4, \dots, A_n$, where n is the number of S units used to form a particular assembly.

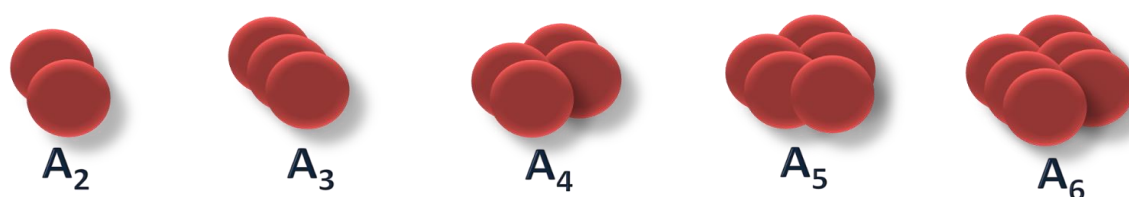


Figure 5.2. Graphical representation of assemblies for the system when there is no fuel involved.

5.2.3. Fuel-driven assembly

Here, the assemblies formed were driven by fuel (T, D, M). Based on the type of fuel (T or D or M) employed, the assemblies formed were classified into the following three types:

5.2.3.1. Monovalent fuel-mediated assembly

Assemblies formed with monovalent fuel got their stability from M and the assemblies formed were denoted as AM , A_2M_2 , A_3M_3 , A_nM_m , where n suggests the number of M used to form a particular assembly and m is the number of fuel molecules involved to stabilize the system. Here, as various formed assemblies suggested that the number of S and M would be the same in each case, i.e., $n = m$.

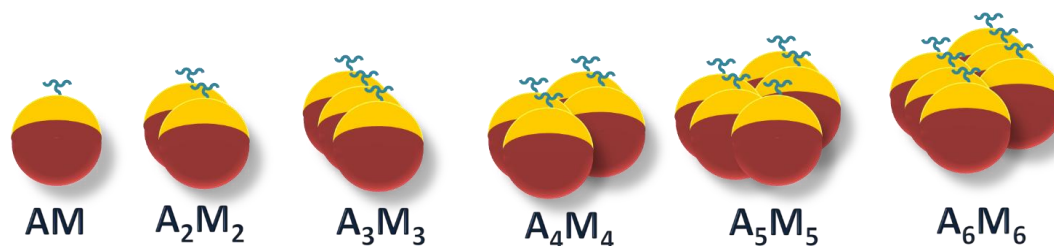


Figure 5.3. Graphical representation of assemblies when monovalent fuel (M) is present.

5.2.3.2. Divalent fuel-mediated assembly

As the name suggests, a divalent fuel (D) have two valent sites where S can bind to form A_2D , that is, two S molecules are employed with one D to form a divalent fuel-mediated assembly. Assemblies involved with A and D were denoted as A_2D , A_4D_2 , A_6D_3 , A_nD_m , where n is the number of S molecules and m be the number of D molecules involved in a particular assembly. In the case of D, the number of D molecules would be half of the number of S molecules in a specific assembly, which means the numerical value of m to be the half of n , i.e., $m = n/2$.

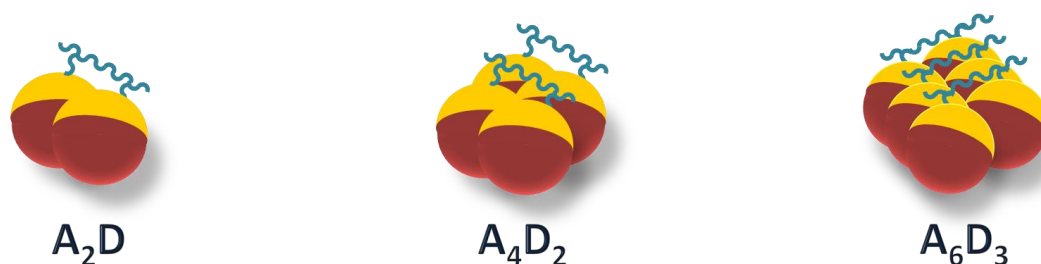


Figure 5.4. Graphical representation of assemblies when a divalent fuel (D) is present in the system.

5.2.3.3. Trivalent fuel-mediated assembly

In this case, the trivalent fuel (T) was used to form an assembly. Here, as the number of valent sites is three in T, so it can stabilize a system of three S molecules with a single fuel molecule.

The assemblies formed here are such that A_3T , A_6T_2 , A_9T_3 ,..... A_nT_m , where n is the number of S molecules and m is the number of T molecules. In the case of T, the number of T molecules will be one-third of the number of S molecules incorporated in a particular assembly, i.e., $m = n/3$.



Figure 5.5. Graphical representation of assemblies formed when a trivalent fuel (T) is present in the system.

5.2.4. Incorporation of enzyme E

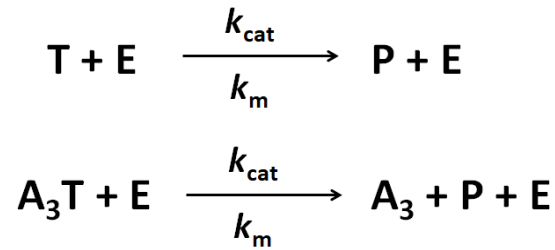
Once done with the above-mentioned systems, the enzyme was introduced into the systems involving fuels. In accordance with section 1, E was used to cleave the fuel, T. But as our assemblies with T were as A_nT_m , (here $m = n/3$) which meant that E could cleave assembly (A_nT_m) as well, to give the relative number of S (as by-product P does not provide any additional stability to form the assembly of S). In this section, the action of the enzyme is described on fuel (T only) and on trivalent-fuel mediated assembly (A_nT_m only).

5.2.4.1. Trivalent fuel (T) with E

T has been considered as the substrate of E. So, E can cleave the T to the by-product, P irreversibly.

5.2.4.2. T mediated assembly in the presence of E

As we have previously mentioned that the E can also react with the A_3T in a similar manner as T. In this case, A_3T will give an A_3 assembly (three S molecules) with P in the presence of an enzyme, E.



Scheme 5.1. Reaction schemes for enzymatic action on fuel, T, and A₃T assembly

5.2.5. Mechanistic study of single-step assembly formation

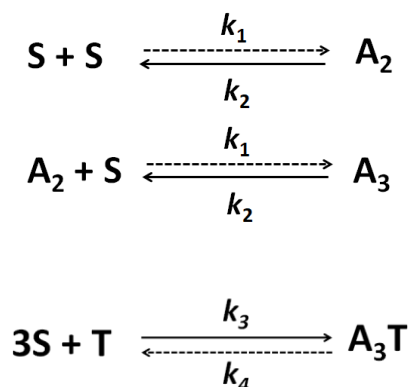
In this section, the mechanism of formation of certain assemblies is studied, which involves the formation of both single steps as well as multistep assemblies. **Python** modeling is employed to measure the rate of change of compositions of participants. The assemblies involved here are classified based on the presence and absence of enzymes.

5.2.5.1. A₃T assembly

A₃T assembly being the smallest assembly in the presence of T is studied in both the presence and absence of enzyme. The composition of various constituents is determined following the mass-action kinetics. In this part of the work, we are concerned about assembly formed only up to A₃T formation, ignoring, what will happen next.

5.2.5.2. A₃T formation in the absence of E

To study the kinetics of A₃T assembly in the absence of an enzyme, the system mentioned in section 5.2.3.3 is considered, as this reaction has S units and T units. For this purpose, we take into account the binding affinities of the formation of A₃T from three S molecules and one T unit and the deformation of A₃T into its constituents. As already mentioned in Section 1 that the binding affinity of S with T is more than its self-binding affinity. Reaction steps included during the formation of the A₃T assembly are given in scheme 5.2 where the solid arrows show the prominent step (it can be either forward or backward independently), on the other hand, dashed arrows show the less probable step.



Scheme 5.2. Reaction scheme for A_3T assembly formation in the absence of enzyme

Where rate constants have been chosen according to their binding affinity such that $k_1 = 0.1 \text{ M}^{-1}\text{s}^{-1}$, $k_2 = 10 \text{ M}^{-1}\text{s}^{-1}$, $k_3 = 10^3 \text{ M}^{-3}\text{s}^{-1}$, $k_4 = 10^{-3} \text{ s}^{-1}$ and the initial concentration of S and T are 100 M for both. After the formation of equations reminding all the probable possibilities, to obtain the rate of change of concentration of each species was treated according to mass-action kinetics which leads to the formation of the following rate expressions:

$$\frac{d[\text{S}]}{dt} = -3(k_3)C_S^3C_T + 3(k_4)C_{A_3T} - 2(k_1)C_S^2 + 2(k_2)C_{A_2} - (k_1)C_S C_{A_2} + (k_2)C_{A_3}$$

$$\frac{d[\text{T}]}{dt} = -(k_3)C_S^3C_T + (k_4)C_{A_3T}$$

$$\frac{d[\text{A}_3\text{T}]}{dt} = (k_3)C_S^3C_T - (k_4)C_{A_3T}$$

$$\frac{d[\text{A}_2]}{dt} = (k_1)C_S^2 - (k_2)C_{A_2} - (k_1)C_S C_{A_2} + (k_2)C_{A_3}$$

$$\frac{d[\text{A}_3]}{dt} = (k_1)C_S C_{A_2} - (k_2)C_{A_3}$$

Where C_x shows the concentration of reactant X at any time t.

To solve the above-formed ordinary differential equations (ODEs), the following written Python model 1 was used. Here, the time limits chosen were from 0 to 35 units. This script is able to calculate the composition of S, T, A₃T, A₂, and A₃ between the provided time limits.

```
#python model 1
#A3T WITHOUT ENZYME
import numpy as np
from scipy.integrate import odeint
%matplotlib inline
import matplotlib.pyplot as plt

def rxn(z,t) :
    k1 = 0.1
    k2 = 10
    k3 = 10**3
    k4 = 10**(-3)

    r1 = k1 * z[0]*z[0]
    r2 = k2 * z[1]
    r3 = k1 * z[0]*z[1]
    r4 = k2 * z[2]
    r5 = k3 * z[0]*z[0]*z[0]*z[3]
    r6 = k4 * z[4]
    dMdt = 2*(-r1 + r2) - r3 + r4 + 3*(-r5 + r6) #S
    dAdt = r1 - r2 - r3 + r4 #A2
    dBdt = r3 - r4 #A3
    dCdt = - r5 + r6 #T
    dDdt = r5 - r6 #A3T
    return[dMdt,dAdt,dBdt,dCdt,dDdt]

t = np.linspace(0,35,71)
z0 =[100,0,0,100,0]
conc = odeint(rxn,z0,t,mxstep = 2000)
cM = conc[:,0]
cA = conc[:,1]
cB = conc[:,2]
cC = conc[:,3]
cD = conc[:,4]
plt.plot(t,cM)
plt.plot(t,cA)
plt.plot(t,cB)
plt.plot(t,cC)
plt.plot(t,cD)
```

The output obtained was a concentration versus time plot showing the composition profile for each involved species. From that output, the conc. of A_3T versus time is shown in Figure 5.7.

5.2.5.3. A_3T formation in the presence of E

After the A_3T assembly in the presence of a fuel (T) the enzyme was introduced into the system. The enzyme acts as a cleaving agent for the multivalent fuel (here, T) and forms by-product P, which doesn't have any influence on assembly or surfactant molecules (according to the assumption). This time also we were eager to know about the concentration of the species (S, T, A_3T , A_2 , and A_3) involved during the reaction. To achieve this goal, we took care to involve all the species that could participate in the formation of the A_3T assembly. To devise such a system, model 1 was considered. According to this model, from the pool of S, T, and E, the three S monomers along with T can form an A_3T assembly, or S units themselves can form an A_3 aggregate (in two steps). Coming to the role of an enzyme in the system, E has two substrates T and A_3T , where T can directly form P and when reacts with A_3T can form three S units/ A_3 assembly. Taking into account the possible fate for each species in the system, the rate equations were prepared and each reactant with enzyme had been treated in accordance with Michaelis-Menton kinetics. After designing this model, the rate-law expression for each involved species was proposed

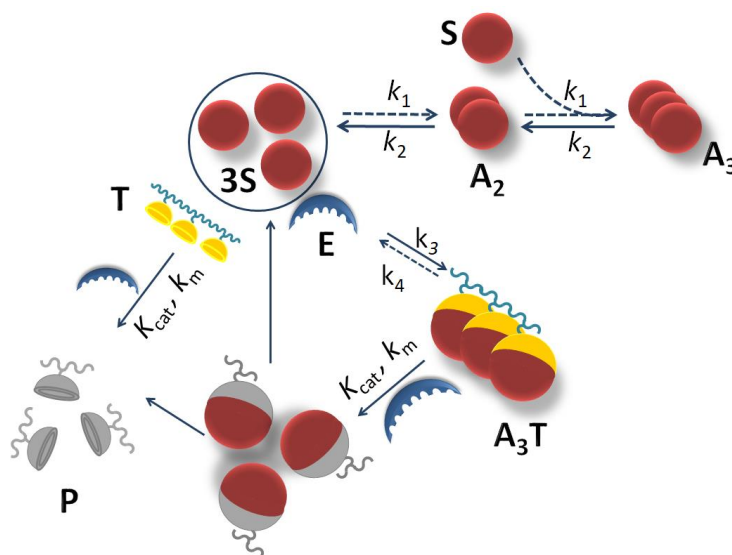
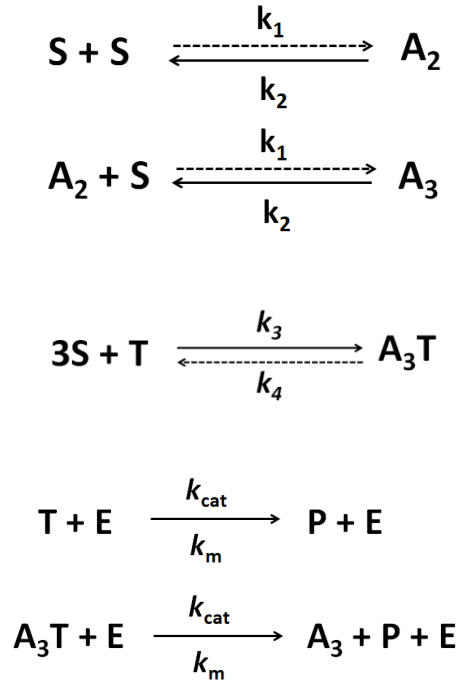


Figure 5.6 Schematic representation of A_3T assembly formation in the presence of an enzyme (model 1)



Scheme 5.3. Reaction scheme for A_3T assembly formation in the presence of enzyme

$$\frac{d[\text{S}]}{dt} = -3(k_3)C_S^3C_T + 3(k_4)C_{A_3T} - 2(k_1)C_S^2 + 2(k_2)C_{A_2} - (k_1)C_S C_{A_2} + (k_2)C_{A_3}$$

$$\frac{d[\text{T}]}{dt} = -(k_3)C_S^3C_T + (k_4)C_{A_3T} - \frac{[\text{E}][\text{T}]k_{\text{cat}}}{[\text{T}] + k_m}$$

$$\frac{d[\text{A}_3\text{T}]}{dt} = (k_3)C_S^3C_T - (k_4)C_{A_3T} - \frac{[\text{A}_3\text{T}][\text{T}]k_{\text{cat}}}{[\text{A}_3\text{T}] + k_m}$$

$$\frac{d[\text{A}_2]}{dt} = (k_1)C_S^2 - (k_2)C_{A_2} - (k_1)C_S C_{A_2} + (k_2)C_{A_3}$$

$$\frac{d[\text{A}_3]}{dt} = (k_1)C_S C_{A_2} - (k_2)C_{A_3} + \frac{[\text{A}_3\text{T}][\text{T}]k_{\text{cat}}}{[\text{A}_3\text{T}] + k_m}$$

```

#python model 2
#A3T assembly in the presence of enzyme
import numpy as np
from scipy.integrate import odeint
%matplotlib inline
import matplotlib.pyplot as plt
#
def rxn(z,t) :
k1 = 0.1
k2 = 10
k3 = 10**3
k4 = 10**(-3)

kcat = 250
km = 1
E = 0.1
k = kcat*E

r1 = k1 * z[0]*z[0]
r2 = k2 * z[1]
r3 = k1 * z[0]*z[1]
r4 = k2 * z[2]
r5 = k3 * z[0]*z[0]*z[0]*z[3]
r6 = k4 * z[4]
ra = (k * z[3])/(km + z[3])
rb = (k * z[4])/(km + z[4])

dMdt = 2*(-r1 + r2) - r3 + r4 + 3*(-r5 + r6) #S
dAdt = r1 - r2 - r3 + r4 #A2
dBdt = r3 - r4 + rb #A3
dCdt = - r5 + r6 - ra #T
dDdt = r5 - r6 - rb #A3T
return[dMdt,dAdt,dBdt,dCdt,dDdt]
t = np.linspace(0,40,41)
z0 =[100,0,0,100,0]
conc = odeint(rxn,z0,t, mxstep = 2000)

cM = conc[:,0]
cA = conc[:,1]
cB = conc[:,2]
cC = conc[:,3]
cD = cD = conc[:,4]
plt.plot(t,cM)
plt.plot(t,cA)

```

```
plt.plot(t,cB)
plt.plot(t,cC)
plt.plot(t,cD)
```

To solve these reactions python model 2 was followed with the following parameters: $k_1 = 0.1 \text{ mM}^{-1}\text{s}^{-1}$, $k_2 = 10 \text{ mM}^{-1}\text{s}^{-1}$, $k_3 = 10^3 \text{ mM}^{-3}\text{s}^{-1}$, $k_4 = 10^{-3} \text{ s}^{-1}$, $k_{\text{cat}} = 250 \text{ s}^{-1}$, $K_m = 1 \text{ mM}$ and the initial concentration of S and T are 100 mM for both while the concentration of E was varied from 0.01 to 0.1 mM. The result obtained using the above constraints was then processed and the concentration of A_3T assembly versus the time graph is shown in Figure 5.8.

5.3. Results and Discussion

Multivalent fuel-driven assembly processes has been previously illustrated in many earlier literatures both theoretically and experimentally, however, mostly in systems having one receptor-one ligand (host-guest) type.³⁸⁻⁴¹ We have demonstrated here how non-covalent multivalent interaction helps to propagate the assembly of monomeric units to form a larger assembly, which is analogous to the formation of micelles, vesicles, bilayers, etc. To understand that, herein we have assumed a model inspired by the theory of kinetics of supramolecular polymerization) as discussed elsewhere (Figure 5.7).⁴²⁻⁴⁴ To begin with, we have classified the assemblies based on the type of fuel present in the system. For simplicity, we have shown how monomer (S) formed a hexameric state in the absence and presence of stabilizing ligand (T, trivalent fuel; D, divalent fuel; M, monovalent fuel) (as shown in Figure 1).^[10a] We have shown how a monomer (S) formed a hexameric state (A_6) in the absence and presence of fuels. The fuels used here have been considered as monovalent (M), divalent (D), and trivalent (T) ligands. We assumed the formation of monomeric S to A_6 is thermodynamically not feasible, resembling to the non-formation of aggregates below its critical aggregation concentration (CAC). The aggregates can only be formed only in the presence of a fuel that provides the stabilizing interaction.

This is akin to the formation of micellar or vesicular aggregates (much before CAC) made up of surfactants containing charged head groups by using oppositely charged counter-ions.^{24,45-46} It has been demonstrated in recent examples that triphosphate can stabilize the formation of micelles having surfactant molecule, having triazacyclononone moiety chelated with Zn^{2+} ion as the head group almost one order of magnitude earlier than its critical micellar concentration, whereas aggregation starts in case of monophosphate only two times before the original CMC of the surfactant. Thus, we assume when M, D, and T are present in the system the initial

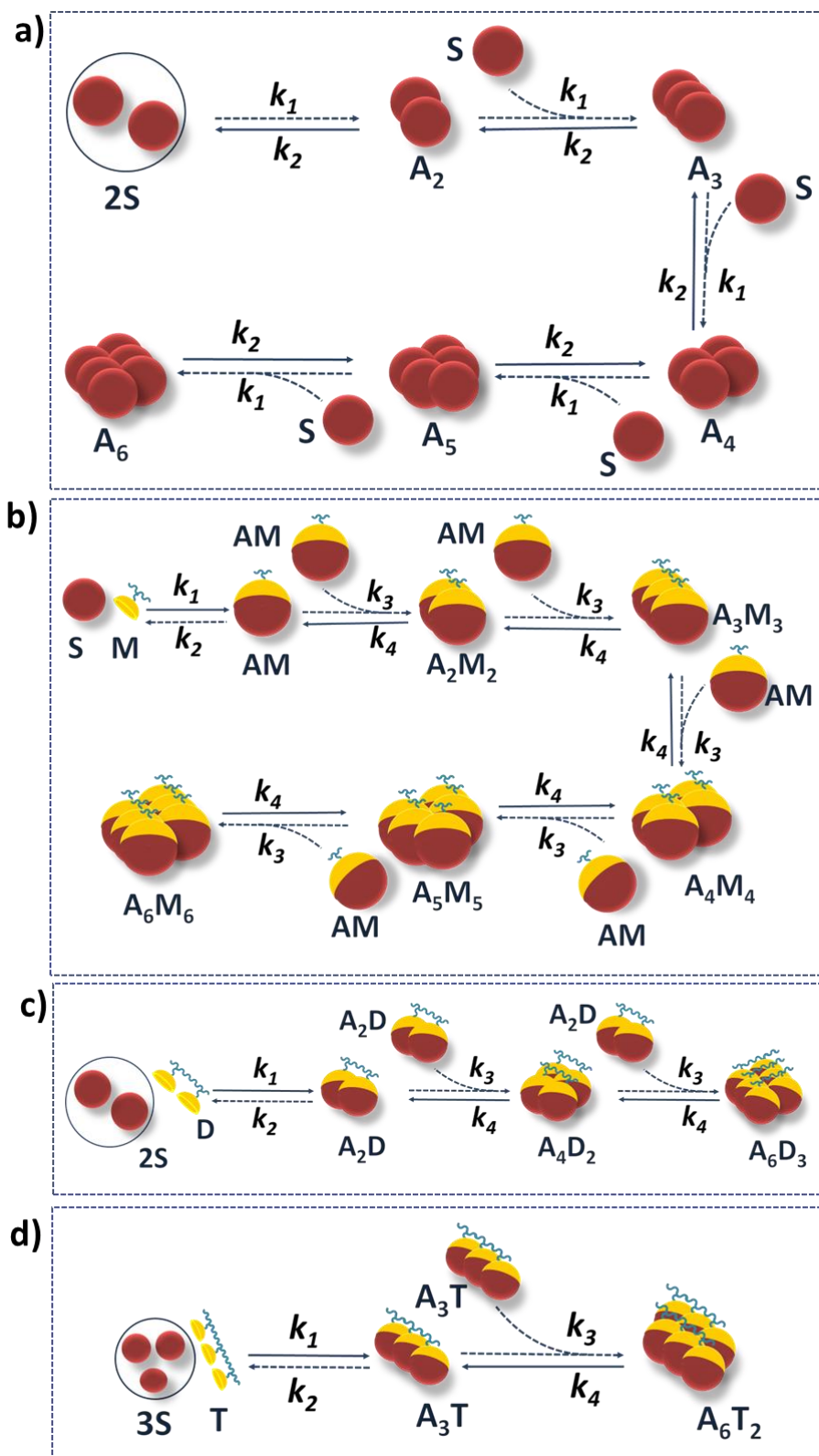


Figure 5.7. Schematic representation of hexameric assemblies formed based on the number of valent sites present in the fuel used to form assembly (a) no fuel or self-assisted assembly ($k_1 = 0.1 \text{ mM}^{-1}\text{s}^{-1}$); (b) monovalent fuel assisted assembly ($k_1 = 10 \text{ mM}^{-1}\text{s}^{-1}$, $k_3 = 0.1 \text{ mM}^{-1}\text{s}^{-1}$); (c) divalent fuel assisted assembly ($k_1 = 10^2 \text{ mM}^{-2}\text{s}^{-1}$, $k_3 = 0.1 \text{ mM}^{-1}\text{s}^{-1}$); (d) trivalent fuel assisted assembly ($k_1 = 10^3 \text{ mM}^{-3}\text{s}^{-1}$, $k_3 = 0.1 \text{ mM}^{-1}\text{s}^{-1}$).

formation constant of the monomer-ligand conjugate (namely, AM, A₂D, and A₃T) has increased from 0.1 mM⁻¹s⁻¹ (in the absence of any stabilizing ligand, Figure 5.7a) to 10 mM⁻¹s⁻¹, 10² mM⁻²s⁻¹ and 10³ mM⁻³s⁻¹, respectively (Figure 5.2-5.5, 5.7b-d). It is worth mentioning here that the chosen unit of concentration is millimolar and the time is in seconds. This assumption in binding constant is in concurrence with previous literature reports where it has been shown that the presence of additional valency can increase the binding efficiency by almost one to three orders of magnitude.⁴⁷⁻⁴⁹ After the formation of the initial adduct the propagation to form a hexameric adduct in all cases has a similar forward constant as assumed in the first case where no stabilizing ligand was present which is 0.1M⁻¹s⁻¹. It means AM to A₂M₂ to A₆M₆, A₂D to A₄D₂ to A₆D₃, and A₃T to A₆T₂ have been formed with a forward rate constant of 0.1 M⁻¹s⁻¹ as there is no additional stability being enforced in the system towards its propagation. The above-mentioned kinetic constants and assumptions have been used in the rest of the study.

The prime aim of this study is to interpret the multivalent fuel-driven multistep assembly processes under dissipative conditions, especially to investigate the temporal compositional behavior of assembly-disassembly of intermediate components. Before that, we used our model to estimate single-step assembly under dissipative conditions. Herein, three monomers in the presence of T will assemble to A₃T, but as the system is premixed with an enzyme-like molecule (E) which can dissociate T to P with an assumption that P has no ability to form the assembly. In all cases, we have taken the overall fourth order forward rate constant between S and T to form A₃T was kept at 10³ mM⁻³s⁻³, and turnover number (k_{cat}) and Michaelis constant (k_m) of the enzyme, E towards its substrate T are 250 s⁻¹ and 1 mM, respectively. We have also performed calculations by assuming overall second order (unimolecular with respect to both S and T) (data not shown). We have assumed that the dissociation of T to P takes place at a similar rate both in free (in T) and bound state (in A₃T). In addition, we have analyzed the product amount using a different pathway where 3S turns to A₃ in the absence of fuel as depicted in Figure 5.7a which is a non-spontaneous process (having forward rate constant 0.1 mM⁻¹s⁻¹ in each step) and then that A₃ combines with T to form A₃T with a forward rate constant of 10³ mM⁻¹s⁻¹ (similar to the combination of 3S and T). However, the amount of excess A₃T is negligible in this case. This prompted us to neglect the contribution of the assembly in this type of pathway where aggregation of only monomer leads to assembly without fuel and then re-associated with fuel. Overall, in the one-step assembly process, it has been found that the lifetime of the assembly depends proportionally on the amount of E at a fixed concentration of fuel, T, or on the amount of T at a fixed concentration of E (Figure 5.9).

It is worth mentioning, these kinds of systems have been reported recently in literature with both experimental and theoretical evidence.²⁴⁻³³ It has been shown that the fuel can control the lifetime of the assembly as well as the properties, like chemical reactivity, fluorescence signal, and chirality associated with the assembly process. Next, we performed calculations based on a two-step assembly process under dissipative conditions. The kinetic parameter has been kept similar as shown in Figure 5.7d for the binding of S and T. The schematic of the overall assembly-disassembly process has been given in Figure 5.10a. Interestingly, here dissociation of T also takes place when the system is in the

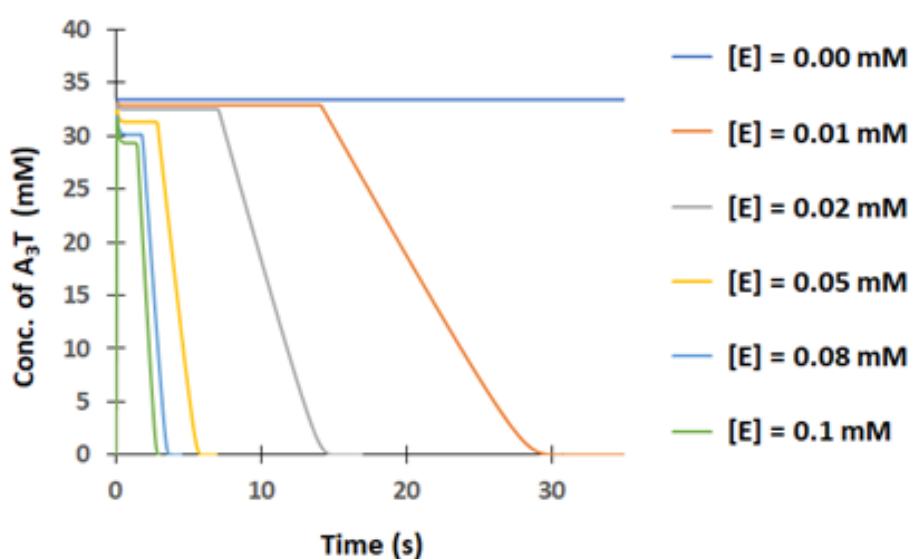


Figure 5.8 Concentration (A_3T in M) versus time (in s) graph in the absence and presence of an enzyme (considering elementary order for each step).

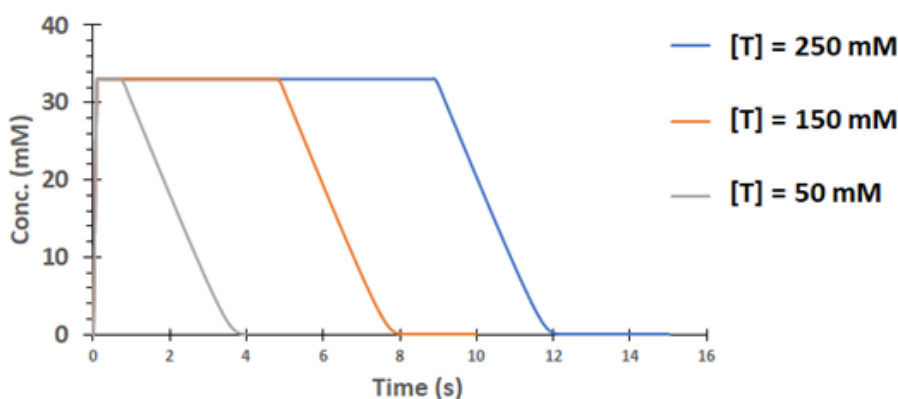


Figure 5.9 Compositional profile for A_3T assembly over time at different concentration of fuel, T (50 mM, 150 mM and 250 mM) at $[E] = 0.05$ mM, $k_1 = 0.1$ mM⁻¹s⁻¹, $k_2 = 10$ mM⁻¹s⁻¹, $k_3 = 10^3$ mM⁻³s⁻¹, $k_4 = 10^{-3}$ s⁻¹, $k_{cat} = 250$ s⁻¹, $k_m = 1$ mM

intermediate A_3T state as well as the A_6T_2 state. Therefore, simultaneously A_3T gets dissociated to A_3 to monomer $3S$ and A_6T_2 gets dissociated to A_3T , A_6 , and $6S$. At first, we run the simulation in the absence of an enzyme to track the compositions of A_3T and A_6T_2 with time to show that the assembly is stable and their compositions remain unchanged over time (5.10b).

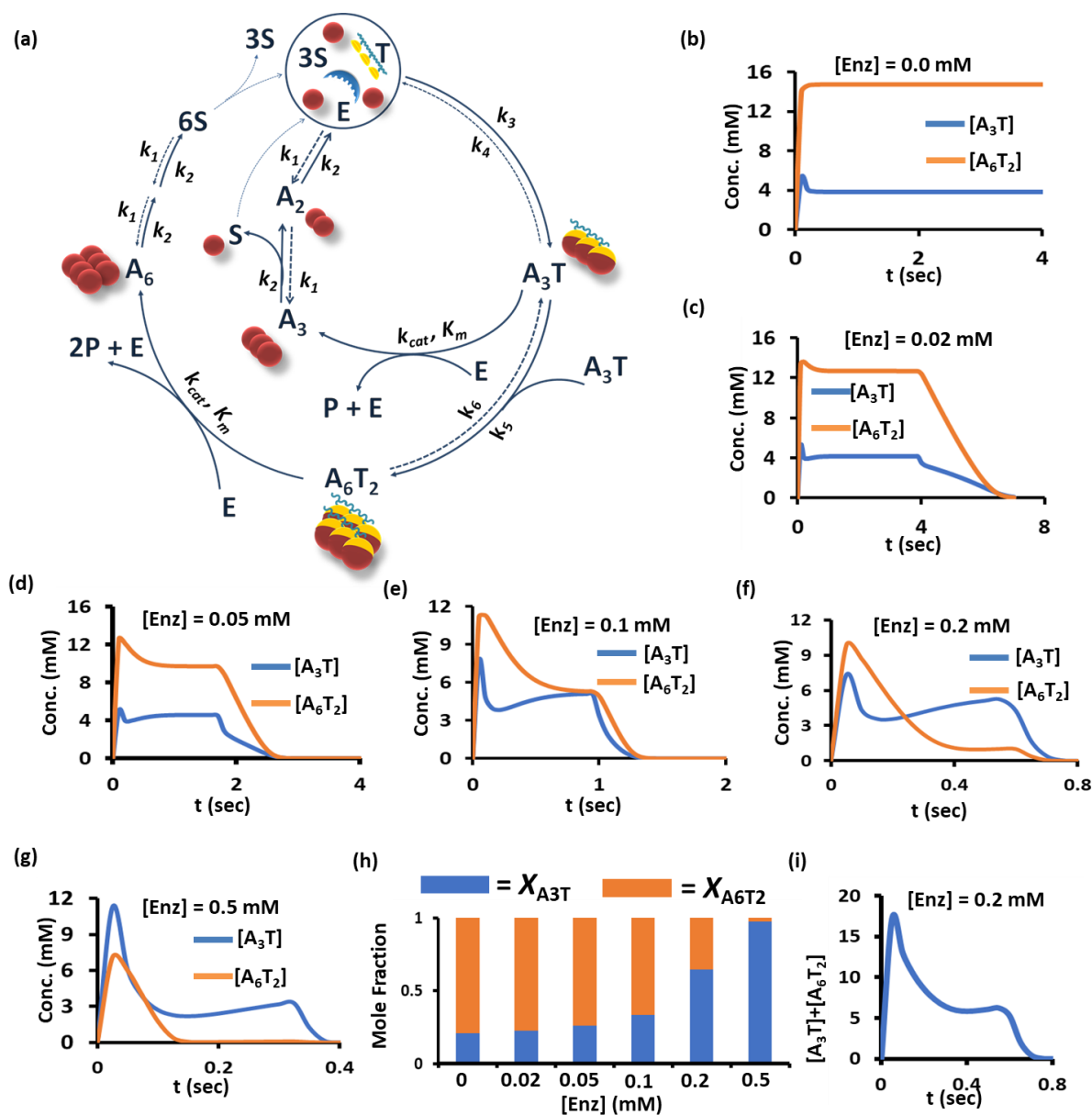


Figure 5.10. (a) Schematic representation of A_6T_2 assembly formation in presence of enzyme having $k_1 = 0.1 \text{ mM}^{-1}\text{s}^{-1}$, $k_2 = 10 \text{ s}^{-1}$, $k_3 = 10^3 \text{ mM}^{-3}\text{s}^{-1}$, $k_4 = 10^{-3} \text{ s}^{-1}$, $k_5 = 1 \text{ mM}^{-1}\text{s}^{-1}$, $k_6 = 1 \text{ s}^{-1}$, $k_{\text{cat}} = 250 \text{ s}^{-1}$, $k_m = 1 \text{ mM}$ with $[S]_{\text{initial}} = [T]_{\text{initial}} = 100 \text{ mM}$ as kinetic constraints. Composition profile of A_3T and A_6T_2 assemblies at an enzyme concentration of (b) 0.0 mM; (c) 0.02 mM; (d) 0.05 mM; (e) 0.1 mM; (f) 0.2 mM; (g) 0.5 mM; (h) Compositional change in A_3T and A_6T_2 in terms of mole fraction at 0.5 sec with change in enzyme concentration; (i) Compositional change in fuel-mediated collective assemblies of A_3T and A_6T_2 with time at $[E] = 0.2 \text{ mM}$.

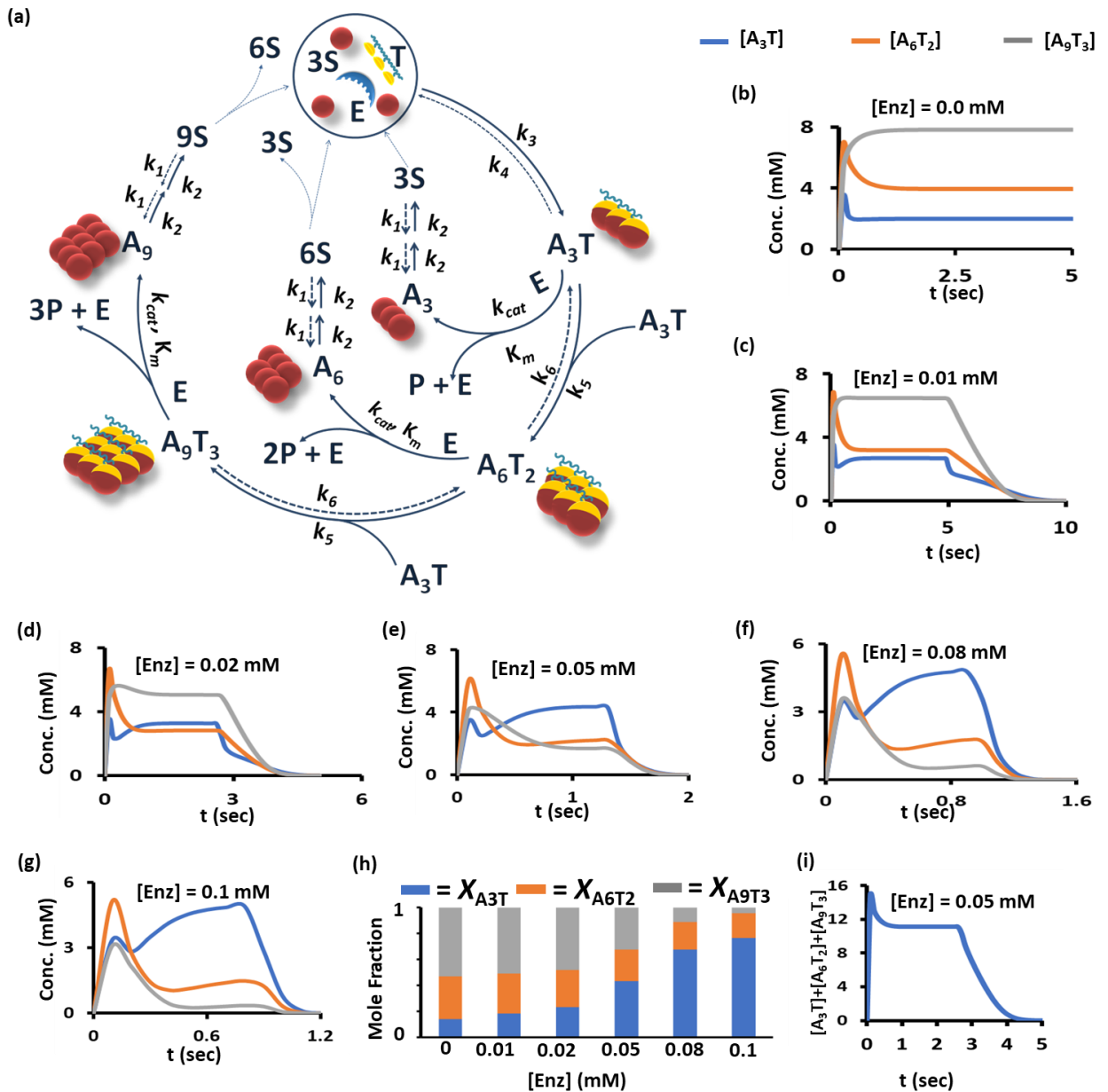


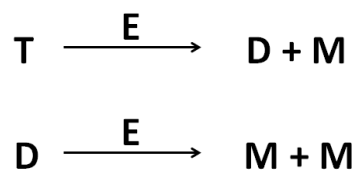
Figure 5.11. (a) Schematic representation of A_9T_3 assembly formation in presence of enzyme, having $k_1 = 0.1 \text{ mM}^{-1}\text{s}^{-1}$, $k_2 = 10 \text{ s}^{-1}$, $k_3 = 10^3 \text{ mM}^{-3}\text{s}^{-1}$, $k_4 = 10^{-3} \text{ s}^{-1}$, $k_5 = 1 \text{ mM}^{-1}\text{s}^{-1}$, $k_6 = 1 \text{ s}^{-1}$, $k_{cat} = 250 \text{ s}^{-1}$, $k_m = 1 \text{ mM}$ with $[S]_{initial} = [T]_{initial} = 100 \text{ mM}$ as kinetic constraints. Composition profile of A_3T and A_6T_2 assemblies at an enzyme concentration of (b) 0.0 mM; (c) 0.01 mM; (d) 0.02 mM; (e) 0.05 mM; (f) 0.08 mM; (g) 0.1 mM. (h) Compositional change in A_3T , A_6T_2 , and A_9T_3 in terms of mole fraction at 0.5 sec with change in enzyme concentration. (i) Collective compositional change of A_3T , A_6T_2 and A_9T_3 in fuel-mediated assemblies with time at $[E] = 0.05 \text{ mM}$

Next, we are curious to understand how the composition changed after imposing dissipative conditions of different strengths in the system i.e. upon introduction of varying concentrations of E. For this at first, we have run the simulation by introducing 0.02 mM of the enzyme and

observed both A_3T and A_6T_2 start to disassemble after a certain time, which is around 4 sec. Subsequently, we have performed a series of simulations with increasing concentrations of enzymes (0.05, 0.1, 0.2, and 0.5 mM) (Figure 5.10c-g). We have observed a very interesting kinetic compositional profile. As we increase the enzyme concentration, the amount of the larger assembled product A_6T_2 is decreasing, whereas the intermediate assembled product, A_3T is increasing. The change in the composition of A_3T and A_6T_2 in terms of mole fraction as well as their total amount at time 0.3 sec with increasing concentration of E has been illustrated in Figure 5.10b-h. The most interesting case was observed at $[E] = 0.2$ mM where in the initial period A_6T_2 dominates, but as time progresses the amount of A_3T gets increased and after a certain period both get disassembled (Figure 5.10f). A similar trend in compositional change over time was also observed at $T = 250$ mM. To illustrate this fact clearly, we have shown that if we only consider a temporal change of the total concentration of A_3T and A_6T_2 (at $E = 0.2$ mM) present in the system then the decay rate is kind of regular and only upon deconvolution their individual components can be seen (Figure 5.10f and 5.10i). Also even at a higher concentration of E (0.5 mM), the amount of A_6T_2 remains lower than A_3T during the period of transient formation of both the assembled species. The simulated result shown here has been done using a fourth-order reaction, however, we have also performed calculations by assuming overall second order (unimolecular with respect to both S and T) (data not shown). Evidently, in a simple two-step process, the composition of the intermediate and final assembled product is highly non-linear in nature, once a dissipative condition is employed. The previous results made us excited and prompted us to analyze this phenomenon in a more complex system. For that, we have investigated a three-step assembly process with two intermediates A_3T and A_6T_2 , and the final product A_9T_3 under dissipative conditions to demonstrate its wider appropriateness. The kinetic parameters, rate constant, etc. have been kept similar as previously mentioned and the overall system has been schematically shown in Figure 2.11a. Here, T dissociates to P by E from all the assembled states, A_3T , A_6T_2 , and A_9T_3 as described in the preceding paragraphs. Here also we have performed the simulations with increasing concentrations of E (0 – 0.1 mM). In absence of any E in the system, the thermodynamically stable composition follows the order: $A_9T_3 > A_6T_2 > A_3T$ and it attained after about 0.5 sec. However, upon introduction of enzyme into the system, the assembled adducts formed in a transient manner and the composition of the intermediates are also started to shuffle with time (Figure 2.11b-h). For example, in the case of 0.02 mM E, at the very initial formation period at 0.1 sec, the composition was in the order of $A_6T_2 > A_9T_3 > A_3T$; immediately after at 0.2 sec, it shifted to $A_9T_3 > A_6T_2 > A_3T$ and then during 1 to 1.5 sec, the compositional order was

$A_9T_3 > A_3T > A_6T_2$ and finally during the disappearance period from 2.9 to 3.6 sec, it shifted back to $A_9T_3 > A_6T_2 > A_3T$ (Figure 2.11d). Similarly, this kind of multiple times switching in compositions between the intermediate and final assembled species over time was also observed in the presence of 0.05 mM E. In Figure 2.11h, an analysis of intermediate and final assembled product composition with respect to mole fraction and amount of the assembled adduct after 0.5 sec has been shown as an example. This time 0.5 sec was chosen arbitrarily for comparison as here in all enzyme concentration (0-0.1 mM) the assembly formation and re-shuffling was going on. It is clear that at this time, the mole fraction of the initial intermediate (A_3T) is increasing with an increase of the concentration of E. Again, if we look at the total concentration of all the components then the decay is regular and concentration change of the intermediates over time are hidden (Figure 2.11i). Here also the behavior of the system has been demonstrated under the overall second-order rate constant (first order with respect to both S and T) where also a highly non-linear compositional change over time was observed data not shown). Thus also in a three-step assembly process, the temporal changes of intermediate composition during dissipative conditions occur in a far more dynamic manner.

Additionally, we have customized a system involving sequential disintegration of fuel from T to D to M in the presence of an enzyme, E which means the number of valent sites got reduced by one with each enzymatic reaction on fuel and have studied assemblies that are supposed to form with six S units at most (modeling details and generated kinetic profile in method section). Here also, we have found a non-linear change in compositions of intermediates with time, and more interestingly A_2D assembly has shown interesting behavior as longer-lived transient intermediate species. It started to grow while A_3T decayed and remains even after the complete disintegration of A_3T (Figure 5.12). In this section, we have studied a special case that involves the presence of an enzyme such that it cleaves T to form D and cleaves D to form M, which means that the enzyme, E has the capability to cleave a T molecule at two sites and can form one M unit and one D unit and D can again be cleaved to give two M molecules with the same kinetic parameters.



Scheme 5.4. Reaction scheme to show sequential disintegration of T to D to M in the presence of enzyme, E

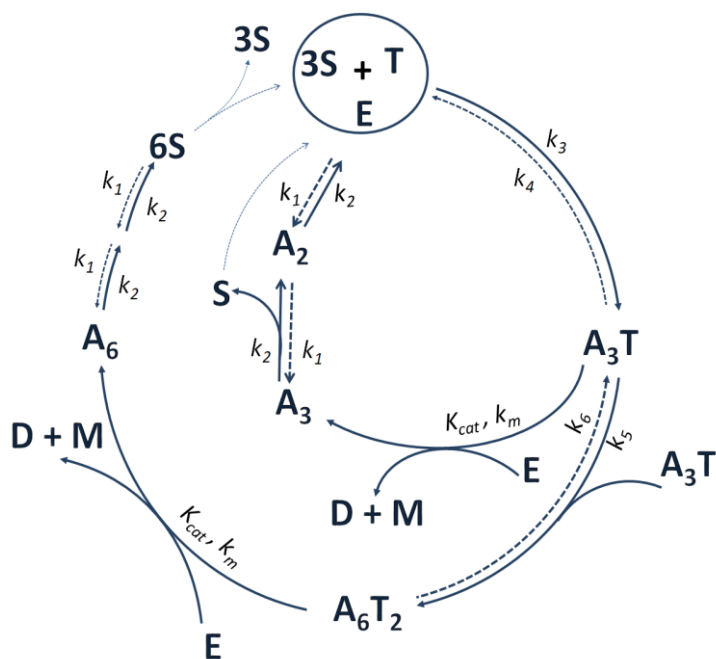


Figure 5.12. Reaction scheme for the formation of assemblies with T in the presence of the enzyme. Firstly, S forms assembly in the presence of T, and when T got cleaved into D and M in the presence of an enzyme (Scheme 5.4), D came into role and a further reaction cycle started to grow. After which, as soon as M is formed along with D and from D (Scheme S12) the monomer, S started to form assembly with M as well.

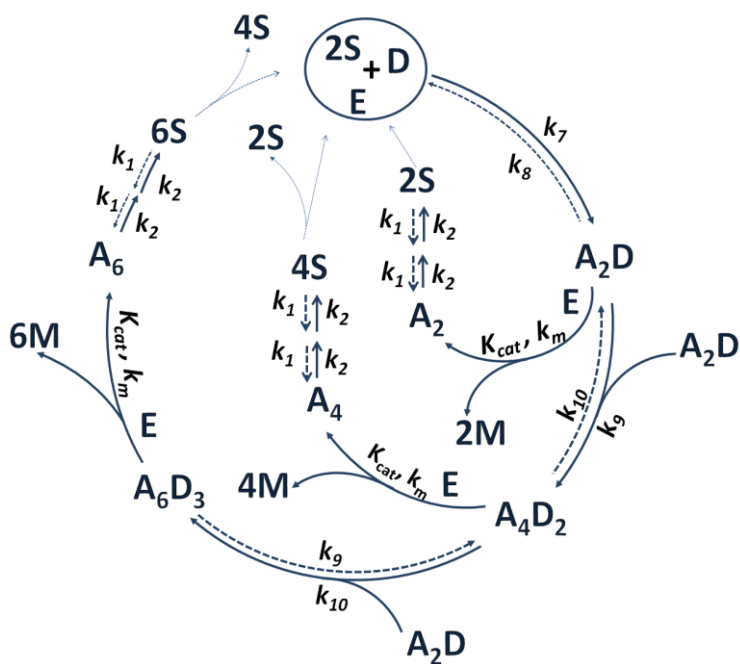


Figure 5.13. Reaction cycle in the presence of D as fuel and E as cleaving agent for D to give two M units

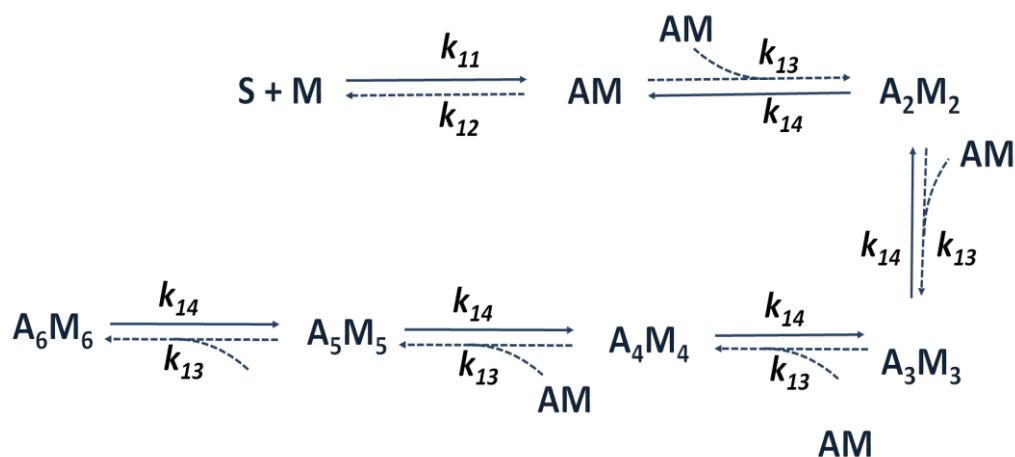


Figure 5.14. Reaction steps in the presence of M as a fuel in order to form A_6M_6 assembly

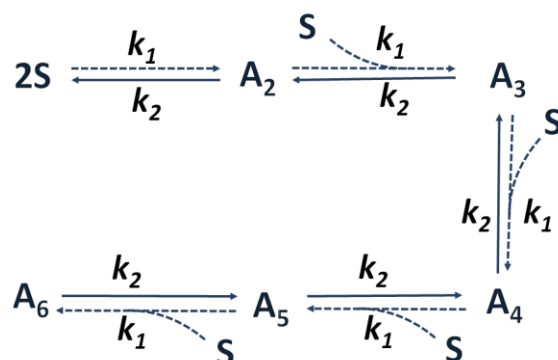


Figure 5.15. Reaction steps followed to form A_6 assembly when there is no fuel involved

With this type of system (taking all these cycles and schemes together), the formation of assemblies involving six S molecules (A_6T_2 , A_6D_3 , A_6M_6) is studied. To make it clearer, the reaction involved here are given below:

For the above reaction set, rate expressions were formed according to mass kinetics and then the resulting ODEs were solved. The kinetic parameters kept during the modeling are given as follows: $k_1 = 0.1 \text{ mM}^{-1}\text{s}^{-1}$, $k_2 = 10 \text{ s}^{-1}$, $k_3 = 10^3 \text{ mM}^{-3}\text{s}^{-1}$, $k_4 = 10^{-3} \text{ s}^{-1}$, $k_5 = 0.1 \text{ mM}^{-1}\text{s}^{-1}$, $k_6 = 10 \text{ s}^{-1}$, $k_7 = 10^2 \text{ mM}^{-2}\text{s}^{-1}$, $k_8 = 10^{-2} \text{ s}^{-1}$, $k_9 = 0.1 \text{ mM}^{-1}\text{s}^{-1}$, $k_{10} = 10 \text{ s}^{-1}$, $k_{11} = 10 \text{ mM}^{-1}\text{s}^{-1}$, $k_{12} = 0.1 \text{ s}^{-1}$, $k_{13} = 0.1 \text{ mM}^{-1}\text{s}^{-1}$, $k_{14} = 10 \text{ s}^{-1}$, $k_{\text{cat}} = 250 \text{ s}^{-1}$ and $K_m = 1 \text{ mM}$.

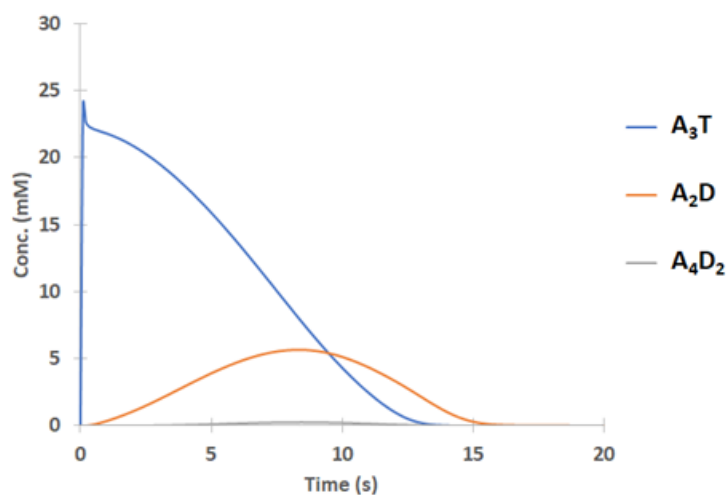


Figure 5.17. Compositional profile for A_3T , A_2D and A_4D_2 assemblies over time at $[E] = 0.01$ mM

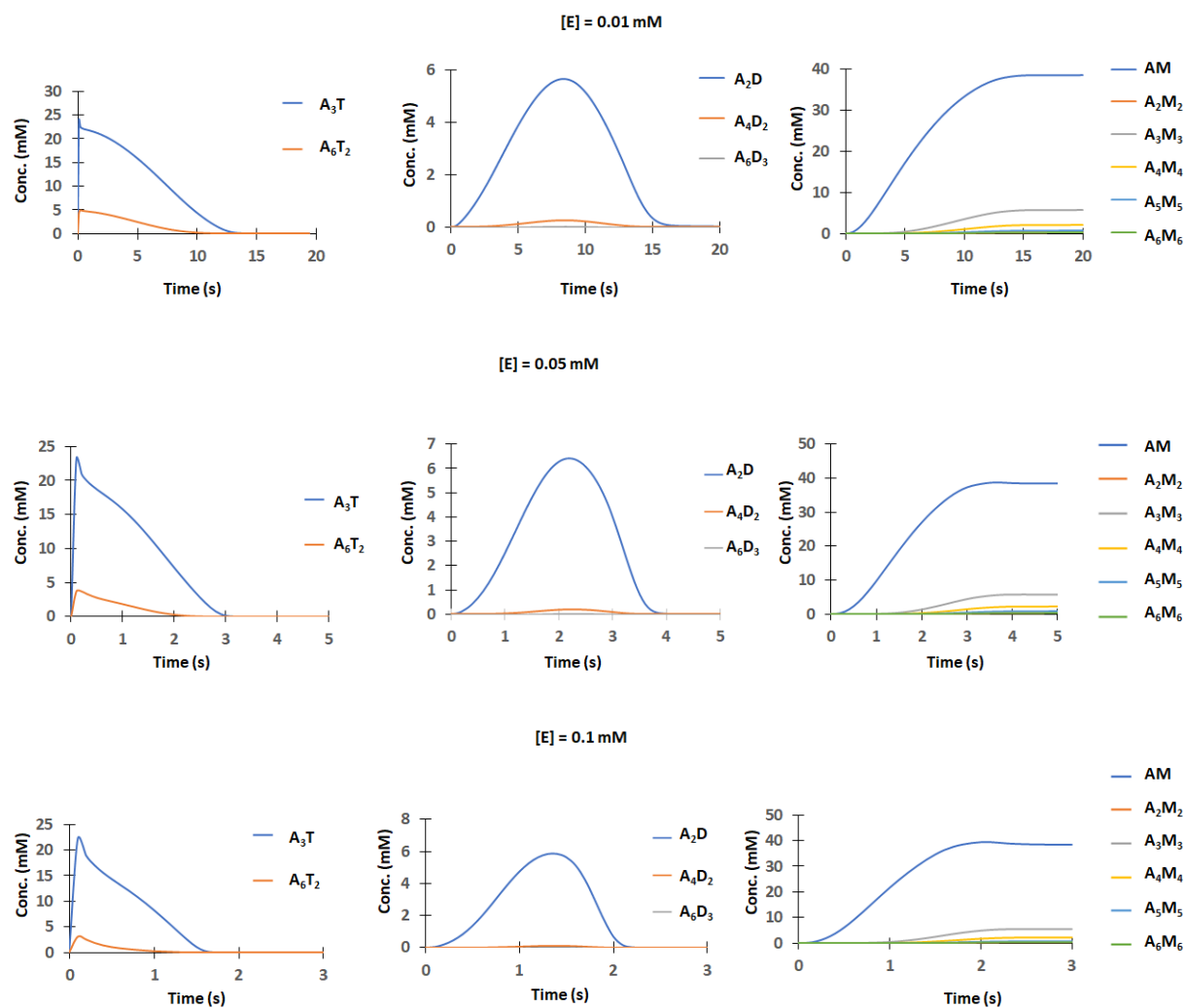


Figure 5.16. Compositional profile for all the assemblies having upto six S units when T (A_3T , A_6T_2) undergoes sequential disintegration to form D (A_2D , A_4D_2 , A_6D_3) and then M (AM , A_2M_2 , A_3M_3 , A_4M_4 , A_5M_5 , A_6M_6) in presence of enzyme.

The initial concentration of S and T was 100 mM for both and the concentration of enzyme was varied from 0.01 mM to 0.1 mM. After running this Python script, the output was a concentration versus time graph for each species. From that, the concentration of assemblies with T i.e., A_3T and A_6T_2 , with D i.e., A_2D , A_4D_2 , and A_6D_3 , and with M i.e., AM , A_2M_2 , A_3M_3 upto A_6M_6 was plotted in separate graphs for clear visualization. Thus plotted compositional profiles with respect to time are shown in Figure 5.16 -5.17 at three different enzyme concentrations (0.01 mM, 0.05 mM, and 0.1 mM).

5.4. Summary

In conclusion, we have deconvoluted the intermediate species of a multistep assembly process under dissipative conditions. The situation demonstrated here is rather complex as the systems feature the following events: i) multivalent fuel-driven assembly, ii) sequentially undergoing assembly, and iii) simultaneously interconverting to other neighboring intermediates, final assembled and initially disassembled units, under dissipative condition. The most interesting finding here is the multiple times compositional switching of the intermediate assembled species with time and that is very non-linear in nature. It means that there is no progressive decrease of the intermediately generated assembled species during its disappearance. In the current trend of systems chemistry research, this outcome is highly significant as it can contribute to the domain of dynamic kinetic chemistry.¹⁻⁵ Till now, how the intermediates formed and changed their composition in a multi-step assembly process has not been considered theoretically as well as experimentally. Thus this knowledge of deconvoluting transient assembled system in each unit of progressing self-assembly would be an important step forward to designing more experiments with a focus on transient compositional behavior of the intermediate assembly species and thus automatically can play a crucial role in the design of materials or system with tunable transient property in terms of material shape/strength or multidimensional chemical reactivity.

5.5 References

1. Ashkenasy, G.; Hermans, T. M.; Otto, S.; Taylor, A. F. Systems Chemistry. *Chem. Soc. Rev.* **2017**, *46* (9), 2543–2554.
2. Mattia, E.; Otto, S. Supramolecular Systems Chemistry. *Nat. Nanotechnol.* **2015**, *10* (2), 111–119.

3. Kroiss, D.; Ashkenasy, G.; Braunschweig, A. B.; Tuttle, T.; Ulijn, R. V. Catalyst: Can Systems Chemistry Unravel the Mysteries of the Chemical Origins of Life? *Chem* **2019**, *5* (8), 1917–1920.
4. Cafferty, B. J.; Wong, A. S. Y.; Semenov, S. N.; Belding, L.; Gmür, S.; Huck, W. T. S.; Whitesides, G. M. Robustness, Entrainment, and Hybridization in Dissipative Molecular Networks, and the Origin of Life. *J. Am. Chem. Soc.* **2019**, *141* (20), 8289–8295.
5. Pross, A. Seeking to Uncover Biology's Chemical Roots. *Emerg. Top. Life Sci.* **2019**, *3* (5), 435–443.
6. *Fragment-based Approaches in Drug Discovery*; Jahnke, W., Erlanson, D. A., Eds.; Wiley, 2006.
7. Huskens, J.; Prins, L. J.; Haag, R.; Ravoo, J. *Multivalency: Concepts, Research and Applications*; Huskens, J., Prins, L. J., Haag, R., Ravoo, B. J., Eds.; John Wiley & Sons: Nashville, TN, 2018.
8. Garnham, C. P.; Vemu, A.; Wilson-Kubalek, E. M.; Yu, I.; Szyk, A.; Lander, G. C.; Milligan, R. A.; Roll-Mecak, A. Multivalent Microtubule Recognition by Tubulin Tyrosine Ligase-like Family Glutamylases. *Cell* **2015**, *161* (5), 1112–1123.
9. Clark, S. A.; Jespersen, N.; Woodward, C.; Barbar, E. Multivalent IDP Assemblies: Unique Properties of LC8-Associated, IDP Duplex Scaffolds. *FEBS Lett.* **2015**, *589* (19 Pt A), 2543–2551.
10. Needleman, D. J.; Ojeda-Lopez, M. A.; Raviv, U.; Miller, H. P.; Wilson, L.; Safinya, C. R. Higher-Order Assembly of Microtubules by Counterions: From Hexagonal Bundles to Living Necklaces. *Proc. Natl. Acad. Sci. U. S. A.* **2004**, *101* (46), 16099–16103.
11. Cabrales Fontela, Y.; Kadavath, H.; Biernat, J.; Riedel, D.; Mandelkow, E.; Zweckstetter, M. Multivalent Cross-Linking of Actin Filaments and Microtubules through the Microtubule-Associated Protein Tau. *Nat. Commun.* **2017**, *8* (1), 1–12.
12. Fletcher, D. A.; Mullins, R. D. Cell Mechanics and the Cytoskeleton. *Nature* **2010**, *463* (7280), 485–492.
13. della Sala, F.; Neri, S.; Maiti, S.; Chen, J. L.-Y.; Prins, L. J. Transient Self-Assembly of Molecular Nanostructures Driven by Chemical Fuels. *Curr. Opin. Biotechnol.* **2017**, *46*, 27–33.

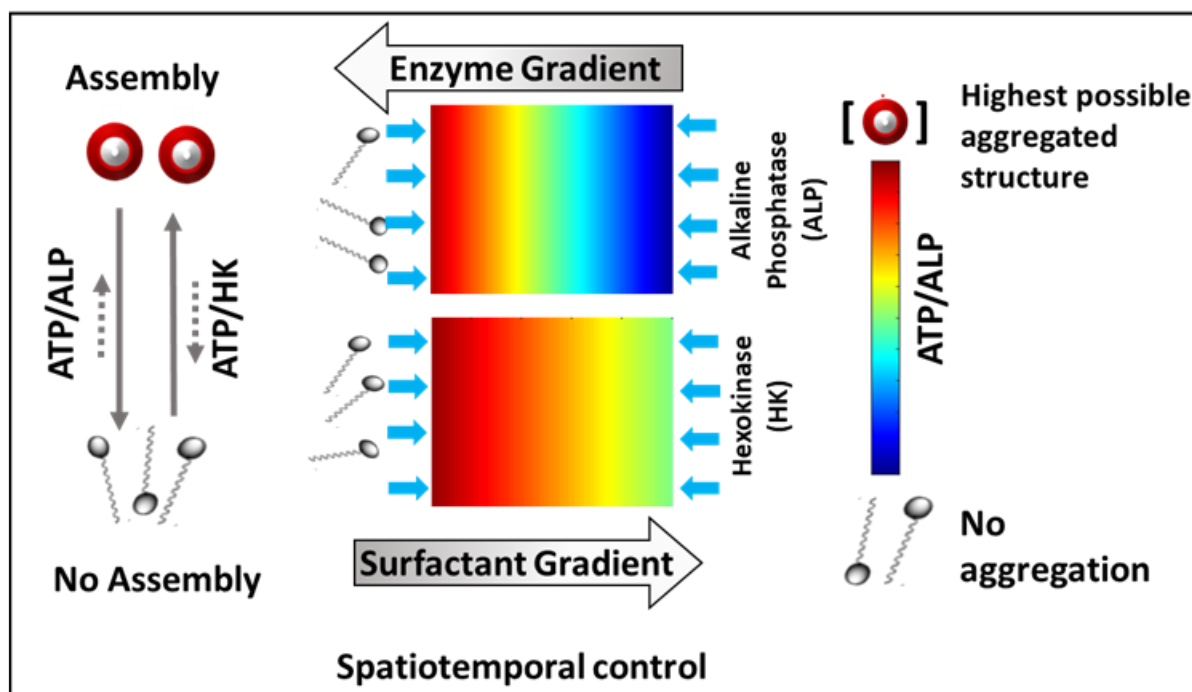
14. Grzybowski, B. A.; Fitzner, K.; Paczesny, J.; Granick, S. From Dynamic Self-Assembly to Networked Chemical Systems. *Chem. Soc. Rev.* **2017**, *46* (18), 5647–5678.
15. Pezzato, C.; Cheng, C.; Stoddart, J. F.; Astumian, R. D. Mastering the Non-Equilibrium Assembly and Operation of Molecular Machines. *Chem. Soc. Rev.* **2017**, *46* (18), 5491–5507.
16. Ragazzon, G.; Prins, L. J. Energy Consumption in Chemical Fuel-Driven Self-Assembly. *Nat. Nanotechnol.* **2018**, *13* (10), 882–889.
17. De, S.; Klajn, R. Dissipative Self-Assembly Driven by the Consumption of Chemical Fuels. *Adv. Mater.* **2018**, *30* (41), e1706750.
18. Merindol, R.; Walther, A. Materials Learning from Life: Concepts for Active, Adaptive and Autonomous Molecular Systems. *Chem. Soc. Rev.* **2017**, *46* (18), 5588–5619.
19. Heuser, T.; Merindol, R.; Loescher, S.; Klaus, A.; Walther, A. Photonic Devices out of Equilibrium: Transient Memory, Signal Propagation, and Sensing. *Adv. Mater.* **2017**, *29* (17).
20. Astumian, R. D. Trajectory and Cycle-Based Thermodynamics and Kinetics of Molecular Machines: The Importance of Microscopic Reversibility. *Acc. Chem. Res.* **2018**, *51* (11), 2653–2661.
21. Boekhoven, J.; Hendriksen, W. E.; Koper, G. J. M.; Eelkema, R.; van Esch, J. H. Transient Assembly of Active Materials Fueled by a Chemical Reaction. *Science* **2015**, *349* (6252), 1075–1079.
22. Fanlo-Virgós, H.; Alba, A.-N. R.; Hamieh, S.; Colomb-Delsuc, M.; Otto, S. Transient Substrate-Induced Catalyst Formation in a Dynamic Molecular Network. *Angew. Chem. Int. Ed.* **2014**, *53* (42), 11346–11350.
23. 5 j and 8d (23) Fanlo-Virgós, H.; Alba, A.-N. R.; Hamieh, S.; Colomb-Delsuc, M.; Otto, S. Transient Substrate-Induced Catalyst Formation in a Dynamic Molecular Network. *Angew. Chem. Weinheim Bergstr. Ger.* **2014**, *126* (42), 11528–11532.
24. te Brinke, E.; Groen, J.; Herrmann, A.; Heus, H. A.; Rivas, G.; Spruijt, E.; Huck, W. T. S. Dissipative Adaptation in Driven Self-Assembly Leading to Self-Dividing Fibrils. *Nat. Nanotechnol.* **2018**, *13* (9), 849–855.
25. Maiti, S.; Fortunati, I.; Ferrante, C.; Scrimin, P.; Prins, L. J. Dissipative Self-Assembly of Vesicular Nanoreactors. *Nat. Chem.* **2016**, *8* (7), 725–731.

26. Hao, X.; Sang, W.; Hu, J.; Yan, Q. Pulsating Polymer Micelles via ATP-Fueled Dissipative Self-Assembly. *ACS Macro Lett.* **2017**, *6* (10), 1151–1155.
27. van Ravensteijn, B. G. P.; Hendriksen, W. E.; Eelkema, R.; van Esch, J. H.; Kegel, W. K. Fuel-Mediated Transient Clustering of Colloidal Building Blocks. *J. Am. Chem. Soc.* **2017**, *139* (29), 9763–9766.
28. Chen, J. L.-Y.; Maiti, S.; Fortunati, I.; Ferrante, C.; Prins, L. J. Temporal Control over Transient Chemical Systems Using Structurally Diverse Chemical Fuels. *Chemistry* **2017**, *23* (48), 11549–11559.
29. Sawczyk, M.; Klajn, R. Out-of-Equilibrium Aggregates and Coatings during Seeded Growth of Metallic Nanoparticles. *J. Am. Chem. Soc.* **2017**, *139* (49), 17973–17978.
30. Pezzato, C.; Prins, L. J. Transient Signal Generation in a Self-Assembled Nanosystem Fueled by ATP. *Nat. Commun.* **2015**, *6* (1), 7790.
31. della Sala, F.; Maiti, S.; Bonanni, A.; Scrimin, P.; Prins, L. J. Fuel-Selective Transient Activation of Nanosystems for Signal Generation. *Angew. Chem. Int. Ed.* **2018**, *57* (6), 1611–1615
32. Jalani, K.; Dhiman, S.; Jain, A.; George, S. J. Temporal Switching of an Amphiphilic Self-Assembly by a Chemical Fuel-Driven Conformational Response. *Chem. Sci.* **2017**, *8* (9), 6030–6036
33. Kumar, M.; Ing, N. L.; Narang, V.; Wijerathne, N. K.; Hochbaum, A. I.; Ulijn, R. V. Amino-Acid-Encoded Biocatalytic Self-Assembly Enables the Formation of Transient Conducting Nanostructures. *Nat. Chem.* **2018**, *10* (7), 696–703.
34. Jain, A.; Dhiman, S.; Dhayani, A.; Vemula, P. K.; George, S. J. Chemical Fuel-Driven Living and Transient Supramolecular Polymerization. *Nat. Commun.* **2019**, *10* (1), 450.
35. Bal, S.; Das, K.; Ahmed, S.; Das, D. Chemically Fueled Dissipative Self-Assembly That Exploits Cooperative Catalysis. *Angew. Chem. Int. Ed.* **2019**, *58* (1), 244–247.
36. Bal, S.; Das, K.; Ahmed, S.; Das, D. Chemically Fueled Dissipative Self-Assembly That Exploits Cooperative Catalysis. *Angew. Chem. Weinheim Bergstr. Ger.* **2019**, *131* (1), 250–253.

37. Solís Muñana, P.; Ragazzon, G.; Dupont, J.; Ren, C. Z.-J.; Prins, L. J.; Chen, J. L.-Y. Substrate-Induced Self-Assembly of Cooperative Catalysts. *Angew. Chem. Weinheim Bergstr. Ger.* **2018**, *130* (50), 16707–16712.
38. Wang, H.; Wang, Y.; Shen, B.; Liu, X.; Lee, M. Substrate-Driven Transient Self-Assembly and Spontaneous Disassembly Directed by Chemical Reaction with Product Release. *J. Am. Chem. Soc.* **2019**, *141* (10), 4182–4185.
39. Badjić, J. D.; Nelson, A.; Cantrill, S. J.; Turnbull, W. B.; Stoddart, J. F. Multivalency and Cooperativity in Supramolecular Chemistry. *Acc. Chem. Res.* **2005**, *38* (9), 723–732.
40. Huskens, J.; Mulder, A.; Auletta, T.; Nijhuis, C. A.; Ludden, M. J. W.; Reinhoudt, D. N. A Model for Describing the Thermodynamics of Multivalent Host-Guest Interactions at Interfaces. *J. Am. Chem. Soc.* **2004**, *126* (21), 6784–6797.
41. Kane, R. S. Thermodynamics of Multivalent Interactions: Influence of the Linker. *Langmuir* **2010**, *26* (11), 8636–8640.
42. Paffen, T. F. E.; Teunissen, A. J. P.; de Greef, T. F. A.; Meijer, E. W. Model-Driven Engineering of Supramolecular Buffering by Multivalency. *Proc. Natl. Acad. Sci. U. S. A.* **2017**, *114* (49), 12882–12887.
43. Stevers, L. M.; de Vink, P. J.; Ottmann, C.; Huskens, J.; Brunsveld, L. A Thermodynamic Model for Multivalency in 14-3-3 Protein-Protein Interactions. *J. Am. Chem. Soc.* **2018**, *140* (43), 14498–14510.
44. Korevaar, P. A.; George, S. J.; Markvoort, A. J.; Smulders, M. M. J.; Hilbers, P. A. J.; Schenning, A. P. H. J.; De Greef, T. F. A.; Meijer, E. W. Pathway Complexity in Supramolecular Polymerization. *Nature* **2012**, *481* (7382), 492–496.
45. Korobov, V. I.; Ochkov, V. F. Multi-Step Reactions: The Methods for Analytical Solving the Direct Problem. In *Chemical Kinetics with Mathcad and Maple*; Springer Vienna: Vienna, 2011; pp 35–72.
46. Ten Eikelder, H. M. M.; Adelizzi, B.; Palmans, A. R. A.; Markvoort, A. J. Equilibrium Model for Supramolecular Copolymerizations. *J. Phys. Chem. B* **2019**, *123* (30), 6627–6642.
47. Wang, Y.; Xu, H.; Zhang, X. Tuning the Amphiphilicity of Building Blocks: Controlled Self-Assembly and Disassembly for Functional Supramolecular Materials. *Adv. Mater.* **2009**, *21* (28), 2849–2864.

CHAPTER 6

Programming Spatiotemporal Organization of Nonlinear Dynamical Systems through Enzyme-Mediated Assembly Formation



This is adapted reproduction from Shandilya, E.; Priyanka; Brar, S. K.; Mahato, R. R.; Maiti, S. Spatiotemporal Dynamics of Self-Assembled Structures in Enzymatically Induced Agonistic and Antagonistic Conditions. *Chem. Sci.* **2021**, *13* (1), 274–282.

6.1 Introduction

In the realm of scientific exploration, the assembly of complex systems driven by interactive chemical components has emerged as a captivating and vital problem to solve.^{1,2} The intricate and unpredictable emergence resulting from the synergistic paradigm among these components has become a focal point of research. Scientists endeavor to decipher the intricate connectivity found in living cells, and neuronal networks, and the creation of next-generation materials with perceptual stability.³⁻⁹ The relationship between various constituents, whether agonistic or antagonistic, plays a pivotal role in the up-and-downregulation of dynamic processes.¹⁰⁻¹⁴ Researchers have employed reaction-diffusion mechanisms in oscillatory systems to generate non-equilibrium assemblies and intricate surface patterns.¹¹⁻¹⁴ Over the past decade, chemists have successfully developed dynamic self-organized systems with remarkable characteristics such as self-sorting, self-replication, and the ability to harness physical and chemical energy from the environment.¹⁵⁻²² These systems have opened up possibilities for temporal control over an array of properties, including chemical reactivity, material strength, time-dependent drug delivery, and optoelectronic properties.²³⁻³⁴

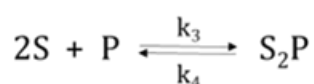
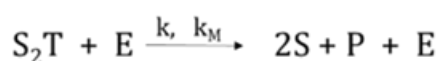
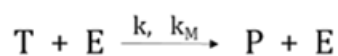
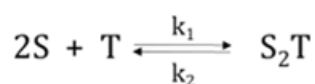
Enzymes, in conjunction with other factors such as light or pH, have been employed to create transient synthetic chemical assemblies. By utilizing enzymes capable of destabilizing the aggregate-stabilizing chemical fuel, researchers have harnessed dynamic instability within these systems.³⁵⁻⁴⁰ The binding of the chemical fuel and the building blocks occurs rapidly, while the degradation of the fuel by the enzyme is relatively slow. Consequently, the products generated by the chemical fuel are unable to stabilize the building blocks, preventing the formation of organized assemblies. However, certain conditions can lead to sustainable assemblies when the products possess the ability to stabilize the aggregates. These cases are referred to as agonistic conditions, in which the assembled structures persist over time. Our work focuses on the intriguing interplay between two enzymes, hexokinase (HK) and alkaline phosphatase (ALP), in creating agonistic and antagonistic self-assembling events. We introduce a surfactant ($C_{16}DPA \cdot Zn^{2+}$), equipped with a dipicolylamine ($DPA \cdot Zn^{2+}$) bound zinc complex, and explore its behavior in the presence of adenosine triphosphate (ATP). HK sustains the self-assembly response by converting ATP to adenosine diphosphate (ADP) and glucose-6-phosphate (G6P), enabling the system to maintain an agonistic condition for self-assembly. Conversely, the hydrolysis of the product by ALP, yielding adenosine (Ade) and phosphate (Pi), cannot sustain the self-assembly response, resulting in an antagonistic

condition. Furthermore, we delve into the fascinating emergence of population dynamics within the self-assembled units under both agonistic and antagonistic conditions. We examine the spatial and temporal behavior of the self-assembled units by introducing concentration gradients of surfactant, enzymes, and substrates in different experimental setups. Through experimental observations and theoretical modeling involving reaction-diffusion systems, we shed light on the intricate processes governing the formation and behavior of these self-assembled structures in two-dimensional space.

6.2. Methods

6.2.1 Temporal evolution of assembly via numerical modeling

Considering a system constituting a monomer S and chemical fuel T such that when two monomeric units of S come in proximity of T forms a dimeric assembly S_2T with a k_1/k_2 as an equilibrium constant. In addition to this, when we introduce an enzyme E to our system it can breakdown down T into P. Now, coming to the enzymatic action, as E can cleave T to P, we now assume that it can cleave T from assembled state S_2T with the same rate constants as k_{cat} and K_M according to the Michaelis-Menten equation. Also, the product has some affinity towards S, such that it is also capable of forming dimeric assembly as S_2P . All the above-mentioned possibilities of assembly formation and deformation can be collectively represented by equations following equations:



The above-coupled equations can be represented by a set of first-order differential equations formed according to the mass-balance principle.

$$\frac{d[S]}{dt} = -2 \left(k_1[S]_t^2[T]_t - k_2[S_2T]_t + k_3[S]_t^2[T]_t - k_4[S]_t^2[T]_t - \frac{k[E][S_2T]_t}{k_M+[S_2T]_t} \right) \quad (6.1)$$

$$\frac{d[T]}{dt} = -k_1[S]_t^2[T]_t + k_2[S_2T]_t - \frac{k[E][T]_t}{k_M+[T]_t} \quad (6.2)$$

$$\frac{d[S_2T]}{dt} = k_1[S]_t^2[T]_t - k_2[S_2T]_t - \frac{k[E][S_2T]_t}{k_M+[S_2T]_t} \quad (6.3)$$

$$\frac{d[P]}{dt} = \frac{k[E][S_2T]_t}{k_M+[S_2T]_t} + \frac{k[E][T]_t}{k_M+[T]_t} - k_3[S]_t^2[P]_t + k_4[S]_t^2[P]_t \quad (6.4)$$

#Note6.1

```
def rxn(z,t):
```

```
    k = kcat*E
```

```
    r1 = k1 * z[0]*z[0]*z[1]
```

```
    r2 = k2 * z[2]
```

```
    r3 = k3 * z[0]*z[0]*z[3]
```

```
    r4 = k4 * z[4]
```

```
    ra = k*z[2]/(km + z[2])
```

```
    rb = k*z[1]/(km + z[1])
```

```
    dMdt = - 2 * r1 + 2 * r2 + 2 * ra - 2* r3 + 2 * r4 #S, MONOMER
```

```
    dWdt = - r1 + r2 - rb #T, chemical fuel
```

```
    dUdt = r1 - r2 - ra #S2T, dimeric assembly with T
```

```
    dNdt = ra + rb - r3 + r4 #P, product formed from T
```

```
    dVdt = -r4 + r3 #S2P, dimeric assembly with P
```

```
    return[dMdt,dWdt,dUdt,dNdt,dVdt]
```

```
t = np.linspace(0,0.1,51)
```

```
z0 =[200,50,0,0,0]
```

```
conc = odeint(rxn,z0,t)
```

```
cM = conc[:,0]
```

```
cW = conc[:,1]
```

```
cU = conc[:,2]
```

```
cN = conc[:,3]
```

```
cV = conc[:,4]
```

$$\frac{d[S_2P]}{dt} = k_3[S]_t^2[P]_t - k_4[S]_t^2[P]_t \quad (6.5)$$

To get a compositional change of each component with respect to time the above-mentioned equations were solved using Python 3.0. To get the compositional change of individual components, the rate constants used in equations S1-S4 were fixed and so formed ordinary differential equations were solved using the *odeint* function of Numpy packages. The code used for solving the above-formed equations is shown in note 6.1. For instance, the parameters used are shown in table 6.1 and the composition of dimeric assembly (S_2T and S_2P) and total assembly formed ($S_2T + S_2P$) is shown in Figure 6.4. In addition to this, to get a broader view of the effect of rate constants on individual components, parameters were varied (table S1) and the relative distribution of composition is shown in Figure 6.4. It is worth noting here time and concentration are dimensionless units in this system, however, for the sake of logical comparison with the experiment, hour has been chosen as the unit of time and μM as the unit of concentration respectively.

Table 6.1 Kinetic parameters used for numerical modelling for case I, case II, and case III.

Parameter (unit)	Case I	Case II	Case III
$k_1 (\mu\text{M}^{-2}\text{h}^{-1})$	100	100	100
$k_2 (\text{h}^{-1})$	0.01	0.01	0.01
$k_3 (\mu\text{M}^{-2}\text{h}^{-1})$	10000	0.01	0.0001
$k_4 (\text{h}^{-1})$	0.0001	100	10000
$k (\text{kcat}, \mu\text{Mh}^{-1})$	250	250	250
$K_m(\mu\text{M})$	50	50	50
[Monomer][S, μM]	200	200	200
[Chemical fuel] ([T], μM)	50	50	50
[Enzyme] (E, μM)	1	1	1

6.2.2. Spatiotemporal study of assembly formation using fluid dynamics

To study the spatiotemporal evolution of S₂T and S₂P (mentioned in section B) under flow conditions, a computational model was designed using MATLAB R2019b, FEATool Multiphysics. Here, we collectively studied the transport mechanism of both reactive and non-reactive species involved in the system along with their rate of formation and deformation using computational fluid dynamics.⁴¹⁻⁵² For this purpose, we designed our system so that T was distributed evenly on the squared grid while either S or S and E were added from opposite boundaries as shown in Figure 6.2 and Figures 6.6a and 6.6d in the chapter. For describing the one-dimensional distribution of reactive species over space with time we have used Fick's second law of fluid dynamics so that

$$\frac{dC(x,t)}{dt} = D_x \frac{\partial^2 C}{\partial x^2} - V_x \frac{\partial C}{\partial x} \pm r_c \quad 6.6$$

where C = the concentration of the species at position x and time t, D_x = diffusion coefficient, V_x = the linear flow velocity, and r_c = rate of change of species, while the '±' symbol denotes the rate of formation and deformation of species. Following the above equation, we rewrote the equations for each component of our system incorporating the previously mentioned mass balance equations (6.1-6.5) in place of r_c . Apart from this, Because of the horizontal placement of the grid, we considered the effect of diffusion on species movement and neglected the velocity term in equation 6.6. Now, to solve our system of coupled differential equations under flow conditions, we first designed a square grid space containing 14,816 grid points and 294,912 triangular grid cells, an example is shown in Figure 6.1.

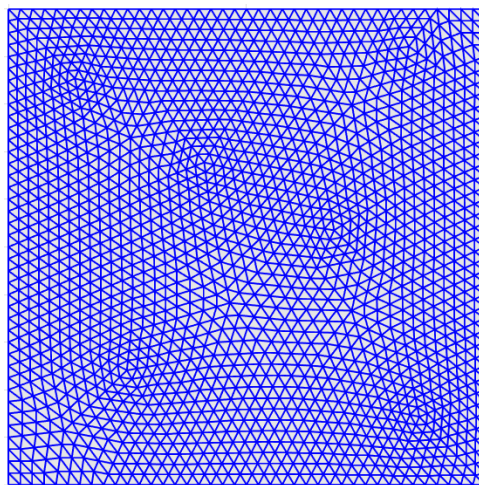


Figure 6.1. A sample square grid space containing 1937 grid points and 3712 triangulations.

For initial conditions, we assumed that T (1 μM) is evenly distributed on the grid. Also, we assumed that the diffusion rate of every monomeric or assembled is equal for the simplification of equations. Firstly, we studied when monomer S was added from one side (boundary 4) of the grid, while all other boundaries were left empty (Figure 6.2a). For solving the coupled equations, we marked the boundary conditions for all the species in accordance with Dirichlet and Neumann boundary conditions at all boundaries. For this case, the only equation to be followed was equation S1, as E was absent. Sample code containing used equations is shown in note 6.2. For quantifying, S_2T assembly formation by holding Neumann condition at boundary 4 and Dirichlet condition at boundary 2. The parameter fixed for S_2T at boundary 4 was 1 $\mu\text{M}/\text{h}$, while 0.2 $\mu\text{M}/\text{h}$ at boundary 2. Also, S followed the Dirichlet condition as 1 $\mu\text{M}/\text{h}$, and 0.5 $\mu\text{M}/\text{h}$ at boundary 4, and boundary 2, respectively. While solving this system of equations, over 5 hours with 0.02-time steps following the Crank-Nicolson time-step scheme, we observed that as time increases S_2T formation increases. The maximum S_2T concentration can be seen at boundary 4 which gradually decreases as moves towards boundary 2 (Figure 6.6b+c).

Note S2:

```
#NoteS2
#Matlab equations when S from boundary 4 and E from boundary 2 (derived from equations 6.1-6.5)
u' - ux_x = m*m*w - u                               #S2T
w' - wx_x = - m*m*w + u                               #T
m'-mx_x = - m*m*w + u                               #S
```

Note S3

```
#NoteS3
#Matlab equations when S from boundary 4 and E from boundary 1 (derived from equations 6.1-6.5)
u' - ux_x = m*m*w - u - (u/1+u)                       #S2T
v' - vx_x = m*m*n - v                                 #S2P
w' - wx_x = - m*m*w + u - (w/1+w)                     #T
n' - nx_x = (u/1+u) + (w/1+w) - m*m*n + v             #P
m' - mx_x = - m*m*w + u + (u/1+u) - m*m*n + v        #S
```

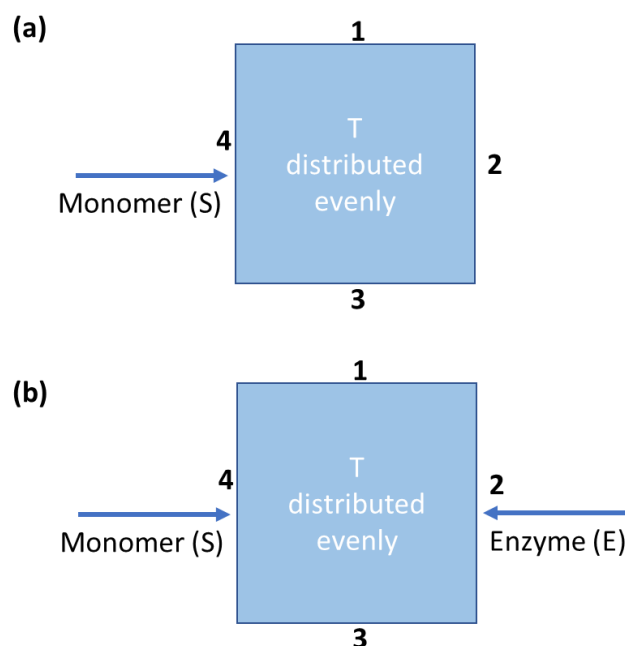


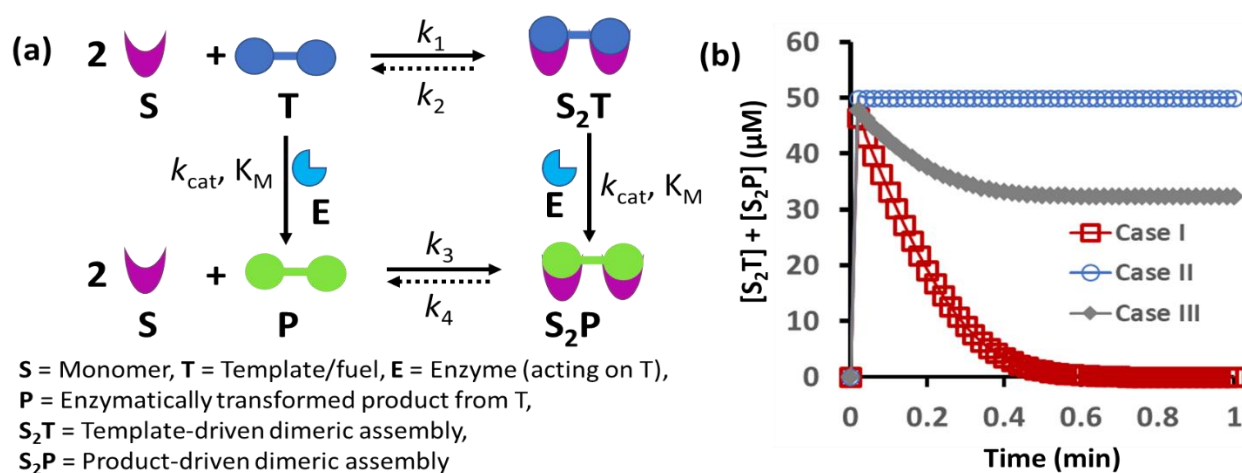
Figure 6.2. Representative grid space where T is distributed evenly in space, and when (a) monomer, S was added from boundary 4; and (b) monomer S, was added from boundary 4, and enzyme, E was added from boundary 2 simultaneously.

Apart from this, when we added S from boundary 4 and E from boundary 2, the set of equations holding were (6.1) – (6.4). The set of equations used in Matlab are shown in note S3. Here also, the parameters for S, R, and S_2T were the same and this set of equations was also solved in a similar way as mentioned in the previous paragraph. Additionally, the rate of product formation and product-driven dimeric assembly (S_2P) formation was added at respective boundaries. For S_2P formation over time, the Neumann boundary parameter was fixed at $0.5 \mu\text{M}/\text{hour}$ at boundary 2. While solving this set of equations over similar time constraints, we observed the formation of S_2T formation at boundary 4 which decreases gradually as we move towards boundary 4, while S_2P assembly formation was more at boundary 2 which gradually decreases as we move towards boundary 4 (Figure 6.6d+e).

6.3. Result and Discussion

In this study, we synthesized a metallosurfactant ($\text{C16DPA}\cdot\text{Zn}^{2+}$) containing a dipicolylamine-bound zinc complex ($\text{DPA}\cdot\text{Zn}^{2+}$) headgroup known for its selective anion recognition properties, particularly toward phosphates.^{53,54} The critical aggregation concentration (CAC) of the surfactant was determined to be approximately $35 \pm 5 \mu\text{M}$. To

investigate assembly formation, we chose a concentration of 25 μM for the surfactant, as it did not form assemblies at this concentration alone. To introduce dynamicity in assembly formation, we employed the enzymes ALP and HK, which can convert ATP to adenosine (Ade) + three molecules of inorganic phosphate (Pi) or adenosine diphosphate (ADP) + glucose-6-phosphate (G6P), respectively. HPLC analysis confirmed these enzymatic conversions under experimental conditions. Computational studies were also performed to examine the binding interactions between the surfactant headgroup and ATP, ADP, G6P, Ade, and Pi, revealing a qualitative binding pattern: $\text{ATP} > \text{G6P} > \text{ADP} > \text{Pi} > \text{Ade}$. Experimental observations indicated that the presence of ATP initiated assembly formation at a concentration significantly lower than the CAC, with the count rate in dynamic light scattering (DLS) increasing after adding only 5–10 μM of $\text{C16DPA} \cdot \text{Zn}^{2+}$. Additionally, the count rate increased at a lower rate in the presence of ADP, and G6P, and remained similar to the surfactant alone in the presence of Ade and Pi. Transmission electron microscopy (TEM) confirmed the presence of ATP-



bound aggregates with sizes around $200 \pm 50 \text{ nm}$. Interestingly, the assembly behavior changed when HK was introduced into the surfactant system, as observed by DLS(The assemblies

formed initially with the assistance of ATP but remained stabilized by ADP and G6P over time. In contrast, in the presence of ALP, the assemblies formed but disappeared within 15 minutes. The different temporal self-assembly responses can be attributed to the multivalency effect of the different end products generated by the action of ALP or HK on the same substrate (ATP). Further DLS measurements showed that the count rate and size of the aggregate decreased over time and eventually returned to levels similar to the surfactant alone after 60 minutes in the ALP-containing system. However, in the HK-containing system, the count rate remained relatively constant. Notably, in the absence of enzymes and in the presence of ATP, the DLS count rate and size remained largely unchanged. In many instances, enzymes have also been used for the development of transient synthetic chemical assembly among others, like – light, pH, etc. In principle, enzymes capable of dissociating the aggregate stabilizing chemical fuel can generate different types of dynamic instability in the system (Figure 6.3).³⁵⁻⁴⁰ Here the binding of chemical fuel and the building block is a faster process and the degradation of the chemical fuel by the enzyme is slower in general, the products generated by the chemical fuel are not able to stabilize the aggregates of the building block to form any organized assembly. In Figure 6.3, it has been shown that two monomers (S) are only able to form a dimeric assembly (S_2T) in the presence of the fuel (T), which is a substrate of enzyme (E). Due to the presence of E, T, and S_2T , both can also be converted to P and S_2P . Now, S_2P can then either dissociate to the monomer (S) and P or remain stable in the aggregate form, only if P also has the templating ability. In Figure 1b, we have explained the possible outcome of these processes by assuming three different cases. For case I, $k_3 \ll k_4$ which implies the dissociation rate of S_2P is much higher than P, in other words, P does not have any aggregate stabilizing ability, thus transiently formed assembly (here, S_2T) can be observed (Figure 6.3b).³⁶⁻³⁸ However, when k_3 nearly equals to or higher than k_4 , implying P also have the aggregate stabilizing ability then sustainable assembly with a mixture of S_2T and S_2P or only S_2P can be observed as shown in case II and III (Figure 6.3b). Here, we have termed cases II and III as agonistic conditions, as here even after enzymatic conversion, the assembled structure remained with time. In this way, the scenario mentioned in case I have been mentioned as an antagonistic condition in this study which has also been termed as self-assembly under dissipative condition in previous literature reports.⁴⁰ However, until now, propagation and sustainability of the chemical fuel-driven

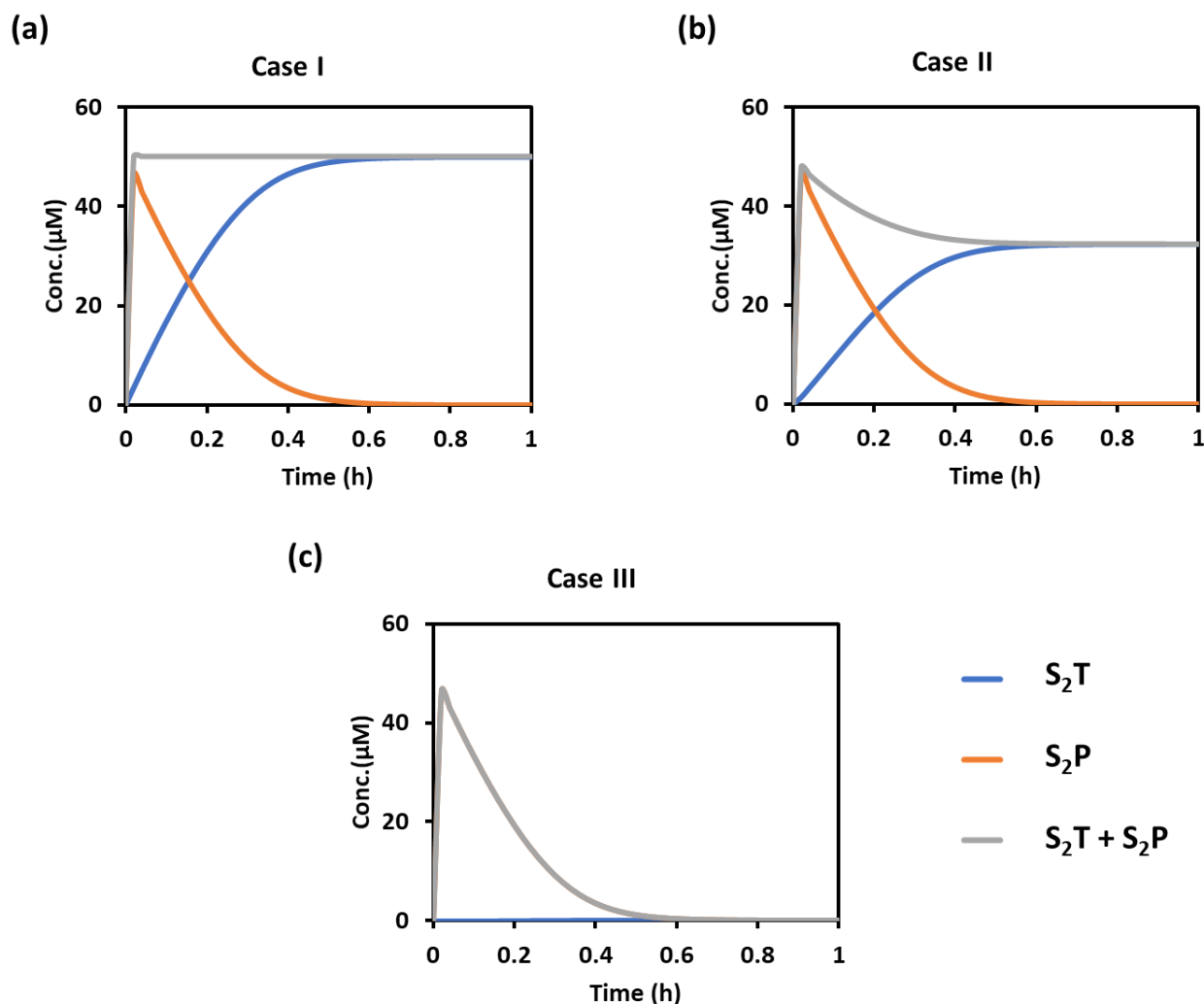


Figure 6.4. Compositional change of dimeric assembly formation S_2T , S_2P , and the sum of S_2T and S_2P over time derived from kinetic modeling. The kinetic parameters for case I, case II, and case III are shown in Table 6.1.

organized system or transiently evolved system owing to the catalytic process has not been explored in detail in a synthetic system, particularly in terms of their spatial organization with time.⁴¹⁻⁴⁷ It is worth mentioning that these kinds of systems are ubiquitous and significant in the cellular system, for e.g. – spatiotemporal dynamics of the proteome, metabolites, formation and growth of protein assemblies, etc.⁴⁸⁻⁵² Also for an experimental part, we synthesized a metallosurfactant ($\text{C16DPA}\cdot\text{Zn}^{2+}$) containing a dipicolylamine-bound zinc complex ($\text{DPA}\cdot\text{Zn}^{2+}$) headgroup known for its selective anion recognition properties, particularly toward phosphates. To investigate assembly formation, we chose a concentration of the surfactant such that it did not form assemblies at this concentration alone. To introduce dynamicity in assembly formation, we employed the enzymes ALP and HK, which can convert ATP to adenosine (Ade) + three molecules of inorganic phosphate (Pi) or adenosine

diphosphate (ADP) + glucose-6-phosphate (G6P), respectively. HPLC analysis confirmed these enzymatic conversions under the experimental conditions (data not shown). Also, we showed how the presence of these two enzymes – hexokinase (HK) and alkaline phosphatase (ALP) can create an agonistic and antagonistic self-assembling event with a surfactant ($C_{16}DPA \cdot Zn^{2+}$, designated as S) containing a headgroup of dipicolylamine (DPA $\cdot Zn^{2+}$) bound zinc complex, in presence of adenosine triphosphate (ATP) under similar experimental condition (Figure 6.5a). HK helps to sustain the self-assembly response of the system as it converts ATP to adenosine diphosphate (ADP) and glucose-6-phosphate (G6P), which helps to sustain the self-assembly response of the system, creating the agonistic condition for the self-assembly. In the contrary, ALP hydrolyzed product adenosine (Ade) and phosphate (Pi) do not have the ability to maintain the self-assembly response, therefore, we termed this as an antagonistic condition for sustaining assembly. Next, we were curious to observe the spatiotemporal assembly behavior when concentration gradients of the surfactant and enzymes were introduced into the system from opposite sides. This part will be of importance for generating dynamic surface patterns that can be controlled by enzymatic processes.^{13,60–63} For this, we first explored the emerging behavior under flow conditions *via* a computational model

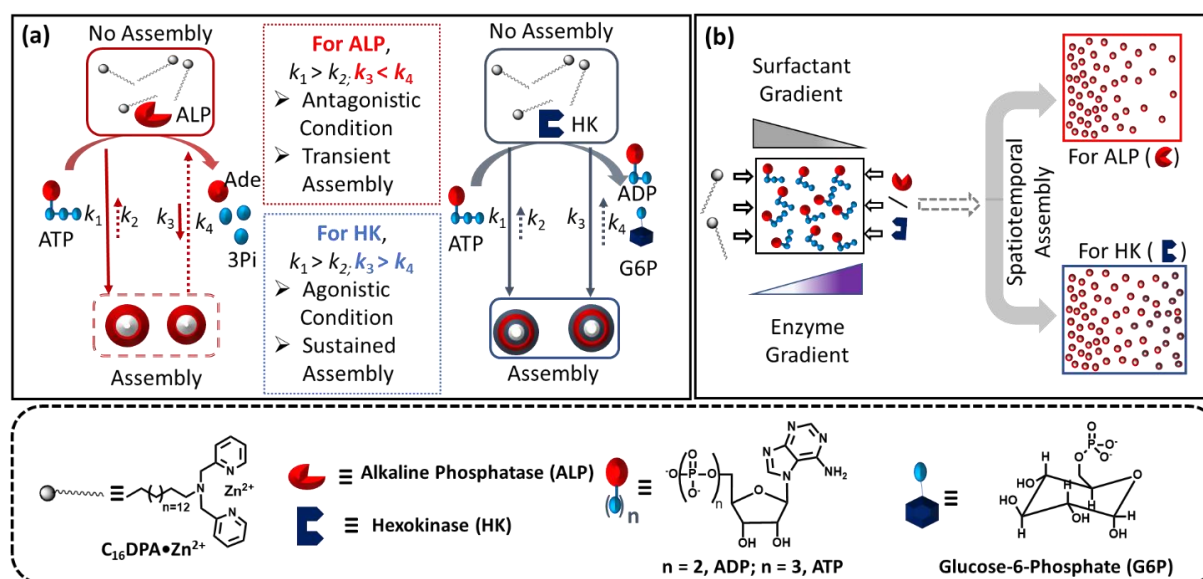


Figure 6.5. (a) Schematic representation of the different types of ATP-driven $C_{16}DPA \cdot Zn^{2+}$ surfactant assembly formation when ALP and HK are used separately. The glucose and $Mg(NO_3)_2$ in the system are not shown in the schematic for simplicity. Solid arrows denote assembly formation, whereas dashed arrows denote dissociation; the extent of association/dissociation is denoted by the length of the arrow. (b) Schematic representation of the spatiotemporal assembly formation of the surfactant templated by ATP when gradients of the surfactant and ALP or HK are maintained from opposite sides.

using MATLAB R2019b, FEATool Multiphysics (Figure 6.6 -6.9).^{60,61} Here, we collectively studied the transport mechanism of both the reactive and non-reactive species involved in the system, along with their rates of formation and dissociation (the mass balance equation described in eqn (6.1)–(6.4) has been employed, which was used for Figure 6.3) using computational fluid dynamics. Here, Fick's second law was used to obtain the distribution of each species involved as functions of time and space in the two-dimensional system. We selected a square-shaped space throughout which T (which helps to form the dimerized

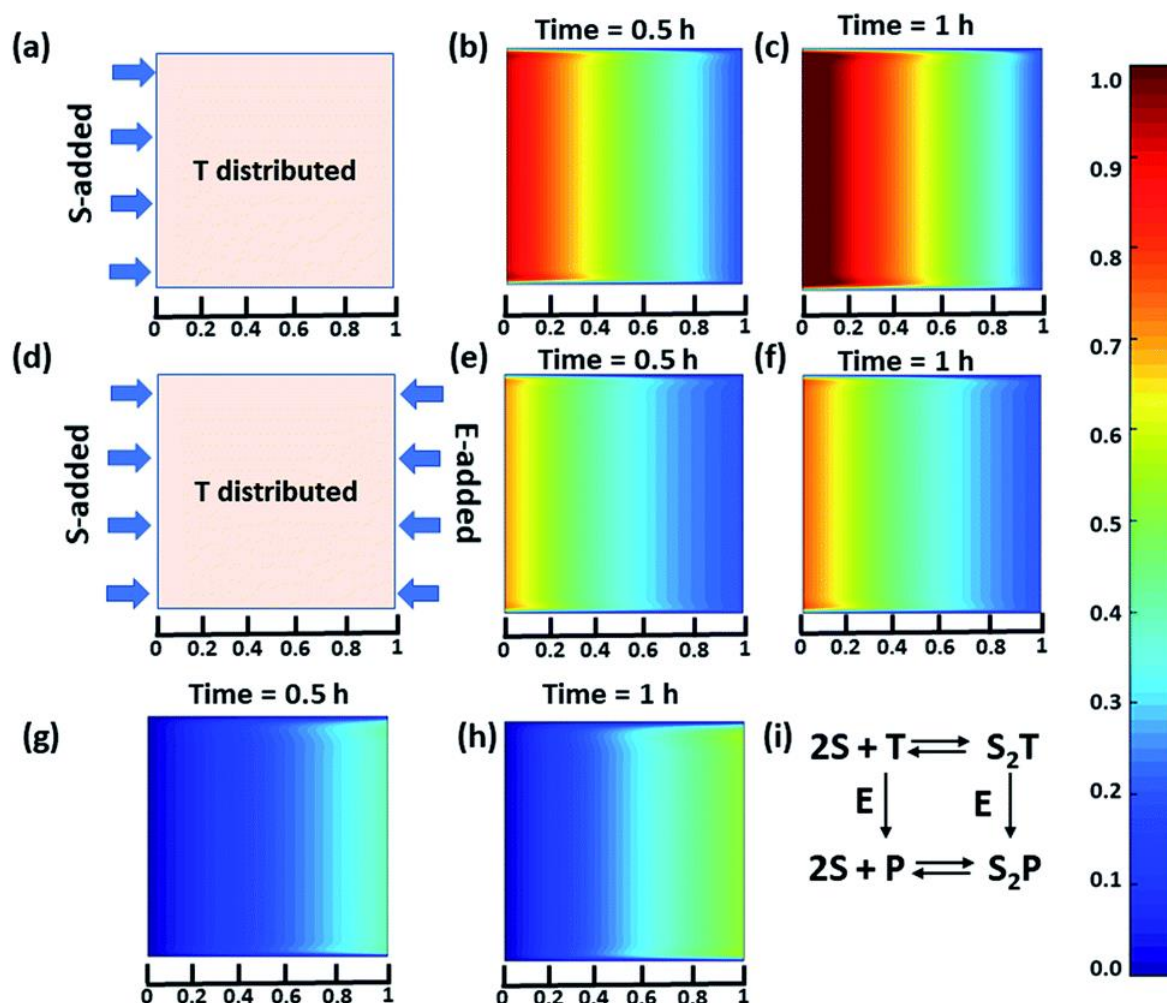


Figure 6.6. (a) Representative grid space when T is homogeneously distributed in space and S is added from the left boundary. Compositional distribution of S₂T (b) 0.5 h and (c) 1 h after adding S from the left boundary. (d) Representative sample space when T is distributed evenly and S and E are added from the left and right boundaries, respectively. S₂T distribution after (e) 0.5 h and (f) 1 h, and S₂P compositional distribution (g) 0.5 h and (h) 1 h after the addition of S and E from the left and right boundaries, respectively. (i) Set of equations followed in presence of E. Time is a dimensionless unit in this system; however, for the sake of logical comparison with the experiment, the hour has been chosen as the unit of time.

assembly of the monomer S) was homogeneously distributed. From the left side, the monomer S, and from the right side, the enzymatically formed P, then decreased in a periodic manner to

simultaneously form S_2T and S_2P in the square-shaped space. We assumed that monomers S and E do not interact, and thus, we did not use any E in the system; instead, only P (enzymatically transformed T) was considered. The color scale ranging from red to blue denotes the relative concentration of the assembled species (either S_2T or S_2P) in the different zones. First, we analyzed the distribution of S_2T in the absence of any product gradient with the addition of S from the left side. In this case, S_2T reached about 60% of the maximum possible intensity in terms of distribution at the exact midpoint after 1 h. However, when the enzyme was also added from the opposite side, the amount of S_2T was almost 30% lower at the left side near the S-rich zone compared to that in the system without the enzyme, and at the midpoint, it reached $\sim 40\%$ of the maximum possible intensity. Interestingly, in this case, the enzyme can convert T to P, which also has the ability to form S_2P . Therefore, we also observed the formation of S_2P with 40% of the maximum possible distribution near the right-side

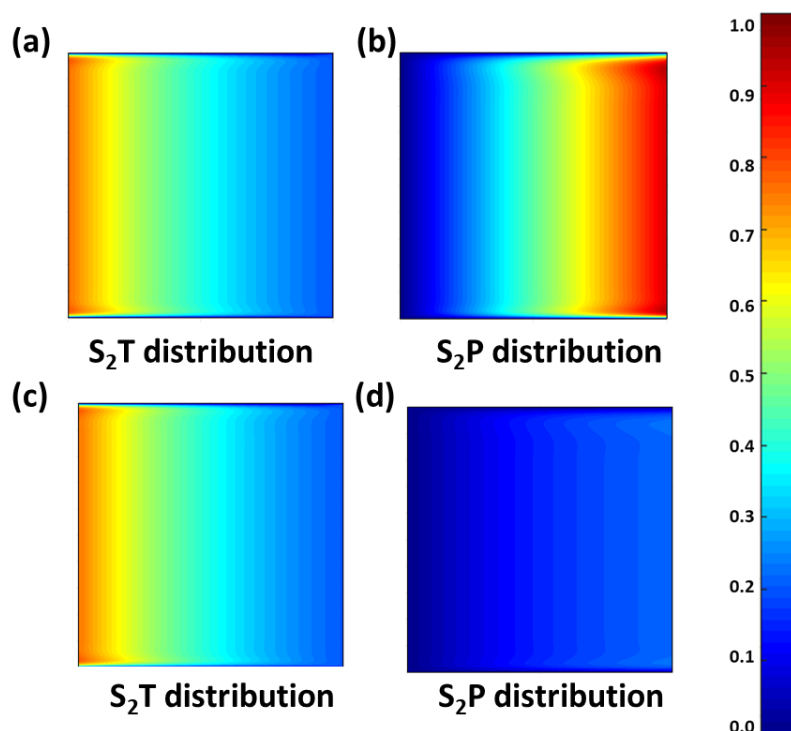


Figure 6.7. Compositional distribution of dimeric assembly that is, (a) S_2T , and (c) S_2P , when overall rate of change of S_2T formation on boundary 4 is $1 \mu\text{M}/\text{h}$, and S_2P formation on boundary 2 is $1 \mu\text{M}/\text{h}$. Compositional distribution of (b) S_2T , and (c) S_2P , when the overall rate of change of S_2T formation on boundary 4 is $1 \mu\text{M}/\text{h}$, and S_2P formation on boundary 2 is $0.1 \mu\text{M}/\text{h}$.

boundary where the enzyme was added. We also analyzed a few other possible scenarios using the same system for which the rate of change of S_2P at the right-side boundary is different (Figure 6.7). For this, we studied the effect of a change of parameters on dimeric assembly

formation. For this purpose, we varied the rate of change of S₂P formation on boundary 2 to 1 $\mu\text{M}/\text{h}$, and 0.1 $\mu\text{M}/\text{h}$, while keeping the rate of change of S₂T formation constant at boundary 4 at 1 $\mu\text{M}/\text{h}$. (Figure 6.7). Additionally, a detailed zone-wise analysis of the theoretical outcome of the spatiotemporal differentiation of the S₂T and S₂P intensity distribution has been given in the for the case described in Figure 6.8 and Figure 6.9. Overall, this analysis showed that the distribution of the assemblies on a 2-D surface can be modulated over time using enzymes, and variable surface patterns can be obtained in this manner. Encouraged by theoretical data, we aimed to observe the growth of assembled structures in spatially separated zones with concentration gradients of substrates (ATP) and enzymes (ALP and HK) on opposite sides. A glass slide was prepared with ATP solution containing C153 for visualization,

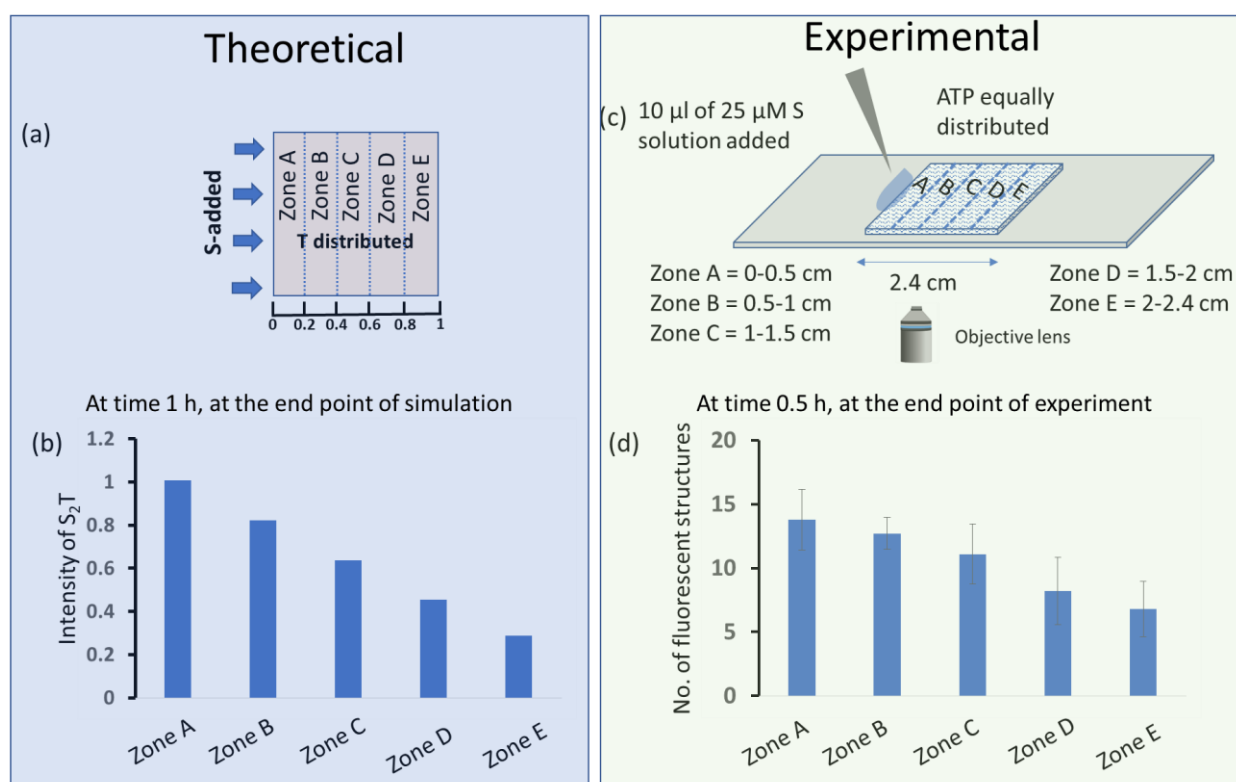


Figure 6.8. (a and c) A comparative study between theory and experiment when only S was added from the left side when T is distributed through the space (for theoretical modeling) and surfactant was added from the left side when ATP was distributed under the cover slip (for the experiment). (b and d) Both assembled structure S₂T (from theory) and the number of self-assembled units for surfactant and ATP assembly (from the experiment) were plotted across zones A to E at the end point of the simulation or experiment.

and a cover slip was placed over it. Concentration gradients were created by adding C16DPA·Zn²⁺ solution and ALP or HK solution at opposite edges of the cover slip. The area under the coverslip was divided into five zones (A-E). Without any enzyme, the number of

fluorescent structures was initially higher in zones A and B, closer to the surfactant addition area, compared to zones C-E. However, after 15 and 30 minutes, the number of structures in zones C-E increased significantly, and the rate of increase in fluorescence structures was similar in all zones. When ALP was added on the opposite side of the surfactant, the fluorescent structures exhibited dynamic changes over time. A sharp change was observed in zone C at 15 minutes, with a higher number of structures in zones A and B compared to zones C-E. The statistical analysis confirmed the significant difference between zones B and C at 15 and 30 minutes. On the other hand, the addition of HK resulted in spatiotemporal assembly behavior similar to the case without enzymes, with slightly higher numbers of structures in zones D and E. Over time, there was convergence in the number of structures among the zones. We also

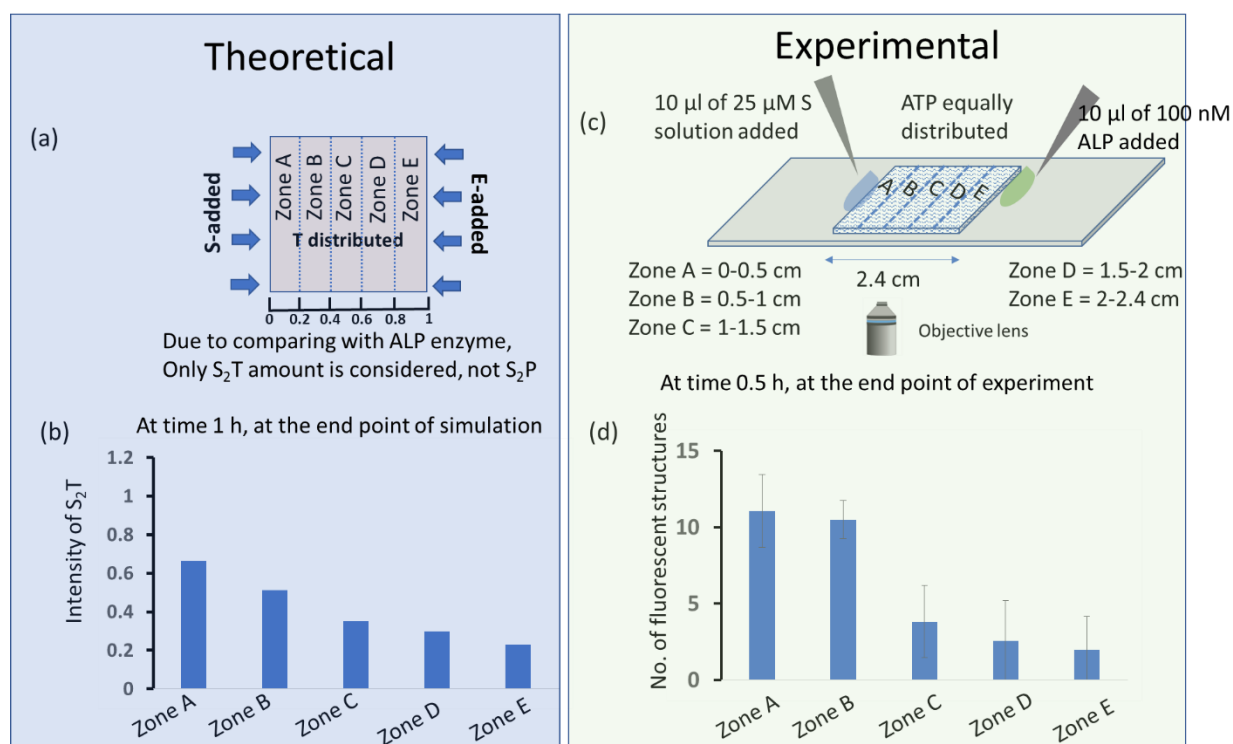


Figure 6.9. (a and c) A comparative study between theory and experiment when S was added from the left side and E from the right when T is distributed through the space (for theoretical modeling) and surfactant was added from the left side and ALP was added from the right when ATP was distributed under the cover slip (for the experiment). (b and d) Both assembled structure S_2T (from theory) and the number of self-assembled units for surfactant and ATP assembly (from the experiment) were plotted across zones A to E at the end point of the simulation or experiment.

carried out a zone-wise comparison of the results obtained from the theoretical prediction and experimental data. For the theoretical points, we plotted the number corresponding to the color intensity and also divided the 2-D space into five equal zones A–E along the x -axis to provide

a similar analysis for comparison with the experimental results. We observed similar trends in the increase in the number of S_2T assemblies (theoretical) and surfactant-bound ATP aggregates (experimental) in the absence of any enzyme, *i.e.*, when only S or the surfactant was added at the left side (please compare Figure 6.8). From this data, the decreasing trend of structures almost in an equal manner from zone A to E has been observed in both cases.

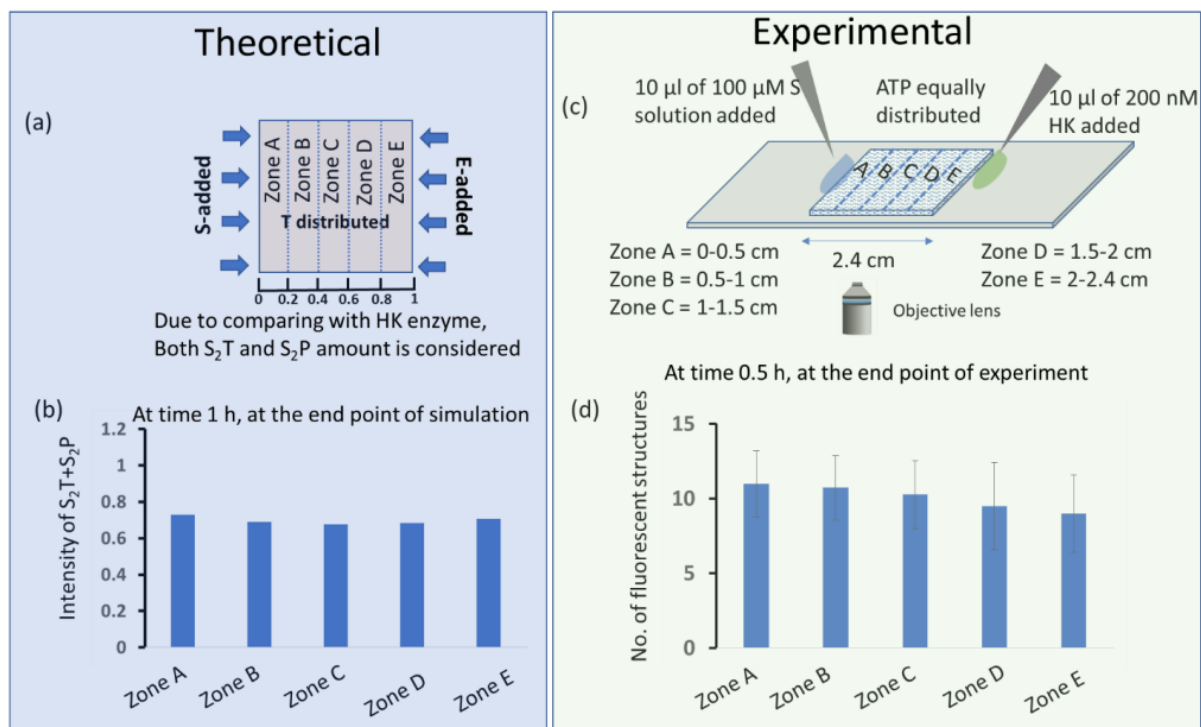


Figure 6.10. (a and c) A comparative study between theory and experiment when S was added from the left side and E from the right when T is distributed through the space (for theoretical modeling) and surfactant was added from the left side and HK was added from the right when ATP was distributed under the cover slip (for the experiment). (b and d) Both assembled structure S_2T (from theory) and the number of self-assembled units for surfactant and ATP assembly (from the experiment) were plotted across zones A to E at the end point of the simulation or experiment.

Also, similar trends of divergence and convergence of the structure population density with time from zone A to E in the presence of the enzymes ALP and HK was observed in both the theoretical and experimental studies (for comparison of ALP, please see Figure 6.9 for the theoretical results and the experimental ones; and for HK, please see Figure 6.10. From ALP data, the decreasing trend of structures and also the much lower number of structures in all zones compared to without E have been observed. The population decrease from zone A to E has been observed in both cases, where in the experiment zone A and B showed a higher number of structures, compared to zone C to E. A similar kind of trend was also observed in

the theoretical trend, however, such a clear discrimination between B and C zone was not observed. Also, from HK data, an almost equal number of structures in all zones have been observed, both in experiment and theory.

6.4 Summary

In conclusion, our study has demonstrated the remarkable potential of enzymes in generating diverse spatiotemporal dynamic self-assembly behaviors. Unlike previous studies focusing on transient self-assembly or self-assembly under dissipative conditions, we have successfully sustained assembly behavior and harnessed the generation of surface patterns through the modulation of aggregate population density in both theoretical and experimental settings. This breakthrough opens exciting possibilities for programmable spatiotemporal organization and the development of complex surface patterns. It is worth noting that similar reaction-diffusion systems have been explored in the past using inorganic salts, leading to the creation of various patterns and advancements in dynamic micro- and nanotechnology, as well as autonomous devices. Furthermore, recent reports have demonstrated spatiotemporal ordering and reaction networking in supramolecular gel networks using organic reaction-, pH-, or enzyme-reaction-based systems. Our work extends this line of research by investigating the assembly formation dynamics between a surfactant and nucleotides/phosphosugars. By utilizing different enzymes, we have revealed three distinct cases: a gradient of agonistic conditions, a gradient of antagonistic conditions, and simultaneous agonistic and antagonistic gradients at opposite sides. This level of control over the population of self-assembling units presents exciting prospects for selectively activating multiple reactions or functionalities at precise locations. Such precise control, whether in the assembled or disassembled state, can enable multilevel spatiotemporal regulation of multiple functions. Consequently, this approach holds significant potential in the design of life-like autonomous and intelligent systems. In a broader sense, our findings contribute to the development of nonlinear dynamical systems with complex life-like properties emerging from relatively simple or low-complexity systems. These results highlight the importance of harnessing chemical dynamics to achieve intricate and intelligent behaviors. By understanding and manipulating the principles underlying spatiotemporal organization, we pave the way for the design and construction of novel materials and devices with advanced functionalities. In summary, our research advances the understanding of enzyme-mediated spatiotemporal dynamic self-assembly, offering new avenues for the development of dynamic materials, nanotechnology, and intelligent systems. The ability to control and manipulate self-

assembly behavior in space and time brings us closer to realizing innovative applications in various fields, and it represents a significant step forward in the quest to create complex and life-like systems from simpler building blocks.

6.5 References

1. Grzybowski, B. A.; Fitzner, K.; Paczesny, J.; Granick, S. From Dynamic Self-Assembly to Networked Chemical Systems. *Chem. Soc. Rev.* **2017**, *46* (18), 5647–5678.
2. Kee, T. P.; Monnard, P.-A. Chemical Systems, Chemical Contiguity and the Emergence of Life. *Beilstein J. Org. Chem.* **2017**, *13* (1), 1551–1563.
3. Aubert, S.; Bezagu, M.; Spivey, A. C.; Arseniyadis, S. Spatial and Temporal Control of Chemical Processes. *Nat. Rev. Chem.* **2019**, *3* (12), 706–722.
4. Tsukada, M.; Ichinose, N.; Aihara, K.; Ito, H.; Fujii, H. Dynamical Cell Assembly Hypothesis - Theoretical Possibility of Spatio-Temporal Coding in the Cortex. *Neural Netw.* **1996**, *9* (8), 1303–1350.
5. Das, K.; Gabrielli, L.; Prins, L. J. Chemically Fueled Self-Assembly in Biology and Chemistry. *Angew. Chem. Int. Ed.* **2021**, *60* (37), 20120–20143.
6. Chaudhuri, A.; Bhattacharya, B.; Gowrishankar, K.; Mayor, S.; Rao, M. Spatiotemporal Regulation of Chemical Reactions by Active Cytoskeletal Remodeling. *Proc. Natl. Acad. Sci. U. S. A.* **2011**, *108* (36), 14825–14830.
7. Legrand, A.; Liu, L.-H.; Royla, P.; Aoyama, T.; Craig, G. A.; Carné-Sánchez, A.; Urayama, K.; Weigand, J. J.; Lin, C.-H.; Furukawa, S. Spatiotemporal Control of Supramolecular Polymerization and Gelation of Metal-Organic Polyhedra. *J. Am. Chem. Soc.* **2021**, *143* (9), 3562–3570.
8. Spreizer, S.; Aertsen, A.; Kumar, A. From Space to Time: Spatial Inhomogeneities Lead to the Emergence of Spatiotemporal Sequences in Spiking Neuronal Networks. *PLoS Comput. Biol.* **2019**, *15* (10), e1007432.
9. Ermentrout, B. Neural Networks as Spatio-Temporal Pattern-Forming Systems. *Rep. Prog. Phys.* **1998**, *61* (4), 353–430.
10. Dhers, S.; Holub, J.; Lehn, J.-M. Coevolution and Ratiometric Behaviour in Metal Cation-Driven Dynamic Covalent Systems. *Chem. Sci.* **2017**, *8* (3), 2125–2130.
11. Inoue, D.; Gutmann, G.; Nitta, T.; Kabir, A. M. R.; Konagaya, A.; Tokuraku, K.; Sada, K.; Hess, H.; Kakugo, A. Adaptation of Patterns of Motile Filaments under Dynamic Boundary Conditions. *ACS Nano* **2019**, *13* (11), 12452–12460.

12. Yashin, V. V.; Balazs, A. C. Pattern Formation and Shape Changes in Self-Oscillating Polymer Gels. *Science* **2006**, *314* (5800), 798–801.
13. Epstein, I. R.; Xu, B. Reaction-Diffusion Processes at the Nano- and Microscales. *Nat. Nanotechnol.* **2016**, *11* (4), 312–319.
14. Leira-Iglesias, J.; Tassoni, A.; Adachi, T.; Stich, M.; Hermans, T. M. Oscillations, Travelling Fronts and Patterns in a Supramolecular System. *Nat. Nanotechnol.* **2018**, *13* (11), 1021–1027.
15. Astumian, R. D.; Brody, R. Thermodynamics of Gradient Driven Transport: Application to Single-Particle Tracking. *J. Phys. Chem. B* **2009**, *113* (33), 11459–11462.
16. Deng, J.; Walther, A. ATP-Powered Molecular Recognition to Engineer Transient Multivalency and Self-Sorting 4D Hierarchical Systems. *Nat. Commun.* **2020**, *11* (1), 3658.
17. Morrow, S. M.; Colomer, I.; Fletcher, S. P. A Chemically Fuelled Self-Replicator. *Nat. Commun.* **2019**, *10* (1), 1011.
18. Fialkowski, M.; Bishop, K. J. M.; Klajn, R.; Smoukov, S. K.; Campbell, C. J.; Grzybowski, B. A. Principles and Implementations of Dissipative (Dynamic) Self-Assembly. *J. Phys. Chem. B* **2006**, *110* (6), 2482–2496.
19. Yu, H.; Jo, K.; Kounovsky, K. L.; de Pablo, J. J.; Schwartz, D. C. Molecular Propulsion: Chemical Sensing and Chemotaxis of DNA Driven by RNA Polymerase. *J. Am. Chem. Soc.* **2009**, *131* (16), 5722–5723.
20. Willner, I.; Basnar, B.; Willner, B. From Molecular Machines to Microscale Motility of Objects: Application as “Smart Materials”, Sensors, and Nanodevices. *Adv. Funct. Mater.* **2007**, *17* (5), 702–717.
21. Yang, S.; Schaeffer, G.; Mattia, E.; Markovitch, O.; Liu, K.; Hussain, A. S.; Ottel , J.; Sood, A.; Otto, S. Chemical Fueling Enables Molecular Complexification of Self-Replicators. *Angew. Chem. Int. Ed.* **2021**, *60* (20), 11344–11349.
22. Liu, B.; Beatty, M. A.; Pappas, C. G.; Liu, K.; Ottel , J.; Otto, S. Self-Sorting in Dynamic Combinatorial Libraries Leads to the Co-Existence of Foldamers and Self-Replicators. *Angew. Chem. Int. Ed.* **2021**, *60* (24), 13569–13573.
23. Pantarotto, D.; Browne, W. R.; Feringa, B. L. Autonomous Propulsion of Carbon Nanotubes Powered by a Multienzyme Ensemble. *Chem. Commun. (Camb.)* **2008**, No. 13, 1533–1535.
24. Jain, A.; Dhiman, S.; Dhayani, A.; Vemula, P. K.; George, S. J. Chemical Fuel-Driven Living and Transient Supramolecular Polymerization. *Nat. Commun.* **2019**, *10* (1), 450.

25. Illien, P.; Golestanian, R.; Sen, A. “Fuelled” Motion: Phoretic Motility and Collective Behaviour of Active Colloids. *Chem. Soc. Rev.* **2017**, *46* (18), 5508–5518.
26. Schwarz, P. S.; Laha, S.; Janssen, J.; Huss, T.; Boekhoven, J.; Weber, C. A. Parasitic Behavior in Competing Chemically Fueled Reaction Cycles. *Chem. Sci.* **2021**, *12* (21), 7554–7560.
27. Weißenfels, M.; Gemen, J.; Klajn, R. Dissipative Self-Assembly: Fueling with Chemicals versus Light. *Chem* **2021**, *7* (1), 23–37.
28. Grosso, E.; Prins, L. J.; Ricci, F. *Angew. Chem. Int. Ed* **2020**, *59*, 13238–13245.
29. Maiti, S.; Fortunati, I.; Ferrante, C.; Scrimin, P.; Prins, L. J. Dissipative Self-Assembly of Vesicular Nanoreactors. *Nat. Chem.* **2016**, *8* (7), 725–731.
30. van der Helm, M. P.; Wang, C.-L.; Fan, B.; Macchione, M.; Mendes, E.; Eelkema, R. Organocatalytic Control over a Fuel-Driven Transient-Esterification Network. *Angew. Chem. Int. Ed.* **2020**, *59* (46), 20604–20611.
31. Mahato, R. R.; Shandilya, E.; Dasgupta, B.; Maiti, S. Dictating Catalytic Preference and Activity of a Nanoparticle by Modulating Its Multivalent Engagement. *ACS Catal.* **2021**, *11* (14), 8504–8509.
32. van der Helm, M. P.; de Beun, T.; Eelkema, R. On the Use of Catalysis to Bias Reaction Pathways in Out-of-Equilibrium Systems. *Chem. Sci.* **2021**, *12* (12), 4484–4493.
33. Mishra, A.; Dhiman, S.; George, S. J. ATP-Driven Synthetic Supramolecular Assemblies: From ATP as a Template to Fuel. *Angew. Chem. Int. Ed.* **2021**, *60* (6), 2740–2756.
34. Ragazzon, G.; Baroncini, M.; Silvi, S.; Venturi, M.; Credi, A. Light-Powered Autonomous and Directional Molecular Motion of a Dissipative Self-Assembling System. *Nat. Nanotechnol.* **2015**, *10* (1), 70–75.
35. Sawczyk, M.; Klajn, R. Out-of-Equilibrium Aggregates and Coatings during Seeded Growth of Metallic Nanoparticles. *J. Am. Chem. Soc.* **2017**, *139* (49), 17973–17978.
36. Dhiman, S.; Jain, A.; George, S. J. Transient Helicity: Fuel-Driven Temporal Control over Conformational Switching in a Supramolecular Polymer. *Angew. Chem. Int. Ed.* **2017**, *56* (5), 1329–1333.
37. Shandilya, E.; Maiti, S. Deconvolution of Transient Species in a Multivalent Fuel-driven Multistep Assembly under Dissipative Conditions. *ChemSystemsChem* **2020**, *2* (2), e1900040.
38. Della Sala, F.; Neri, S.; Maiti, S.; Chen, J. L.-Y.; Prins, L. J. Transient Self-Assembly of Molecular Nanostructures Driven by Chemical Fuels. *Curr. Opin. Biotechnol.* **2017**, *46*, 27–33.

39. Wang, G.; Liu, S. Strategies to Construct a Chemical-fuel-driven Self-assembly. *ChemSystemsChem* **2020**, *2* (4).
40. Astumian, R. D. Kinetic Asymmetry Allows Macromolecular Catalysts to Drive an Information Ratchet. *Nat. Commun.* **2019**, *10* (1), 3837.
41. Ragazzon, G.; Prins, L. J. Energy Consumption in Chemical Fuel-Driven Self-Assembly. *Nat. Nanotechnol.* **2018**, *13* (10), 882–889.
42. te Brinke, E.; Groen, J.; Herrmann, A.; Heus, H. A.; Rivas, G.; Spruijt, E.; Huck, W. T. S. Dissipative Adaptation in Driven Self-Assembly Leading to Self-Dividing Fibrils. *Nat. Nanotechnol.* **2018**, *13* (9), 849–855.
43. Rothfield, L.; Taghbalout, A.; Shih, Y.-L. Spatial Control of Bacterial Division-Site Placement. *Nat. Rev. Microbiol.* **2005**, *3* (12), 959–968.
44. Ramm, B.; Goychuk, A.; Khmelinskaia, A.; Blumhardt, P.; Eto, H.; Ganzinger, K. A.; Frey, E.; Schwille, P. A Diffusiophoretic Mechanism for ATP-Driven Transport without Motor Proteins. *Nat. Phys.* **2021**, *17* (7), 850–858.
45. Krabbenborg, S. O.; Veerbeek, J.; Huskens, J. Spatially Controlled Out-of-Equilibrium Host-Guest System under Electrochemical Control. *Chemistry* **2015**, *21* (27), 9638–9644.
46. Yang, X.; Lu, H.; Tao, Y.; Zhou, L.; Wang, H. Spatiotemporal Control over Chemical Assembly in Living Cells by Integration of Acid-Catalyzed Hydrolysis and Enzymatic Reactions. *Angew. Chem. Int. Ed.* **2021**, *60* (44), 23797–23804.
47. Zhou, J.; Du, X.; Berciu, C.; He, H.; Shi, J.; Nicastro, D.; Xu, B. Enzyme-Instructed Self-Assembly for Spatiotemporal Profiling of the Activities of Alkaline Phosphatases on Live Cells. *Chem* **2016**, *1* (2), 246–263.
48. Maiti, S.; Fortunati, I.; Sen, A.; Prins, L. J. Spatially Controlled Clustering of Nucleotide-Stabilized Vesicles. *Chem. Commun. (Camb.)* **2018**, *54* (38), 4818–4821.
49. Malinowska, L.; Kroschwald, S.; Munder, M. C.; Richter, D.; Alberti, S. Molecular Chaperones and Stress-Inducible Protein-Sorting Factors Coordinate the Spatiotemporal Distribution of Protein Aggregates. *Mol. Biol. Cell* **2012**, *23* (16), 3041–3056.
50. Merino-Salomón, A.; Babl, L.; Schwille, P. Self-Organized Protein Patterns: The MinCDE and ParABS Systems. *Curr. Opin. Cell Biol.* **2021**, *72*, 106–115.
51. Beck, M.; Topf, M.; Frazier, Z.; Tjong, H.; Xu, M.; Zhang, S.; Alber, F. Exploring the Spatial and Temporal Organization of a Cell's Proteome. *J. Struct. Biol.* **2011**, *173* (3), 483–496.
52. Robinson, C. V.; Sali, A.; Baumeister, W. The Molecular Sociology of the Cell. *Nature* **2007**, *450* (7172), 973–982.

53. Niethammer, P.; Kueh, H. Y.; Mitchison, T. J. Spatial Patterning of Metabolism by Mitochondria, Oxygen, and Energy Sinks in a Model Cytoplasm. *Curr. Biol.* **2008**, *18* (8), 586–591.
54. Blayo, C.; Houston, J. E.; King, S. M.; Evans, R. C. Unlocking Structure-Self-Assembly Relationships in Cationic Azobenzene Photosurfactants. *Langmuir* **2018**, *34* (34), 10123–10134.
55. Philips, D. S.; Ghosh, S.; Sudheesh, K. V.; Suresh, C. H.; Ajayaghosh, A. An Unsymmetrical Squaraine-dye-based Chemical Platform for Multiple Analyte Recognition. *Chemistry* **2017**, *23* (71), 17973–17980.
56. Moro, A. J.; Cywinski, P. J.; Körsten, S.; Mohr, G. J. An ATP Fluorescent Chemosensor Based on a Zn(II)-Complexed Dipicolylamine Receptor Coupled with a Naphthalimide Chromophore. *Chem. Commun. (Camb.)* **2010**, *46* (7), 1085–1087.
57. Gao, H.; Chen, L.; Chen, J.; Guo, Y.; Ye, D. A Computational Study on the Hydrogenation of CO₂ Catalyzed by a Tetraphos-Ligated Cobalt Complex: Monohydride vs. Dihydride. *Catal. Sci. Technol.* **2015**, *5* (2), 1006–1013.
58. Chai, J.-D.; Head-Gordon, M. Long-Range Corrected Hybrid Density Functionals with Damped Atom-Atom Dispersion Corrections. *Phys. Chem. Chem. Phys.* **2008**, *10* (44), 6615–6620.
59. Korzec, M. D.; Ahnert, T. Time-Stepping Methods for the Simulation of the Self-Assembly of Nano-Crystals in Matlab on a GPU. *J. Comput. Phys.* **2013**, *251*, 396–413.
60. Potter, M. E.; Armstrong, L.-M.; Raja, R. Combining Catalysis and Computational Fluid Dynamics towards Improved Process Design for Ethanol Dehydration. *Catal. Sci. Technol.* **2018**, *8* (23), 6163–6172.
61. Groaz, A.; Moghimianavval, H.; Tavella, F.; Giessen, T. W.; Vecchiarelli, A. G.; Yang, Q.; Liu, A. P. Engineering Spatiotemporal Organization and Dynamics in Synthetic Cells. *Wiley Interdiscip. Rev. Nanomed. Nanobiotechnol.* **2021**, *13* (3), e1685.
62. Grace, M.; Hütt, M.-T. Regulation of Spatiotemporal Patterns by Biological Variability: General Principles and Applications to Dictyostelium Discoideum. *PLoS Comput. Biol.* **2015**, *11* (11), e1004367.
63. Dhiman, S.; Jain, A.; Kumar, M.; George, S. J. Adenosine-Phosphate-Fueled, Temporally Programmed Supramolecular Polymers with Multiple Transient States. *J. Am. Chem. Soc.* **2017**, *139* (46), 16568–16575.

CHAPTER 7

Conclusion and Future Perspectives

In conclusion, our study has provided valuable insights into the significant role of multivalent interactions in governing dynamicity and self-assembly phenomena in the context of colloidal systems. By leveraging the synergistic interactivity between enzymes, substrates, and nanoparticles, we have demonstrated the ability to achieve spatiotemporally controlled assembly formation and colloidal transport at both micro and macro scales. Our findings have shed light on the complex nature of multivalent interactions and their implications across various scientific and technological domains. Multivalency, characterized by the simultaneous binding of multiple ligands to a receptor, offers unique advantages such as enhanced affinity, selectivity, and cooperative binding events. While multivalency has been extensively studied in fields like chemistry, biology, and materials science, its impact on colloidal assembly, catalysis, and phoresis has remained relatively unexplored.

Through our experimental and theoretical investigations, we have showcased the diverse applications of multivalent interactions. One significant aspect of our study was the patterning of colloids through the binding of multivalent adenosine nucleotides to cationic nanoparticles in the presence of the enzyme alkaline phosphatase (ALP). This controlled assembly formation process allowed us to modulate the aggregation patterns of nanoparticles and enzymes in microfluidic channels and on glass slides. Additionally, we exploited the coffee ring effect, observed during the evaporation of colloidal droplets, by introducing ATP-loaded nanoparticles into blood serum, presenting a potential low-cost approach for disease diagnostics. Moreover, we have demonstrated the potential of multivalent interactions in catalytic applications. By utilizing the assembled nanoparticles as reactors for hydrophobic substrates, we enhanced catalytic reactivity for the Kemp elimination reaction. This approach harnesses the hydrophobic sites provided by the assembly formation, offering a unique platform for optimizing catalytic reactions. In addition to the experimental investigations, we delved into the theoretical aspects of multivalent interactions. By employing kinetic modeling with Python, we explored the temporal evolution of intermediate species during multistep assembly under dissipative conditions. This approach allowed us to examine the compositional behavior and survival period of each species, providing deeper insights into the dynamics of multivalent interactions.

The understanding of multivalent interactions and their impact on colloidal assembly, catalysis, and phoresis opens up exciting opportunities for future research and applications. Further exploration in this field can lead to the development of advanced functional materials, targeted therapies, and programmable systems with enhanced adaptability and performance. One

avenue for future research lies in unraveling the dynamics of intermediate species formed during multistep assembly formation. By investigating the strength of dissipation, such as enzyme concentration, researchers can gain a better understanding of the compositional behavior of each species over time. This knowledge can pave the way for the design of more sophisticated self-organized systems with programmed functionality, offering greater control over spatial organizational adaptability.

Furthermore, the application of multivalent interactions can be expanded to other areas of nanotechnology, biomedicine, and materials science. By leveraging the power of multivalency, researchers can explore new possibilities in sensor technology, smart materials, and responsive devices. The ability to precisely control assembly formation, colloidal transport, and phoresis opens doors for the development of innovative solutions in drug delivery systems, diagnostics, and nanoscale devices.. The insights gained from this research lay the groundwork for a myriad of exciting possibilities across scientific and technological realms. As we venture into the uncharted territory of the future, several key directions emerge that promise to advance our understanding and harness the potential of multivalent interactions:

Precision Engineering of Multivalent Systems:

As researchers delve deeper into the world of multivalent interactions, they can employ advanced computational simulations, molecular modeling, and machine learning algorithms to predict and optimize the behavior of multivalent systems. This will enable the design of tailor-made ligands and receptors with specific binding affinities and kinetic profiles. The ability to precisely engineer multivalent interactions opens doors to creating intricate assembly patterns, programmable nanostructures, and controlled release mechanisms. These advancements could find applications in nanofabrication, nanoelectronics, and even in the development of designer molecules for specific tasks.

Dynamic and Adaptive Materials:

Building on the understanding of multivalent interactions, researchers can pioneer the development of materials that respond dynamically to external stimuli. By incorporating multivalent interactions into the structural design, materials can undergo reversible transformations, changing their properties based on environmental conditions. These materials could reshape themselves in response to temperature changes, pH fluctuations, or other triggers. Such innovations could lead to self-repairing materials, shape-shifting surfaces, and adaptive coatings with applications in aerospace, robotics, and beyond.

Therapeutics and Drug Delivery:

The potential impact of multivalent interactions in the field of therapeutics is profound. Researchers can engineer nanoparticles with multivalent ligands that target specific receptors on diseased cells, enhancing the precision of drug delivery. Multivalency can also be leveraged to design drug carriers that respond to cellular cues, releasing therapeutic payloads only when certain conditions are met. This targeted approach can improve therapeutic efficacy, minimize side effects, and reduce the development of drug resistance. Also, as multivalent interactions can lead to more stable colloidal assemblies compared to assemblies formed through single-site interactions. The presence of multiple binding sites and receptors enhances the overall strength of the interactions, making the aggregates less prone to dissociation or disassembly in the physiological environment. This enhanced stability is crucial for drug delivery vehicles to effectively reach their target sites without prematurely releasing the encapsulated drugs. Apart from this, the long-term stability provided by multivalent interactions allows for better control over the release of drugs from the colloidal assemblies. The aggregates can be designed to gradually release their cargo over time, ensuring a sustained and controlled release profile. This is essential for achieving the desired therapeutic effect and minimizing potential side effects. Moreover, multivalent interactions can be tailored to achieve specific targeting of colloidal assemblies to particular cells or tissues. By designing ligands that recognize specific receptors on target cells, the aggregates can be directed to the intended site of action, increasing the precision of drug delivery and minimizing off-target effects.

Nanomedicine and Diagnostics:

In the realm of nanomedicine, the understanding of multivalent interactions can lead to the creation of highly sensitive and specific diagnostic tools. Researchers can design nanoparticles with multivalent ligands that bind to disease markers, enabling early detection of illnesses. Additionally, multivalent interactions can facilitate the development of imaging agents that provide detailed insights into cellular processes. These advancements could revolutionize medical diagnostics, allowing for more accurate and timely disease detection.

Environmental Applications:

The principles of multivalent interactions can contribute to innovative solutions for environmental challenges. Researchers can engineer nanoparticles with multivalent receptors that selectively bind to pollutants or contaminants, facilitating efficient removal from water sources. Multivalency-driven materials can also be used to capture and store renewable energy

sources, such as sunlight or kinetic energy, for later use. These applications have the potential to contribute significantly to sustainable resource management and environmental protection.

Integration with Emerging Technologies:

Multivalent interactions can intersect with emerging technologies in transformative ways. For instance, in the field of quantum computing, understanding and controlling multivalent interactions could lead to improved qubit stability and enhanced quantum information processing. In synthetic biology, multivalency-driven cellular interactions could be harnessed to engineer novel biological circuits with advanced functionalities.

In summary, the future perspectives outlined here illustrate the vast potential that the understanding of multivalent interactions holds across various scientific and technological domains. By delving deeper into these directions, researchers have the opportunity to reshape industries, revolutionize healthcare, address environmental challenges, and pioneer groundbreaking technologies that contribute to the betterment of society as a whole.

Overall, our study has provided a foundation for future perspectives that highlight the pivotal role of multivalent interactions in shaping dynamicity and self-assembly phenomena within colloidal systems. The study of multivalent interactions in the context of colloidal systems holds immense potential for future advancements. By deepening our understanding of the intricacies of multivalency and its influence on dynamic self-assembly phenomena, researchers can unlock transformative breakthroughs that impact various scientific and technological disciplines. The exploration of multivalent interactions in colloidal systems not only expands our fundamental understanding but also offers practical applications with wide-ranging implications for industry, healthcare, and beyond.